Humidity related magnetite alteration

Dissertation

der Mathematisch-Naturwissenschaftlichen Fakultät

der Eberhard Karls Universität Tübingen

zur Erlangung des Grades eines

Doktors der Naturwissenschaften

(Dr. rer. nat.)

vorgelegt von

M.Sc. Qi Zhang

aus Beijing/China

Tübingen

2020

Gedruckt mit Genehmigung der Mathematisch-Naturwissenschaftlichen Fakultät der Eberhard Karls Universität Tübingen.

Tag der mündlichen Qualifikation:	06.11.2020
Stellvertretender Dekan:	Prof. Dr. József Fortágh
1. Berichterstatter:	Prof. Dr. Erwin Appel
2. Berichterstatter:	Prof. Dr. Tilo von Dobeneck

Declaration of Collaborative Publications

I declare that this accumulative dissertation has been composed by myself. I confirm that I am the lead author of the work presented in Chapters III, IV, V. My contribution and those of the other authors to each paper were explicitly indicated at the beginning of each Chapter. The paper in Chapter III is accepted for publication in ***Geophysical Journal International***. The paper in Chapter V is accepted for publication in ***Journal of Geophysical Research: Solid Earth***, and the manuscript in Chapter IV will be submitted soon after further revision.

Abstract

Maghemitization of magnetite is an important topic in rock magnetism. It happens as low-temperature oxidation (LTO) under normal atmospheric conditions, causing gradual transformation of magnetite to maghemite, and potentially culminating in transformation to hematite. Better understanding of how humidity and temperature affect LTO is of great interest for paleoclimate studies, which use magnetic properties as proxies.

A laboratory experiment was conducted under controlled humidity and temperature conditions. Natural magnetite powder samples were exposed to different relative humidity (rH) at room temperature (room humidity and rH >90 %) and at 70 °C (rh of 5 %, 13 %, >90 %). After one year, the magnetite sample that was exposed to highest relative humidity (>90 %) at 70 °C showed the strongest increase in the oxidation degree by ~3 % according to Verwey transition temperature (T_V), and it was the only setup in which hematite was detected by Mössbauer analysis. Other setups at 70 °C also showed a measurable change in the degree of LTO, but the dependence on humidity was found to be non-linear. For better understanding the influence of humidity and temperature on magnetite oxidation in natural environments, magnetic properties of basalts and weathered pebble samples directly above the fresh rock were studied. Basalts and pebble samples were collected from the Deccan traps in India along a gradient of mean annual precipitation (MAP) between ~500 and ~4000 mm, and from the Emeishan traps in SW-China allowing a comparison of alteration at approximately same MAP (~1000 mm) but ~15 °C different mean annual temperatures. The selected basalts contain magnetite that probably derived from exsolution during cooling. The weathered pebbles were divided into five groups by their grain size, and an increasing tendency of alteration is expected with grain size fining. The results suggest no systematic humidity-related changes of magnetic parameters between basalts and their weathered pebbles. Combining the results of both the laboratory experiment and the study of natural basalts, a humidity and temperature influence on the degree of oxidation is evidenced, however, it does not occur in a linear way, and the initial rock composition seems to mask the climate-related alteration effects in nature. Further studies on natural rock settings with other rock types and laboratory experiments with more variable humidity and temperature conditions are needed.

LTO could also play a role when material is translocated from the source to a sink. Soil and lake sediments archives often preserve important paleoclimate signals. In a source-sink setting, in which soil contributes as the major source for lake sediments or basin deposits, the possible

changes of the properties of magnetic minerals during transport are important factors for interpreting magnetic properties in the sink material as climate proxies. A study was conducted, in which the only important magnetic source material delivered to a small lake (Caohai Lake) is highly magnetic red soil with susceptibilities (χ) of ~10^{-5} m^3/kg, dominated by pedogenic highly maghemitized nano-magnetite (~10-15 nm) arranged in aggregates of ~100 nm, causing superparamagnetic (SP) behavior that tails into the stable single-domain (SSD) range. Partial disintegration of the aggregates and increasing alteration of the magnetite nanoparticles to hematite during transfer of the source material to Caohai Lake was interpreted from transmission electron microscopy results and frequency dependence of χ. The results indicate that the contribution of magnetite nano-particles to the magnetic properties of lake sediments diminishes by disintegration of aggregates and increased magnetite-to-hematite transformation and may even become neglectable compared to the larger sized detrital magnetic fraction. The ratio of saturation magnetization and χ is suggested as a useful proxy in red soil, caused by climate-related initial LTO degree in the nano-particles of the aggregates.

Zusammenfassung

Die Maghemitisierung von Magnetit ist von großer Bedeutendung im Gesteinsmagnetismus. Sie erfolgt als Niedertemperatur-Oxidation (LTO) unter normalen atmosphärischen Bedingungen und verursacht eine graduelle Umwandlung von Magnetit in Maghemit, welche zur Umwandlung in Hämatit führen kann. Ein besseres Verständnis darüber, wie Feuchtigkeit und Temperatur LTO beeinflussen, ist von großem Interesse für Paläoklimastudien, die magnetische Eigenschaften als Proxy verwenden.

Ein Laborexperiment wurde unter kontrollierten Feuchtigkeits- und Temperaturbedingungen durchgeführt. Proben aus natürlichem Magnetitpulver wurden bei Zimmertemperatur (Raumfeuchte und rh >90 %) und bei 70 °C (rh von 5 %, 13 %, >90 %) unterschiedlichen relativen Feuchten (rh) ausgesetzt. Nach einem Jahr zeigte die Magnetitprobe, die bei 70 °C der höchsten relativen Luftfeuchtigkeit (>90 %) ausgesetzt war, die stärkste Zunahme des Oxidationsgrades um ~3 %, entsprechend der Verwey Übergangstemperatur (T_v), und es war die einzige Anordnung, in der Hämatit durch Mössbauer-Analyse nachgewiesen wurde. Andere Anordnungen bei 70 °C zeigten ebenfalls eine messbare Änderung des LTO-Grades, aber die Abhängigkeit von der Feuchtigkeit war nicht linear. Um den Einfluss von Feuchtigkeit und Temperatur auf die Magnetit-Oxidation in natürlicher Umgebung besser zu verstehen, wurden die magnetischen Eigenschaften von Basalten und Verwitterungspartikel direkt über dem frischen Gestein untersucht. Dazu wurden Proben in zwei Gebieten genommen, entlang eines Gradienten des mittleren Jahresniederschlags (MAP) zwischen ~500 und ~4000 mm in den Deccan-Flutbasalten in Indien und in den Emeishan-Flutbasalten in SW-China, welche einen Vergleich bei~15 °C verschiedenen Jahresmitteltemperaturen bei ungefähr gleichem MAP (~1000 mm) ermöglichten. Die ausgewählten Basalte enthalten Magnetit, welcher wahrscheinlich durch Entmischung beim Abkühlen entstanden ist. Die Verwitterungspartikel wurden nach ihrer Korngröße in fünf Gruppen unterteilt, wobei angenommen wird, dass mit Korngrößenverfeinerung eine Tendenz zunehmender Alteration verbunden ist. Die Ergebnisse zeigen keine systematischen feuchtigkeitsbedingten Veränderungen der magnetischen Parameter zwischen Basalten und den Verwitterungspartikel. Kombiniert man die Ergebnisse des Laborexperiments und der Untersuchung der Basalte, so lässt sich ein Einfluss der Feuchtigkeit und der Temperatur auf den Oxidationsgrad feststellen, welcher jedoch nicht linear ist und wobei die anfängliche Gesteinszusammensetzung die klimabedingten Veränderungen zu überdecken scheint. Weitere Studien natürliche Gesteinssettings mit anderen

Gesteinsarten und Laborexperimente mit variableren Feuchtigkeits- und Temperaturbedingungen sind erforderlich, um zusätzliche Informationen zu gewinnen.

LTO könnte auch eine Rolle spielen, wenn Material von der Quelle in eine Senke umgelagert wird. In Böden und Seesedimenten werden oft wichtige Paläoklimasignale gespeichert. In einem Quelle-Senke-Szenario, in der der Böden als Hauptquelle für Seesedimente oder Beckenablagerungen fungieren, sind die möglichen Veränderungen der Eigenschaften von magnetischen Mineralien während des Transports wichtige Faktoren für die Interpretation der magnetischen Eigenschaften als Klima-Proxies. Es wurde eine Studie durchgeführt, in der hochmagnetische rote Böden mit Suszeptibilitäten (χ) von ~10^{-5} m^3/kg das einzige wichtige magnetische Ausgangsmaterial für einen kleinen See (Caohai-See) sind. Die Böden werden von pedogenem hochmagnetischen Nanomagnetit-Partikel (~10-15 nm) dominiert, welche in Aggregaten von ~100 nm angeordnet sind. Dadurch werden superparamagnetische (SP) Eigenschaften verursacht und teilweise auch stabiles Einbereichsteilchen (SSD) Verhalten. Anhand der Ergebnisse von Transmissionselektronenmikroskopie und der Frequenzabhängigkeit von χ wurde ein teilweiser Zerfall der Aggregate und eine zunehmende Umwandlung der Magnetit-Nanopartikel in Hämatit während des Materialtransfers in den Caohai-Seeinterpretiert. Die Ergebnisse deuten darauf hin, dass der Beitrag von Magnetit-Nanopartikeln zu den magnetischen Eigenschaften von Seesedimenten durch den Zerfall von Aggregaten und eine verstärkte Magnetit-Hämatit-Umwandlung abnimmt und im Vergleich zur detritischen Fraktion mit größeren Magnetitpartikeln sogar vernachlässigbar werden kann. Das Verhältnis der Sättigungsmagnetisierung und χ könnte ein aussagekräftiger Proxy in roten Böden darstellen, verursacht durch den klimabedingten LTO-Grad in den Nanopartikeln der Aggregate bei deren Bildung.

Acknowledgement

This dissertation would not have become a reality without all the helps and supports from many individuals. First, I would like to thank the German Research Foundation (DFG) for the financial support of my doctoral research, and the Geophysics research group of Tübingen Universität for offering me the opportunity to study here.

I would like to express my deeply gratitude to Prof. Erwin Appel, who has been helping me, supporting me and motivating me with all the patience and enthusiasm through these years. My sincere thanks extent to my second supervisor, Prof. Shouyun Hu, it has been wonderful working with him. I honestly appreciate their help and support at field works, measurements arrangements, results discussions, guide for paper writing and many other supports.

Furthermore, I would also like to say thank you to those whom I have had the pleasure to work with during the past years, members of the geophysics group, the administration department of geosciences, Prof. Nathani Basavaiah, Prof. Longsheng Wang, Dr. Nicolai Thüns, Julian Sorwat, Timm Bayer and several student assistants who helped me with tons of measurements. Especially to Dr. Wolfgang Rösler, Dr. James Byrne and Prof. Helge Stanjek, for their constant support and help with lab experiment designs, improvement of specific measurements and valuable discussions.

Last but not the least, my thanks go out to my dearest family, my wonderful parents, for offering me nothing but unconditional love and understanding. Especially to Yizhou, for his enduring love, and always be there comforting me when I feel down, encouraging me when I question myself, inspiring me in so many ways. I could not have come this far without their unparalleled support.

Table of contents

Chapter I: Thesis organization and list of publications

In this cumulative doctoral thesis three papers are included, two of them are accepted (Chapter III & V), one is in preparation and will be ready for submitting soon (Chapter IV).

Published/Accepted paper

Zhang, Q., Appel, E., Stanjek, H., Byrne, J.M., Berthold, C., Sorwat, J., Rösler, W., Seemann, T., 2020. Humidity related magnetite alteration in an experimental setup. Geophysical Journal International. DOI: 10.1093/gji/ggaa394

Zhang, Q., Appel, E., Hu, S., Pennington, R.S., Meyer, J., Neumann, U., Burchard, M., Allstädt, F., Wang, L.S., 2020. Nano-magnetite aggregates in red soil on low magnetic bedrock, their change during transport and implications for paleoclimate studies. Journal of Geophysical Research: Solid Earth. DOI: 10.1029/2020JB020588

Manuscript in preparation

Zhang, Q., Appel, E. Basavaiah, N., Hu, S.Y., Zhu, X.H., Neumann, U., Is alteration of magnetite in rock weathering related to climate? (in progress)

Chapter II: Introduction

Rock magnetism deals with magnetic properties of various materials such as rocks, sediments, soils, sands, dusts, contaminants, archeological materials, meteorites. Magnetic minerals in rocks and sediments carry information of the ambient geomagnetic field during their formation, and they record the past climate change history. Thus, magnetic characteristics could be used for reconstruction and semi-quantifying of paleoclimate conditions.

Magnetite is the most common and important magnetic mineral in nature, and its alteration in basalts was intensively studied with regard to the interpretation of remanent magnetizations (Irving, 1970; Petersen & Vali, 1987; Xu et al., 1997; Zhou et al., 2001). Low-temperature oxidation (LTO), also known as maghemitization, is a common alteration process of magnetite under normal atmospheric conditions. LTO gradually alters magnetite by oxidation of Fe(II) to Fe(III), leading to lattice vacancies, with maghemite (γ-Fe_2O_3) as the fully oxidized form (Readman & O'Reilly, 1972; O'Reilly 1984). Van Velzen & Dekkers (1999) suggested that LTO could occur during weathering in the outcrop and also during transport and deposition. Preliminary studies show that oxidation in air at room temperature can take place in time scales of several hundred days (Topsøe et al., 1974; Bourgeois et al., 2013), when grain-size is getting smaller from about 100 nm to sizes of few nm (Demortière et al., 2011; Byrne et al., 2016). Presence of bacterial activity can speed up the reactions to days (Byrne et al., 2015). Ahmed & Maher (2018) also reported a strong dependence of LTO on geochemical conditions such as pH. Paleoenvironmental studies have so far paid only little attention to climatic related magnetite alteration that happens during rock weathering. This is the basic motivation for the present dissertation study.

Maghemitization and the transformation of magnetite to hematite or goethite likely depends on moisture availability as iron oxidation requires an electrolyte such as water to occur (Davison & Seed, 1983). In some recent paleoclimate archives studies humidity-control of magnetite weathering in the catchment was proposed (Basavaiah & Khadikar, 2004; Herb et al., 2013; Basavaiah et al., 2015; Hu et al., 2015). Using magnetic properties as paleoclimate proxies needs improved understanding on how humidity and temperature affect such processes.

The fundamental question underlying the work in my PhD addresses the possible humidity control of magnetite alteration during rock weathering. How can this hypothesis be tested and analyzed? An actualistic study of natural rock weathering in different climates is certainly the

most direct way, but controlled humidity and temperature conditions and time can be better achieved in laboratory experiments. For better understanding the influence of humidity and temperature on the alteration of magnetite and how it impacts paleomagnetic studies, both a laboratory study (Fig. 1A) and an actualistic study (Fig. 1B) were chosen in the present work. First, magnetite alteration was studied under controlled temperature and humidity conditions in laboratory setups (Chapter III). The challenge in interpreting the results obtained for laboratory conditions is the transformation to natural processes in which much longer times are involved. Second, in an actualistic approach, magnetite alteration was investigated on natural rocks in different settings of mean annual precipitation and mean annual temperature, for which basalts and related weathered pebbles from the Deccan traps in India and the Emeishan traps in SW-China were investigated (Chapter IV). However, natural processes are always affected by the complexity of different influencing factors, which are often very difficult to discriminate. The uncertainties in this study arise from unknown initial stoichiometry, cation substitution, and the presence of other magnetic mineral phases, which partly obscure the results.

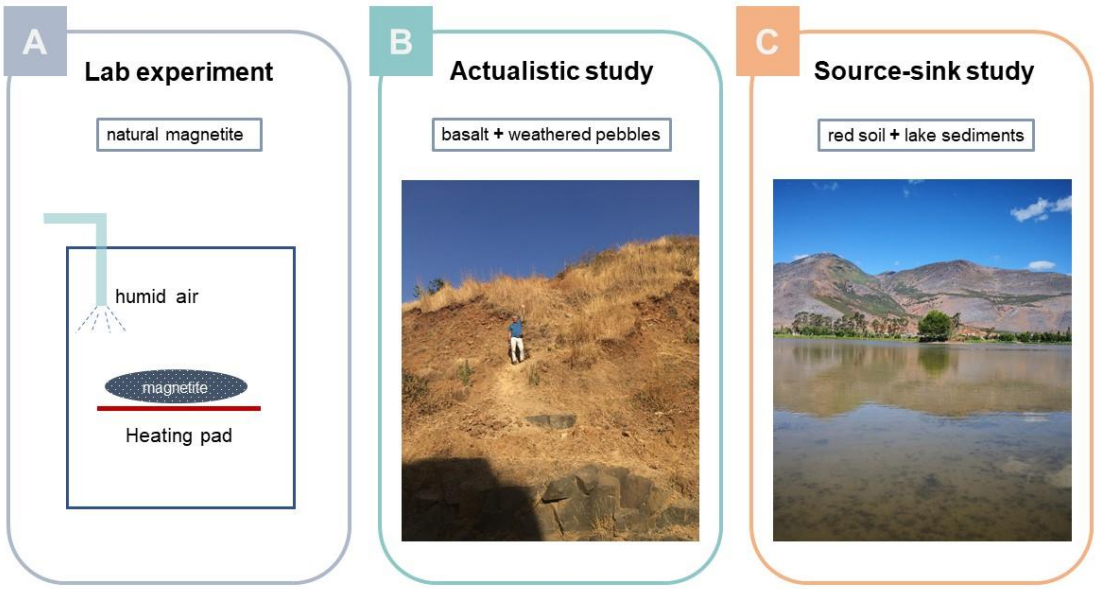

Figure 1. The three approaches of the PhD work.

Another important issue is the question where and under which conditions alteration happens between in situ rock weathering, producing the source material for erosion, and the arrival of the weathered materials in a sink such as in a lake. Lake sediments are important archives for paleoenvironment studies (Gasse et al., 1991; An et al., 2011). To investigate such scenarios magnetic proxies are often considered because of fast and non-constructive measurement

procedures. However, the link between soil (source material of sediments) and sediments (sink of source material) are rarely studied. Changes of source areas, weathering in the catchment area, transport-related effects, and authigenic processes, potentially influence magnetic properties of the sediments. Knowledge of the catchment characteristics can provide a better understanding of response mechanisms of paleoclimate variation and changes during material translocation. A source-sink case study is presented in Chapter V, which addresses magnetite alteration during relocation of weathered material for a specific case (Fig. 1C).

Magnetite alteration in a laboratory experiment (Chapter III)

Natural magnetite from Sweden was chosen for a one-year laboratory experiment (Chapter III). Grain sizes of these magnetite particles range from <1 µm to ~30 µm as detected by micrographs. According to the results of X-ray diffraction and thermomagnetic analyses (Verwey transition temperature and Curie temperature), the used magnetites are near stoichiometric (~2 % of LTO).

Magnetite samples were placed into six 20x26x30-cm large experimental containers at different temperature (T) and relative humidity (rH) conditions (Fig. 2) for one year. A heating pad and a humidifier with self-regulation devices were used to control temperature and relative humidity. The magnetite starting material was sealed and sheltered from sunlight. When ending the experimental exposure after one year, the samples were air dried at room temperature. (Zhang et al., 2020)

Low-temperature thermomagnetic curves are often used to determine the Verwey transition of magnetite. Result from this experiment show a systematic shift of the Verwey transition towards lower temperature for all 70 °C setups. The sample from setup HH shows the lowest Verwey transition temperature (T_v), followed by HD and HH-HD with almost the same T_v shift (Fig.3). The χ-T slope of the χ-T curves at T=T_v were additionally calculated. All 70 °C setups show a flatter slope compared to the original magnetite, with similar flattening for HS, HD and HH-HD, and a clearly flattest slope for HH (Fig. 4). Increasing flattening suggests a stronger gradient of different LTO degree. Sample HH also show the highest Curie Temperature (T_c) (596 °C) compared to all the other setups (T_c~584-586 °C), which is in agreement with the concluded highest degree of oxidation for HH.

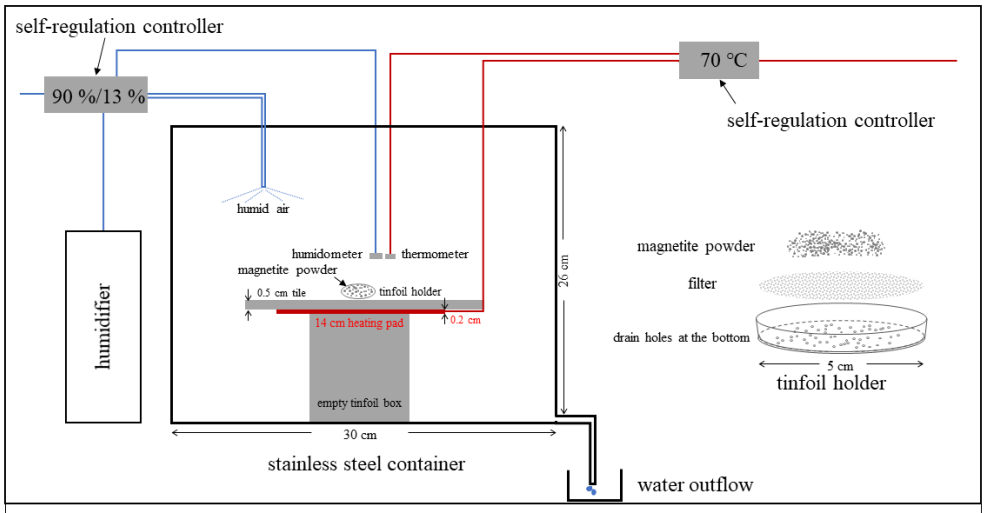

	Temperature [°C]	Relative Humidity [%]
HH	70	>90
HH-HD	70	2 weeks switch HH <=> HD
HS	70	13 (equals specific humidity as for rH=100 % at T=25 °C)
HD	70	5
RH	RT varying at 20~30	>90
RR	RT varying at 20~30	variable room humidity

Figure 2. Scheme of the laboratory experimental setup model (drawing not to scale).

Lattice constants (*a*) show significant differences between each sample, sample HH with the lowest value of *a* corresponding to the highest degree of maghemitization. The combined results of T_V and *a* indicate that the alteration affects the particles as a whole, not only a surface layer. Strongly altered thin particle surfaces may also exist and may escape our analytical results. However, such thin surface layers will only make up a minor fraction of the total particle volumes and therefore will only contribute little to macroscopic magnetic properties.

Samples placed in extremely dry conditions at 70 °C (HD), and also samples which were alternatingly exposed to extremely dry and wet conditions (HH-HD) both acquired a smaller degree of LTO. The smallest change of the high temperature setups was revealed for the sample with intermediate rH of ~13 % (HS). Mössbauer analysis indicates that hematite was produced during the experimental period in setup HH, even though it is not detected by the X-ray diffraction result.

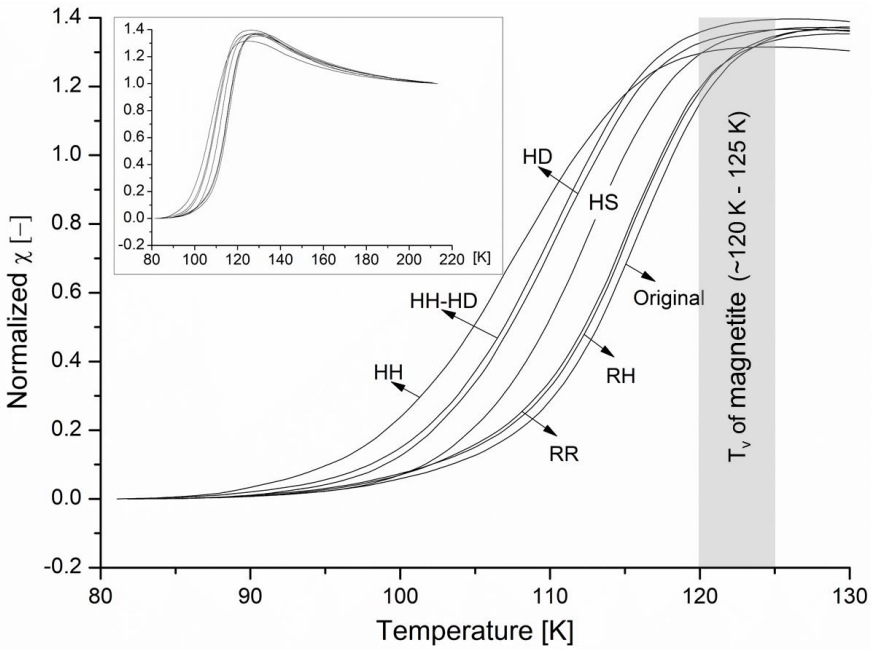

Figure 3. Low-temperature thermomagnetic curves (normalized to room temperature χ-values), shown as full curves (small plot) and enlarged for T<130 K Verwey transition (main plot).

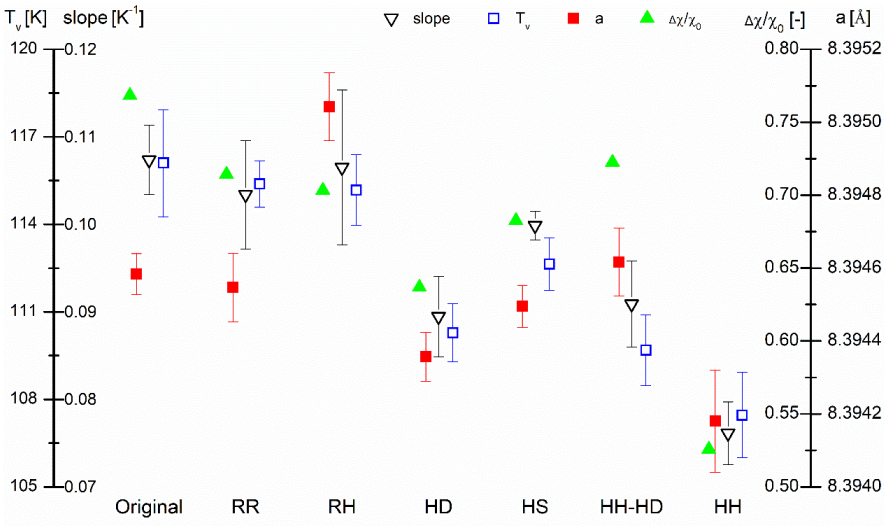

Figure 4. Verwey transition temperature (T_v), slope at T_v (lower value means flatter slope), $\Delta\chi/\chi_0$ ratios (relative χ-loss between heating and cooling curves), and lattice constant (a).

Magnetite alteration in rock weathering (Chapter IV)

Even though the laboratory experiment already demonstrates that humidity and temperature affect the alteration process (Zhang et al., 2020, Chapter III), studies on natural rocks could bring insights and useful information about how these conditions influence the characteristics in natural weathering. Basalts were chosen as they contain a large magnetite fraction that allows

studies of representative small samples. The Deccan traps on the Indian subcontinent provide suitable material for our study with its large area of flood basalts, a large gradient of mean annual precipitation, and magnetite or near-magnetite as the dominating ferrimagnetic phase that formed by exsolution during cooling and is thus a primary component of the fresh rock.

The Deccan traps are located in central and southern India (Fig. 5), covering nearly 500,000 km^2 large area, which were erupted at around the Cretaceous-Tertiary boundary (Allegre et al., 1999; Basavaiah et al., 2018). At present, a strong MAP gradient exists in this area ranging from ~500 mm to ~4000 mm (Fig. 5, right). The MAT is relatively high across the whole Deccan plateau area (~25 °C to ~28 °C).

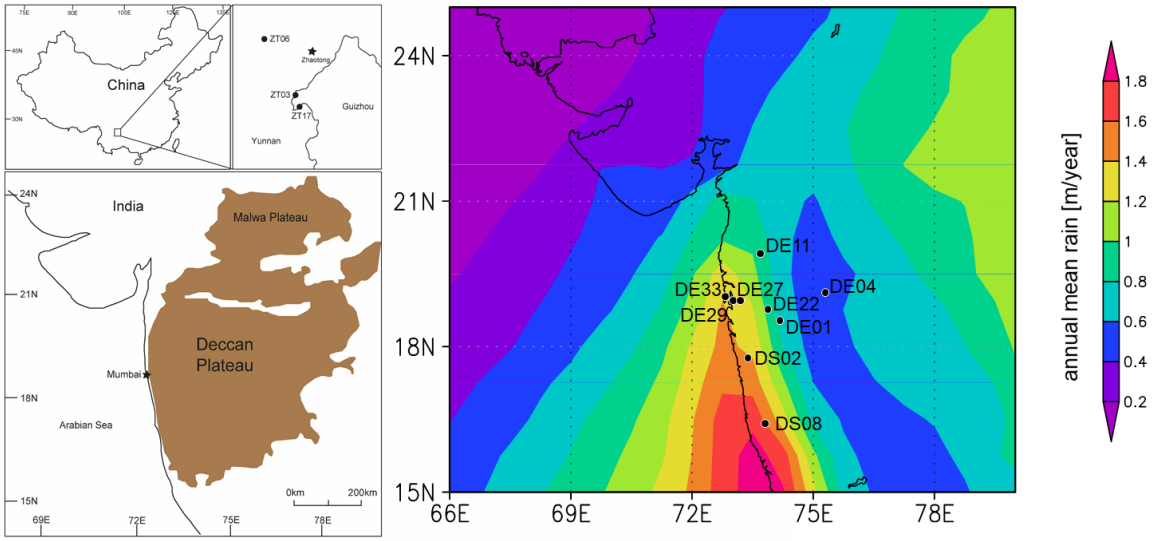

Figure 5. Upper left: Three sampling sites from Emeishan traps, China. Lower left: geology map of Deccan traps modified from Sheth (2005). Right: Nine sampling sites from Deccan traps with ERA-Interim MAP map (35-years climate averages reanalysis data; Dee et al., 2011).

The Emeishan traps are located in south-western China (Fig. 5, upper left), between the western margin of the Yangtze Block and the eastern margin of the Tibetan Plateau, covering an area of ~0.3×10^6 km^2 (Shellnutt & Jahn, 2011). Geochemical data indicates both high-Ti and low-Ti lavas are existing within Emeishan basalt province (Xu et al. 2001). Across the sampled area the MAP is ~800 mm and the MAT is ~12.8 °C.

Fresh basalts and weathered pebbles nearby (Fig. 6) were sampled from 42 locations in the Deccan traps, distributed across the MAP gradient, and 17 sample sets were obtained from the Emeishan traps. Preferred samples are those with coexisting magnetite and ilmenite, formed by exsolution during relatively slow cooling. After careful site selection, 9 sites from the Deccan

traps and 3 sites from the Emeishan traps (Fig. 5) were chosen. At each site, material was collected from 5 sub-sites for obtaining information on site-internal consistency. Detailed sampling was done in 2017. Polished sections were prepared for light microscopy analysis. Main results were obtained from bulk magnetic parameters measurements, low-and high-temperature thermomagnetic runs and light microscopy analysis.

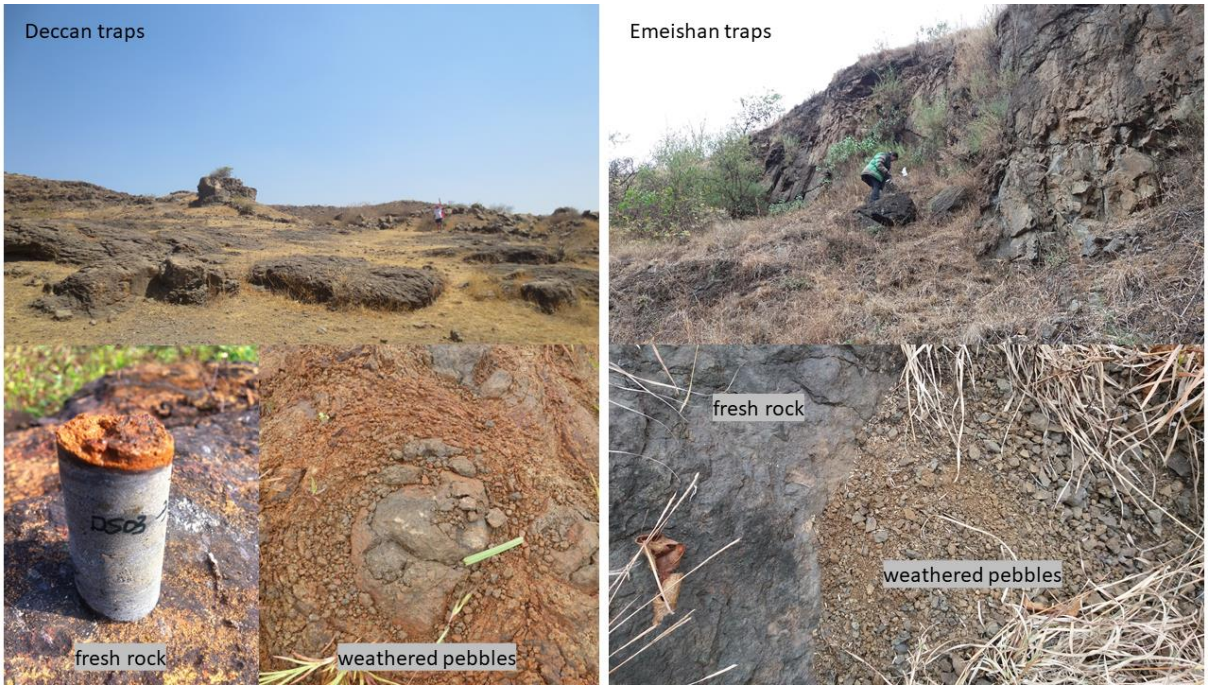

Figure 6. Photographs of sampling areas in the Deccan traps and Emeishan traps, showing fresh rock and weathered pebbles and how they are related to each other.

The results in Fig. 7 show magnetic susceptibility values of all sample materials from three representative sites (DE04, DS02, ZT06). With fining of the pebbles, the alteration of magnetic mineral is assumed to increase. A linear trend line of several parameters and parameter ratios was analyzed (χ, χ_{fd}%, *SIRM*, *SIRM*/χ, *S-ratio*, *ARM*/*SIRM*). For checking the reliability of the regression results, four different grouping methods were applied : (i) all sample material (FR, WP1-5), (ii) only pebbles, to exclude uncertainties that pebbles did not originate directly from the underlying fresh rock (WP1-5), (iii) excluding the finest fraction that may be influenced by pedogenesis (FR, WP1-4), (iv) excluding both fresh rock and finest pebble (WP1-4). The results show both cases an increasing (DE04, DS02) and decreasing (ZT06) trend of magnetic susceptibility (χ) with fining of the pebbles grain size, but the results from different grouping methods are mostly similar.

A decrease in concentration dependent parameters (χ and *SIRM*) is an indicator of transformation of magnetite (i.e., maghemitized magnetite) to hematite. An increase of *ARM*/*SIRM* can be related to grain size fining (i.e., magnetic domain state shifting towards single-domain behavior), due to higher degree of weathering that increases the inhomogeneity in terms of magnetic domain states within particles. A simultaneous decrease of *SIRM*/χ, which is partly observed, can be explained by finer particle-internal subdivisions with a shift towards superparamagnetic behavior in parts of the particles. As shown in Fig. 8, the results of the Emeishan basalts show a clear decrease of concentration dependent parameters, however only part of the Deccan basalts display a decrease, and there is no obvious systematic dependence on MAP.

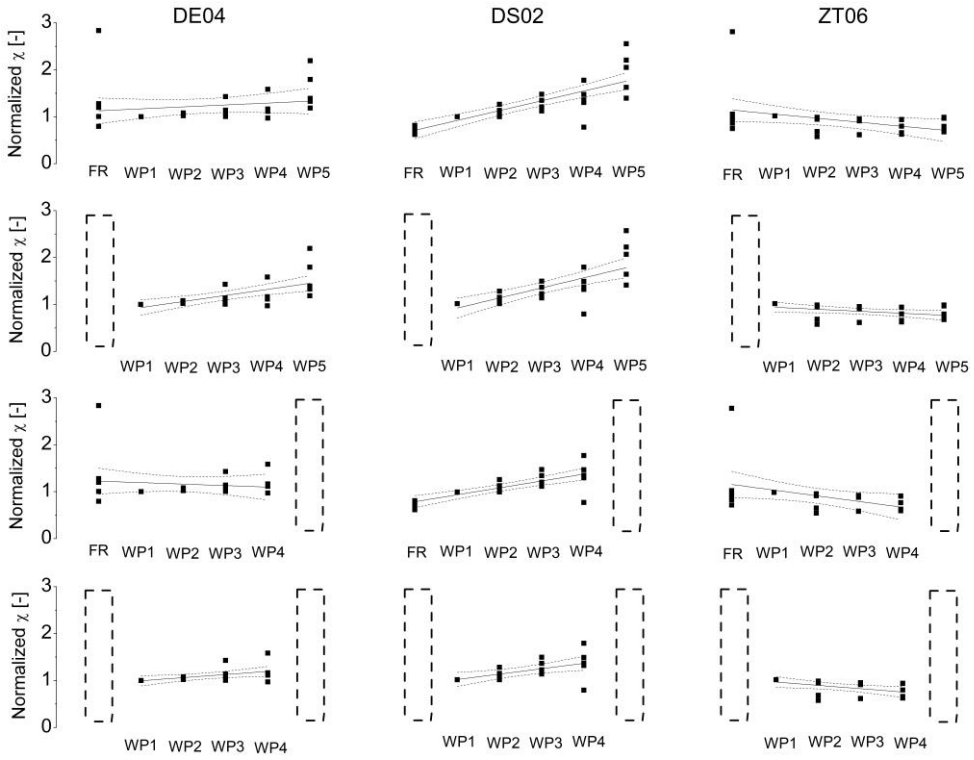

Figure 7. Magnetic susceptibility (χ) of all sample material from 3 representative sites (DE04, DS02, ZT06). Four different grouping strategies are shown: FR: basalts fresh rock, WP: weathered pebble samples (WP1 >4 mm, WP2 2-4 mm, WP3 1-2 mm, WP4 0.5-1 mm, WP5 <0.5 mm). All values are normalized to WP1 of the sub-sample set, linear fit with 95 % confidence interval.

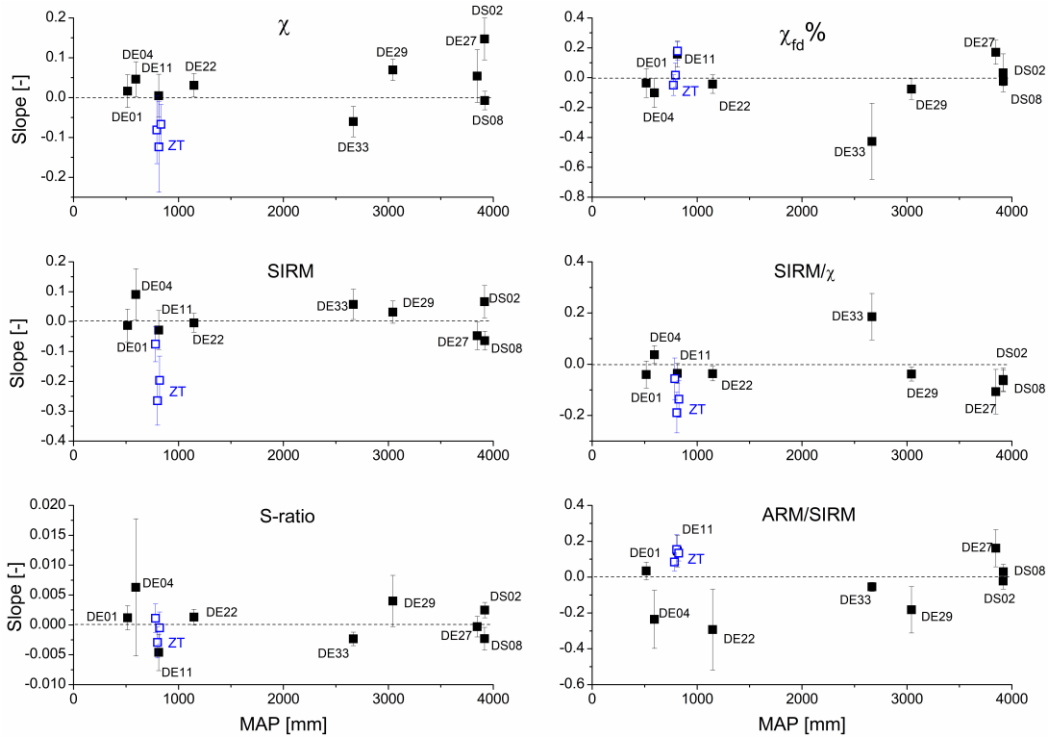

Figure 8. Slope of regression line for each sampling setting (including 5 fresh basalts and 20 pebble samples WP1-4) with confidence limits (95 %) plot of magnetic susceptibility χ, percentage frequency-dependent susceptibility χ_{fd}%, saturation isothermal remanence (*SIRM*), *SIRM*/χ ratio, *S-ratio*, *ARM*/*SIRM* ratio. Black and blue symbols denote Deccan and Emeishan results, respectively.

Unfortunately, the results from natural rock and weathered pebble materials does not show consistent oxidation signal based on our studies. The complexity of the rocks, i.e., the variations of rock magnetic behavior of the fresh rock between sampled sites, and even within sampled sites, likely override the climate-related weathering effects.

Red soil and lake sediments in a source-sink transfer (Chapter V)

The Heqing Basin (Fig. 9) in Yunnan province (SW China) is situated at about 2200 m above sea level, and present climate conditions are subtropical, with mean annual temperature of 13.5 °C and mean annual precipitation of nearly 1000 mm (Xiao et al., 2010). Hu et al. (2005, 2015) interpreted magnetic properties of a 168-m deep lacustrine drill core (Core-HQ; Fig. 9) from Heqing basin in terms of paleoclimate evolution during the past ~900 ka. They identified magnetite, maghemite and hematite as the main ferro(i)magnetic mineral components. Hu et al. (2015) also proposed that the superparamagnetic magnetite fraction which dominates the strongly magnetic red soil all around the basin is almost absent in Core-HQ, and the detrital fraction inherited from weathering of the very low magnetic bedrock in the surrounding of Heqing Basin dominates the magnetic properties in the lacustrine sediments. It was speculated

that superparamagnetic magnetite particles were lost during transport into the lake due to dissolution in surface water.

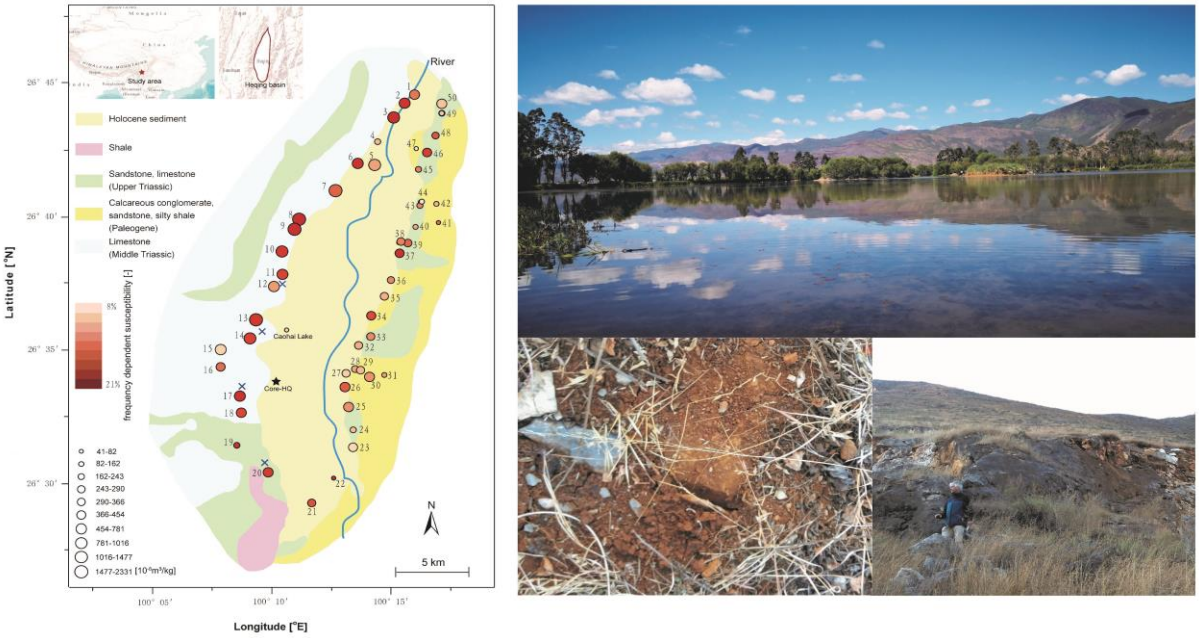

Figure 9. Study area and sampling conditions, Caohai Lake (upper right), red soil and bedrocks (lower right).

The crucial question concerns the possible fading of fine magnetite particles on the pathway from their origin to the sink. A source-sink setting with both red soil and sediments from the Caohai Lake in the basin was studied. A total of 45 red soil samples were collected from the uppermost ~10 cm all around the basin. Three short (~45 cm) sediment cores were recovered from Caohai Lake. From the main bedrock (limestone), 4 samples were collected at the western basin margin (Fig. 9).

Magnetic parameters and geochemical parameters were measured, and in addition, X-ray diffraction and TEM analyses were applied. Data from those measurements provides important information related to the identification of magnetic minerals, the characterization of the magnetic grain size (i.e., magnetic domain state), and the spatial (red soil) and vertical (lake sediments) distribution of magnetic parameters, aiming to decipher the change of magnetic properties during the pathway from the source to the sink.

The highly magnetic red soil with susceptibilities (χ) of ~10^{-5} m^3/kg are the only important source material for the Caohai Lake. Observations by TEM show that pedogenic nano-magnetites (~10-15 nm) are dominating in red soil. They are arranged in aggregates of ~100 nm, with particle interaction that causes a wide effective grain size distribution in the

superparamagnetic (SP) range tailing into stable single-domain (SSD) behavior. Corresponding with broadband-frequency χ(f) results, an assumption has been made that partial disintegration of the aggregates happened during the transfer of source material (red soil) to the sink (Caohai Lake), and the alteration of magnetite nanoparticles to hematite is increased. Both changes shift the domain state behavior to smaller effective magnetic grain sizes, resulting in lower χ_{fd}% and χ values. (Chapter V)

A conceptual sketch shown in Fig. 10 illustrate the expected dependence of χ-values as a function of grain size and frequency. The dependence of χ versus grain size shows a peak-shaped behavior with highest values and strong frequency dependence in the range of thermal activation, a constant and frequency-independent lower χ when approaching the SSD range, and decreasing χ-values towards smaller SP particle sizes (underlying χ-relationships are given in Fig. 10).

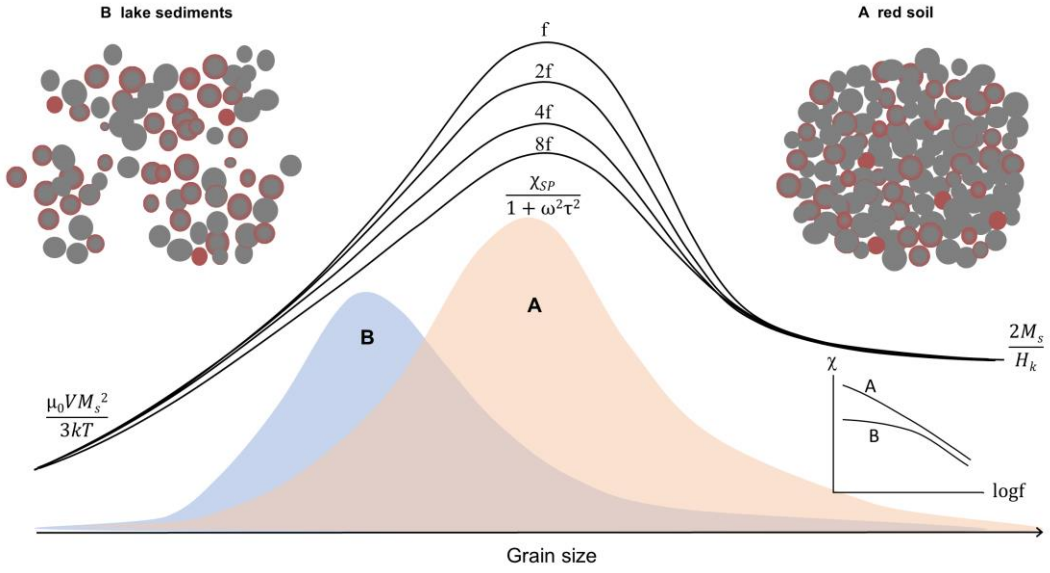

Figure 10. Sketch of the conceptual relationship of χ versus grain diameter (d) for four frequencies in logarithmically equal increments (increasing from f to 8f), modified from Kodama (2013), and following the theory presented by Worm (1998) and Shcherbakov and Fabian (2005). The principle relationships for smaller SP grains (below thermal activation), SP grains in the range of thermal activation (frequency-dependent; in-phase part), and larger grains in the SSD range are shown (M_s: saturation magnetization, H_k: microcoercivity, χ_{SP}: superparamagnetic susceptibility for zero frequency, V: grain volume, τ: relaxation time, T: temperature, f: frequency, ω: angular frequency, μ_0: magnetic permeability of free space, k: Boltzmann constant). The orange and gray fields display schematic distributions of effective grain sizes of the nano-magnetite aggregates in red soil (A) and lake sediments (B), respectively. Aggregates in red soil are assumed to be tighter packed and possibly also larger than in lake sediments, and according to the ELNES results more hematite is existing in the nanoparticles of the lake sediments.

Hematite in the nanoparticles, either existing as full nanoparticles or as shells of magnetite cores (Fig. 10), will increase the distance between neighboring magnetite. Both the hematite fraction in the aggregates and the tighter or looser packing of nanoparticles affect the interaction between the magnetites, and therefore will have an impact on the resulting χ_{fd}% and χ values. Aggregates in state (B) have a looser packing and more hematite than aggregates in state (A), thus the frequency dependence in the lower frequency range is decreased.

References

Ahmed, I.A.M. & Maher, B.A. (2018). Identification and paleoclimatic significance of magnetite nanoparticles in soils. Proc. Natl. Acad. Sci., 115(8), 1736-1741. https://doi.org/10.1073/pnas.1719186115

Allegre, C.J., Birck, J.L., Capmas, F. & Courtillot, V. 1999. Age of the Deccan traps using 187Re–187Os systematics. Earth and Planetary Science Letters, 170, 3, 197-204. https://doi.org/10.1016/S0012-821X(99)00110-7

An, Z.S., Clemens, S.C., Shen, J., Qiang, X., Jin, Z.D., Sun, Y.B., et al. (2011). Glacial-interglacial Indian summer monsoon dynamics. Science, 333, 719-723. https://doi.org/10.1126/science.1203752

Basavaiah, N. & Khadkikar, A.S. (2004). Environmental magnetism and its application towards palaeomonsoon reconstruction. Journal of the Indian Geophysical Union, 8/1, 1-14.

Basavaiah, N., Mahesh Babu, J.L.V., Gawali, P.B., Naga Kumar, K.Ch.V., Demudu, G., Prizomwala, S.P., Hanamgond, P.T. & Nageswara Rao, K. (2015). Late Quaternary environmental and sea level changes from Kolleru Lake, SE India: Inferences from mineral magnetic, geochemical and textural analyses. Quat. Int., 371, 197-208. https://doi.org/10.1016/j.quaint.2014.12.018

Basavaiah, N., Satyanarayana, K.V.V., Deenadayalan, K. & Prasa, J.N. (2018). Does Deccan Volcanic Sequence contain more reversals than the three-Chron N–R–N flow magnetostratigraphy? a palaeomagnetic evidence from the dyke-swarm near Mumbai. Geophys. J. Int., 213, 1503-1523. https://doi.org/10.1093/gji/ggy041

Bourgeois, F., Gergaud, P., Renevier, H., Leclere, C. & Feuillet, G. (2013). Low temperature oxidation mechanisms of nanocrystalline magnetite thin film. J. Appl. Phys., 113, 013510. https://doi.org/10.1063/1.4772714

Byrne, J.M., Klueglein, N., Pearce, C., Rosso, K.M., Appel, E. & Kappler, A. (2015). Redox cycling of Fe(II) and Fe(III) in magnetite by Fe-metabolizing bacteria. Science, 347, 1473-1476. https://doi.org/10.1126/science.aaa4834

Byrne, J.M., van der Laan, G., Figueroa, A.I., Qafoku, O., Wang, C.M., Pearce, C.I., Jackson, M., Feinberg, J., Rosso, K.M. & Kappler, A. (2016). Size dependent microbial oxidation and reduction of magnetite nano- and micro-particles. Sci. Rep., 6, 30969. https://doi.org/10.1038/srep30969

Davison, W. & Seed, G. (1983). The kinetics of the oxidation of ferrous iron in synthetic and natural waters. Geochim. Cosmochim. Acta., 47, 67-79. https://doi.org/10.1016/0016-7037(83)90091-1

Dee, D.P., Uppala, S.M., Simmons, A.J., Berrisford, P., Poli, P., Kobayashi, S., Andrae, U., Balmaseda, M.A. et al. (2011). The ERA-Interim reanalysis: configuration and performance of the dataassimilation system. Q. J. R. Meteorol. Soc., 137, 553–597. https://doi.org/10.1002/qj.828

Demortière, A., Panissod, P., Pichon, B.P., Pourroy, G., Guillon, D., Donnio, B. & Bégin-Colin, S. (2011). Size-dependent properties of magnetic iron oxide nanocrystals. Nanoscale. 3(1), 225-32. https://doi.org/10.1039/c0nr00521e

Gasse, F., Arnold, M., Fontes, J.C., Fort, M., Gibert, E., Huc, A., et al. (1991). A 13,000-year climate record from western Tibet. Nature, 353, 742-745. https://doi.org/ 10.1038/353742a0

Herb, C., Zhang, W.L., Koutsodendris, A., Appel, E., Fang, X.M. & Pross, J. (2013). Environmental implications of the magnetic record in Pleistocene lacustrine sediments of the Qaidam Basin, NE Tibetan Plateau. Quat. Int., 313-314, 218-229. https://doi.org/10.1016/j.quaint.2013.06.015

Hu, S.Y., Goddu, S.R., Appel, E., Verosub, K., Yang, X.D., & Wang, S. (2005). Palaeoclimatic changes over past one million years derived from lacustrine Sediments of Heqing Basin (Yunnan, China). Quaternary International, 136, 123-129. https://doi.org/10.1016/j.quaint.2004.11.013

Hu, S.Y., Goddu, S.R., Herb, C., Appel, E., Gleixner, G., Wang, S.M., Yang, X.D. & Zhu, X.H. (2015). Climate variability and its magnetic response recorded in a lacustrine sequence in Heqing basin at the SE Tibetan Plateau since 900 ka. Geophys. J. Int., 201, 444-458. https://doi.org/10.1093/gji/ggv033

Irving, E. (1970). The Mid-Atlantic Ridge at 45°N, XIV, Oxidation and magnetic properties of basalts: Review and discussion. Can. J. Earth Sci., 7, 1528-1538. https://doi.org/10.1139/e70-144

Kodama, K. (2013). Application of broadband alternating current magnetic susceptibility to the characterization of magnetic nanoparticles in natural materials. Journal of Geophysical Research Solid Earth, 118, 1-12. https//doi.org/10.1029/2012JB009502

O'Reilly, W. (1984). Rock and Mineral Magnetism. Blackie London, 220 p.

Petersen, N. & Vali, H. (1987). Observation of shrinkage cracks in ocean floor titanomagnetites. Phys. Earth Planet. Inter., 46, 197-205. https://doi.org/10.1016/0031-9201(87)90182-8

Readman, P. & O'Reilly, W. (1972). Magnetic properties of oxidized (cation-deficient) titanomagnetites (Fe,Ti)3O4. J. Geomag. Geoelec., 24, 69-90. https://doi.org/10.5636/jgg.24.69

Shcherbakov, V.P., & Fabian, K. (2005). On the determination of magnetic grain-size distributions of superparamagnetic particle ensembles using the frequency dependence of susceptibility at different temperatures. Geophysical Journal International, 162, 736-746. https://doi.org/ 10.1111/j.1365-246X.2005.02603.x

Shellnutt, J.G. & Jahn, B.-M. (2011). Origin of Late Permian Emeishan basaltic rocks from the Panxi region (SW China): Implications for the Ti-classification and spatial–compositional distribution of the Emeishan flood basalts. J. Volcanol. Geoth. Res., 199, 85-95. https://doi.org/10.1016/j.jvolgeores.2010.10.009

Sheth, H. C., 2005. From Deccan to Réunion: no trace of a mantle plume. In: Foulger, G. R., Natland, J. H., Presnall, D. C., Anderson, D. L. (Eds.), Plates, Plumes, and Paradigms. Geol. Soc. Am. Spec. Pap. 388, 477-501.

Topsøe, H., Dumesic, J.A. & Boudart, M. (1974). Mössbauer spectra of stoichiometric and nonstoichiometric Fe3O4 Smicrocrystal. J. Phys. (Paris), 35, C6-411-C6-413. http://dio.org/ 10.1051/jphyscol:1974680

Van Velzen, A.J. & Dekkers, M. (1999). Low-temperature oxidation of magnetite in loess-paleosol sequences: A correction of rock magnetic parameters. Stud. Geophys. Geod., 43, 357-375. http://doi.org/10.1023/A:1023278901491

Worm, H.U. (1998). On the superparamagnetic-stable single domain transition for magnetite, and frequency dependence of susceptibility. Geophysical Journal International, 133, 201-206. https://doi.org/10.1046/j.1365-246X.1998.1331468.x

Xiao, X.Y., Shen, J., Wang, S.M., Xiao, H.F., & Tong, G.B. (2010). The variation of the southwest monsoon from high resolution pollen record in Heqing Basin, Yunnan Province, China for the last 2.78 Ma. Palaeogeography, Palaeoclimatology, Palaeoecology, 287, 45-57. https://doi.org/10.1016/j.palaeo.2010.01.013

Xu, Y.G., Chung, S.L., Jahn, B. & Wu, G.Y. (2001). Petrologic and geochemical constraints on the petrogenesis ofPermian–Triassic Emeishan flood basalts in southwestern China. Lithos, 58, 145-168. https://doi.org/10.1016/S0024-4937(01)00055-X

Xu, W.X., Peacor, D.R., Dollase, W.A., Van der Voo, R. & Beaubouef, R. (1997). Transformation of titanomagnetite to titanomaghemite: A slow, two-step, oxidation-ordering process in MORB. Amer. Miner., 82, 1101-1110. https://doi.org/10.2138/am-1997-11-1207

Zhang, Q., Appel, E., Stanjek, H., Byrne, J.M., Berthold, C., Sorwat, J., Rösler, W. & Seemann, T. (2020). Humidity related magnetite alteration in an experimental setup. Geophys. J. Int. https://doi.org/10.1093/gji/ggaa394

Zhou, W.M., Van der Voo, R., Peacor, D.R., Wang, D.M. & Zhang, Y.X. (2001). Low-temperature oxidation in MORB of titanomagnetite to titanomaghemite: A gradual process with implications for marine magnetic anomaly amplitudes. J. Geophys. Res. Solid Earth, 106(B4), 6409-6421. https://doi.org/10.1029/2000JB900447

Chapter III: Humidity related magnetite alteration in an experimental setup

Author	Author position	Scientific ideas %	Data generation %	Analysis & interpretation %	Paper writing %
Qi Zhang	1	40	65	35	50
Erwin Appel	2	40	-	30	35
Helge Stanjek	3	10	15	10	10
James Byrne	4	-	5	10	5
Christoph Berthold	5	-	5	5	-
Julian Sorwat	6	-	5	5	-
Wolfgang Rösler	7	10	-	-	-
Timo Seemann	8	-	5	5	-
Status in publication process:		Accepted			

Humidity related magnetite alteration in an experimental setup

Qi Zhang[1], Erwin Appel[1]*, Helge Stanjek[2], James M. Byrne[3,4], Christoph Berthold[5], Julian Sorwat[3], Wolfgang Rösler[1], Timo Seemann[2]

[1] *Geophysics, Center for Applied Geoscience, University of Tübingen, Hölderlinstr.12, 72074 Tübingen, Germany*

[2] *Clay and Interface Mineralogy (CIM), RWTH Aachen University, Bunsenstraße 8, 52072 Aachen, Germany*

[3] *Geomicrobiology, Center for Applied Geoscience, University of Tübingen, Hölderlinstr.12, 72074 Tübingen, Germany*

[4] *School of Earth Sciences, University of Bristol, Wills Memorial Building, Queens Road, Bristol BS8 1RJ, United Kingdom*

[5] *Mineralogy and Geodynamics, Department of Geosciences, University of Tübingen, Lothar-Meyer Bau, Wilhelmstr. 56, 72074 Tübingen, Germany*

Summary

Low-temperature oxidation (LTO) of magnetite is an alteration process which occurs under normal atmospheric conditions, causing maghemitization. The use of magnetic properties as paleoclimate proxies requires improved understanding of how humidity and temperature affect such processes. We exposed natural magnetite, with grain size ranging from <1 μm to ~30 μm, to different humidity conditions at room temperature and 70 °C for one year. Changes in room temperature setups were very minor, but in all 70 °C setups alteration was detected by magnetic and mineralogical properties. Lowering of the Verwey transition temperature (T_v) turned out to be the most sensitive indicator of LTO, and also lattice constants correlate well with the shift of T_v. Thermomagnetic curves and XRD-results indicate that LTO affects the entire volume of the particles rather than only surface layers. The sample exposed to high relative humidity (rH) >90 % at 70 °C showed the strongest degree of LTO with an increase of the oxidation degree by ~3 % according to T_v, and it was the only setup where partial alteration to hematite was indicated by Mössbauer analysis. The sample with extremely dry conditions (rH of ~5 %) at 70 °C, and the sample that was exposed to cycles of high and low humidity in 2-weeks alternation at 70 °C, both revealed a smaller degree of LTO. The smallest change of the high temperature setups was observed for the sample with intermediate rH of ~13 %. The results suggest a non-linear sensitivity of magnetite alteration to humidity conditions, high humidity strongly favors alteration, but alteration is strongly reduced when extreme humidity alternates with dry conditions, suggesting an importance of seasonality in natural weathering.

1. Introduction

Alteration of magnetite has been extensively studied for understanding magnetic remanences carried by (titano-)magnetite in basalts (Irving, 1970; Petersen & Vali, 1987; Xu et al., 1997; Zhou et al., 2001), principles of rock weathering, sediment transport and deposition related to paleoclimate research (Van Velzen & Dekkers, 1999; Demory et al., 2005; Herb et al., 2013), many of them in the field of pedogenic processes (Chen et al., 2005; Liu Q.S. et al., 2005) and core-shell structures in pedogenic nanoparticles (Ge et al., 2014; Ahmed & Maher, 2018), but also in other fields such as heavy metal remediation (Liu W. et al., 2015), medical and bio-applications (Widdrat et al., 2014; Schwaminger et al., 2017), and technical applications such as thin films (Bourgeois et al., 2013). Magnetite is the most common of ferro(i)magnetic minerals in nature, and it plays an important role in the use of magnetic properties as paleoclimate proxies in terrestrial archives such as soil, eolian deposits, and lake sediments. Changes of source areas, weathering in the catchment area, transport-related effects, and authigenic processes, potentially influence magnetic properties of the sediments. In this paper, we address the impact of humidity on the oxidation kinetics of magnetite, which is relevant for climate-related inorganic magnetite alteration during weathering of source rocks. Oxidation of magnetite with oxygen preserves the spinel structure, but with vacancies (□) on the octahedral site:

$$8Fe^{3+}[Fe^{2+}Fe^{3+}]O_4 + 2O_2 \leftrightharpoons 9[Fe^{3+}_{1.67}\ \square_{0.33}]O_4 \qquad (1)$$

Magnetite and maghemite form a continuous solid-solution series (Basta, 1959), in which intermediate oxidation states written as $Fe[Fe_{2-\delta}\ \square_{\delta}]O_4$ ($0 \leq \delta \leq 1/3$) show Vegard behavior for cell edge length *a*, summarized by Gorski & Scherer (2010) and Cervellino et al. (2014). The oxidation mechanism involves attachment of an oxygen molecule to the surface of the magnetite, where it oxidizes two surficial Fe^{2+} ions and becomes incorporated into the surface. This topotactic reaction does not change the morphology (Feitknecht & Lehmann, 1959; Jolivet & Tronc, 1988), the surface area remains the same and no porosity develops (Sidhu et al., 1977). The Fe has to diffuse within a solid, the kinetics of which has been addressed manifold (e.g., Gallagher et al., 1968; Gillot et al., 1978; Mazanek et al., 1973; Bourgeois et al., 2013). Apart from particle size (Elder, 1965; Colombo et al., 1968; Haneda & Morrish, 1977; Gillot et al., 1978) the kind of diffusion mechanism (grain boundary diffusion, diffusion along defects and through a defect-free structure) is important (Bourgeois et al., 2013). The concomitant activation energies of about 81 kJ/mol (Sidhu et al., 1977) are small enough to convert

nanosized magnetite within years to maghemite. Murad & Schwertmann (1993) observed on synthetic magnetite of submicron size that within five years its oxidation state increased from an initial δ=0.14 to δ=0.18. For magnetite characteristic first-order phase transitions occur at the Curie temperature (T_c) of ~580 °C (Petersen & Bleil, 1982) and a low temperature transition at around 120 K to 125 K known as the Verwey transition at which the crystal lattice transforms from cubic (T>T_v) to monoclinic (T<T_v) (Hamilton, 1958; Jackson et al., 2011). Just above T_v the magnetocrystalline anisotropy shows a zero-intersection.

Increase of δ lowers the saturation magnetization (Readman & O'Reilly, 1972), increases T_c (Readman & O'Reilly, 1972), decreases T_v (Aragón et al., 1985) and decreases the lattice constant (Basta, 1959; Cervellino et al., 2014). Maghemite can transform to low-magnetic hematite (DeBoer & Selwood, 1954; Swaddle & Oltmann, 1980; Sidhu, 1988; Li et al., 2019), but depending on particle size, hematite can also form by direct oxidation of magnetite at temperatures above about 300 °C (Nasrazadani & Raman, 1993; Li et al., 2019; Knafelc et al., 2019), and also through martitization in natural environments (Davis et al., 1968). Temperature does not only determine the speed of reactions, but also whether magnetite-to-hematite conversion happens directly, or via low-temperature oxidation (LTO). Taylor & Schwertmann (1974 a & b) found that maghemite forms through slow oxidation under certain pH conditions, while fast oxidation preferentially produces hematite. Depending on water availability the final product can be goethite instead of hematite (Abrajevitch & Kodama, 2009).

The governing question behind our study is whether climate-specific weathering of bedrock, in particular the influence of humidity, produces typical magnetic characteristics of magnetite contained in the rocks. Van Velzen & Dekkers (1999) suggested that LTO could occur during weathering in the outcrop, as well as during transport and deposition. Weathered rock materials serve as primary source for paleoclimate archives such as lake sediments (Demory et al., 2005) or loess deposits (Begét et al., 1990; Liu et al., 2004a). Paleoclimate investigations so far paid surprisingly little attention to the effects of LTO on iron-oxide stability as a function of climatic conditions. In some studies, humidity-control of magnetite weathering in the catchment was proposed (Basavaiah & Khadikar, 2004; Herb et al., 2013; Basavaiah et al., 2015; Hu et al., 2015). Swaddle & Ostmann (1980) suggested that the rate of LTO depends on dry or wet conditions, but their experimental study was performed under hydrothermal conditions which are different from rock weathering processes. In principle, oxidation in air at room temperature can take place in time scales of several hundred days (Topsøe et al., 1974; Bourgeois et al.,

2013), with increasing oxidation rate for grain-size fining from about 100 nm to sizes of few nm (Demortière et al., 2011; Byrne et al., 2016), and presence of bacterial activity can speed up the reactions to even days (Byrne et al., 2015). Ahmed & Maher (2018) found a strong dependence of LTO on geochemical conditions such as pH.

Investigating weathered sample materials of natural rocks in different climates as a function of humidity and temperature is a possible approach to tackle the question of climate-related magnetite alteration. However, studying magnetite alteration in natural environments is a complex task due to the unavoidable mineralogical variability, which makes it difficult to obtain suitable sample collections from different climatic settings. We therefore performed a laboratory experiment using well-characterized natural magnetite as starting material, investigated the alteration of magnetite after one year of exposure to different controlled conditions of humidity and temperature. In our experimental setup, we used a maximum temperature of 70 °C, which is high enough to detect magnetite alteration, and still as close as possible to natural conditions for minimizing uncertainty in transferring the results to natural processes. To the best of our knowledge, controlled experiments with well-defined natural magnetite particles at or near ambient temperatures have not been previously attempted. We then applied a combination of mineralogical, spectroscopic, magnetic and chemical techniques to elucidate which factors most strongly influence LTO.

2. Samples and methods

2.1 Starting material and control sample

The magnetite sample used in our experimental setup was selected upon the following criteria: (i) The crystallographic structure should be as close as possible to stoichiometric magnetite, and (ii) the sample should comprise a wide grain size range of particles to represent a suitable analogue of magnetite released by bedrock weathering. Magnetite particles smaller than about one micron would be principally most suitable because of their high surface-to-volume ratio, but they do not fulfill the second criterion, and it is also difficult to obtain such material without notable alteration from natural sources or by synthesizing sufficiently homogeneous non-oxidized particles (Tang et al., 2013). We tested a series of different natural and synthetic samples, based on these test results we selected a commercial magnetite (sampled from Sweden, probably Kiruna). Micrographs show a grain size range of <1 µm to ~30 µm, and the results from X-ray diffraction and thermomagnetic analyses (Verwey transition and Curie temperature)

document magnetite close to a stoichiometric composition (for presentation of results we refer to the ‘Results’ section).

The chosen laboratory setups differed in temperature (T) and relative humidity (rH) conditions. The results after one year of exposure are presented in this paper. The original magnetite material, which was kept in a self-sealed plastic bag during this year in the same room as the experimental setups, was re-analyzed after terminating the experiment as a control sample for comparison with the treated setups.

2.2 Experimental approach

For the experimental setups, we used 20x26x30-cm large experimental containers made of stainless steel (Fig. 1). We equipped them with a heating pad as thermal source, connected with a self-regulation thermometer for switching the heating pad on or off when the temperature deviated ±5 °C from 70 °C. Water vapor produced by a humidifier was added into the container via a rubber tube, and a self-regulation hygrometer was installed in the container to keep the humidity constant. Around 4 g of the magnetite starting material was placed on a non-magnetic tinfoil plat. Small holes at the bottom of the plates avoided water accumulation, and a fine filter membrane above the holes prevented the loss of magnetite. The containers were sealed and placed in the laboratory at University of Tübingen for one year, sheltered from sunlight. Temperature and humidity conditions in the 70 °C-setups HH, HH-HD, HS, and HD were kept constant by the temperature and humidity controllers, respectively. The setup RH varied with the ambient room temperature in the laboratory temperature of about 20-30 °C while humidity was kept constant, and RR was exposed to the laboratory conditions of both temperature and humidity. After one year of exposure in the experimental setups, the samples were collected from the containers and air dried at room temperature for two weeks.

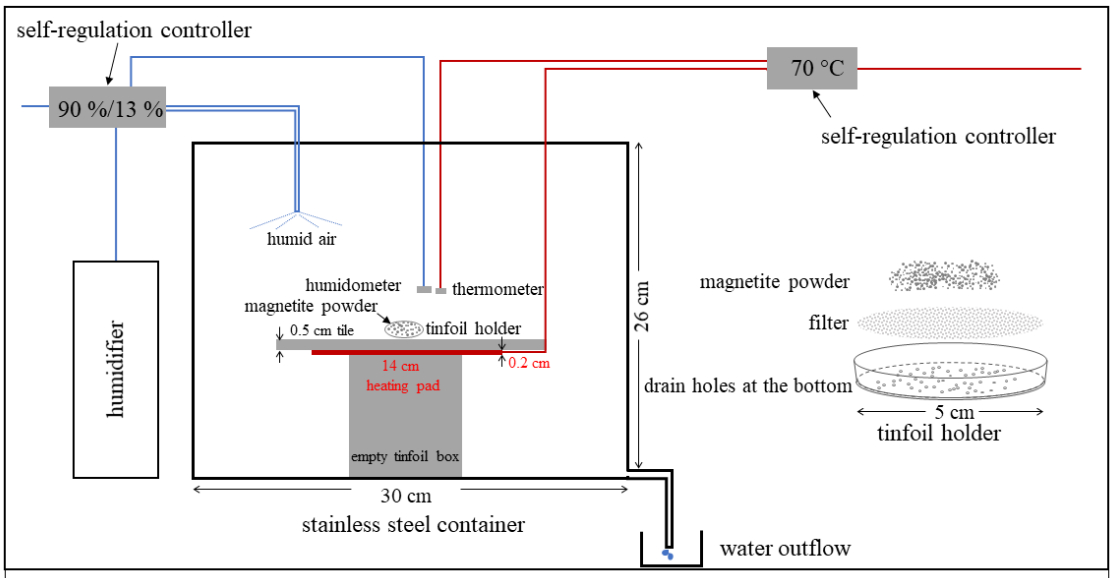

	Temperature [°C]	Relative Humidity [%]
HH	70	>90
HH-HD	70	2 weeks switch HH <=> HD
HS	70	13 (equals specific humidity as for rH=100 % at T=25 °C)
HD	70	5
RH	RT varying at 20~30	>90
RR	RT varying at 20~30	variable room humidity

Figure 1. Schematic laboratory setup; temperature and relative humidity conditions of each experimental container.

2.3 Analytical methods

Magnetic susceptibility (χ) was measured with an MFK-1 Kappabridge (Agico) at frequencies of 976 Hz and 15616 Hz (χ_{lf} and χ_{hf}), then normalized to mass-specific values. For accurate measurement of small amounts of material (0.4-1.0 g), and for minimizing anisotropy effects, we wrapped the magnetite samples with plastic film into a spherical shape and fixed it in the middle of a 2x2x2-cm plastic sample box with non-magnetic plasticine. Magnetic susceptibility was then measured in three orthogonal directions, averaging the three values to obtain the sample result. The measurement was only accepted when χ-values of the three orthogonal directions differed by less than 5 %. We repeated the above procedure ten times, preparing new samples from the same material, and from these ten sets, we calculated the mean and standard deviation. Percentage frequency-dependence (χ_{fd}%) was calculated by $[(\chi_{lf}-\chi_{hf})/\chi_{lf}]$x100 (Dearing et al., 1996). In addition, we determined the broadband-frequency dependence of χ with an SM150L device (ZH Instruments) at 9 frequencies between 65 Hz and 16 kHz.

Low- and high-temperature thermomagnetic curves of magnetic susceptibility (χ-T curves) were performed with sample masses of ~0.15 g on a KLY-3 Kappabridge combined with a CS-3 furnace and a CS-4 cryostat, warming the sample from liquid nitrogen to room temperature and heating it to 700 °C in argon atmosphere. For each sample type, we measured low-temperature thermomagnetic curves for five different sub-samples, and then calculated an average curve.

Ten sub-samples (~0.01 g) of each sample type were prepared for measuring hysteresis curves with a PMC MicroMag 2900 AGM (Lake Shore Cryotronics), to obtain the saturation magnetization (M_s) and the saturation isothermal remanent magnetization (*SIRM*) at 0.8 T. Moreover, we measured first-order reversal curves (FORC) and processed these results with the software FORCinel (Harrison & Feinberg, 2008). With the MicroMag, we obtained IRM acquisition curves at 100 steps in regular log-increments up to 0.8 T, for five sub-samples (~0.01 g) from each sample type. The *IRM* curves were unmixed by log-normal Gaussian distributions utilizing the program MAX UnMix of Maxbauer et al. (2016), extracting B_h (field at which *SIRM*/2 is reached) and *DP* (width of distribution) values.

In addition, we characterized the sample materials for their mineralogical and chemical composition. For these analyses, we used the bulk sample powders, and also produced polished sections after embedding some sample materials (last polishing step with 1-µm diamond paste).

On the polished sections, we performed reflected light microscopy with immersion oil lenses and applied ferrofluid on the surface for safely discriminating strong magnetic phases from others. After additional coating with carbon (twice 2-4 nm), we analyzed the polished sections with a PHENOM XL scanning electron microscope (SEM) with a CeB6 electron source, operated in back-scattered mode (15 kV; working distances 10-30 µm) to reveal contrasts potentially related to different maghemitization degrees. Another SEM (LEO 1450VP) microscope equipped with tungsten filament was used for bulk powder material to measure size and shape of the magnetite particles (8 kV, working distance 10 mm). The size of magnetite particles was determined from SEM images by utilizing ImageJ software.

Powder X-ray diffraction (XRD) measurements were performed on several samples (original magnetite, HH, original magnetite after annealing at 300 °C and 380 °C in argon) using a BRUKER D8-advance diffractometer equipped with Cu-sealed tube running at 40 kV/20 mA, a Goebel-mirror parallel beam optic to suppress CuKβ and measuring with the CuKα duplet

with a weighted mean value (0.15418 nm), a 0.2 mm primary divergence slit, a knife edge with fixed 1 mm distance to the sample surface to suppress air scattering, and a 1D-VÅNTEC-1 detector with 3° window in scanning mode. The sample was prepared without grinding on a low background silicon wafer and fixed with hairspray. There was a certain surface roughness, which could influence the peak profile, but this influence can be neglected due to the used parallel beam optic by the Goebel mirror mounted on the primary side. Quartz powder was mixed to some of the samples as internal standard. The sample was rotated during measurement, step size was 0.008°Θ, and the measurement time was 1600-7700 s per step (line detector) depending on the sample amount. Additional powder scans were run on a conventional BRUKER D8 diffractometer for magnetite samples from all setups, using a low-background sample holder (Si crystal) by mixing KCl with the magnetites. Before the measurements, the samples were ground by hand in a bornitrate mortar under ethanol, together with the KCl. The cell edge length of KCl was calibrated against NIST corundum and held fix during the refinement with BGMN/Profex (Doebelin & Kleeberg, 2015). Both size and strain broadening parameters were refined and corrected for instrumental broadening.

^{57}Fe Mössbauer spectroscopy was used to measure the Fe-bearing mineralogy of bulk powder materials of the original magnetite (the control sample) and all treated setups. Samples were loaded as dried powders into 1 cm² plexiglas holders and transferring them to a closed-cycle exchange gas cryostat (Janis cryogenics). Data were collected at 140 K with a constant acceleration drive system (WissEL) in transmission mode with a ^{57}Co/Rh source and calibrated against a 7 μm thick α-^{57}Fe foil measured at room temperature. All spectra were analyzed utilizing the software Recoil (University of Ottawa) by applying a Voight Based Fitting (VBF) routine (Rancourt et al., 1991). The half-width at half maximum was fixed to a value of 0.133-0.136 mm/s for all samples.

Argon physisorption isotherms were measured on 90-350 mg of dried magnetite powder using the manometric Quantachrome Autosorb 1 MP equipped with a CryoSync thermostat (regulating the temperature at 87.3 K). Uptake of Ar was determined at 43 and 25 discrete pressure points in ad- and desorption mode between 0.001 to 0.995 P/P_0. The saturation pressure of the adsorptive was specified manually at 10.1297 MPa (normal boiling point at 87.3 K). Tolerance to partial pressure fluctuations was zero below 0.1 P/P_0 and 2 above 0.1 P/P_0. Thermodynamic equilibrium was assumed when the pressure drop rate was <15 Pa/min for 5 min. All samples were first evacuated to <10 μPa for several hours at ambient

temperature (~25 °C). After pre-drying, the sample material was stepwise heated under vacuum to 105 °C for 24 h before measuring full ad- and desorption isotherms. To check the drying state of the sample, a pressure-rise test (~30-40 mPa/min) was performed before each measurement. For quantitative analysis of the micropore range and the specific surface area, we used the Dubinin-Astakhov (DA) and Brunauer-Emmett-Teller (BET) theories, respectively (Dubinin and Astakhov, 1971; Brunauer et al., 1938). The analysis of the specific surface area (A_BET) was performed according to the principles laid out by Rouquerol et al. (2007).

3. Results

3.1 Properties of the original magnetite material (control sample)

SEM analysis indicated a large variability of grain sizes (Fig. 2c) ranging from larger particles with a diameter of about 5-30 µm to many smaller particles <1 µm. Edges of the larger grains are expected to be more sensitivity to alteration due to a locally higher surface-to-volume ratio, and edges will also contribute to fine magnetic domain state behavior (Pokhil & Moskowitz 1997). The cell edge length of 8.39458(6) Å agrees with almost stoichiometric magnetite (Fig. 2a), and the Mössbauer spectrum (see section 3.2) can be well fitted by stoichiometric magnetite. The Verwey transition is at 116.1 K (see section 3.2), which according to Aragón et al. (1985) indicates a very small (<2 %) degree of maghemitization. The high temperature thermomagnetic curve (Fig. 2b) yields a Curie temperature (T_c) of 586 °C determined by extrapolation of $1/\chi$ to χ=0 (Petrovský & Kapička, 2006). The ~6 °C higher than expected T_c is within an acceptable limit regarding uncertainties residing in the T_c determination method and temperature calibration. A hump occurs in the heating curve culminating at around 300-350 °C followed by a strong decay to ~400 °C. Irreversible partial heating-cooling cycles reveal that the decay is caused by transformation of magnetite to a low-magnetic phase (Fig. 2b). The XRD results show no mineralogical change after annealing the original magnetite material at 300 °C, but transformation of magnetite to hematite is clearly evidenced after 380 °C annealing (Fig. 2a), which proves that the decay in the χ-T behavior at ~300-400 °C is caused by magnetite-to-hematite transformation, as often described in literature (Liu et al., 2005; Knafelc et al., 2019). Semiquantitative Rietveld analysis of the crystalline phase yields ~40 wt% hematite in the 380 °C annealed sample, consistent with the χ-loss at ~300-400 °C during heating.

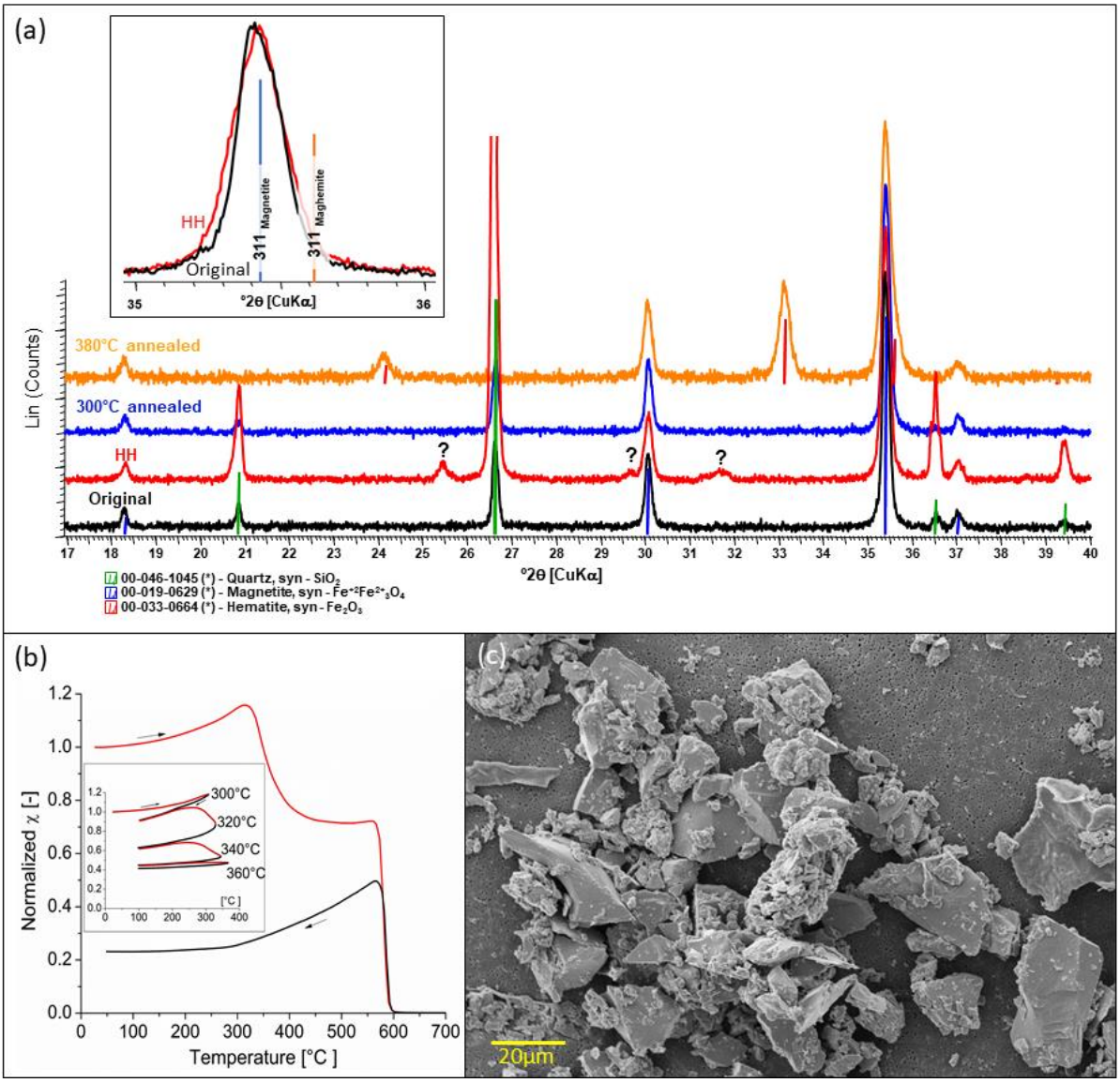

Figure 2. (a) XRD results of the original magnetite, HH, and original magnetite after annealing at 300 °C and 380 °C (Fe-fluorescence background subtracted; diffractograms scaled for similar intensity of the magnetite main peak). The small plot shows a comparison of the characteristic (311) magnetite peak for the original magnetite and HH. Expected peak positions of magnetite and maghemite, as well as hematite, are indicated; quartz was added as standard; peaks in HH marked by "?" cannot be assigned to any known Fe-oxide or Fe-hydroxide phase; microscopy results (Fig. 8a) indicate that they stem from contamination of the sample with filter material used for the high-humidity setups. (b) Thermomagnetic χ-T curve and partial heating-cooling cycles (inlet figure). (c) SEM image of the original magnetite.

The measured saturation magnetization of M_S=82.49 Am^2/kg is lower than the theoretical value of 92 Am^2/kg for magnetite, most likely because of the known decrease of M_S for fine particles (Mascolo et al., 2013; Li et al., 2017), which could be due to physically fine particles and particle-internal sub-division. Pre-existing slight LTO cannot explain the effect, as a ~10 % decrease in M_S would correspond to nearly 50 % oxidation (Readman & O'Reilly, 1972).

Reflected light microscopy (Fig. 8a) revealed that the original magnetite sample contains impurities, but their contribution is too low to influence concentration-dependent magnetic parameters as M_s.

3.2 Treated samples

Figure 3a shows the concentration-dependent parameters (χ, *SIRM*, M_s) after one year of exposure. There are no discernible differences between the results for the original magnetite (our control) and RR exposed to air; RH also does not show a change. In contrast, these three parameters are lower for the 70 °C setups, with a similar relative decrease for χ and M_s, and a larger one for the *SIRM*. The HH sample shows the by far most pronounced drop (χ: -13.4 %, *SIRM*: -31.6 %, M_s: -12.3 %), and for two of the three parameters (χ, *SIRM*) the results do not overlap with the control sample (original magnetite) within standard deviations.

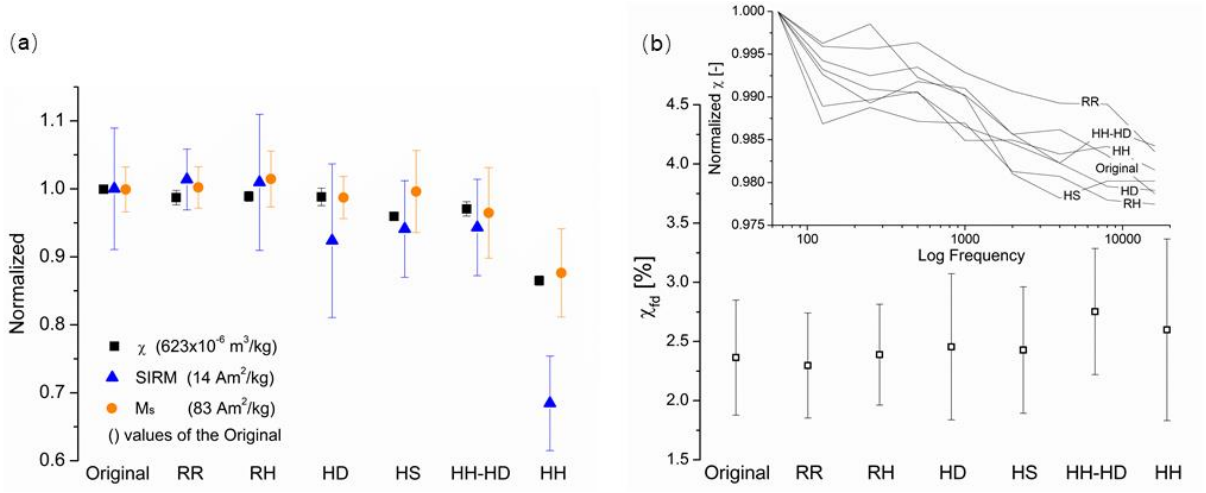

Figure 3. (a) Means and standard deviations for magnetic susceptibility (χ), saturation magnetization (M_s), and saturation isothermal remanence (*SIRM*). (b) Frequency-dependent susceptibility (χ_{fd}%) with means and standard deviations (lower plot), and broadband-frequency dependence of χ normalized to the 65 Hz value (upper plot).

Broadband-frequency results of χ (Fig. 3b; Table A1, appendix A) show a slightly decreasing trend with frequency that indicates a contribution of superparamagnetic behavior. However, frequency-dependent χ (χ_{fd}%) is generally low (~2.3-2.7 %; Fig. 3b), which means that the superparamagnetic contribution is only minor, with no detectable differences for all setups.

Parameters (B_h, *DP*) resulting from *IRM* modeling, using a single log-Gaussian distribution, are plotted in Figure 4. The width of the coercivity distribution (*DP*) is higher for all treated setups

(2.27-2.34; highest for HH and HD) compared to the original magnetite (2.24). The measure of the mean coercivity (B_h) is similar for all samples (21-23 mT) except for HH (26 mT).

The use of FORC diagrams for identifying magnetic grain sizes and particle interactions is becoming increasingly common (Roberts et al., 2014). For our samples, the obtained FORC diagrams do not show relevant differences (Fig. 4).

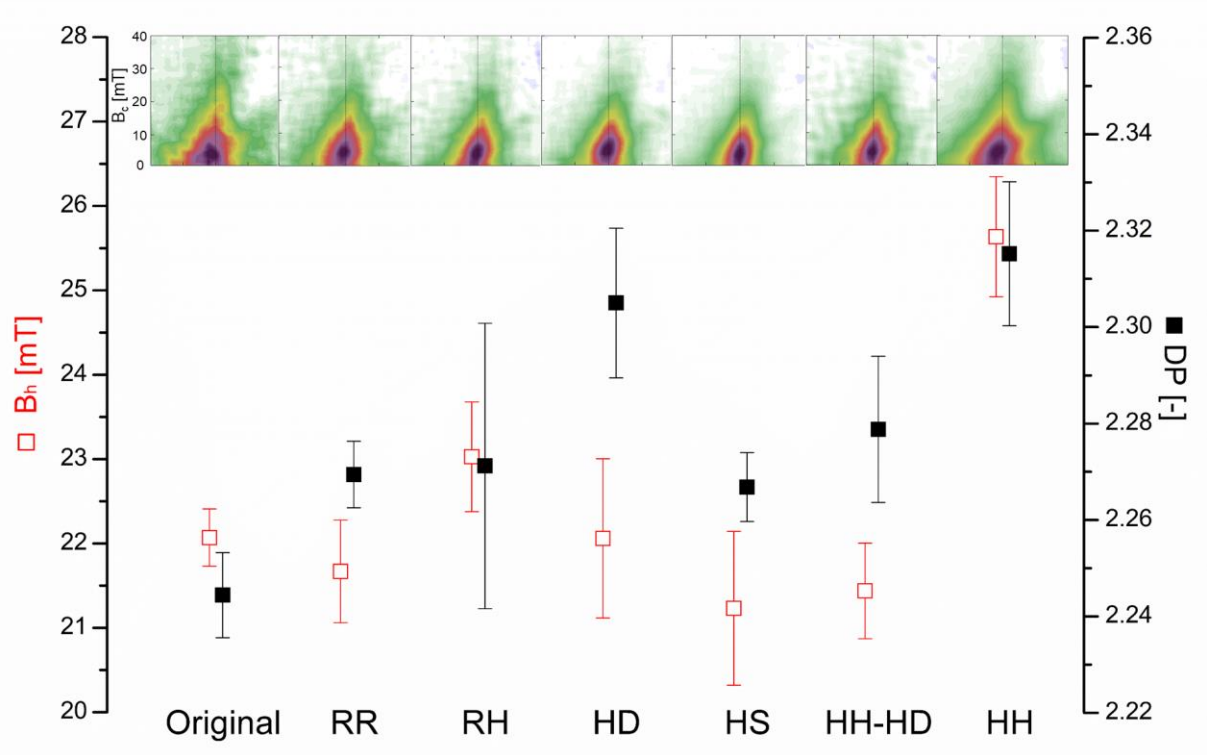

Figure 4. B_h and *DP* from cumulative log-Gaussian unmixing of IRM acquisition curves after Maxbauer et al. (2016); B_h: applied field at which the mineral phase acquires half of its saturation IRM (*SIRM*), *DP*: dispersion parameter (width of the log-Gaussian distribution). Top: FORC diagrams (smoothing factor 4).

The measured Mössbauer spectra (Fig. 5) are characteristic of magnetite, with two sextets corresponding to tetrahedral (MagT) Fe^{3+} and octahedral (MagO) Fe^{2+}-Fe^{3+} sites (for modeling results see Table A2, appendix A). The only sample showing an additional sextet is HH (for spectra of other setups see Figure B1, appendix B). This modeled additional sextet accounts for ~9 % of the spectral area. It is characterized by a negative quadrupole shift (Q-shift), which is typical of an Fe oxide such as hematite or goethite. As we measured at 140 K, the high hyperfine field value (50 T) is more indicative of hematite than goethite. A significant contribution of ferrihydrite (Fh) can be excluded. Above 77 K, 2-line Fh is characterized by a duplet, and even though 6-line Fh shows some magnetic ordering, it is relatively incomplete and the hyperfine

parameters are very different from those expected for hematite. The integrated areas of the magnetite sextets (i.e., relative abundances of MagT and MagO) allows to estimate the stoichiometry (i.e. Fe^{2+}/Fe^{3+} ratio) of the sample using the equation $Fe^{2+}/Fe^{3+}=0.5 \times MagO/(0.5 \times MagO+MagT)$ (Gorski & Scherer, 2010). In general, all samples obey the expected stoichiometric ratio for magnetite (i.e. 0.5).

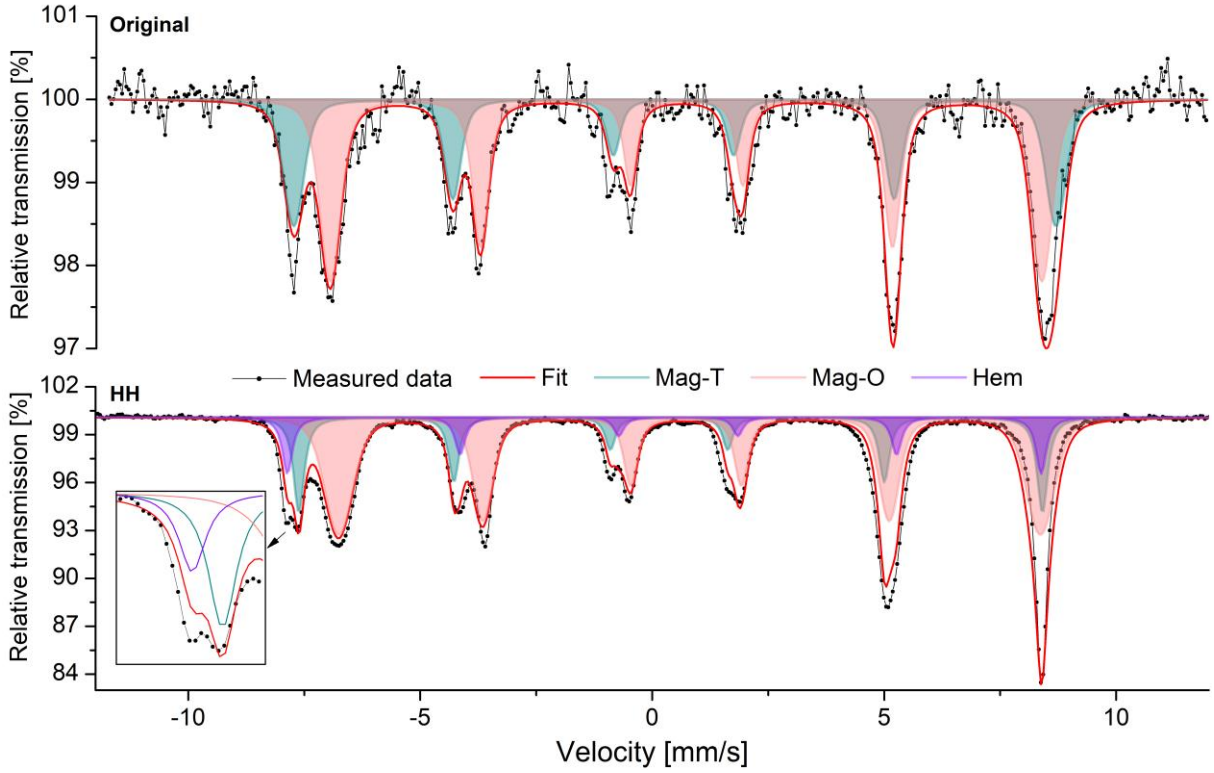

Figure 5. Mössbauer spectra of the original magnetite and the HH setup. Enlarged parts reveal the additional contribution of a second phase in HH, likely hematite.

The XRD result of HH (Fig. 2a) does not show a skew or broadening of the characteristic magnetite diffraction peak (311 peak) towards larger 2Θ-angles. In contrast to the Mössbauer result, hematite is not detected in the diffractogram of HH, but there are several small peaks which cannot be assigned to any Fe-containing phase. A significant contribution of ferrihydrite can be excluded based on the Mössbauer results and because of the fact that ferrihydrite will not survive at 70 °C for one year (Schwertmann et al., 2004). In order to check whether the small peak shift for the HH samples towards larger diffraction angles (Fig. 2a) represents a significant maghemitization effect, we analyzed the lattice constants from the XRD results of the different setups (Fig. B2, appendix B). The lattice constants vary on the third digit (in Å), with a reproducibility of 0.0001 Å determined by preparing and measuring samples twice (Table 1). They show significant differences between different samples (Fig. 7), with the lowest

value for the sample HH corresponding to the highest degree of maghemitization. The grain sizes calculated from the pure size broadening parameter *B1* range from 100 to 130 nm, and the strain broadening parameter *k2* is consistently zero in contrast to the KCl, which showed some strain broadening. The differences between the measured and the calculated magnetite peaks did not show any indication of asymmetry.

Thermomagnetic curves show the most distinct changes between the different setups (Fig. 6). The onset of the decay in the low-temperature χ-T curves is approximately matching with the expected Verwey transition of stoichiometric magnetite, but the T_V-values determined by the inflection point of the χ-T curve (i.e., the maximum of the first derivative), are up to ~10 °C lower. A homogeneous phase (stoichiometric or homogeneously oxidized magnetite) would exhibit a steep drop in the χ-T curve at T_V. The slope in the measured curves probably indicates gradual maghemitization. The low-temperature χ-T curves (Fig. 6a) show a systematic shift of the Verwey transition towards lower temperature for all 70 °C setups. The determined T_V is lowest for HH, followed by HD and HH-HD with almost the same T_V shift (Fig. 7). HS also shows a clear T_V shift, while no significant change compared to the original magnetite is observed for RH and RR. We additionally calculated the χ-T slope of the χ-T curves at $T=T_V$. For this, we normalized the curves to the difference between the cold and warm ends to eliminate the effect of the peak slightly above T_V, which is due to magnetocrystalline isotropy. All 70 °C setups show a flatter slope compared to the original magnetite, with similar flattening for HS, HD and HH-HD, and a clearly flattest slope for HH (Fig. 7).

High-temperature χ-T curves of all samples, including RR, show a less pronounced hump and smaller decrease at ~300-400 °C than the original magnetite; the biggest change is again observed for the sample HH setup. The χ values in the cooling curves are much lower indicating a strong loss of magnetite that occurs in two temperature intervals during heating, at ~300-400 °C and above T_C of magnetite. All samples except HH show a very similar Curie temperature (T_C ~584-586 °C). The clearly higher T_C for HH (596 °C) is reversible in heating and cooling curves and the slope of the χ-T curve near T_C is equally steep as for the other setups.

The experimental argon sorption isotherms (Fig. B3, appendix B) are classified as type II according to the most recent IUPAC classification (Thommes et al., 2015). Neither a plateau nor hysteresis are observed. All isotherms possess an ill-defined point B indicating overlap of mono- and multilayering processes. The absence of a plateau close to $P/P_0=1$ suggests continuous and unrestricted thickening of the adsorbate layer up to the saturation pressure. This

is typical for nonporous or macroporous adsorbents (Rouquerol et al., 2013). Quantitative analysis of the micropore range (P/P_0 <0.15) using the Dubinin-Astakhov theory of volume filling yields no evidence of microporosity. This is in qualitative agreement with the shape of the isotherms and the anticipated material properties. Application of BET-theory provides specific surface areas between 1.4 and 0.8 m^2/g applying a Rouquerol-plot for objective constraints of the fitting range (Rouquerol et al., 2007).

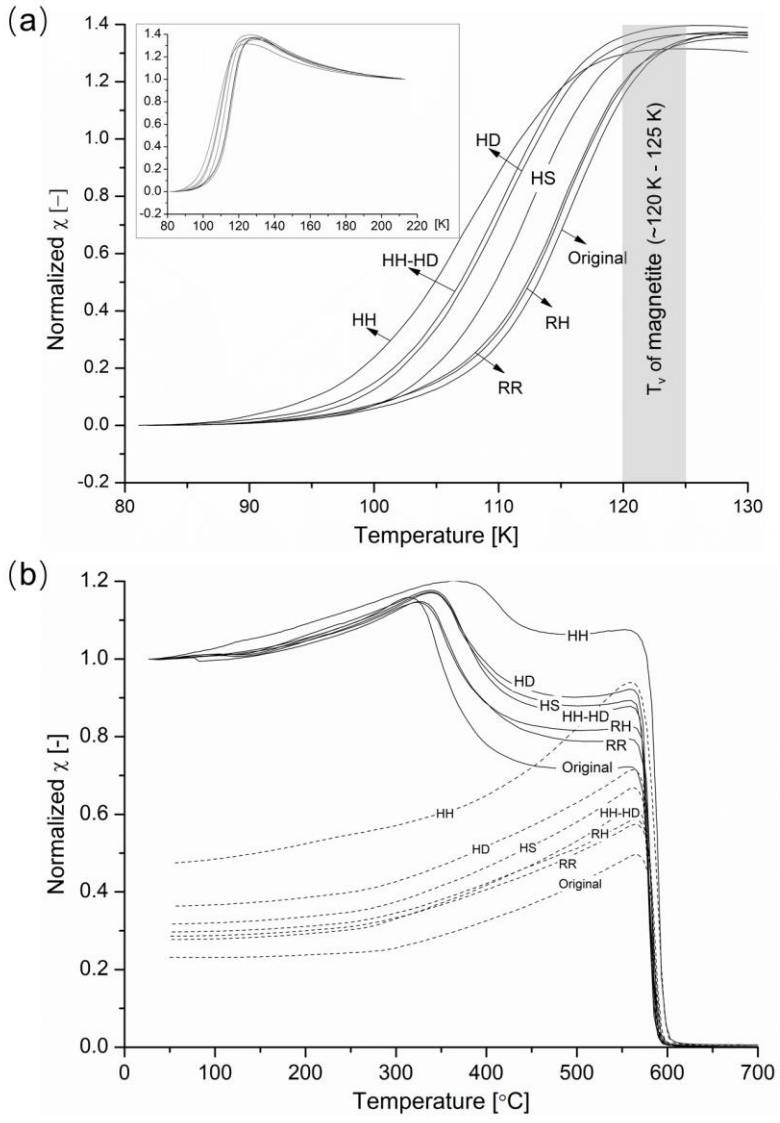

Figure 6. Thermomagnetic curves of magnetic susceptibility χ (each the mean from ten curves): (a) Low-temperature χ-T (warming) curves (normalized to room temperature χ-values), shown as full curves (small plot) and enlarged for T<130 K; the range of expected T_v values for stoichiometric magnetite is shown by the gray bar (Aragón et al., 1985; Brabers et al., 1998; García et al., 2001; Jackson et al., 2011); the peak at slightly above T_v is due to the isotropic point of magnetocrystalline anisotropy. (b) High-temperature thermomagnetic χ-T curves (normalized to the starting value).

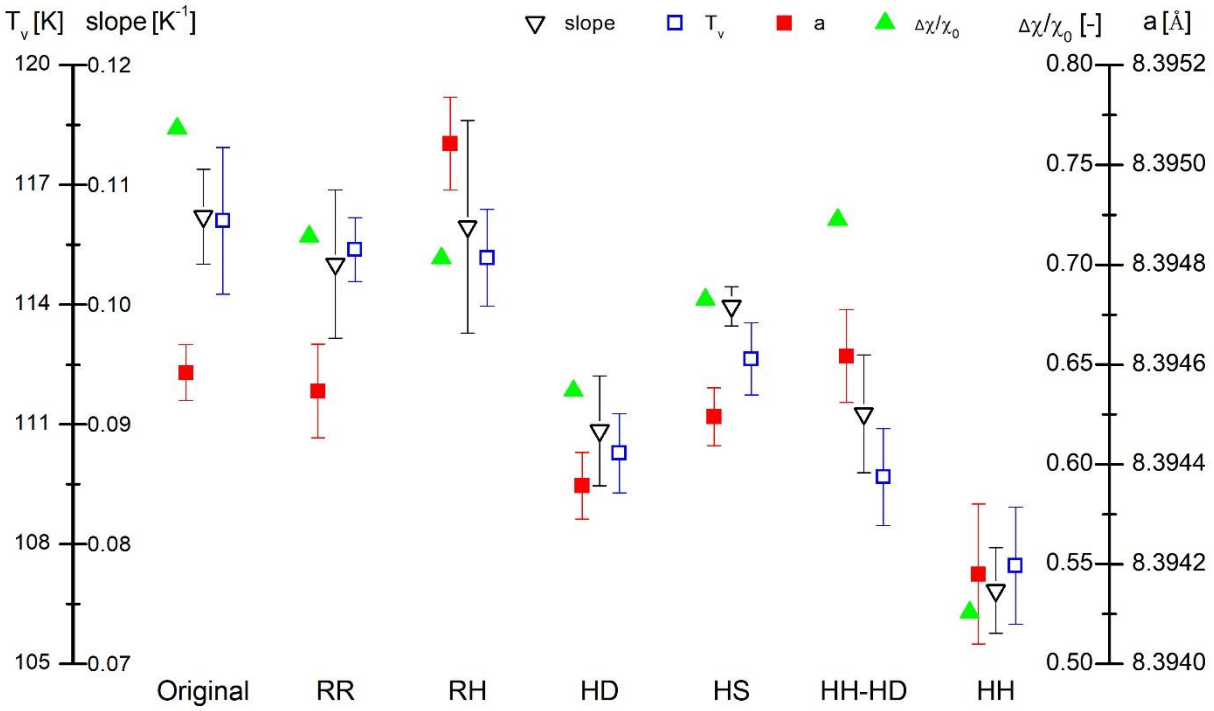

Figure 7. Verwey transition temperature (T_v) represented by the inflection point of χ-T curves, slope at T_v (lower value means flatter slope), $\Delta\chi/\chi_0$ ratios (relative χ-loss between heating and cooling curves), and lattice constant (a), for the measured setups.

Light microscopy (Fig. 8) revealed magnetite surfaces homogeneously covered with ferrofluid for all samples except sample HH, where small spots with no ferrofluid cover are visible inside of particles (Fig. 8e). These ferrofluid-free spots unambiguously represent non-magnetic or weakly magnetic inclusions. In sample HH, also some larger parts of particles are not covered with ferrofluid and the transition between these parts and the ferrofluid-covered magnetite is diffuse (Fig. 8b). Moreover, there are non-magnetic areas not covered with ferrofluid with a sharp contact to magnetite (Figs 8a and c). They represent impurities, which could be intergrowths with ilmenite due to exsolution during formation. The back-scattered electron images of the SEM results indicate patches with different reflectivity in sample HH (Fig. 9c), which might be due to partial maghemitization or hematite. However, this conclusion has to be considered with great caution as the smoothness of sample surfaces could be different, and the contrast could be also influenced by the electron beam characteristics.

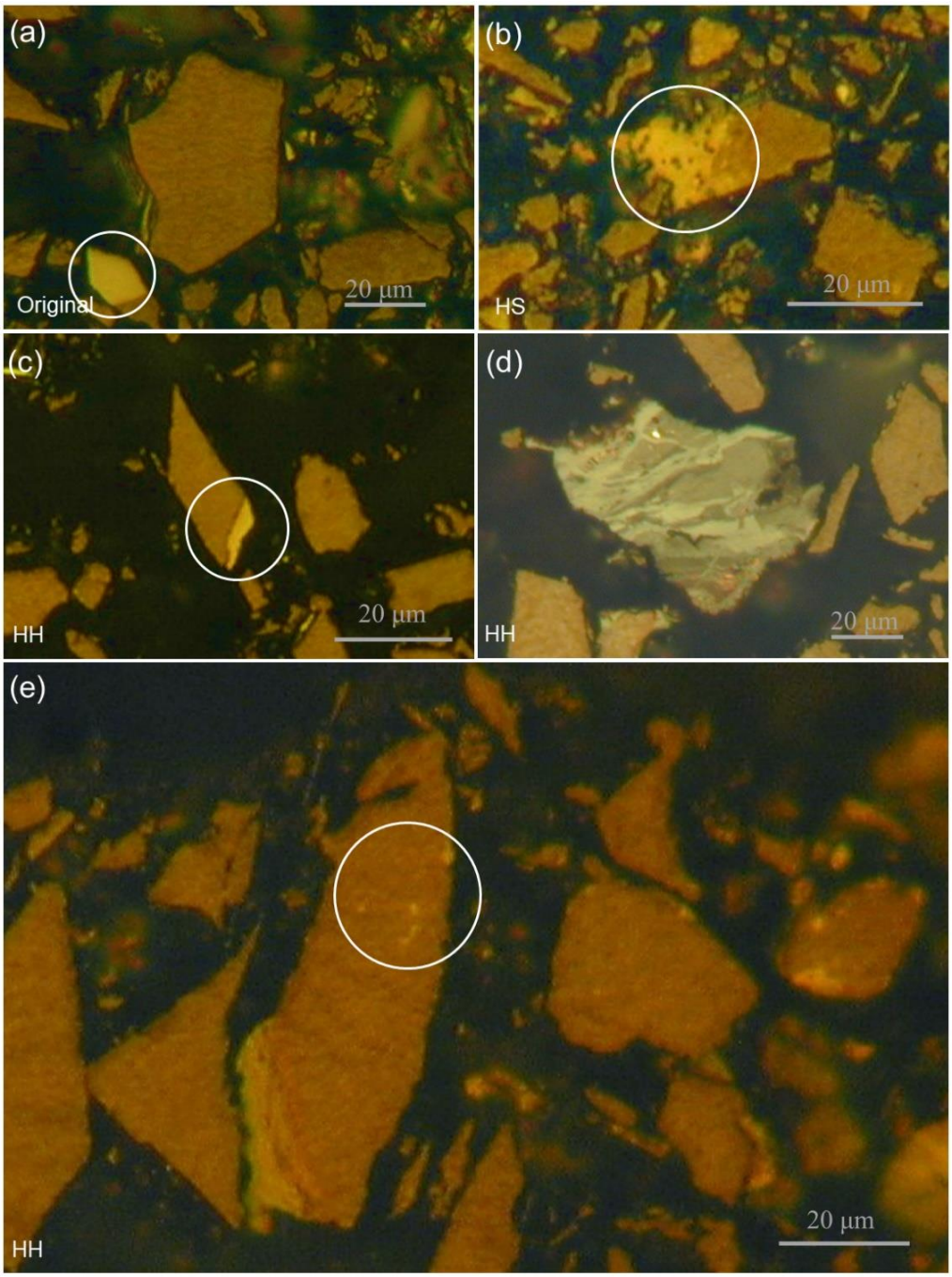

Figure 8. Micrographs from reflected light microscopy. All shown images are taken with ferrofluid cover (brownish fine patterns of ferrofluid nanoparticles accumulation, which mainly represent maze patterns due to polishing-induced inhomogeneous surface stresses) that identify strongly magnetic phases, and unambiguously document magnetite or maghemitized magnetite. Non-magnetic or weakly magnetic impurities with sharp boundary to magnetite are visible in (a) and (c), marked by circles. Small spots inside particles without ferrofluid cover in (e) within the marked circle are non-magnetic or weakly magnetic and could represent hematite. The particle within the circle of (b) shows a larger area without ferrofluid cover with diffuse transition to the magnetite. In (d) contamination with filter material is identified.

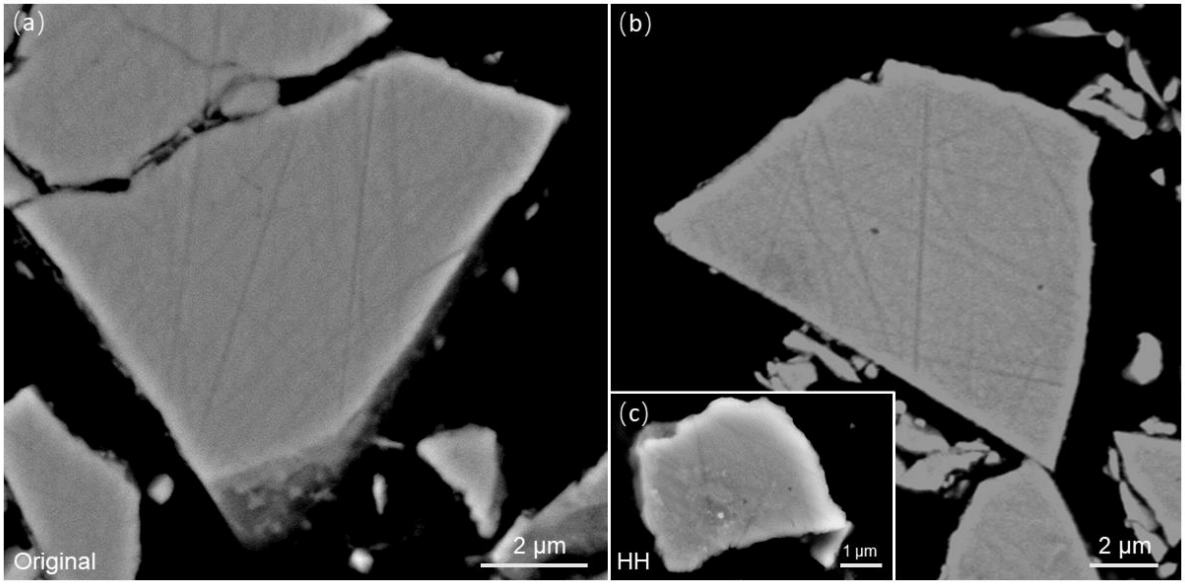

Figure 9. SEM images in back-scattered mode, comparing surfaces of (a) the original magnetite sample and (b, c) the altered HH setup (line meshes are scratches from polishing). The surface in (c) shows patches with different reflectivity. The lighter rim at the particle edges is most probably caused by surface relief.

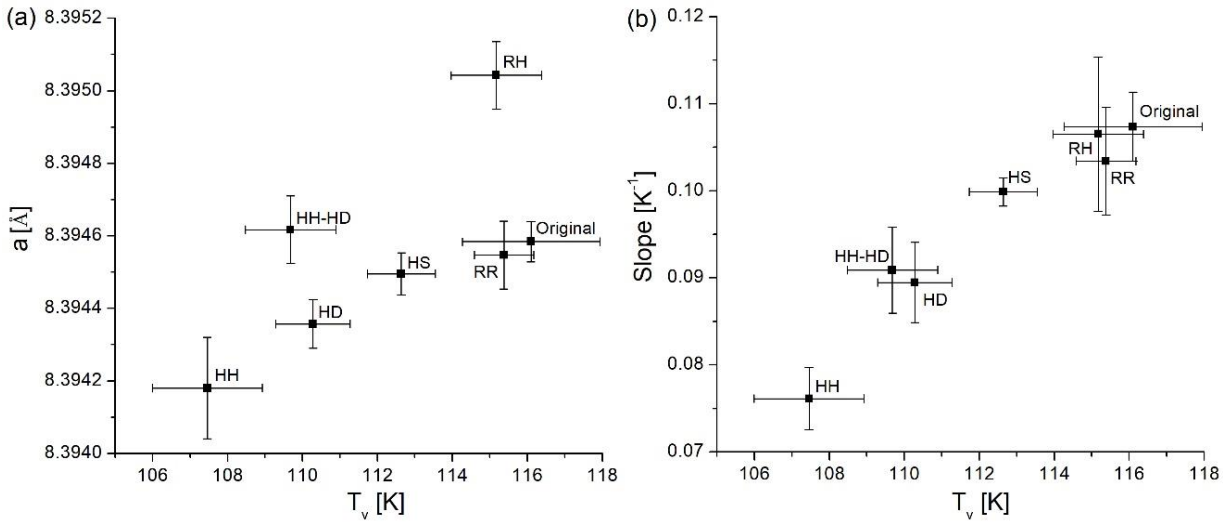

Figure 10. Bivariate plots of lattice constants (*a*) versus Verwey transition temperatures (T_v), and slope factors (of χ-T curves at T_v) versus T_v. Correlation coefficients for a vs T_v and slope vs T_v are r=0.65 and r=0.97, respectively.

Table 1. Means and standard deviations for relevant parameters, χ: magnetic susceptibility; *SIRM*: saturation isothermal remanent magnetization; M_s: saturation magnetization; χ_{fd}: percentage-frequency dependence of χ; B_h, *DP*: IRM unmixing parameters; T_v: Verwey transition temperature; *slope*: slope factor at T_v; *a*: lattice constant (with control measurements for RH and HH-HD, marked by stars); T_c: Curie temperature; $\Delta\chi/\chi_0$: relative χ-loss between heating and cooling curves). Number of samples for standard deviations: N=10 for χ, *SIRM*, M_s, χ_{fd}, B_h, *DP*; N=5 for T_v and *slope* (except N=4 for RH); internal single sample error for *a*.

	χ	SIRM	M_s	χ_{fd}	B_h	DP	T_v	slope	*a*	T_c	$\Delta\chi/\chi_0$
	[10^{-6} m^3/kg]	[Am^2/kg]	[Am^2/kg]	[%]	[mT]	[-]	[K]	[K^{-1}]	[Å]	[°C]	[-]
Original	623.5 ± 2.97	14.01 ± 1.25	82.49 ± 2.72	2.36 ± 0.49	22.07 ± 0.34	2.24 ± 0.01	116.10 ± 1.83	0.107 ± 0.0040	8.39458 ± 0.000056	586	0.77
RR	615.8 ± 6.64	14.20 ± 0.63	82.75 ± 2.51	2.30 ± 0.44	21.69 ± 0.61	2.27 ± 0.01	115.38 ± 0.79	0.103 ± 0.0062	8.39455 ± 0.000094	585	0.71
RH	616.9 ± 4.65	14.14 ± 1.40	83.77 ± 3.39	2.39 ± 0.43	23.03 ± 0.65	2.27 ± 0.03	115.18 ± 1.21	0.107 ± 0.0089	*8.39504 ± 0.000093	586	0.70
HD	616.5 ± 8.06	12.94 ± 1.58	81.52 ± 2.55	2.45 ± 0.62	22.06 ± 0.94	2.31 ± 0.02	110.28 ± 0.99	0.089 ± 0.0046	8.39436 ± 0.000067	584	0.64
HS	598.6 ± 3.62	13.18 ± 0.99	82.24 ± 4.98	2.43 ± 0.53	21.23 ± 0.91	2.27 ± 0.01	112.64 ± 0.91	0.100 ± 0.0016	8.39450 ± 0.000058	584	0.68
HH-HD	605.5 ± 6.57	13.21 ± 0.99	79.66 ± 5.49	2.75 ± 0.53	21.44 ± 0.57	2.28 ± 0.02	109.69 ± 1.21	0.091 ± 0.0049	**8.39462 ± 0.000093	584	0.72
HH	539.8 ± 4.32	9.59 ± 0.97	72.37 ± 5.35	2.60 ± 0.77	25.64 ± 0.71	2.32 ± 0.01	107.46 ± 1.47	0.076 ± 0.0036	8.39418 ± 0.000140	596	0.53

*8.39514 ± 0.000068 **8.39462 ± 0.000056

4. Discussion

The variants of storing the magnetite samples at room temperature and 70 °C with relative humidity range between dry and humid. Regarding relative humidity, a sequence (from higher to lower alteration) was expected starting with HH (permanently at >90 %), followed by HH-HD (cycling between 5 % and >90 %), HS (permanently at 13 %), HD (permanently at 5 %), all at 70 °C, and ending with the room temperature setups RH and RR, and the original magnetite (control sample). In the sub-sections below, we discuss the observed changes of properties as a function of humidity and the possible mechanism of alteration, and we identify the most sensitive indicators for LTO.

4.1 Observed changes for the different setups related to humidity

Some parameters remained constant within experimental errors. Specific surface areas remained constantly low, crystal coherence lengths did not change and Ar sorption isotherms provided no indication for micro- and mesoporosity. This agrees with findings of Sidhu et al. (1977). The apparent absence of micro- and mesoporosity and the low specific surface areas limit also potential amounts of ferrihydrite, because ferrihydrite has specific surface areas >200 m^2/g and substantial microporosity (Cornejo et al., 1984; Stanjek & Weidler, 1992). Furthermore, within one year at 70 °C ferrihydrite would fully transform to hematite or goethite (Schwertmann et al., 2004). The formation of hematite (observed by Mössbauer spectroscopy in sample HH only) is also less likely, as the direct transformation of magnetite to hematite (martitization) involves the development of substantial porosity (Anand & Gilkes, 1984). Pores could speed up Fe diffusion inside of particles akin to ion exchange reactions in minerals, where the replacement of larger cations by smaller ones produces microporosity (Putnis, 2002).

Other parameters, however, did change, and relevant numerical results are summarized in Table 1. Alterations after one year of exposure are small, as expected, but detectable. Both

low- and high-temperature χ-T curves show clear differences between the setups, also lattice constants and concentration-dependent magnetic parameters (χ, M_s, *SIRM*), as well as *IRM* acquisition curves (B_h, *DP*) reveal changes. FORCs and frequency-dependence of χ turned out to be not sensitive enough within their limits of uncertainty and therefore these results will be omitted in the discussion. Moreover, there are several striking observations, which are difficult to explain and require further research.

The first is the smaller hump and smaller subsequent decrease at ~300-400 °C in the high-temperature χ-T curves which appears in all altered setups and is most pronounced for HH (Fig. 6). The weaker the hump, the smaller is the χ-loss after heating (Figs 6 and 7). It seems that the type of alteration acquired during the one year of exposure protects the magnetite from oxidation during heating.

The second remarkable observation is the almost double as large decrease of the *SIRM* compared to χ and M_s for HH (Fig. 3a), which implies that HH is magnetically softer. Magnetic hardness is expected to increase with maghemitization due to inhomogeneous stress distribution (Appel, 1987; Van Velzen & Dekkers, 1999) and only decreases again near full (90 %) maghemitzation (Ge et al., 2014). However, a decrease of the magnetocrystalline constant K_1 (Goss, 1988) would cause the opposite effect in case of low stress. Moreover, inhomogeneous maghemitization could lead to particle-internal fining (Appel & Soffel, 1984), which may cause increasing superparamagnetic behavior, thereby reducing the *IRM* capacity. Particle-internal fining is in fact supported by the slight symmetric peak broadening of the main 311 magnetite XRD peak for HH (Fig. 2a), but the generally low χ_{fd}% values (Fig. 3b) put this in question as a major effect. Eventually, explaining the inconsistency in the decrease of *SIRM*, χ and M_s remains an open issue. In this context, also the higher B_h-value for HH (Fig. 4) is of importance that indicates an increase in magnetic hardness, which is another enigma.

The Mössbauer result for HH (Fig. 5) suggests the presence of a considerably large hematite content (~9 %), but surprisingly hematite is not detected in the XRD results (Fig. 2a). The presence of ferrihydrite would give a different spectrum in the Mössbauer result and can be excluded as mentioned above. Moreover, at 70 °C ferrihydrite would transform into hematite within weeks (Schwertmann et al., 2004). The ~12-13 % drop of χ and M_s for HH compared to the original magnetite (Fig. 3a) might be interpreted as a measure of the amount of magnetite transformed to hematite. However, because of the unknown amount of contamination with filter material, the decrease in χ and M_s should be generally interpreted with caution. The indication

of hematite by the Mössbauer result is a rather robust result, and even if the 9 % hematite content is strongly overestimated, which might be the case, it should still be in the detection range of XRD. It could be speculated that ultrafine crystallite size of the newly formed hematite fraction that causes extreme broadening of the XRD peaks might lower the peak heights to below the noise level.

As expected, the most obvious deviations in all parameters occurred for sample HH, held at 70 °C and high relative humidity >90 %. Sample HH is different from all other samples by the lowest Verwey transition temperature, in agreement with the lowest lattice constant (Figs 7 and 10). It shows the highest B_h and *DP* values (Fig. 4), the lowest concentration-dependent magnetic parameters (χ, M_s, *SIRM*) relative to the other samples (Fig. 7), and the high-temperature χ-T curve shows a broader hump at ~300-400 °C with a subsequent decrease which is lowest of all samples (Figs 6 and 7). Within the samples HH-HD, HD and HS, the sequence is different from the expected one, as HD shows larger changes than HS, and the changes observed for HH-HD and HD are similar. Properties of the room temperature setups (RR, RH) are very similar to the original magnetite. Slight effects in high-temperature χ-T curves (less intense hump and smaller loss of χ after heating-cooling) and in the Verwey transition (slight slope decrease) indicate a very minor change (Figs 6 and 7). This does not mean that humidity has no effect on magnetite alteration at room temperature, but either the alteration process is too slow at this low temperature to be detectable within the one-year period, or only an altered thin surface layer has formed with a too small volume fraction to influence the analytical results.

The deviations from the expected sequence could be due to stoichiometric gradients within the particles (so-called core-shell structures) stemming from diffusional migration of Fe^{2+} towards the particle surface (Signorini et al., 2003). Gallagher et al. (1968) monitored the 440 reflection, which changed from a symmetric peak at the beginning of the oxidation reaction to an asymmetric peak in the middle of the reaction and became symmetric again after full oxidation to maghemite. Our XRD data gave no evidence of this kind of broadening, as the strain parameter *k2* converged for all samples to zero, whereas the KCl consistently had some strain. The presence of significant chemical gradients across larger parts of particle volumes is therefore less likely.

A linear decrease of T_v with maghemitization has been observed by Aragón et al. (1985), reaching a value of 82 K for about 15 % of oxidation (corresponding to δ of ~0.05 in equation 1), the strongest degree of non-stoichiometry at which a Verwey transition was still observed.

According to the results of Aragón et al. (1985), the observed 8.5 °C decrease of T_v for HH compared to the original magnetite corresponds to an increase of the LTO degree by about 3 % (change of δ by about 0.01). The change of the lattice constant yields a lower LTO degree of ~1 % by using the relationship of Cervellino et al. (2014) and Gorski & Scherer (2010). Regardless of this discrepancy in the absolute degree of LTO, there is a good correlation (r=0.65) between the T_v values and the lattice constants (Fig. 10).

From the above-mentioned results, it is obvious that we obtained consistent data, and that the Verwey transition is the most sensitive parameter tracing the detected LTO effects, accompanied by a small but well-correlated change in the slope of the χ-T curves at T_v (Fig. 10). However, the observed changes do not confirm the expected sequence, which indicates that water vapor at 70 °C seems to influence the oxidation reaction in a non-linear manner. In the second next sub-section, we discuss this in detail.

4.2 Whole particle alteration versus core-shell structure

A remarkable observation is the increase of the Curie temperature for HH (Fig. 6) by about 10 °C compared to the original magnetite and also all other setups (Figs 6 and 7). LTO is known to cause an increase of T_c, as often observed for oceanic basalts (Nishitani & Kono, 1983). However, the determination of T_c for maghemite is uncertain due to its thermal instability. Dunlop & Özdemir (1997) proposed a value of T_c=675 °C, which corresponds to an LTO degree of ~10 % for an increase of T_c by 10 °C. This differs substantially from the degree of maghemitization resulting from the shift of T_v and from the decrease of the lattice constant.

If as often proposed, a core-shell structure exists (Cui et al., 1994; Liu et al., 2004b; Byrne et al., 2015), the gradient across different LTO degrees will cause a tail in the low temperature χ-T curves towards lower temperatures. A flatter slope is in fact observed for HH (and also for other 70 °C setups), and there is a very strong bivariate relationship (r=0.97) between T_v and the slope factor of the χ-T curves at T_v (Fig. 10), indicating that a stronger gradient of alteration developed in parallel increasing LTO. However, the shift of the low-temperature χ-T curve as a whole is more pronounced (Fig. 6) than the slope change. The almost parallel shift of the decay at T_c in the high-temperature χ-T curve of HH (Fig. 6), and the consistently zero strain broadening parameter *k2* in the XRD curves, both support the interpretation that the gradient of the oxidation degree is relatively minor compared to the absolute change of the LTO degree throughout the whole volume of particles. Observations from reflected light microscopy and

back-scattered electron SEM additionally support the interpretation that alteration happens within the interior of particles (Fig. 8e). Still, thin surface layers with significantly stronger LTO might exist, making up extremely little of the total particle volume and thus are undetected by the applied analyses. Nedkov et al. (2006) reported oxidized very thin layers of about 3 nm, where the oxidation state varied from zero to about 0.2, revealed by surface-sensitive Mössbauer spectroscopy.

How could the interior of the particles acquire a relatively homogeneous degree of alteration without a strong gradient? Shrinkage cracks forming at advanced LTO due to the decreasing lattice parameter (Petersen & Vali, 1987) create internal surfaces and allow water vapor and oxygen to penetrate into the interior of particles, which could decrease the inhomogeneity of LTO. However, the oxidation degree in the studied samples is most probably not sufficient to initiate shrinkage cracks, and the Ar isotherm results clearly show that no porosity developed. The rate limiting step of the well-established oxidation mechanism of magnetite is the diffusion of Fe ions towards the surface, which has an activation energy of about 81 kJ/mol (Sidhu et al., 1977). This activation energy is low enough to oxidize submicron magnetites even at room temperature, as Murad & Schwertmann (1993) documented by an increase of the oxidation state from δ=0.14 to δ=0.18 within five years for synthetic magnetites of submicron size.

4.3 The impact of water on the oxidation reaction

Albeit the oxidation reaction (equation 1) does not contain water molecules, the presence of water or OH groups within or on magnetite has been reported already by David & Welch (1956) and Egger & Feitknecht (1962), who observed that even after heating samples in Ar to 960 °C magnetites retained residual water contents of 2 mg/g. These water contents stem very likely from the solution pathway, where green rust precursors yield some incorporation of OH groups into the spinel structure (e.g. Olowe et al., 1989; Ruby, 2015). We did not find any information about structural OH contents in natural magnetites.

Water contents of 2 to 10 mg/g sorbed on magnetite correspond to a monolayer of water molecules, which is liberated by heating to 100 °C (Egger & Feitknecht, 1962). These water molecules interact with surface OH groups on magnetite, which are of variable coordination. Rustad et al. (2003) distinguish twelve different coordination sites ranging from singly coordinated ones (e.g. Fe^tOH and Fe^oOH) to triply coordinated surface groups $Fe^o_2Fe_2O(H)$ and $Fe^o_3O(H)$. These functional sites are not all fully protonated, but on freshly cleaved magnetite

hydroxylation starts at water pressures as low as 0.1 Pa and produces hydroxylation extending several layers (up to 8 Å) into the bulk structure (Kendelewicz et al., 2000). The oxidation state of iron, however, does not change after converting a water molecule into two structural OH groups (Kendelewicz et al., 2000). Yet, Eltouny & Ariya (2014), found slight oxidation of magnetite after adsorbing water vapor.

Regardless of whether the surface undergoes redox reactions or not, these surface OH groups provide sufficient bonding strength for adsorbing additional water molecules. Egger & Feitknecht (1962) mention that magnetite dried over P_2O_5 warms up considerably after adding water vapor. This chemical bonding expresses also as a pronounced hysteresis in the water adsorption isotherm between P/P_0 =0.15 and 1.0 (Tombacz et al., 2009). Regarding our measurements, the magnetites held at relative humidity of >90 % should be covered by at least a monolayer of water molecules. In a simple interpretation, this adsorbed water layer should hinder the free access of oxygen molecules to the surface and, therefore, oxidation rates should decrease with adsorbed water. Eltouny & Ariya (2014) found that the adsorption of toluene onto magnetite was reduced or completely hindered by varying relative humidities.

This interpretation, however, is in contrast to our finding because sample HH is the most oxidized one. This indicates that adsorption of water molecules itself might enhance the oxidation kinetics. Calculations with density functional theory by Mulakaluri et al. (2009) and Kendelewicz et al. (2013) show that the surface layer of magnetite exclusively contains Fe^{3+}, which results in an enlarged band gap of 0.3 eV in the surficial octahedral layer. Adsorption of water molecules and the formation of surface hydroxyl groups, however, lower this band gap towards half-metallic behavior (Mulakaluri et al., 2009). Water adsorption in combination with the complex restructuring of magnetite surfaces may therefore enhance the redox kinetics of the magnetite-maghemite transformation.

The discrepancy between the expected sequence and the observed degrees of LTO for the experimental setups, however, remains to be solved in future work, in which the presumably non-linear interaction of water sorption needs to be investigated. The only work known to us, where redox kinetics were measured at various water vapor pressures is from Viswanath et al. (1975), who observed minima and maxima in the reduction kinetics of hematite with hydrogen and increasing partial water pressures.

5. Conclusions

Maghemitization is observed in all 70 °C setups by a shift of the Verwey transition temperature (T_V). The Verwey transition is the most sensitive property for discriminating different LTO degrees, also lattice constants show a significant change correlating well with the observed trend of T_V. Effects in the high-temperature χ-T curves are likewise sensitive, however the underlying mechanism remains an open question.

Our study provides evidence that the interaction of water at ambient conditions (in contrast to ultrahigh vacuum conditions of most studies) may enhance LTO. Permanently high relative humidity >90 % caused the strongest degree of alteration (HH setup), and only for this setup there is an indication for transformation of magnetite to hematite. However, our results do not support a linear humidity dependence. The sample that stayed at permanently dry conditions of ~5 % relative humidity (HD setup) and alternating relative humidity between >90 % and ~5 % (HH-HD setup) show clearly lower alteration than the HH setup, and both developed a very similar degree of LTO. Intermediate relative humidity (HS setup) seems to cause less alteration than extremely dry conditions. While a humidity effect on magnetite alteration at relatively low temperature (70 °C) is obvious from our results, we are still far from establishing any transfer function for magnetic properties. The much lower alteration of HH-HD compared to HH is an important indication of seasonality effects in natural weathering.

The χ-T curves, in particular low-temperature curves, and the XRD results, suggest that alteration affects the particles as a whole, without developing a strong gradient in the particle interior. Possibly existing stronger altered thin particles will escape our analytical results because of their small contribution to the total volume.

In future studies, surface-sensitive methods could be applied to tackle the open question of thin surface layers with higher degree of LTO. A larger number of setups should be installed at different temperatures for more detailed assessment of humidity control, and sampling after regular time intervals would allow further insight into the timing of progressing processes.

Acknowledgments

This research work is supported by the German Research Foundation (DFG; AP 34/44-1). Qi Zhang was the lead author in all parts of this research work, Erwin Appel defined the research question and contributed to the interpretation and paper writing, James Byrne and Julian Sorwat

performed and interpreted the Mössbauer analysis, Helge Stanjek and Christoph Berthold performed and interpreted the XRD analysis, Helge Stanjek and Timo Seemann performed and interpreted the Argon physisorption isotherms analysis, Wolfgang Rösler designed the experimental setup. We thank Hartmut Schulz, Timm Bayer, Tatiana Miranda, Simone Schafflick and Sebastian Staude for their support in SEM analysis and light microscopy. The data presented in this study are listed in Table 1 and in the appendix.

References

Abrajevitch, A. & Kodama, K. (2009). Biochemical vs. detrital mechanism of remanence acquisition in marine carbonates: A lesson from the K-T boundary interval. Earth Planet. Sci. Lett., 286, 269-277. https://doi.org/10.1016/j.epsl.2009.06.035

Ahmed, I.A.M. & Maher, B.A. (2018). Identification and paleoclimatic significance of magnetite nanoparticles in soils. Proc. Natl. Acad. Sci., 115(8), 1736-1741. https://doi.org/10.1073/pnas.1719186115

Anand, R. & Gilkes, R. (1984). Mineralogical and chemical properties of weathered magnetite grains from lateritic saprolite. J. Soil Sci.35, 559-567. https://doi.org/10.1111/j.1365-2389.1984.tb00613.x

Appel, E. (1987). Stress anisotropy in Ti-rich titanomagnetites. Phys. Earth Planet. Inter., 46, 233-240. https://doi.org/10.1016/0031-9201(87)90185-3

Appel, E. & Soffel, H.C. (1984). Model for the domain state of Ti-rich titanomagnetites. Geophys. Res. Lett., 3, 189-192. https://doi.org/10.1029/GL011i003p00189

Aragón, R., Buttrey, D., Shepherd, J.P. & Honig, J.M. (1985). Influence of nonstoichiometry on the Verwey transition. Phys. Rev., B31,430. https://doi.org/10.1103/PhysRevB.31.430

Basavaiah, N. & Khadkikar, A.S. (2004). Environmental magnetism and its application towards palaeomonsoon reconstruction. Journal of the Indian Geophysical Union, 8/1, 1-14. http://14.139.123.141:8080/jspui/handle/123456789/271

Basavaiah, N., Mahesh Babu, J.L.V., Gawali, P.B., Naga Kumar, K.Ch.V., Demudu, G., Prizomwala, S.P., Hanamgond, P.T. & Nageswara Rao, K. (2015). Late Quaternary environmental and sea level changes from Kolleru Lake, SE India: Inferences from mineral magnetic, geochemical and textural analyses. Quat. Int., 371, 197-208. https://doi.org/10.1016/j.quaint.2014.12.018

Basta, E. (1959). Some mineralogical relationships in the system Fe_2O_3-Fe_3O_4 and the composition of titanomaghemite. Econ. Geol., 54, 698-719. https://doi.org/10.2113/gsecongeo.54.4.698

Begét, J.E., Stone, D.B. & Hawkins, D.B. (1990). Paleoclimatic forcing of magnetic susceptibility variations in Alaskan loess during the late Quaternary. Geology, 18, 40-43. https://doi.org/10.1130/0091-7613(1990)018<0040:PFOMSV>2.3.CO;2

Bourgeois, F., Gergaud, P., Renevier, H., Leclere, C. & Feuillet, G. (2013). Low temperature oxidation mechanisms of nanocrystalline magnetite thin film. J. Appl. Phys., 113, 013510. https://doi.org/10.1063/1.4772714

Brabers, V.A.M., Walz, F. & Kronmüller, H. (1998). Impurity effects upon the Verwey transition in magnetite. Phys. Rev., B58, 14163. https://doi.org/10.1103/PhysRevB.58.14163

Brunauer, S., Emmett, P.H. & Teller, E. (1938). Adsorption of gases in multimolecular layers. J. Am. Chem. Soc., 60(2), 309-319. https://doi.org/10.1021/ja01269a023

Byrne, J.M., Klueglein, N., Pearce, C., Rosso, K.M., Appel, E. & Kappler, A. (2015). Redox cycling of Fe(II) and Fe(III) in magnetite by Fe-metabolizing bacteria. Science, 347, 1473-1476. https://doi.org/10.1126/science.aaa4834

Byrne, J.M., van der Laan, G., Figueroa, A.I., Qafoku, O., Wang, C.M., Pearce, C.I., Jackson, M., Feinberg, J., Rosso, K.M. & Kappler, A. (2016). Size dependent microbial oxidation and reduction of magnetite nano- and micro-particles. Sci. Rep., 6, 30969. https://doi.org/10.1038/srep30969

Cervellino, A., Frison, R., Cernuto, G., Guagliardib, A. & Masciocchi, N. (2014). Lattice parameters and site occupancy factors of magnetite–maghemite core–shell nanoparticles. A critical study. J. Appl. Cryst., 47, 1755–1761. doi:10.1107/S1600576714019840

Chen, T.S., Xu, H.F., Xie, Q.Q., Chen, J., Ji, J.F. & Lu, H.Y. (2005). Characteristics and genesis of maghemite in Chinese loess and paleosols: Mechanism for magnetic susceptibility enhancement in paleosols. Earth Planet. Sci. Lett., 240, 790-802. https://doi.org/10.1016/j.epsl.2005.09.026

Colombo, U., Fagherazzi, G., Gazzarrini, F., Lanzavecchia, G. & Sironi, G. (1968). Mechanism of low temperature oxidation of magnetites. Nature, 219, 1036-1037. https://doi.org/10.1038/2191036a0

Cornejo, J., Serna, C. & Hermosin, M. (1984). Nitrogen adsorption on synthetic ferrihydrite. J. Colloid Interf. Sci., 102, 101-106. https://doi.org/10.1016/0021-9797(84)90203-0

Cui, Y., Verosub, K.L. & Roberts, A. (1994). The effect of low-temperature oxidation on large multi-domain magnetite. Geophys. Res. Lett., 21(9), 757-760. https://doi.org/10.1029/94GL00639

David, I. & Welch, A. (1956). The oxidation of magnetite and related spinels. J. Chem. Soc. Faraday Trans, 52, 1642-1650. https://doi.org/10.1039/TF9565201642

Davis, B.L., Rapp, G. & Malawender, M.J. (1968). Fabric and structural characteristics of the martitization process. Am. J. Sci., 226, 482-486. https://doi.org/10.2475/ajs.266.6.482

Dearing, J.A., Dann, R.J.L., Hay, K., Lees, J., Loveland, P.J., Maher, B.A. & O'Grady, K. (1996). Frequency-dependent susceptibility measurements of environmental materials. Geophys. J. Int., 124, 228-240. https://doi.org/10.1111/j.1365-246X.1996.tb06366.x

DeBoer, F.E. & Selwood, P.W. (1954). The activation energy for the solid state reaction γ-$Fe_2O_3 \rightarrow \alpha$-$Fe_2O_3$. J. Am. Chem. Soc., 76, 13, 3365–3367. https://doi.org/10.1021/ja01642a003

Demortière, A., Panissod, P., Pichon, B.P., Pourroy, G., Guillon, D., Donnio, B. & Bégin-Colin, S. (2011). Size-dependent properties of magnetic iron oxide nanocrystals. Nanoscale. 3(1), 225-32. https://doi.org/10.1039/c0nr00521e

Demory, F., Oberhänsli, H., Nowaczyk, N.R., Gottschalk, M., Wirth, R. & Naumann, R. (2005). Detrital input and early diagenesis in sediments from Lake Baikal revealed by rock magnetism. Glob. Planet. Change, 46(1-4), 145-166. https://doi.org/10.1016/j.gloplacha.2004.11.010

Doebelin, N. & Kleeberg, R. (2015). Profex: a graphical user interface for the Rietveld refinement program BGMN. J. Appl. Crystallogr., 48, 1573-1580. https://doi.org/10.1107/S1600576715014685

Dubinin, M.M. & Astakhov, V.A. (1971). Description of adsorption equilibria of vapors on zeolites over wide ranges of temperature and pressure. Adv. Chem., 102(69), 65-69. https://doi.org/10.1021/ba-1971-0102.ch044

Dunlop, D.J. & Özdemir, Ö. (1997). Rockmagnetism: fundamentals and frontiers. Cambridge University Press. 573 p.

Egger, K. & Feitknecht, W. (1962). Über die Oxidation von Fe_3O_4 zu γ- und α-Fe_2O_3. Die differenzthermoanalytische (DTA) und thermogravimetrische (TG) Verfolgung des Reaktionsablaufes an künstlichen Formen von Fe_3O_4. Helv. Chim. Acta, 45, 2042-2057. https://doi.org/10.1002/hlca.19620450642

Elder, T. (1965). Particle-size effect in oxidation of natural magnetite. J. Appl. Phys., 36, 1012-1013. https://doi.org/10.1063/1.1714076

Eltouny, N. & Ariya, P.A. (2014). Enhanced reactivity toward oxidation by water vapor: Interactions of toluene and NO_2 on hydrated magnetite nanoparticles. J. Phys. Chem. C, 118, 41, 23654–23663. https://doi.org/10.1021/jp503762k

Feitknecht, W. & Lehmann, H. (1959). Über die Oxidation von Magnetit zu γ-Fe_2O_3. Helv. Chim. Acta, 42, 2035-2039. https://doi.org/10.1002/hlca.19590420634

Gallagher, K., Feitknecht, W. & Mannweiler, U. (1968). Mechanism of oxidation of magnetite to γ-Fe_2O_3. Nature, 217, 1118-1121. https://doi.org/10.1038/2171118a0

García, J. & Subías, G. (2004). The Verwey transition-a new perspective. J. Phys. Condens. Matter., 16, R145. https://doi.org/10.1088/0953-8984/16/7/R01

García, J., Subías, G., Proietti, M.G., Blasco, J., Renevier, H., Hodeau, L. & Joly, Y. (2001). Absence of charge ordering below the Verwey transition temperature in magnetite. Phys. Rev., B63, 054110. http://dio.org/10.1103/PhysRevB.63.054110

Ge, K.P., Williams, W., Liu, Q.S. & Yu, Y.J. (2014). Effects of the core-shell structure on the magnetic properties of partially oxidized magnetite grains: Experimental and micromagnetic investigations. Geochem. Geophys. Geosyst., 15, 2021-2038. https://doi.org/10.1002/2014GC005265

Gillot, B., Rousset, A. & Dupre, G. (1978). Influence of crystallite size on the oxidation kinetics of magnetite. J. Solid State Chem., 25, 263-271. https://doi.org/10.1016/0022-4596(78)90111-1

Gorski, C.A. & Scherer, M.M. (2010). Determination of nanoparticulate magnetite stoichiometry by Mössbauer spectroscopy, acidic dissolution, and powder X-ray diffraction: A critical review. Am. Mineral., 95, 1017-1026. https://doi.org/10.2138/am.2010.3435

Goss, C.J. (1988). Saturation magnetisation, coercivity and lattice parameter changes in the system Fe_3O_4-γFe_2O_3, and their relationship to structure. Phys. Chem. Miner., 16,164-171. https://doi.org/10.1007/BF00203200

Hamilton, W.C. (1958). Neutron diffraction investigation of the 119 K transition in magnetite. Phys. Rev., 110(5), 1050-1057. https://doi.org/10.1103/PhysRev.110.1050

Haneda, K. & Morrish, A. (1977). Magnetite to maghemite transformation in ultrafine particles. J. Phys. Colloques, 38, 321-323. https://doi.org/10.1051/jphyscol:1977166

Harrison, R.J. & Feinberg, J. M. (2008). FORCinel: An improved algorithm for calculating first-order reversal curve distributions using locally weighted regression smoothing. Geochem. Geophy. Geosy., 9, Q05016. https://doi.org/10.1029/2008GC001987

Herb, C., Zhang, W.L., Koutsodendris, A., Appel, E., Fang, X.M. & Pross, J. (2013). Environmental implications of the magnetic record in Pleistocene lacustrine sediments of the Qaidam Basin, NE Tibetan Plateau. Quat. Int., 313-314, 218-229. https://doi.org/10.1016/j.quaint.2013.06.015

Hu, S.Y., Goddu, S.R., Herb, C., Appel, E., Gleixner, G., Wang, S.M., Yang, X.D. & Zhu, X.H. (2015). Climate variability and its magnetic response recorded in a lacustrine sequence in Heqing basin at the SE Tibetan Plateau since 900 ka. Geophys. J. Int., 201, 444-458. https://doi.org/10.1093/gji/ggv033

Irving, E. (1970). The Mid-Atlantic Ridge at 45°N, XIV, Oxidation and magnetic properties of basalts: Review and discussion. Can. J. Earth Sci., 7, 1528-1538. https://doi.org/10.1139/e70-144

Jackson, M., Moskowitz, B., Bowles, J. & IRM. (2011). Interpretation of Low-temperature Data Part III: The Magnetite Verwey Transition (Part A). The IRM Quarterly, ISSN:2152-1972, 20,4.

Jolivet, J. & Tronc, E. (1988). Interfacial electron transfer in colloidal spinel iron oxide. Conversion of iron oxide (Fe_3O_4) in aqueous medium. J. Colloid Interf. Sci., 125, 688-701. https://doi.org/10.1016/0021-9797(88)90036-7

Kendelewicz, T., Liu, P., Doyle, C., Brown, G. J., Nelson, E. & Chambers, S. (2000). Reaction of water with the (100) and (111) surfaces of Fe3O4. Surf. Sci., 453, 32-46. https://doi.org/10.1016/S0039-6028(00)00305-8

Kendelewicz, T., Kaya, S., Newberg, J.T., Bluhm, H., Mulakaluri, N., Moritz, W., Scheffler, M., Nilsson, N., Pentcheva, R. & Brown, G.E. (2013). X-ray photoemission and density functional theory study of the interaction of water vapor with the Fe_3O_4 (001) surface at near-ambient conditions. J. Phys. Chem. C, 117, 6, 2719–2733. https://doi.org/10.1021/jp3078024

Knafelc, J., Filiberto, J., Ferré, E.C., Conder, J.A., Costello, L., Crandall, J.R., Dyar, M.D., Friedman, S.A., Hummer, D.R. & Schwenzer, S.P. (2019). Effect of oxidation on the mineralogy and magnetic properties of olivine. Am. Mineralogist, 104, 694-702. https://doi.org/10.2138/am-2019-6829

Li, Q., Kartikowati, C.W., Horie, S., Ogi, T., Iwaki, T. & Okuyama, K. (2017). Correlation between particle size/domain structure and magnetic properties of highly crystalline Fe_3O_4 nanoparticles. Sci. Rep., 7, 9894. http://doi.org/10.1038/s41598-017-09897-5

Liu, Q.S., Banerjee, S.K., Jackson, M.J., Chen, F., Pan, Y.X. & Zhu, R.X. (2004a). Determining the climatic boundary between the Chinese loess and palaeosol: evidence from aeolian coarse-grained magnetite, Geophys. J. Int., 156(2), 267-274. https://doi.org/10.1111/j.1365-246X.2003.02148.x

Liu, Q.S., Banerjee, S.K., Jackson, M.J., Deng, C.L., Pan, Y.X. & Zhu, R.X. (2004b). New insights into partial oxidation model of magnetites and thermal alteration of magnetic mineralogy of the Chinese loess in air. Geophys. J. Int., 158(2), 506-514. https://doi.org/10.1111/j.1365-246X.2004.02348.x

Liu, Q.S., Deng, C.L., Yu, Y.J., Torrent, J., Jackson, M.J., Banerjee, S.K. & Zhu, R.X. (2005). Temperature dependence of magnetic susceptibility in an argon environment: implications for pedogenesis of Chinese loess/palaeosols. Geophys. J. Int., 161, 102–112. https://doi.org/0.1111/j.1365-246X.2005.02564.x

Liu, W., Tian, S.T, Zhao, X., Xie, W.B., Gong, Y.Y. & Zhao, D.Y. (2015). Application of stabilized nanoparticles for in situ remediation of metal-contaminated soil and groundwater: A critical review. Curr. Pollution Rep. 1, 280-291 (2015). https://doi.org/10.1007/s40726-015-0017-x

Li, Z., Chanéac, C., Berger, G., Delaunay, S., Graff, A. & Lefèvre, G. (2019). Mechanism and kinetics of magnetite oxidation under hydrothermal conditions. RSC Adv., 9, 33633. https://doi.org/10.1039/c9ra03234g

Li, Z.M., Chaneac, C., Berger, G., Delaunay, S., Graff, A. & Lefevre, G. (2019). Transformation mechanism of magnetite nanoparticles. Mater. Sci-Poland. RSC Advances, 9, 33633-33642. http://doi.org/ 10.1039/C9RA03234G

Mazanek, E., Krupinska, Z. & Kulgawczuk, D. (1973). Zur Oxidationsreaktion von Magnetit. Arch. Eisenhüttenwesen, 44, 571-577.

Maxbauer, D.P., Feinberg, J.M. & Fox, D.L. (2016). MAX UnMix: A web application for unmixing magnetic coercivity distributions. Comput. Geosci. UK, 95, 140-145. https://doi.org/10.1016/j.cageo.2016.07.009

Mascolo, M.C., Pei, Y.B. & Ring, T.A. (2013). Room temperature co-precipitation synthesis of magnetite nanoparticles in a large pH window with different bases. Materials, 6, 5549-5567. https://doi.org/10.3390/ma6125549

Mulakaluri, N., Pentcheva, R., Wieland, M., Moritz, W. & Scheer, M. (2009). Partial dissociation of water on Fe_3O_4(001): Adsorbate induced charge and orbital order. Phys. Rev. Lett., 103, 176102-1. https://doi.org/10.1103/PhysRevLett.103.176102

Murad, E. & Schwertmann, U. (1993). Temporal stability of a fine-grained magnetite. Clays Clay Miner., 41, 111-113. https://doi.org/10.1346/CCMN.1993.0410112

Nasrazadani, S. & Raman, A. (1993). The application of infrared spectroscopy to the study of rust systems—II. Study of cation deficiency in magnetite (Fe_3O_4) produced during its transformation to maghemite (γ-Fe_2O_3) and hematite (α-Fe_2O_3). Corros. Sci., 34(8), 1355-1365. https://doi.org/10.1016/0010-938X(93)90092-U

Nedkov, I., Merodiiska, T., Slavov, L., Vandenberghe, R.E., Kusano, Y. & Takada, J. (2006). Surface oxidation, size and shape of nano-sized magnetite obtained by co-precipitation. J. Magn. Magn. Mater, 300,2,358-367. https://doi.org/10.1016/j.jmmm.2005.05.020

Nishitani, T. & Kono, M. (1983). Curie temperature and lattice constant of oxidized titanomagnetite. Geophys. J. Int., 74, 585-600. https://doi.org/10.1111/j.1365-246X.1983.tb01890.x

Olowe, A., Rezel, D. & Génin, J.-M. R. (1989). Mechanism of formation of magnetite from ferrous hydroxide in aqueous corrosion processes. Hyperfine Interact., 46, 429-436. https://doi.org/10.1007/BF02398227

Petersen, N. & Bleil, U. (1982). Magnetic properties of rocks, in Numerical Data and Functional Relationships in Science and Technology, Landolt-Börnstein V/1b, edited by G. Angenheister. http://doi.org/10.1007/10201909_76

Petersen, N. & Vali, H. (1987). Observation of shrinkage cracks in ocean floor titanomagnetites. Phys. Earth Planet. Inter., 46, 197-205. https://doi.org/10.1016/0031-9201(87)90182-8

Petrovský, E. & Kapička, A. (2006). On determination of the Curie point from thermomagnetic curves. J. Geophys. Res. Solid Earth, 111, B12S27. http://doi:10.1029/2006JB004507

Pokhil, T.G. & Moskowitz, B.M. (1997). Magnetic domains and domain walls in pseudo-single-domain magnetite studied with magnetic force microscopy. J. Geophys. Res. Solid Earth, 102, B10, 22,681-22,694. https://doi.org/10.1029/97JB01856

Putnis, A. (2002). Mineral replacement reactions: from macroscopic observations to microscopic mechanisms. Mineral. Mag., 66, 689-708. https://doi.org/10.1180/0026461026650056

Roberts, A.P., Heslop, D., Zhao, X. & Pike, C.R. (2014). Understanding fine magnetic particle systems through use of first-order reversal curve diagrams. Rev. Geophys., 52, 557-602. https://doi.org/10.1002/2014RG000462

Rouquerol, J., Llewellyn, P. & Rouquerol, F. (2007). Is the BET equation applicable to microporous adsorbents. Stud. Surf. Sci. Catal., 160, 49-56. https://doi.org/10.1016/S0167-2991(07)80008-5

Rouquerol, J., Rouquerol, F., Llewellyn, P., Maurin, G. & Sing, K.S. (2013). Adsorption by powders and porous solids: principles, methodology and applications. Academic press.

Ruby, C. (2015). Green rust and related iron containing compounds: Structure, redox properties and environmental applications: Part I. Curr. Inorg. Chem., 5, 152-155. https://doi.org/10.2174/1877944105031507141148 19

Rustad, J., Felmy, A. & Bylaska, E. (2003). Molecular simulation of the magnetite water interface. Geochimica et Cosmochimica Acta, 67, 1001-1016. https://doi.org/10.1016/S0016-7037(02)00900-6

Schwaminger, S.P., Bauer, D., Fraga-García, P., Wagner, F.E. & Berensmeier, S. (2017). Oxidation of magnetite nanoparticales: impact on surface and crystal properties. CrystEngComm, 19, 246. https://doi.org/10.1039/C6CE02421A

Schwertmann, U., Stanjek, H. & Becher, H.-H. (2004). Long-term in vitro transformation of 2-line ferrihydrite to goethite/hematite at 4, 10, 15 and 25 °C. Clay Miner., 39, 433-438. https://doi.org/10.1180/0009855043940145

Sidhu, P.S. (1988). Transformation of trace element-substituted maghemite to hematite. Clay Miner., 36(1), 31-38. http://doi.org/10.1346/CCMN.1988.0360105

Sidhu, P.S., Gilkes, R.J. & Posner, A. M. (1977). Mechanism of the low-temperature oxidation of synthetic magnetites: J. Inorg. Nucl. Chem. 39, 1953-1958. https://doi.org/10.1016/0022-1902(77)80523-X

Signorini, L., Pasquini, L., Savini, L., Carboni, R., Boscherini, F. & Bonetti, E. (2003). Size-dependent oxidation in iron/iron oxide core-shell nanoparticles. Phys. Rev. B, 68, 195423. https://doi.org/10.1103/PhysRevB.68.195423

Stanjek, H. & Weidler, P. (1992). The effect of dry heating on the chemistry, surface area, and oxalate solubility of synthetic 2-line and 6-line ferrihydrites. Clay Miner., 27, 397-412. https://doi.org/10.1180/claymin.1992.027.4.01

Swaddle, T.W. & Oltmann, P. (1980). Kinetics of the magnetite–maghemite–hematite transformation, with special reference to hydrothermal systems. Can. J. Chem., 58 (17), 1763-1772. https://doi.org/10.1139/v80-279

Tang, Y., Qin, J., Wu, K., Guo, Q. & Guo, J. (2013). The reduction and oxidation of Fe_2O_3(0001) surface investigated by scanning tunneling microscopy. Surf. Sci., 609, 67-72. https://doi.org/10.1016/j.susc.2012.11.005

Taylor, R.M. & Schwertmann, U. (1974a). Maghemite from dehydration of green rust (goethite). Maghemite in soils and its origin: I. Properties and observations on soil maghemites. Clay Miner., 10, 289-298. https://doi.org/10.1180/claymin.1974.010.4.07

Taylor, R.M. & Schwertmann, U. (1974b). Maghemite from dehydration of green rust (goethite). Maghemite in soils and its origin: II. Maghemite syntheses at ambient temperature and pH7. Clay Miner., 10, 299-310. https://doi.org/10.1180/claymin.1974.010.4.08

Thommes, M., Kaneko, K., Neimark, A.V., Olivier, J.P., Rodriguez-Reinoso, F., Rouquerol, J. & Sing, K.S. (2015). Physisorption of gases, with special reference to the evaluation of surface area and pore size distribution (IUPAC Technical Report). Pure Appl. Chem., 87(9-10), 1051-1069. https://doi.org/10.1515/pac-2014-1117

Tombacz, E., Hajdu, A. & Illés, E. (2009). Water in contact with magnetite nanoparticles, as seen from experiments and computer simulations. Langmuir, 25, 13007-13014. https://doi.org/10.1021/la901875f

Topsøe, H., Dumesic, J.A. & Boudart, M. (1974). Mössbauer spectra of stoichiometric and nonstoichiometric Fe_3O_4 Smicrocrystal. J. Phys. (Paris), 35, C6-411-C6-413. Http://dio.org/ 10.1051/jphyscol:1974680

Van Velzen, A.J. & Dekkers, M. (1999). Low-temperature oxidation of magnetite in loess-paleosol sequences: A correction of rock magnetic parameters. Stud. Geophys. Geod., 43, 357-375. http://doi.org/10.1023/A:1023278901491

Viswanath, R. P., Viswanathan, B. & Sastri, M. V. C. (1975). Hydrogen spillover effects in the reduction of iron oxide. React. Kineti. Catal. Lett., 2, 51-56. https://doi.org/10.1007/BF02060952

Widdrat, M., Kumari, M., Tompa, E., Pósfai, M., Hirt, A.M. & Faivre, D. (2014). Keeping nanoparticles fully functional: Long-term storage and alteration of magnetite. ChemPlusChem, 79, 1225-1233 https://doi.org/10.1002/cplu.201402032

Xu, W.X., Peacor, D.R., Dollase, W.A., Van der Voo, R. & Beaubouef, R. (1997). Transformation of titanomagnetite to titanomaghemite: A slow, two-step, oxidation-ordering process in MORB. Amer. Miner., 82, 1101-1110. https://doi.org/10.2138/am-1997-11-1207

Zhou, W.M., Van der Voo, R., Peacor, D.R., Wang, D.M. & Zhang, Y.X. (2001). Low-temperature oxidation in MORB of titanomagnetite to titanomaghemite: A gradual process with implications for marine magnetic anomaly amplitudes. J. Geophys. Res. Solid Earth, 106(B4), 6409-6421. https://doi.org/10.1029/2000JB900447

Appendix A

Table A1. Broadband-frequency dependence of magnetic susceptibility

Frequency [Hz]	Original	RR	RH	HD	HS	HH-HD	HH
65	1.000	1.000	1.000	1.000	1.000	1.000	1.000
125	0.993	0.996	0.987	0.996	0.994	0.993	0.989
250	0.989	0.996	0.989	0.999	0.992	0.991	0.990
500	0.992	0.996	0.987	0.992	0.993	0.990	0.991
1000	0.991	0.993	0.987	0.990	0.990	0.987	0.985
2000	0.986	0.991	0.981	0.986	0.981	0.985	0.985
4000	0.986	0.989	0.981	0.982	0.978	0.982	0.983
8000	0.983	0.989	0.978	0.980	0.980	0.986	0.984
16000	0.979	0.984	0.977	0.979	0.980	0.984	0.981

Table A2. Fitting results of Mössbauer spectroscopy. *CS*: center shift; *Qshift*: quadrupole shift; *H*: hyperfine magnetic field; *stdev(H):* standard deviation of hyperfine field; *R.A.*: Relative abundance; χ^2: goodness of fit.

		CS [mm/s]	Qshift [mm/s]	H [T]	stdev(H) [T]	R.A. [%]	Error	χ^2	$Fe(II)/Fe(III)_{Mag}$
Original	MagT	0.45	0.02	50.9	0.9	40.3	2.3	1.1	0.43
	MagO	0.72	0.01	47.5	1	59.7	2.3		
RH	MagT	0.37	0	50.4	0.4	35.2		1.9	0.48
	MagO	0.75	0	47.9	1.3	64.8			
HD	MagT	0.37	0	50.4	0.4	34	0.8	2.2	0.49
	MagO	0.74	0	47.9	1.3	66	0.8		
HS	MagT	0.37	0	50.4	0.3	32.2	1.9	0.9	0.51
	MagO	0.75	0.01	48	1.5	67.8	1.9		
HH-HD	MagT	0.37	0	50.5	0.5	34.1	1.2	1.6	0.49
	MagO	0.74	0	47.8	1.4	65.9	1.2		
HH	MagT	0.38	-0.01	49.8	0	29.4	1.2	42.3	0.51
	MagO	0.76	0.04	46.9	1.4	61.6	1.3		
	Hem	0.39	-0.15	50.6	0	9	1.4		

Appendix B

Figure B1. Mössbauer spectra collected at 140 K

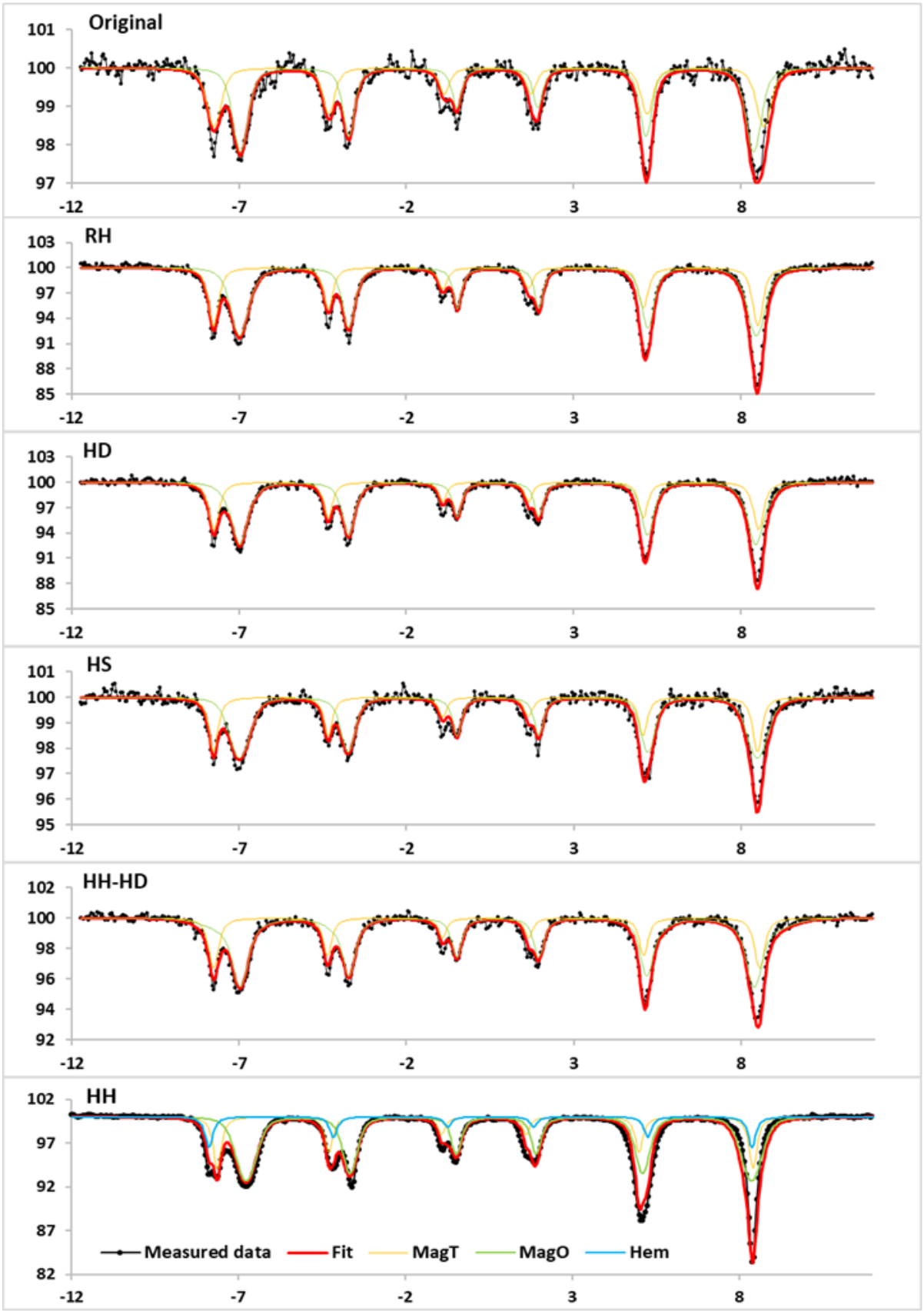

Figure B2. Rietveld fits of X-ray diffraction results of all magnetite samples measured on the conventional BRUKER D8, prepared on a Si wafer and KCl added as an internal standard. The top curve (black) shows the scan of the original magnetite (control sample), the green curve is the fit of this scan and the red curve is the residual (difference between measured and calculated results). Peaks other than magnetite belong to KCl. The two strongest reflections of KCl and magnetite are capped for improving vertical resolution. For all other magnetite samples, only the residuals are shown, because the scans look de facto identical to each other.

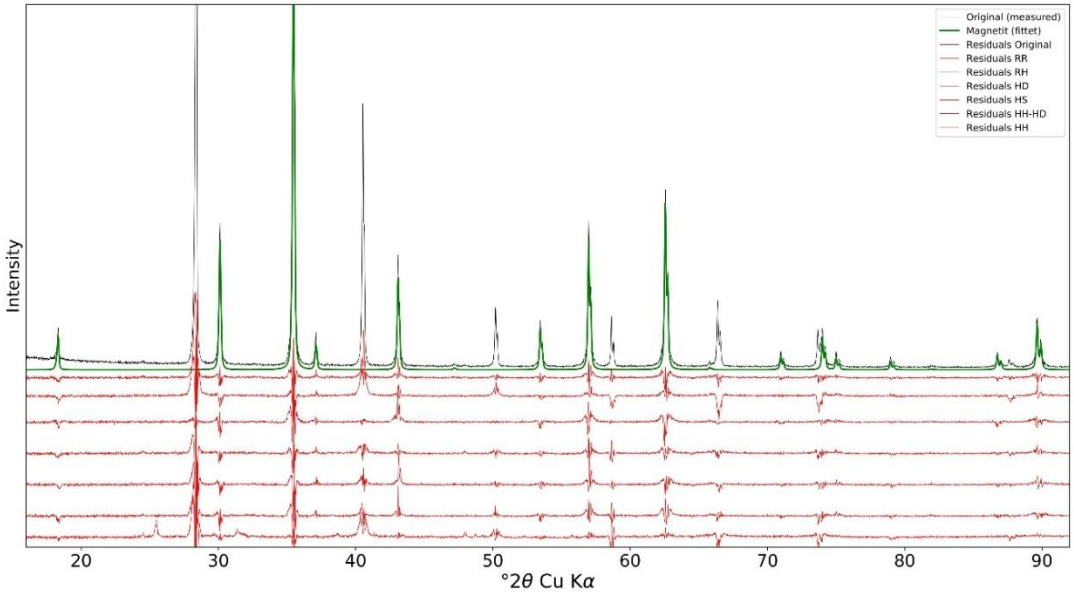

Figure B3. Argon physisorption isotherms at 87 K, measured on ~0.09-0.35 g of dry sample material using the manometric method.

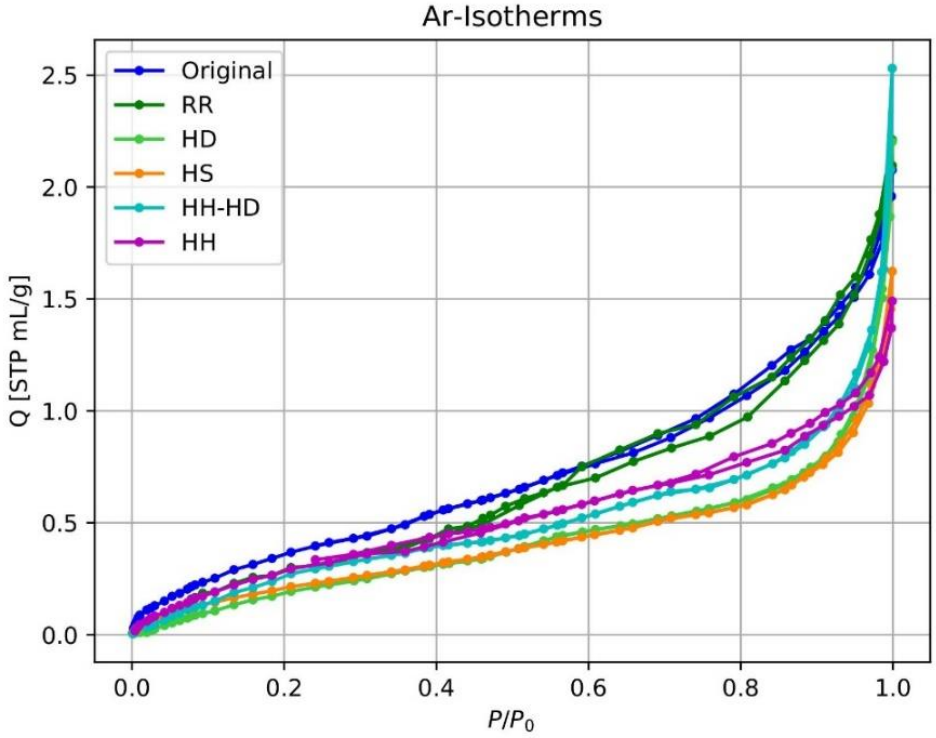

Chapter IV: Is alteration of magnetite in rock weathering related to climate?

Author	Author position	Scientific ideas %	Data generation %	Analysis & interpretation %	Paper writing %
Qi Zhang	1	50	85	50	60
Erwin Appel	2	40	-	30	40
Nathani Basavaiah	3	5	-	5	-
Shouyun Hu	4	5	-	5	-
Xiuhua Zhu	5	-	10	5	-
Udo Neumann	6	-	5	5	-
Status in publication process:		in progress			

Is alteration of magnetite in rock weathering related to climate?

Qi Zhang[1], Erwin Appel[1*], Nathani Basavaiah[2], Shouyun Hu[3], Xiuhua Zhu[4], Udo Neumann[1]

[1]*Geophysics, Center for Applied Geoscience, University of Tübingen, Hölderlinstr.12, 72074 Tübingen, Germany*

[2]*Environmental Magnetism Laboratory, Indian Institute of Geomagnetism, New Panvel, Navi Mumbai 410 218, India*

[3]*State Key Laboratory of Lake Science and Environment, Nanjing Institute of Geography and Limnology, Chinese Academy of Sciences, 73 East Beijing Rd, Nanjing 210008, China*

[4]*Center for Earth System Research and Sustainability, University of Hamburg, Grindelberg 5, 20144 Hamburg, Germ*

Summary

Knowledge on the (in)stability of magnetic minerals is crucial when using magnetic properties as paleoclimate proxies or interpreting paleomagnetic results. Magnetic minerals preserved in paleoclimate archives may be related to weathering under different climate conditions. We present an actualistic study on magnetic properties of magnetite in basalts and weathered pebbles at basalt surfaces, using samples from the Deccan traps in India and the Emeishan traps in SW-China. The magnetite occurs mainly in magnetite-ilmenite lamellae structures related to exsolution during magma cooling. The Deccan samples comprise sites across a large gradient of mean annual precipitation (MAP; ~500-4000 mm). The Emeishan samples allow a comparison at same MAP in the order of ~1000 mm, but with ~10-15 °C different mean annual temperature. In order to investigate the effect of gradual magnetite alteration, the weathered pebbles were divided into five groups by their grain sizes. Alteration is assumed to increase with grain size fining. Along with the degree of weathering no systematic changes of both concentration and grain size dependent parameters were observed. Based on our results, we suggest that magnetic properties of ferrimagnetic minerals in basalts and their weathering materials mainly dependent on the rock types, overriding climate-related alteration effects. The latter may cause distracting noise on magnetic properties in paleoclimate archives such as lake sediments.

1.Introduction

Studies on concentration, specific compositions, and magnetic domain state of magnetic minerals in sedimentary archive such as marine or lake sediments and loess deposits can provide

valuable information on paleoclimate (Maher & Hu, 2006). Variation of magnetic properties can be caused by dilution with non-magnetic fractions (Peck et al., 1994), dissolution of magnetic phases (Negrini et al., 2000), authigenic formation of magnetic minerals (Snowball et al., 2002), and changes in the catchment influencing the erosional input (Eriksson & Sandgren, 1999) or pedogenic processes (Lise-Pronovost et al., 2014). Moreover, alteration of magnetic minerals can influence remanent magnetizations in rocks and understanding the effects of alteration on the stability of magnetic remanence is crucial (Irving, 1970). Basalts play an important role for conservation of remanence in rocks and as source materials for paleoclimate archives. In this respect, weathering processes of (titano-)magnetite have to be considered that may critically depend on climate conditions.

Kent & Gee (1996) showed that already zero-age oceanic basalt can be magnetically altered before further aging. The alteration process of magnetite under normal atmospheric conditions starts from the particle surface and progresses into the interior gradually alters magnetite towards maghemite by oxidation of Fe(II) to Fe(III), diffusion of Fe(II) to the crystal's surface, and the formation of lattice vacancies (Readman & O'Reilly, 1972; O'Reilly 1984) associated with lattice shrinking and shrinkage cracks at advanced alteration (Petersen & Vali, 1987). As a result of this low-temperature oxidation (LTO) or so-called maghemitization, the internal crystal structure and the internal stress distribution become inhomogeneous, thereby causing an increase of magnetic hardness (Appel, 1987; Cui et al., 1994; Keller & Schmidbauer, 1999; Wang et al., 2006). The formation of shrinkage cracks will allow moisture and oxygen to penetrate into the interior of particles, and through chemical weathering maghemite can finally transform into hematite (Sidhu 1988; Torrent et al. 2006) or goethite (He & Traina, 2007).

Recently, variation of magnetic properties due to maghemitization and hematite formation in lacustrine sediments around the Tibetan Plateau (Herb et al., 2013; Hu et al., 2015) and on the Indian subcontinent (Basavaiah et al., 2015) were interpreted as humidity-induced changes of magnetite alteration in the catchment area, and likewise humidity in soil is seen as a major driver of pedogenic magnetite alteration (Maxbauer et al., 2016). In a laboratory experiment we have studied magnetite oxidation under different humidity conditions at low temperature (70 °C) during one year of exposure, and the results of this study showed that extreme humidity accelerates the alteration process (Zhang et al. 2020). The controlled laboratory experiment suggests that relatively higher humidity in natural environments could lead to a higher degree of magnetite oxidation, however, it also indicates that the relationship of magnetite alteration and humidity could be non-linear. To further investigate the possible influence of humidity, an

actualistic study of magnetite alteration during rock weathering in different climates is desirable. In this paper, we present magnetic property changes of magnetite during rock weathering as a function of humidity, and also compare regions with different temperature ranges but same mean annual precipitation (MAP). Such a study requires (i) an area with sufficiently similar rock magnetic mineralogy, that (ii) spreads across sufficiently different climatic settings.

Basalts have the advantage of containing a large ferro(i)magnetic fraction that allows studies of representative small samples, including microscopic observations. The Deccan traps on the Indian subcontinent provide a promising natural laboratory for our study with its large area of flood basalts and a large MAP-gradient. The Deccan basalts were intensively studied in the past decades, however, most of this research focused on paleomagnetism. Basic rock properties investigations started with simple instrumentation, especially conducted by Radhakrishnamurty et al. (1967, 1977, 1978, 1981). Their results from a huge number of basalt sites of different ages and modes of origin suggest a variety of different characteristics in domain structure, in composition of the (titano-)magnetites, and also in the degree of cation deficiency (Radhakrishnamurty et al. 1978). Additionally, we investigated the magnetic properties of the Emeishan basalts in south-western China, as they are expected to represent a similar genesis of flood basalts as the Deccan traps, and located in an area with much lower mean annual temperature (MAT) at an overlapping range of MAP.

2. Samples and methods

The Deccan traps are located in central and southern India (Fig. 1). The nearly 500,000 km^2 large Deccan flood basalts erupted at around the Cretaceous-Tertiary boundary (Allegre et al., 1999; Basavaiah et al., 2018) and is one of the largest known continental basalts. The Deccan lavas are predominantly tholeiitic with a wide variety in textural character (Wensink, H., 1973), they were extensively altered and leached in position (Widdowson & Cox, 1996; Kısakürek et al., 2004). At present, a strong MAP gradient exists in this area ranging from ~500 mm to ~4000 mm (Fig. 1). About 80 % of rainfall occurs during the monsoon season (June to September). The MAT is relatively high across the whole Deccan plateau area (~25 °C to ~28 °C).

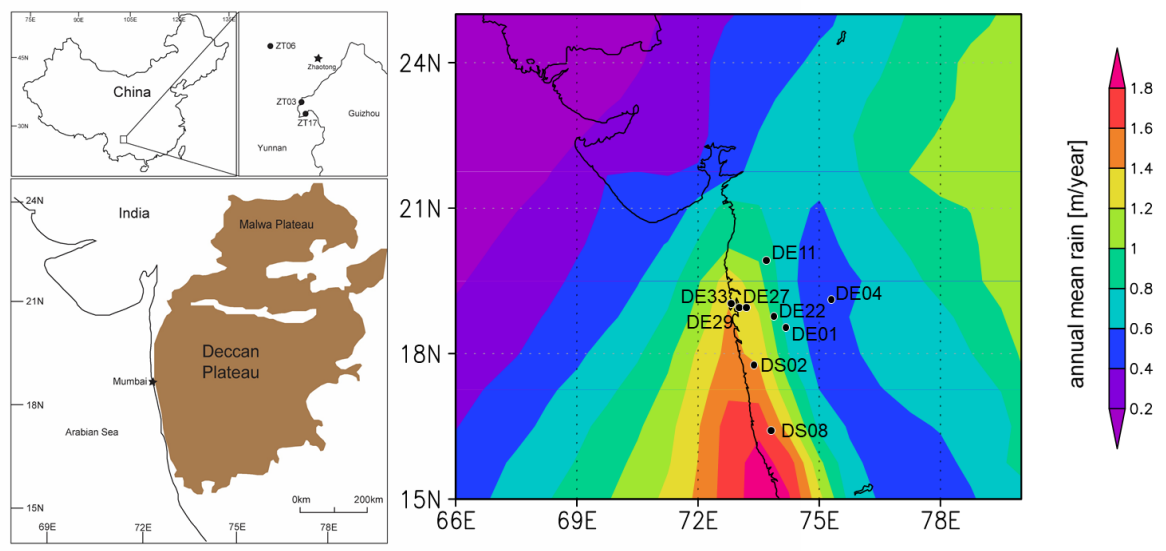

Figure 1. Upper left: Three sampling sites from the Emeishan traps, SW-China. Lower left: Geology map of the Deccan traps modified from Sheth (2005). Right: Nine sampling sites from the Deccan traps plotted on ERA-Interim MAP distribution (35-years climate averages reanalysis maps after Dee et al., 2011).

The Emeishan traps are located in south-western China (Fig. 1), between the western margin of the Yangtze Block and the eastern margin of the Tibetan Plateau, covering an area of ~0.3×10^6 km^2 (Shellnutt & Jahn, 2011). Studies on Emeishan Basalts started in the late 1970s, geochemical data indicates both high-Ti and low-Ti lavas (Xu et al. 2001). Across the sampled area of the Emeishan basalts, the MAP is ~800 mm and the MAT is ~12.8 °C. (MAP and MAT data are from: climate-data.org).

We sampled fresh rock and well-related weathered pebbles on top of the fresh rock (Fig. 2). In a first field campaign in 2015, forty-two locations from the Deccan traps and seventeen locations from the Emeishan traps were collected and tested for obtaining a most suitable sample collection. Careful site selection is crucial to obtain sample sets with as best as possible similar rock magnetic mineralogy. Preferred samples are those with coexisting magnetite and ilmenite, that formed by exsolution during relatively slow cooling, avoiding a mixture with Ti-rich titanomagnetites that may survive metastable during fast cooling. After this site selection, nine sites from the Deccan traps and three sites from the Emeishan traps (Fig.1) were chosen, based on microscopic observations, thermomagnetic curves (-194 °C to 700 °C) and bulk magnetic properties (magnetic susceptibility, anhysteretic remanent magnetization, isothermal remanent magnetization. In 2017, we then sampled these twelve sites in detail.

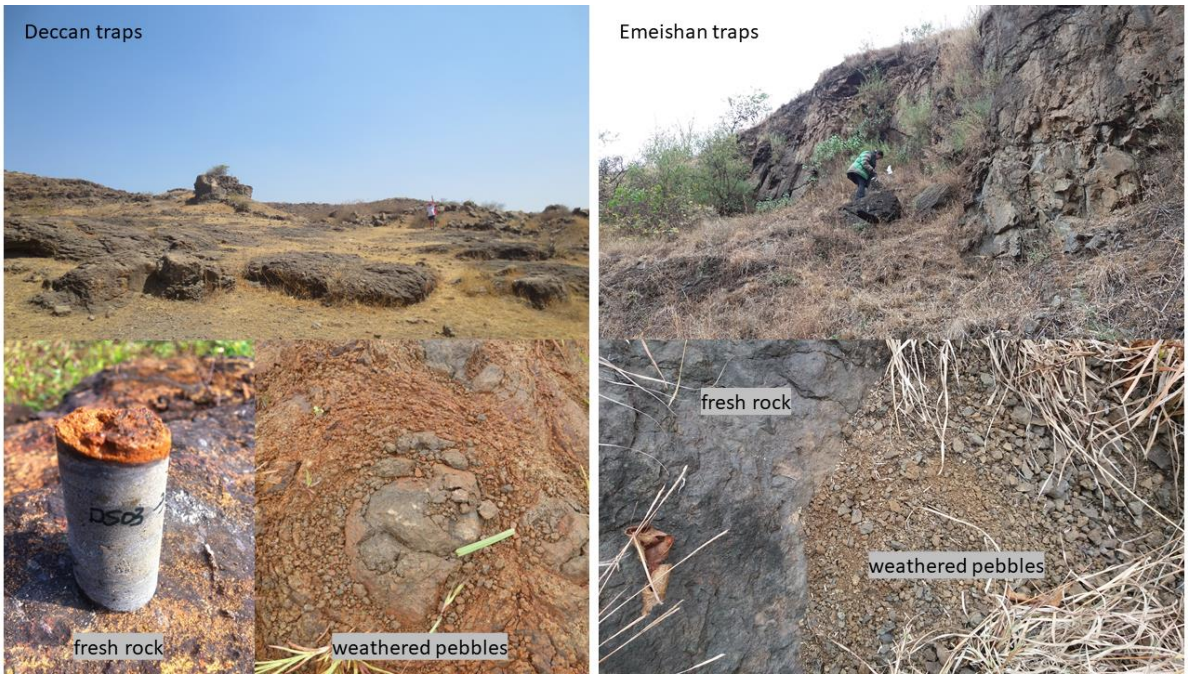

Figure 2. Deccan traps and Emeishan traps (images on top show outcrop settings), example show basalt sample and how pebbles are related to the rock.

For detailed sampling, we collected fresh bedrock (core samples obtained by drilling and rock samples crushed by hammer) and pebbles (~100 g) from five different spots at each site within an area of maximum ~50 m. The pebbles were collected as best as possible from spots with direct association to the underlying rock (Fig. 2). Barren locations were chosen for avoiding an influence of soil formation in the pebbles. Visible organic matters such as withered grass etc. were carefully removed from the weathered pebble material. In the laboratory, the weathered pebble materials were sieved and divided into five individual samples by grain size (WP1 >4 mm, WP2 2-4 mm, WP3 1-2 mm, WP4 0.5-1 mm, WP5 <0.5 mm). The degree of weathering is assumed to increase with fining of the pebbles. For further bulk measurements, the sample materials were then placed into cylindrical plastic sample boxes and weighed.

High-temperature (between room temperature and 700 °C) and low-temperature (from -196 °C to room temperature) thermomagnetic curves of magnetic susceptibility (χ-T curves) were measured by using a KLY-3 Kappabridge combined with a CS-3 furnace and a CS-L cryostat. Magnetic susceptibility (χ) at frequencies of 976 Hz and 15616 Hz (χ_{lf} and χ_{hf}) were measured with an MFK-1 Kappabridge (Agico), then normalized to mass-specific values. Percentage frequency-dependence (χ_{fd}%) was calculated by $[(\chi_{lf}-\chi_{hf})/\chi_{lf}] \times 100$ (Dearing et al.,1996). For remanence measurements, we imparted an anhysteretic remanent magnetization (*ARM*) using a DC-SQUID magnetometer (2G Enterprises) with attached degausser and DC coil,

superimposing a 50 µT DC field and a decaying alternating field (max. 100 mT). Saturation isothermal remanent magnetizations ($SIRM_{2T}$) were imparted at a 2 T field with a MMPM9 pulse magnetizer, and then a reverse IRM was produced in a field of 300 mT ($IRM_{-0.3T}$). IRMs were measured with Molspin spinner magnetometer. An S-ratio was calculated by [1-$IRM_{-0.3T}$/$SIRM_{2T}$]/2 (Bloemendal et al., 1992).

Polished sections of representative samples from each sampling location have been examined in reflection mode by using an optical microscope with immersion oil and ferrofluid to detect strong magnetic phases. All measurements were carried out in the Geoscience Department of University of Tübingen.

For bulk measurements, we first normalized all values from the same spot of a site to the value of WP1. With these data, we applied linear regression analysis for the entire sample set of one site using all sub-location samples, determining the slope and its 95 % confidence interval for the sequence 'fresh rock, followed by coarser to finer pebble fractions, i.e., from assumed low to high alteration degree. We choose four different grouping methods for the regression analysis, (i) fresh rock and weathered pebbles 1-5, (ii) weathered pebbles 1-5, (iii) fresh rock and weathered pebble 1-4, (iv) weathered pebbles 1-4. Due to the lack of material, DE01 and DE27 are without WP5 (<0.5 mm). A lateral shift of pebble material cannot be ruled out with absolute certainty, and therefore direct relation of the weathered pebble material to the underlying fresh rock is not guaranteed, which matters in consideration of variable rock magnetic properties of the bedrock at different spots. The finest pebble fraction is also special as it could be influenced by pedogenic influences although no signs of soil formation processes are visible. The sampling strategy and separation of the pebble material into different grain size fractions ensures that the pebble fractions 1-4 are exactly from the same spot, and that there is no possible influence of pedogenetic processes.

3. Results

Thermomagnetic curves of both fresh basalt rocks and weathered pebbles were measured, allowing to identify ferro(i)magnetic phases by their Curie temperature and other phase transitions such as the Verwey transition. In Figure 3, representative high temperature χ-T curves of basalts and weathered pebbles from each sampling sites are presented (for clearness only heating curves are shown). Curie temperatures range from ~580 °C to ~660 °C. At around 300 – 350 °C most samples show a hump-like peak, and for part of the samples a second

increase occurs before fully dropping at the Curie temperature. An irreversible hump-like peak at ~350 °C is mostly explained by meta-stable maghemite that transforms to hematite (Dunlop & Ozdemir, 1997; Deng et al., 2004), or it may be caused by Ti-rich titanomagnetite. However, for part of the sites such as DE11, DS08 and ZT03, the fresh rock does not show a hump (or the hump is small), while a larger hump is observed for the related pebble fractions, which cannot be explained by Ti-rich titanomagnetite, since it is expected that during weathering Ti-rich titanomagnetite is not formed but destroyed. According to a recent study on magnetite alteration in a laboratory experiment (Zhang et al., 2020), the decrease after the hump at around 300-350 °C may due to fine-particle behavior. Some of the samples show a more pronounced increase of the hump-like peak with decreasing particle size, which is most systematic for DE22. On the other hand, site DS02 shows an opposite trend, i.e., fresh rock and larger pebbles show more pronounced peaks, and as the grain size decrease both the first and second peak become less obvious. It should be noted that most of the fresh rock curves show less significant changes than weathered pebbles between heating and cooling curves.

It is noteworthy that only a few low-temperature thermomagnetic curves show a Verwey transition (Fig. 2), which is an indication of relatively high maghemitization degree. The Verwey transition is a very sensitive property for discrimination the degree of maghemitization (Zhang et al., 2020), and according to Aragón et al. (1985) the Verwey transition does not exist for an oxidation degree of >15 %.

Optical micrographs of polished sections are shown in Figure 4. Differently shaped and sized magnetites are observed, occurring predominantly as large (DE01, DE04, DE11, DE22, DE29, DE33, DS02, DS08, ZT03, ZT06) or small crystals (DE27, ZT17). Intergrowths of magnetite with a non-ferrimagnetic phase are clearly revealed in particles, which are large enough to be well resolved by the light microscopy. (Ti-)Magnetite is evidenced in such particles by coverage with ferrofluid (dark cover). The coexistence of magnetite with a non-ferrimagnetic phase could reflect an alteration of magnetite (such as DE01), but in most cases it occurs as lamellae structures, which are very likely magnetite-ilmenite intergrowths formed by exsolution during magma cooling (Mücke, 2003). These lamellae-structures are more (DE04, DE11, DE22, DE29, DS02, DS08) or less (ZT03, ZT06) clear, and also entirely ferrofluid-covered particles (DE33) are observed which indicates a different type magma source. The particles of DE27 and ZT17 are too small to be adequately resolved by light microscopy.

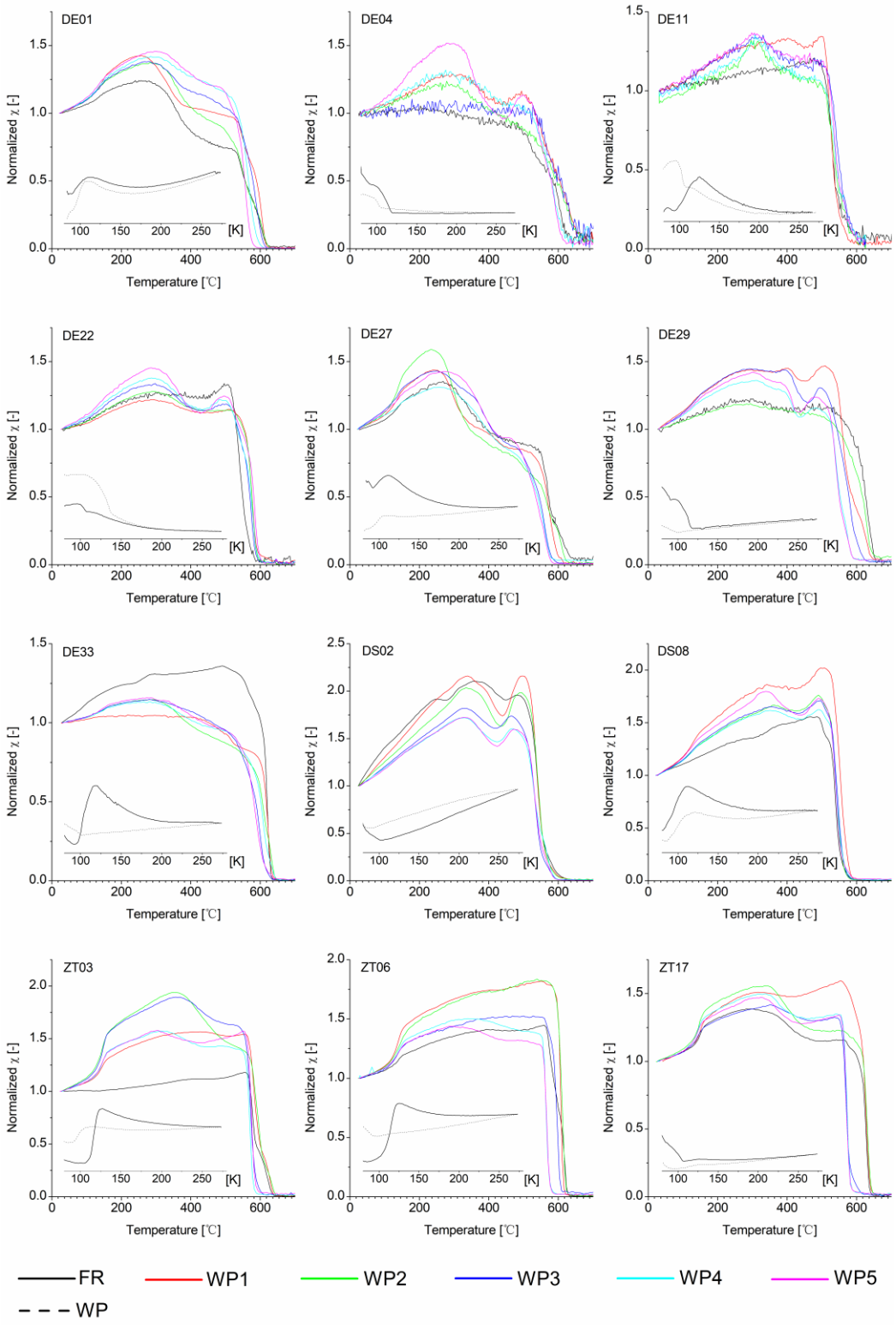

Figure 3. High and low-temperature thermomagnetic curves (χ-T) of fresh rock (FR) and weathered pebbles (WP) from all sites (WP1 >4 mm, WP2 2-4 mm, WP3 1-2 mm, WP4 0.5-1 mm, WP5 <0.5 mm). Only heating curves are shown for high-temperature thermomagnetic curves. Solid and dashed lines of low-temperature thermomagnetic curves represent fresh rock and one representative weathered pebble from each of the sampling sites.

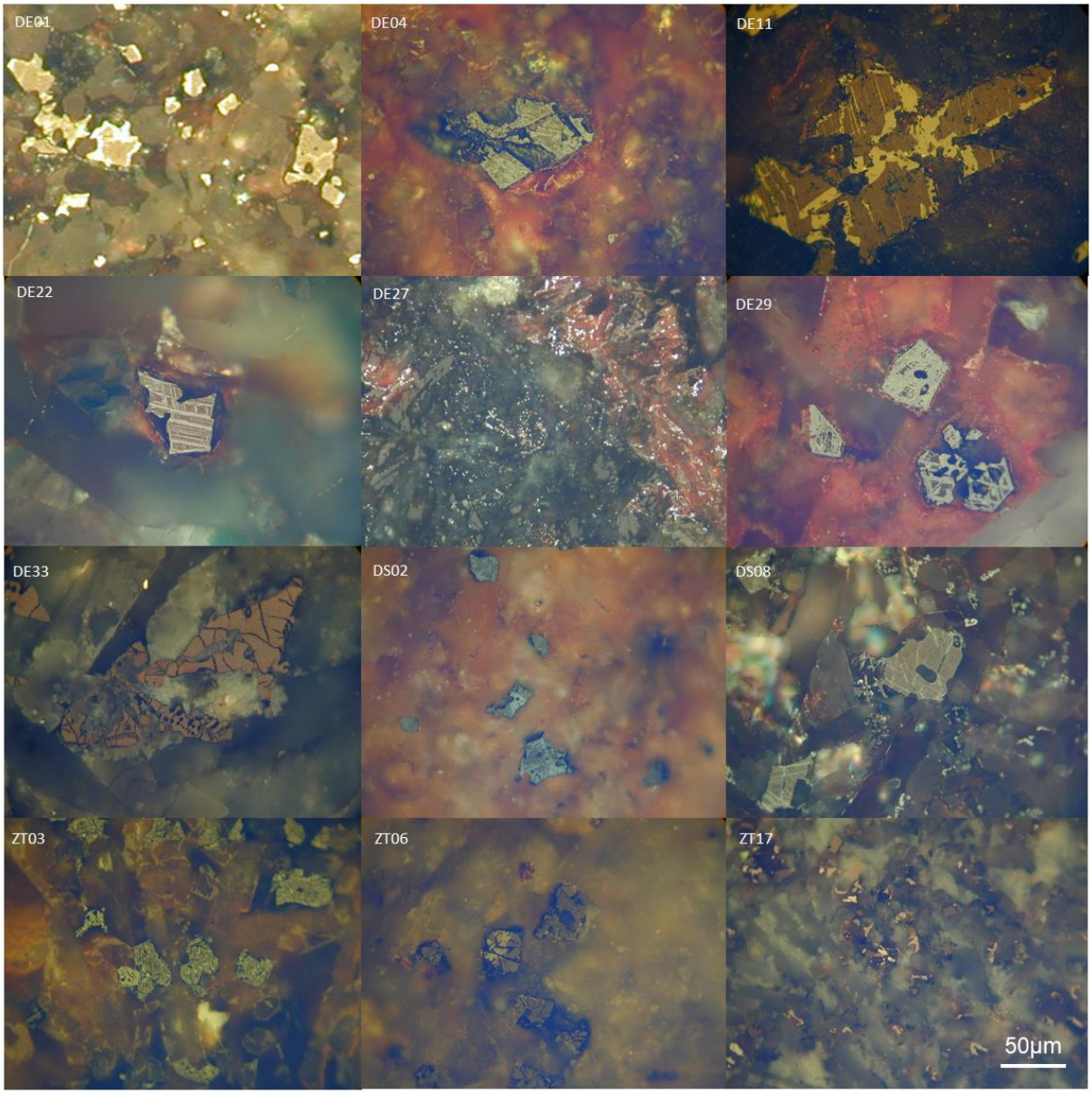

Figure 4. Optical micrographs of basalt samples from each site

One of the concentration dependent parameters (χ) and one domain-state (or magnetic mineral composition) dependent parameter (*SIRM/*χ) are presented in Figure 5 and Figure 6. More results (*SIRM*, *S-ratio*, χ_{fd}%, *ARM/SIRM*) can be found in appendix. MAP values (source: climate-data.org) of the 12 sites, and mean absolute values of WP1 from the 5 sub-sites and their standard deviations are listed in Table.1. Slope values of the linear regression fits and their 95 % confidence limits are shown in Figure 7.

Magnetic susceptibility (χ) and saturation isothermal remanent magnetization (SIRM) are both intensity indicators of the concentration of ferrimagnetic minerals. The results in Figure 5 show both an increasing (DE01, DE04, DE11, DE22, DE27, DE29, DS02) and a decreasing (DE33,

DS08, ZT03, ZT06, ZT17) trend of χ with fining of the pebbles grain size, and all four different grouping ensembles yield similar results (appendix). The SIRM shows a more consistent decreasing trend, except for DE04, DE33 and DS02. The S-ratio values are very close to the maximum value (1.00) for all sites and thus do not provide discriminative results. The frequency-dependent susceptibility (χ_{fd}%) is known to be very sensitive on grain sizes at the superparamagnetic (SP) and stable single domain (SSD) boundary. DE04 and DE29 show relatively higher χ_{fd}% (~8-9 %) while all other sites have a similar small value (~2-5 %). Increasing χ_{fd}% values with decreasing pebble size indicate more finer particle behavior in smaller pebbles, however, most sites show an opposite trend. *ARM/SIRM* and *SIRM/*χ ratios are related to the magnetic domain state and the latter is also sensitive for magnetic mineralogy. For the studied basalts particle-internal subdivision is expected to play an important role for the domain state. For the *ARM/SIRM* and *SIRM/*χ ratios, four Deccan sites (DE01, DE11, DE27, DS08) and all three Emeishan sites (ZT03, ZT06, ZT17) show a tendency of increasing *ARM/SIRM* ratio and simultaneously decreasing *SIRM/*χ ratio with fining of the pebble grain size. As paramagnetic contributions to magnetic parameters are meaningless in strongly magnetic basalts, this can only be explained by a shift towards fine particle behavior with increasing weathering that partly reaches into the superparamagnetic range and thus causes a relative increase in χ (i.e., in the finer pebble fractions). A simultaneous decrease of the absolute value of χ (as obvious in DS08 and all three ZT sites) implies that part of the magnetite was transformed to a non-ferrimagnetic phase (such as hematite), which causes a decrease of all three concentration dependent parameters (χ, SI*RM*, *ARM*).

The behavior of magnetic parameters and ratios of the Emeishan basalts is more consistent than for the Deccan basalts. All three sample sets have high χ, a high *S-ratio* close to 1.0, and similar low χ_{fd}% (~2.7-4.0 %). Along with decreasing pebble grain size, χ and the *SIRM* show a decreasing tendency, *SIRM/*χ decreases (ZT03 within confidence limits) while *ARM/SIRM* shows an increasing tendency, and χ_{fd}% increases (within confidence limits).

Table 1. Mean values with standard deviations of the 5 sub-samples from pebble fraction 1 (WP 1). Magnetic susceptibility (χ); *SIRM*; *S-ratio*; χ_{fd}%; *SIRM/*χ; *ARM/SIRM*.

	MAP [mm]	**χ** [10^{-8} m^3kg^{-1}]	**SIRM** [Am^2kg^{-1}]	**S-ratio** [-]	**χ_{fd}** [%]	**SIRM/χ** [kAm^{-1}]	**ARM/SIRM** [-]
DE01	515	1402.6±492.8	0.44±0.24	0.99±0.009	3.34±1.67	30.57±9.08	0.0043±0.0009
DE04	593	340.6±102.8	0.08±0.03	0.94±0.025	8.13±3.4	23.13±6.25	0.0065±0.0018
DE11	812	455.9±170.9	0.08±0.03	0.97±0.017	4.96±2.82	16.78±1.56	0.0054±0.0013
DE22	1148	632.9±155.2	0.17±0.03	0.98±0.005	3.33±1.42	27.01±6.44	0.0043±0.0025
DE27	3846	852.5±227.5	0.21±0.02	0.98±0.009	2.7±0.54	26.91±11.39	0.0049±0.0018
DE29	3044	602.3±127.3	0.09±0.02	0.95±0.020	9.74±2.12	14.92±1.96	0.0097±0.0007
DE33	2667	2358.3±187.0	0.08±0.02	0.99±0.003	2.58±0.14	3.43±1.10	0.0104±0.0012
DS02	3917	1543.9±192.6	0.23±0.03	0.99±0.007	3.98±0.72	14.71±0.75	0.0082±0.0005
DS08	3918	2525.9±120.6	0.38±0.06	0.99±0.004	3.76±0.22	14.89±2.70	0.0056±0.0010
ZT03	~800	1282.9±337.8	0.34±0.07	0.99±0.008	3.19±0.07	26.99±3.63	0.0053±0.0006
ZT06	~800	2483.8±431.3	0.31±0.11	0.99±0.004	2.70±0.18	12.73±4.44	0.0050±0.0015
ZT17	~800	1232.6±225.6	0.25±0.04	0.99±0.008	3.14±0.27	20.32±4.62	0.0060±0.0008

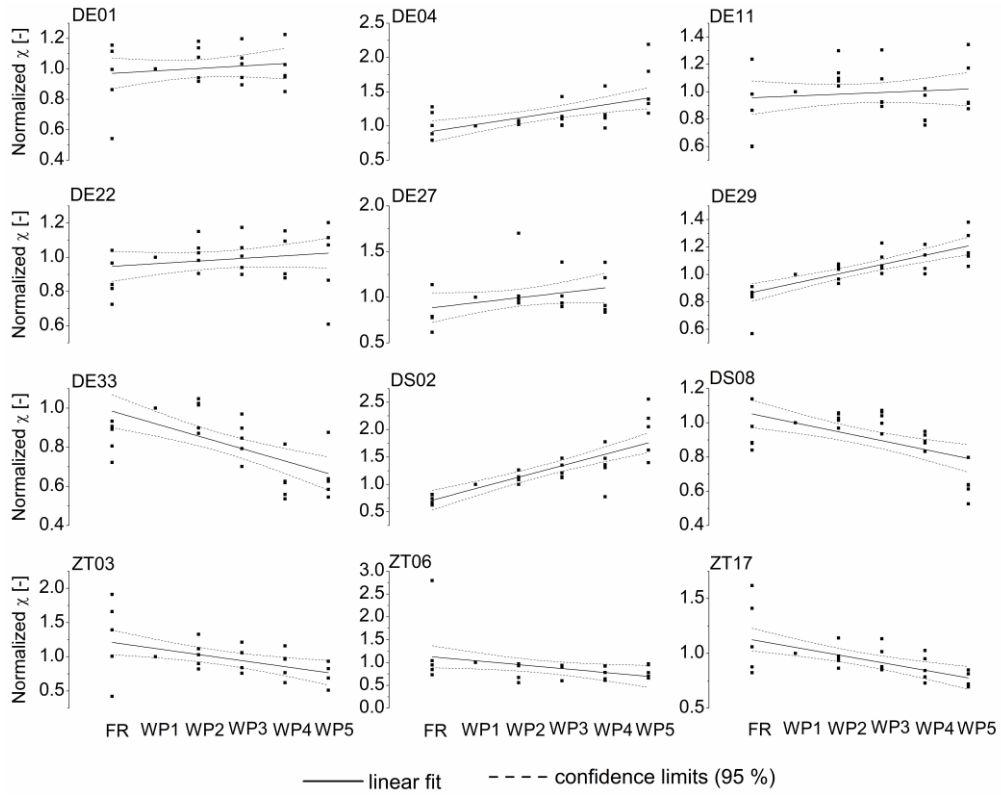

Figure 5. Magnetic susceptibility (χ) versus alteration degree (increasing from FR to WP5), all values normalized to WP1 of each sub-sample set. Linear fits with 95 % confidence intervals are shown.

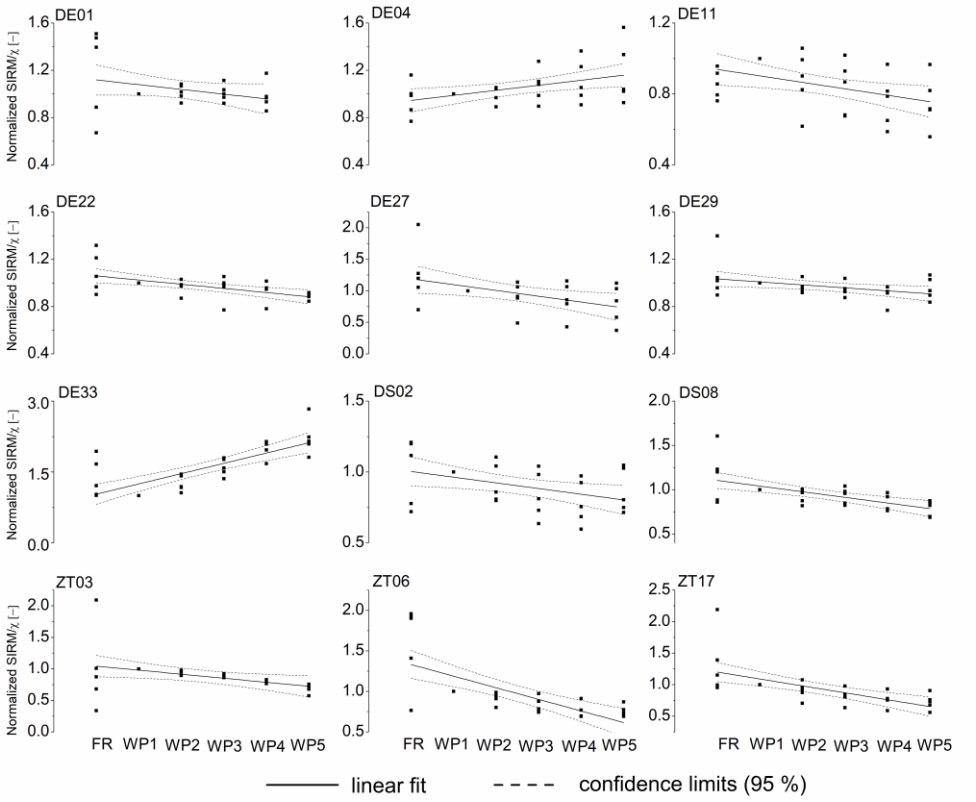

Figure 6. *SIRM/χ* ratio versus alteration degree (increasing from FR to WP5), all values normalized to WP1 of each sub-sample set. Linear fits with 95 % confidence intervals are shown.

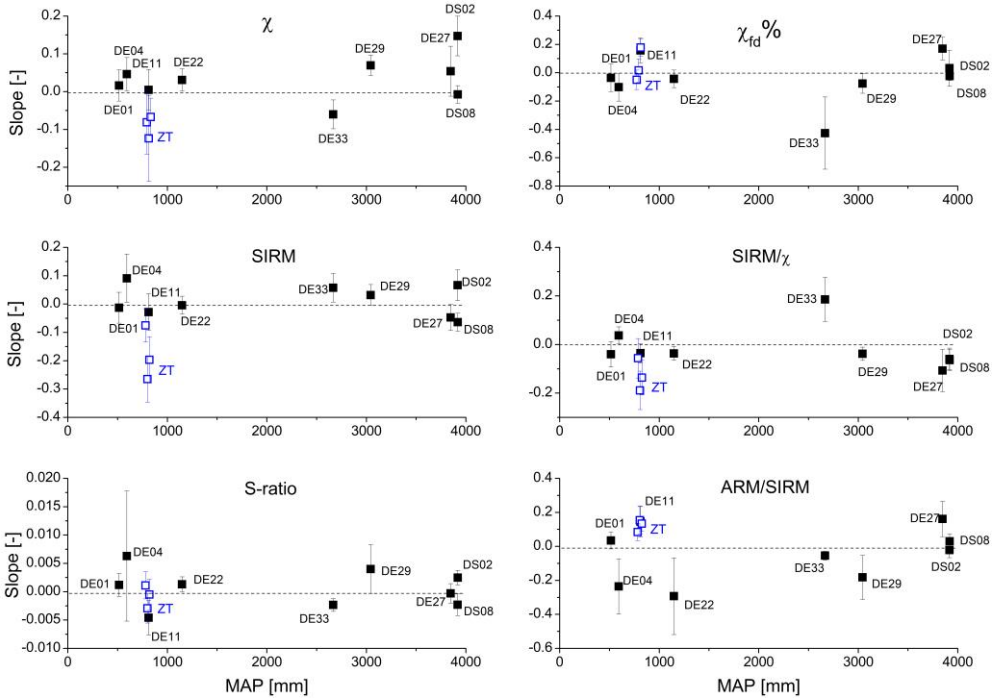

Figure 7. Slope values of regression lines (including FR and WP1-4) with 95 % confidence limits. χ: magnetic susceptibility, χ_{fd}%: percentage frequency-dependent susceptibility, *SIRM*: saturation isothermal remanent magnetizations, *S-ratio* and ratios of *SIRM*/χ and *ARM*/*SIRM*. Black and blue symbols denote Deccan and Emeishan results, respectively.

4. Discussion

4.1 Magnetic properties

Studies on the Deccan traps at the beginning mainly focused on paleomagnetism (Bhimasankaram, 1965; Wensink & Klootwijk, 1971). Later rock magnetic studies suggested that variability of domain structures is the main factor explaining the magnetic properties, and that also differences in the composition and cation deficiency of the magnetite play a role (Radhakrishnamurty et al. 1978). Based on these results, the authors proposed a classification of more than 95 % of the studied basalts into three categories. Later results of Senanayake & McElhinny (1981, 1982) principally agreed with these findings, however, they disagreed with the cation-deficient type which was interpreted by Radhakrishnamurty et al. (1978) based on the thermal behavior of susceptibility and coercivity. Senanayake & McElhinny presented a similar approach of grouping the basalts, in which the cation-deficient type proposed by Radhakrishnamurty et al. was associated with titanomagnetites containing exsolved ilmenite lamellae. Our study is in accordance with the conclusion of Senanayake & McElhinny, that lamellae-structured samples have a higher magnetic susceptibility value at liquid nitrogen temperature (-196 °C) compared to room temperature. In general, it has to be noted that the exsolution into magnetite and ulvöspinel (the latter then usually altered to ilmenite) is a primary feature of the original genesis of the basalts during cooling. For the later alteration of magnetite, the relative portions of magnetite and ilmenite are meaningless, but the shape and embedding of the magnetite is relevant, which is causing a difference in the climate-related alteration processes. Therefore, a bias of the results in terms of ambient humidity and temperature conditions by the variability in the rock mineralogy is expected.

The relatively higher observed Curie temperature than expected for magnetite is indicating cation-deficient magnetite. An increase of T_c by LTO was often observed on oceanic basalts (Nishitani & Kono, 1983). During rock weathering, magnetite oxidation happens first at its outer shell or through fissures, along with proceeding processes of oxidation, magnetite properties are affected by lowering saturation magnetization and increasing Curie temperature. However, in the recent study of controlled laboratory experiments (Zhang et al., 2020) it was surprisingly found that LTO occurs relatively uniform across the entire particle volume except of a possible higher oxidized shell that does not contribute much to the results of macroscopic measurements.

Cation-deficient magnetite can be easily converted by slight heating (Dunlop & Özdemir, 1997). A susceptibility drop that follows a hump-like peak in thermomagnetic curves between ~300 °C and ~450 °C was often explained by the existence of thermally unstable maghemite based on the studies of Chinese loess and paleosols (Deng et al, 2004), and such an explanation was also proposed recently by Bilardello & IRM (2020). However, we suggest it can be also explained by fine particle effects, caused by particle-internal subdivision that creates sub-regions acting like stable single domain (SSD) particles, which then become superparamagnetic (SP) during heating. Inhomogeneous alteration causing increased portions of vortex structures (Appel & Soffel, 1984), which will likely lead to an increasing proportion of sub-regions, with a broad range of unblocking temperatures, and also could tail into SP contributions.

A decrease in concentration dependent parameters (χ and *SIRM*) would be a perfect indicator of transformation of magnetite (i.e., maghemitized magnetite) to hematite. As shown in Figure 7, the results of the Emeishan basalts show a clear decrease of concentration dependent parameters with alteration, while only part of the Deccan basalts display a decrease. The increase of *ARM/SIRM* combined with a decrease of *SIRM*/χ reveal domain state fining along with higher degree of weathering, which is likely related to the increased formation of particle-internal sub-regions with more SP contribution that increases χ.

Do these effects of alteration systematically appear as a function of humidity and temperature? In case of a linear relationship with these parameters, a higher degree of weathering is expected for higher MAT and higher MAP. In general, the magnetic properties variation of the Deccan basalts and their weathered pebbles show less consistency than the Emeishan basalts. Sample sets from low MAP (<800 mm) Deccan traps area (DE01, DE04, DE11) show a quite consistent increase of χ, but the sample sets from high MAP (>3800 mm) areas of Deccan traps (DE27, DS02, DS08) are internally inconsistent. As mentioned above, along with the weathering degree, formation of particle-internal subregions could lead to an increase of χ because of more SP contributions, but the change of the *ARM*/*SIRM* and *SIRM*/χ ratios for DE01, DE04, DE11 is not compatible with such a scenario. The increase of χ could be also caused by Ti-rich titanomagnetite exsolution that forms magnetite with higher χ. The results from the relatively lower MAT area of the Emeishan basalts (with similar MAP as the Deccan sites DE01, DE04, DE11) show an interestingly consistent decrease of χ, and a decrease of *SIRM*/χ together with an increase of *ARM*/*SIRM*. These results are well compatible with the scenario of particle-internal subdivision tailing into SP behavior.

Although there are no consistent signals of humidity related weathering, there are effects of weathering, which are likely related to climate conditions, but strongly biased by the original rock composition. The laboratory experiments of Zhang et al. (2020) have demonstrated a dependence of magnetite alteration on humidity, with a strongest effect for persistently high humidity, but a non-linear behavior for drier conditions or alternating dry-humid conditions. One would like to validate this observation for natural environments. However, this study of basalts reveals that the natural rock-magnetic variability overrides the climate effect, and the results within the sub-samples of the same site show that a considerable variability of rock magnetic properties already exists of rather small scale $<10^2$ to 10^3 m^2, i.e., the size of individual sites in our sampling. Weathered pebbles are not always clearly related to the rock that crops out at the sampling spot, and the finest pebble fraction could be influenced by soil forming processes. However, as the slope tendencies are quite similar when excluding the fresh rock and WP5 fraction (see table and figures in the Appendix), this cannot be the reason for the missing systematic climate-dependence in our study results.

Our results have consequences when studying a sedimentary archive such as a lake sediment sequence, for which climate-related weathering conditions in the catchment area are considered for interpretation. Lake sediments will receive material from a larger catchment and source rocks in the catchment are inhomogeneous even at smaller scale. The variability of rock magnetic mineralogy will therefore matter a lot when climate variation is associated with a shift in collective input from different parts of the catchment. Such shifts will naturally occur by displacements of river systems and atmospheric circulation changes that impact the transport of material from the source area to the sedimentary sink. Thus, climate-related effects of rock weathering in the catchment will most probably be hidden in the magnetic properties of sedimentary archives.

As shown by the macroscopic results in Figure 5, Figure 6 and Figure 7, most weathered pebbles do not show a strong signature of LTO or indication for significant magnetite-to-hematite transformation. In general, comparing the magnetic properties of fresh rock and pebbles, the alteration of magnetite during strong weathering causes only relatively small changes in the macroscopic parameters, which is a good meassage for paleomagnetic studies. Basalt material that is weathered, but still not decomposed from the solid rock, as shown in Figure 2, is likely not altered to a degree where magnetic remanences are strongly affected.

5. Conclusions

Magnetic properties of magnetite in basalts and their weathering material mainly depend on the rock type, climate-related weathering may be important, but plays a subordinate role compared to the rock-type dependent variability, at least among the studied basalts.

The variability of weathering-related magnetic properties is already strong within the scale of the studied individual sites (i.e., below 10^2 to 10^3 m^2 large areas). Therefore, changes in the relative mixing proportions of weathered material from an area at such scale can lead to significant changes of the rock magnetic properties in the material that is transported to a sink (climate archive such as lake sediments). This may happen without a systematic climate related dependence and thus add significantly to the magnetic proxy record at the sink. Climate related properties in the archive sequence such as authigenic processes could therefore suffer from considerable noise due to non-climate related processes routing in the rock variability in the catchment.

However, there is also a good message from the results of this study. According to the relatively small differences of magnetic properties in the fresh rocks and their related weathered pebbles, the alteration of magnetite is relatively small in the course of rock weathering. In consequence it is likely that magnetic remanences recorded in the rocks are only little affected by the alteration, and weathering will not easily destroy paleomagnetic information.

Acknowledgements

This study was supported by the German Research Foundation (DFG; AP 34/44-1), the National Natural Science Foundation of China (NO. 41572152), and the Chinese Academy of Sciences Visiting Professorship for Senior International Scientists (NO. 2012T1Z0004, 131432WGZJTPYJY2015002). Qi Zhang was the lead scientist in all parts of this paper, Erwin Appel contributed to the interpretation and paper writing, Xiuhua Zhu performed the ERA INTERIM data compilation, Udo Neumann guided the microscope analysis and interpretation, Nathani Basavaiah and Shouyun Hu participated in the field work and contributed to the interpretation. We thank Tatiana Miranda for her support in the SEM studies, Per Jeisecke and Simone Schafflick for embedding and polishing basalts sections. Data presented in this paper are listed in the Appendix.

References

Allegre, C.J., Birck, J.L., Capmas, F. & Courtillot, V. (1999). Age of the Deccan traps using 187Re–187Os systematics. Earth Planet. Sci. Lett., 170, 3, 197-204. https://doi.org/10.1016/S0012-821X(99)00110-7

Appel, E. (1987). Stress anisotropy in Ti-rich titanomagnetites. Phys. Earth Planet. Inter., 46, 233-240. https://doi.org/10.1016/0031-9201(87)90185-3

Appel, E. & Soffel, H.C. (1984). Model for the domain state of Ti-rich titanomagnetites. Geophys. Res. Lett., 3, 189-192. https://doi.org/10.1029/GL011i003p00189

Aragón, R., Buttrey, D., Shepherd, J.P. & Honig, J.M. (1985). Influence of nonstoichiometry on the Verwey transition. Phys. Rev., B31,430. https://doi.org/10.1103/PhysRevB.31.430

Basavaiah, N., Mahesh Babu, J.L.V., Gawali, P.B., Naga Kumar, K.Ch.V., Demudu, G. & Prizomwala, S.P., et al. (2015). Late Quaternary environmental and sea level changes from Kolleru Lake, SE India: Inferences from mineral magnetic, geochemical and textural analyses, Quatern. Int., 371, 197–208. https://doi.org/10.1016/j.quaint.2014.12.018

Basavaiah, N., Satyanarayana, K.V.V., Deenadayalan, K. & Prasa, J.N. (2018). Does Deccan Volcanic Sequence contain more reversals than the three-Chron N–R–N flow magnetostratigraphy? a palaeomagnetic evidence from the dyke-swarm near Mumbai. Geophys. J. Int., 213, 1503-1523. https://doi.org/10.1093/gji/ggy041

Bhimasankaram, V.L.S. (1965). Palaeomagnetic Directions of the Deccan Traps of Rajahmundry, Andhra Pradesh, India. GeoPhys. J. Int. 9, 2-3, 113-119. https://doi.org/10.1111/j.1365-246X.1965.tb02065.x

Bilardello, D. & IRM. (2020). Practical Magnetism II: Humps and a Bump, the Maghemite Song. The IRM Quarterly, 30(1), 15-17. ISSN: 2152-1972

Bloemendal, J., King, J.W., Hall, F.R., & Doh, S.J. (1992). Rock magnetism of Late Neogene and Pleistocene deep-sea sediments: Relationship to sediment source, diagenetic processes, and sediment lithology. J. Geophys. Res. Solid Earth, 97(B4), 4361-4375. https://doi.org/10.1029/91JB03068

Cui, Y., Verosub, K.L. & Roberts, A. (1994). The effect of low-temperature oxidation on large multi-domain magnetite. Geophys. Res. Lett., 21(9), 757-760. https://doi.org/10.1029/94GL00639

Dearing, J.A., Dann, R.J.L., Hay, K., Lees, J., Loveland, P.J., Maher, B.A. & O'Grady, K. (1996). Frequency-dependent susceptibility measurements of environmental materials. Geophys. J. Int., 124, 228-240. https://doi.org/10.1111/j.1365-246X.1996.tb06366.x

Dee, D.P., Uppala, S.M., Simmons, A.J., Berrisford, P., Poli, P., Kobayashi, S., Andrae, U., Balmaseda, M.A. et al. (2011). The ERA-Interim reanalysis: configuration and performance of the dataassimilation system. Q. J. R. Meteorol. Soc., 137, 553–597. https://doi.org/10.1002/qj.828

Deng, C.L., Zhu, R.X., Verosub, K.L., Singer, M.J., & Vidic, N.J. (2004). Mineral magnetic properties of loess//paleosol couplets of the central loess plateau of China over the last 1.2 Myr. J. Geophys. Res., 109, B01103. https://doi.org/10.1029/2003JB002532

Dunlop, D.J. & Özdemir, Ö. (1997). Rockmagnetism: fundamentals and frontiers. Cambridge University Press. 573 p.

Eriksson, M.G., Sandgren, P. (1999). Mineral magnetic analyses of sediment cores recording recent soil erosion history in central Tanzania. Palaeogeogr. Palaeoclimat., Palaeoecol., 152, 365−383. https://doi.org/10.1016/S0031-0182(99)00043-7

He, Y. & Traina, S.J. (2007). Transformation of magnetite to goethite under alkaline pH conditions, Clay Miner., 42, 13–19. https://doi.org/10.1180/claymin.2007.042.1.02

Herb, C., Zhang, W.L., Koutsodendris, A., Appel, E., Fang, X.M. & Pross, J. (2013). Environmental implications of the magnetic record in Pleistocene lacustrine sediments of the Qaidam Basin, NE Tibetan Plateau. Quat. Int., 313-314, 218-229. https://doi.org/10.1016/j.quaint.2013.06.015

Hu, S.Y., Goddu, S.R., Herb, C., Appel, E., Gleixner, G., Wang, S.M., et al. (2015). Climate variability and its magnetic response recorded in a lacustrine sequence in Heqing basin at the SE Tibetan Plateau since 900 ka. Geophys. J. Int., 201, 444-458. https://doi.org/10.1093/gji/ggv033

Irving, E. (1970). The Mid-Atlantic Ridge at 45°N, XIV, Oxidation and magnetic properties of basalts: Review and discussion. Can. J. Earth Sci., 7, 1528-1538. https://doi.org/10.1139/e70-144

Kent, D.V. & Gee, J. (1996). Magnetic alteration of zero-age oceanic basalt. Geology, 24, 703-706. https://doi.org/10.1130/0091-7613(1996)024<0703:MAOZAO>2.3.CO;2

Keller, R. & Schmidbauer, E. (1999). Magnetic hysteresis properties and rotational hysteresis losses synthetic stress-controlled titanomagnetite ($Fe_{2.4}Ti_{0.6}O_4$) particles - I. Magnetic hysteresis properties. Geophys. J. Int., 138, 319-333. https://doi.org/10.1046/j.1365-246X.1999.00852.x

Kısakürek, B., Widdowson, M. & James, R.H. (2004). Behaviour of Li isotopes during continental weathering: the Bidar laterite profile, India. Chem. Geol., 212, 1-2, 27-44. https://doi.org/10.1016/j.chemgeo.2004.08.027

Lise-Pronovost, A., St-Onge, G., Gogorza, C., Jouve, G., Francus, P., Zolitschka, B., PASADO Science Team. (2014). Rock-magnetic signature of precipitation and extreme runoff events in southeastern Patagonia since 51,200 cal BP from the sediments of Laguna Potrok Aike. Quat. Sci. Rev., 98, 110-125. https://doi.org/10.1016/j.quascirev.2014.05.029

Maher, B.A. & Hu, M. (2006). A high-resolution record of Holocene rainfall variations from the western Chinese Loess Plateau: antiphase behaviour of the African/Indian and East Asian summer monsoons. The Holocene, 16,3, 309-319. https://doi.org/10.1191/0959683606hl929rp

Maxbauer, D.P., Feinberg, J.M., Fox, D.L. & Clyde, W.C. (2016). Magnetic minerals as recorders of weathering, diagenesis, and paleoclimate: A core–outcrop comparison of Paleocene–Eocene paleosols in the Bighorn Basin, WY, USA. Earth Planet. Sci. Lett., 452, 15-26. https://doi.org/10.1016/j.epsl.2016.07.029

Mücke, A. (2003). Magnetite, ilmenite and ulvite in rocks and ore deposits: petrography, microprobe analyses and genetic implications. Mineral. Petrol., 77, 215–234. https://doi.org/10.1007/s00710-002-0216-1

Negrini, R.M., Erbes, D.B., Faber, K., Herrera, A.M., Roberts, A.P., Cohen, A.S., Wigand, P.E., Foit, Jr. F.F. (2000). A paleoclimate record for the past 250,000 years from Summer Lake, Oregon, USA: I.Chronology and magnetic proxies for lake level. J. Paleolimnology, 24, 125–149. https://doi.org/10.1023/A:1008144025492

Nishitani, T. & Kono, M. (1983). Curie temperature and lattice constant of oxidized titanomagnetite. Geophys. J. Int., 74, 585-600. https://doi.org/10.1111/j.1365-246X.1983.tb01890.x

O'Reilly, W. (1984). Rock and Mineral Magnetism. Blackie London, 220 p.

Peck, J.A., King, J.W., Colman, S.M., & Kravchinsky, V.A. (1994). A rock magnetic record from Lake Baikal, Siberia: evidence for Late Quaternary climatic change. Earth and Planetary Science Letters, 122, 221-238. https://doi.org/10.1016/0012-821X(94)90062-0

Petersen, N. & Vali, H. (1987). Observation of shrinkage cracks in ocean floor titanomagnetites. Phys. Earth Planet. Inter., 46, 197-205. https://doi.org/10.1016/0031-9201(87)90182-8

Radhakrishnamurty, C., Likhite, S.D., Deutsch, E.R. & Murthy, G.S. (1978). Nature of magnetic grains in basalts and implications for palaeomagnetism. Proc. Indian Acad. Sci., A (E & P Sciences) 87, 235–243. https://doi.org/10.1007/BF02861518

Radhakrishnamurty, C., Likhite, S.D., Deutsch, E.R. & Murthy, G.S. (1981). A comparison of the magnetic properties of synthetic titanomagnetites and basalts. Phys. Earth Planet. In., 26, 1-2, 37-46. https://doi.org/10.1016/0031-9201(81)90095-9

Radhakrishnamurty, C., Likhite, S.D. & Sahasrabudhe, P.W. (1977). Nature of magnetic grains and their effect on the remanent magnetization of basalts. Phys. Earth Planet. In., 13, 4, 289-300. https://doi.org/10.1016/0031-9201(77)90112-1

Radhakrishnamurty, C. & Sahasrabudhe, P.W. (1967). On the magnetic and mineralogical properties of basalts. PAGEOPH, 66, 69-76. https://doi.org/10.1007/BF00875312

Readman, P. & O'Reilly, W. (1972). Magnetic properties of oxidized (cation-deficient) titanomagnetites (Fe,Ti)3O4. J. Geomag. Geoelec., 24, 69-90. https://doi.org/10.5636/jgg.24.69

Senanayake, W. E. & McElhinny, M. W. (1981). Hysteresis and susceptibility characteristics of magnetite and titanomagnetites: interpretation of results from basaltic rocks. Phys. Earth Planet. Inter., 26, 1-2, 47-55. https://doi.org/10.1016/0031-9201(81)90096-0

Senanayake, W. E. & McElhinny, M. W. (1982). The effects of heating on low-temperature susceptibility and hysteresis properties of basalts, Phys. Earth Planet. Inter., 30, 4, 317-321, 1982. https://doi.org/10.1016/0031-9201(82)90030-9

Sidhu, P.S. (1988). Transformation of trace element-substituted maghemite to hematite. Clay Miner., 36(1), 31-38. http://doi.org/10.1346/CCMN.1988.0360105

Shellnutt, J.G. & Jahn, B.-M. (2011). Origin of Late Permian Emeishan basaltic rocks from the Panxi region (SW China): Implications for the Ti-classification and spatial–compositional distribution of the Emeishan flood basalts. J.Volcanol. Geoth. Res., 199, 85-95. https://doi.org/10.1016/j.jvolgeores.2010.10.009

Sheth, H. C. (2005). From Deccan to Réunion: no trace of a mantle plume. In: Foulger, G. R., Natland, J. H., Presnall, D. C., Anderson, D. L. (Eds.), Plates, Plumes, and Paradigms. Geol. Soc. Am. Spec. Pap. 388, 477-501.

Snowball, I., Zillen, L., Sandgren, P. (2002). Bacterial magnetite in Swedish varved lake sediments: A potential bio-marker of environmental change. Quat. Int., 88, 13-19. https://doi.org/10.1016/S1040-6182(01)00069-6

Torrent, J., Barron, V., & Liu, Q. (2006). Magnetic enhancement is linked to and precedes hematite formation in aerobic soil. Geophys. Res. Lett., 33, L02401. https://doi.org/10.1029/2005GL024818

Wang, D., Van der Voo, R. & Peacor, D.R. (2006). Low-temperature alteration and magnetic changes of variably altered pillow basalts. Geophys. J. Int., 164, 25-35. https://doi.org/10.1111/j.1365-246X.2005.02819.x

Wensink, H. (1973). Newer paleomagnetic results of the Deccan traps, India. Tectonophysics. 17, 1-2, 41-59. https://doi.org/10.1016/0040-1951(73)90064-4

Wensink, H. & Klootwijk, C.T. (1971). Paleomagnetism of the Deccan Traps in the Western Ghats near Poona (India). Tectonophysica, 11,3,175-190. https://doi.org/10.1016/0040-1951(71)90029-1

Widdowson, M. & Cox, K.G. (1996). Uplift and erosional history of the Deccan Traps, India: Evidence from laterites and drainage patterns of the Western Ghats and Konkan Coast. Earth Planet. Sci. Lett., 137, 1-4, 57-69. https://doi.org/10.1016/0012-821X(95)00211-T

Xu, Y.G., Chung, S.L., Jahn, B.M. & Wu, G.Y. (2001). Petrologic and geochemical constraints on the petrogenesis of Permian–Triassic Emeishan flood basalts in southwestern China. Lithos, 58, 3-4, 145-168. https://doi.org/10.1016/S0024-4937(01)00055-X

Zhang, Q., Appel, E., Stanjek, H., Byrne, J.M., Berthold, C. & Sorwat, J., et al. (2020). Humidity related magnetite alteration in an experimental setup. Geophys. J. Int. https://doi.org/10.1093/gji/ggaa394

Appendix A

Table 1. Slope and confidence limits values of χ, *SIRM*, *S-ratio*, χ_{fd}%, *SIRM*/χ, *ARM*/*SIRM* by four grouping methods (0: Fresh rock, 1: WP1, 2: WP2, 3: WP3, 4: WP4, 5: WP5).

			Slope	confidence limits		Slope	confidence limits		Slope	confidence limits		Slope	confidence limits
χ	DE01	0-5			1-5			0-4	0.0161	0.0413	1-4	-0.0020	0.0440
	DE04		0.0971	0.0507		0.1299	0.0671		0.0461	0.0442		0.0667	0.0574
	DE11		0.0126	0.0403		-0.0172	0.0454		0.0048	0.0538		-0.0501	0.0573
	DE22		0.0154	0.0289		-0.0053	0.0374		0.0309	0.0295		0.0067	0.0373
	DE27								0.0542	0.0661		0.0044	0.0924
	DE29		0.0679	0.0212		0.0500	0.0235		0.0697	0.0270		0.0409	0.0278
	DE33		-0.0637	0.0280		-0.1033	0.0302		-0.0601	0.0381		-0.1239	0.0393
	DS02		0.2094	0.0592		0.2153	0.0866		0.1471	0.0525		0.1153	0.0806
	DS08		-0.0521	0.0266		-0.0843	0.0296		-0.0074	0.0230		-0.0313	0.0234
	ZT03		-0.0886	0.0593		-0.0680	0.0486		-0.0777	0.0849		-0.0361	0.0689
	ZT06		-0.0859	0.0795		-0.0423	0.0440		-0.1203	0.1137		-0.0707	0.0623
	ZT17		-0.0698	0.0343		-0.0597	0.0273		-0.0635	0.0497		-0.0427	0.0403
SIRM	DE01	0-5			1-5			0-4	-0.0131	0.0543	1-4	-0.0078	0.0501
	DE04		0.1626	0.0987		0.2103	0.1356		0.0908	0.0857		0.1223	0.1190
	DE11		-0.0236	0.0488		-0.0746	0.0578		-0.0284	0.0650		-0.1166	0.0738
	DE22		-0.0180	0.0284		-0.0309	0.0351		-0.0043	0.0317		-0.0166	0.0371
	DE27								-0.0476	0.0462		-0.0786	0.0554
	DE29		0.0431	0.0310		0.0319	0.0363		0.0316	0.0373		0.0053	0.0382
	DE33		0.0713	0.0470		0.0962	0.0615		0.0577	0.0507		0.0902	0.0652
	DS02		0.1458	0.0682		0.1462	0.0983		0.0663	0.0539		0.0141	0.0713

	DS08		-0.1008	0.0272		-0.1168	0.0283		-0.0641	0.0314		-0.0664	0.0275
	ZT03		-0.0999	0.0432		-0.1262	0.0384		-0.0721	0.0591		-0.0973	0.0536
	ZT06		-0.1963	0.0633		-0.0946	0.0414		-0.2613	0.0820		-0.1352	0.0579
	ZT17		-0.1709	0.0563		-0.1131	0.0294		-0.1933	0.0812		-0.1117	0.0459
S-ratio	DE01								0.0012	0.0020		-0.0004	0.0022
	DE04		0.0075	0.0095		0.0114	0.0131		0.0063	0.0115		0.0120	0.0169
	DE11		-0.0038	0.0022		-0.0027	0.0020		-0.0046	0.0030		-0.0032	0.0030
	DE22		0.0006	0.0010		0.0002	0.0009		0.0013	0.0013		0.0013	0.0013
	DE27								-0.0003	0.0017		-0.0012	0.0026
	DE29	**0-5**	0.0064	0.0033	**1-5**	0.0050	0.0031	**0-4**	0.0040	0.0043	**1-4**	0.0000	0.0024
	DE33		-0.0015	0.0009		-0.0018	0.0011		-0.0023	0.0011		-0.0033	0.0014
	DS02		-0.0025	0.0013		-0.0028	0.0014		-0.0023	0.0019		-0.0027	0.0022
	DS08		0.0016	0.0012		0.0006	0.0015		0.0025	0.0013		0.0015	0.0016
	ZT03		-0.0012	0.0017		-0.0016	0.0024		0.0011	0.0024		-0.0018	0.0037
	ZT06		-0.0026	0.0018		-0.0010	0.0015		-0.0029	0.0026		-0.0003	0.0021
	ZT17		-0.0010	0.0020		-0.0015	0.0024		-0.0005	0.0027		-0.0010	0.0036
χ_{fd}%	DE01								-0.0359	0.0965		-0.0042	0.0679
	DE04		-0.1099	0.0677		-0.0713	0.0602		-0.1018	0.0980		-0.0320	0.0893
	DE11		0.1820	0.1360		0.2187	0.1916		0.1578	0.0881		0.2028	0.1087
	DE22		-0.0516	0.0443		-0.0144	0.0508		-0.0430	0.0614		0.0247	0.0694
	DE27								0.1702	0.0810		0.1697	0.1227
	DE29	**0-5**	-0.1065	0.0488	**1-5**	-0.0919	0.0376	**0-4**	-0.0760	0.0688	**1-4**	-0.0316	0.0424
	DE33		-0.3733	0.1748		-0.0723	0.0654		-0.4265	0.2549		0.0397	0.0675
	DS02		-0.0310	0.0950		0.0682	0.1061		0.0319	0.1271		0.2392	0.1037
	DS08		-0.0688	0.0292		-0.0784	0.0323		-0.0240	0.0296		-0.0101	0.0135
	ZT03		0.0023	0.0523		0.0793	0.0269		-0.0414	0.0687		0.0578	0.0253
	ZT06		0.0421	0.0569		0.0875	0.0286		0.0254	0.0811		0.0899	0.0356
	ZT17		0.1654	0.0431		0.0846	0.0286		0.1873	0.0603		0.0672	0.0383
SIRM/χ	DE01								-0.0402	0.0525		-0.0061	0.0308
	DE04		0.0427	0.0324		0.0459	0.0442		0.0374	0.0351		0.0393	0.0488
	DE11		-0.0364	0.0293		-0.0610	0.0389		-0.0357	0.0392		-0.0761	0.0546
	DE22		-0.0353	0.0195		-0.0262	0.0188		-0.0366	0.0286		-0.0222	0.0299
	DE27								-0.1072	0.0870		-0.0666	0.0973
	DE29	**0-5**	-0.0251	0.0211	**1-5**	-0.0163	0.0190	**0-4**	-0.0383	0.0275	**1-4**	-0.0324	0.0217
	DE33		0.2176	0.0702		0.3190	0.0608		0.1857	0.0905		0.3335	0.0642
	DS02		-0.0400	0.0340		-0.0399	0.0409		-0.0595	0.0444		-0.0723	0.0540
	DS08		-0.0637	0.0302		-0.0483	0.0222		-0.0640	0.0432		-0.0386	0.0307
	ZT03		-0.0641	0.0556		-0.0778	0.0119		-0.0523	0.0812		-0.0674	0.0116
	ZT06		-0.1432	0.0571		-0.0650	0.2206		-0.1850	0.0791		-0.0830	0.0304
	ZT17		-0.1096	0.0505		-0.0686	0.0313		-0.1321	0.0714		-0.0788	0.0437
ARM/SIRM	DE01								0.0342	0.0490		0.0094	0.0433
	DE04		-0.1848	0.1133		-0.0255	0.0486		-0.2354	0.1620		-0.0037	0.0681
	DE11		0.1192	0.0737		0.1338	0.0998		0.1453	0.0890		0.1872	0.1240
	DE22		-0.1832	0.1619		0.0708	0.0451		-0.2931	0.2254		0.0570	0.0519
	DE27								0.1610	0.1036		0.1693	0.1589
	DE29	**0-5**	-0.1585	0.0891	**1-5**	-0.0394	0.0290	**0-4**	-0.1825	0.1296	**1-4**	0.0000	0.0295
	DE33		-0.0492	0.0199		-0.0451	0.0194		-0.0545	0.0252		-0.0513	0.0204
	DS02		-0.0281	0.0313		0.0004	0.0312		-0.0215	0.0455		0.0303	0.0450
	DS08		0.0332	0.0317		0.0226	0.0310		0.0301	0.0420		0.0104	0.0371
	ZT03		0.0878	0.0379		0.0663	0.0377		0.0833	0.0500		0.0446	0.0435
	ZT06		0.1343	0.0637		0.1234	0.0929		0.1529	0.0826		0.1470	0.1324
	ZT17		0.1133	0.0319		0.0565	0.0246		0.1330	0.0439		0.0514	0.0359

Appendix B

Figure B1. *SIRM* values of all sample sets (0: Fresh rock, 1: WP1, 2: WP2, 3: WP3, 4: WP4, 5: WP5) with linear regression analysis and 95 % confidence limits.

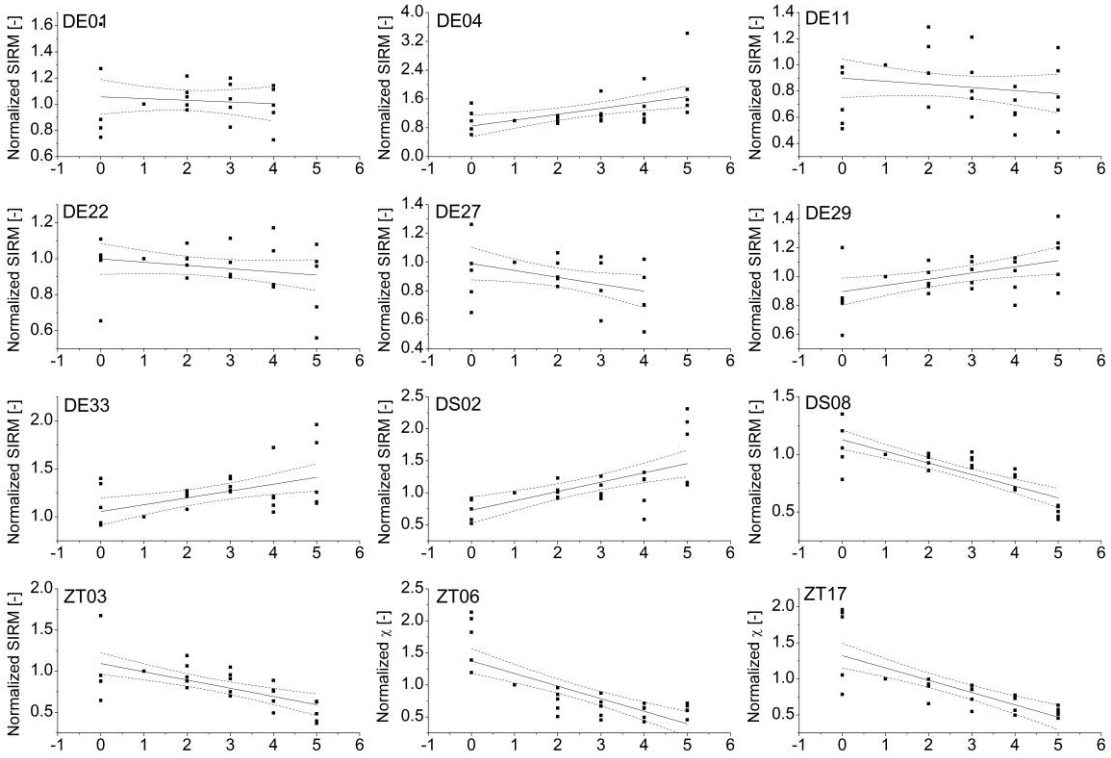

Figure B2. *S-ratio* values of all sample sets (0: Fresh rock, 1: WP1, 2: WP2, 3: WP3, 4: WP4, 5: WP5) with linear regression analysis and 95 % confidence limits.

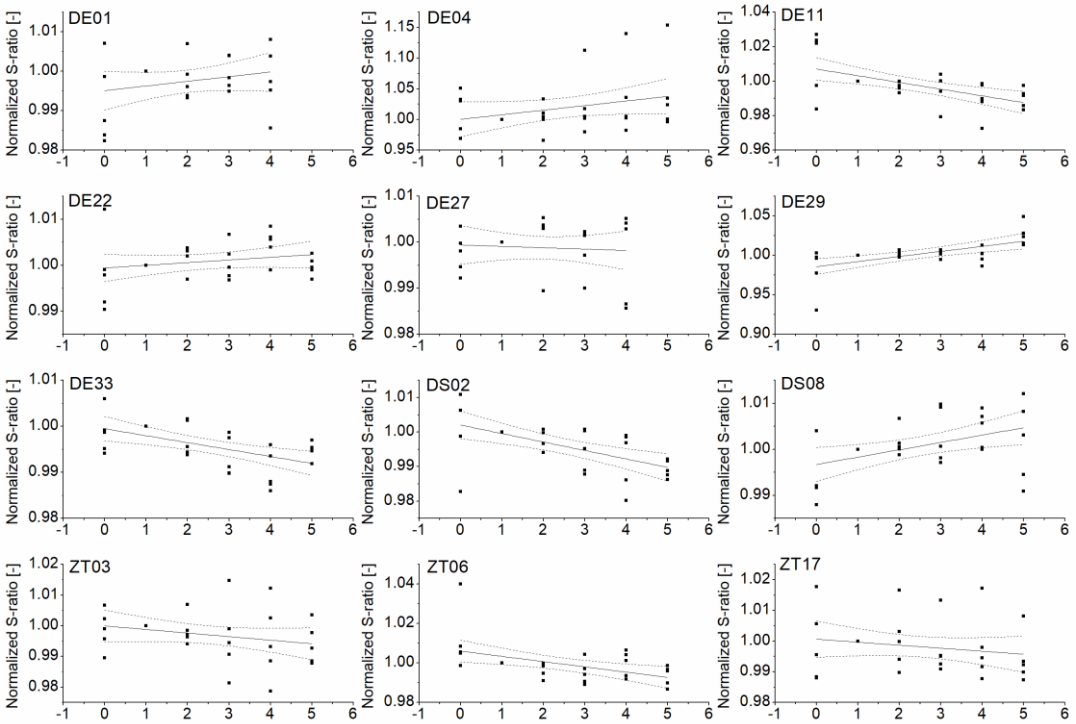

Figure B3. χ_{fd}% values of all sample sets (0: Fresh rock, 1: WP1, 2: WP2, 3: WP3, 4: WP4, 5: WP5) with linear regression analysis and 95 % confidence limits.

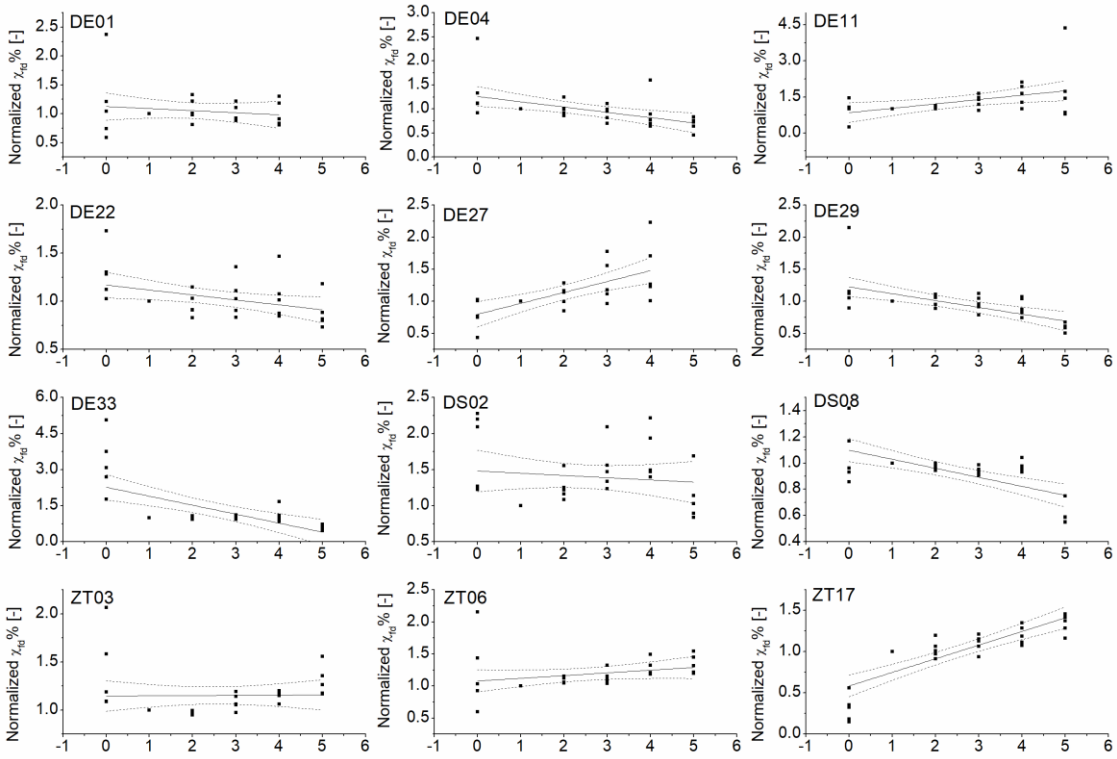

Figure B4. *ARM*/*SIRM* values of all sample sets (0: Fresh rock, 1: WP1, 2: WP2, 3: WP3, 4: WP4, 5: WP5) with linear regression analysis and 95 % confidence limits.

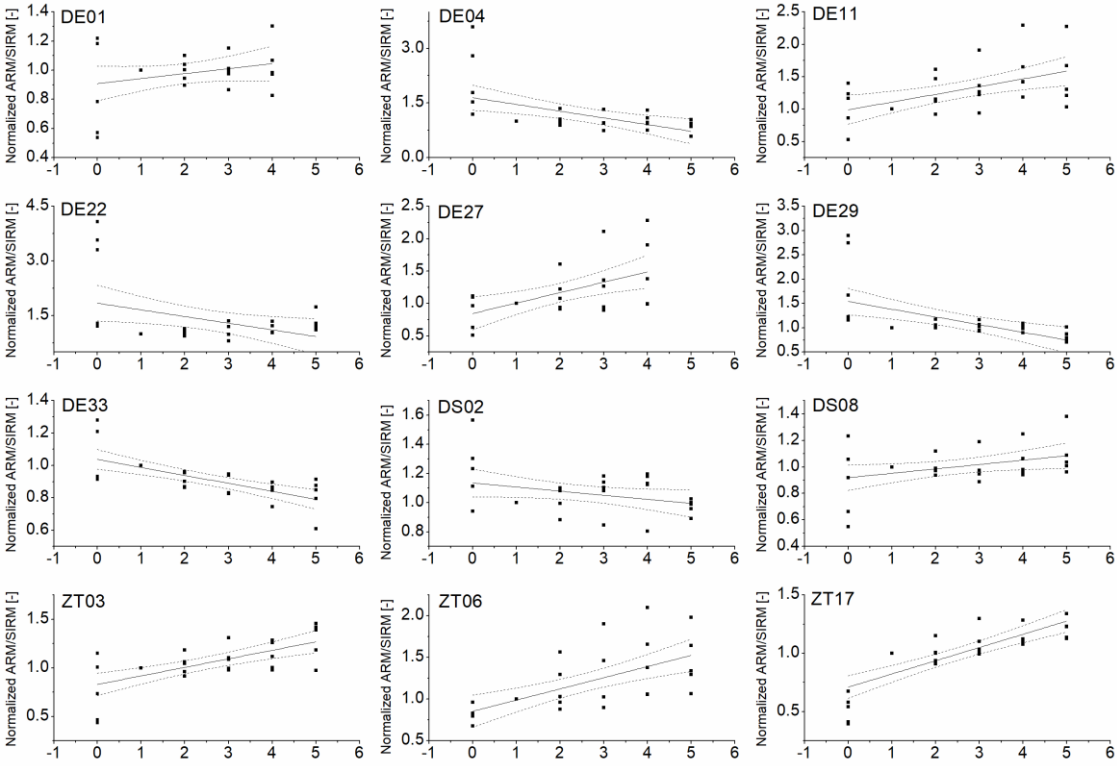

Figure B5. Slope values of χ sample sets, with linear regression analysis for the different groups of fresh rock (FR) and weathered pebble (WP1 to 5).

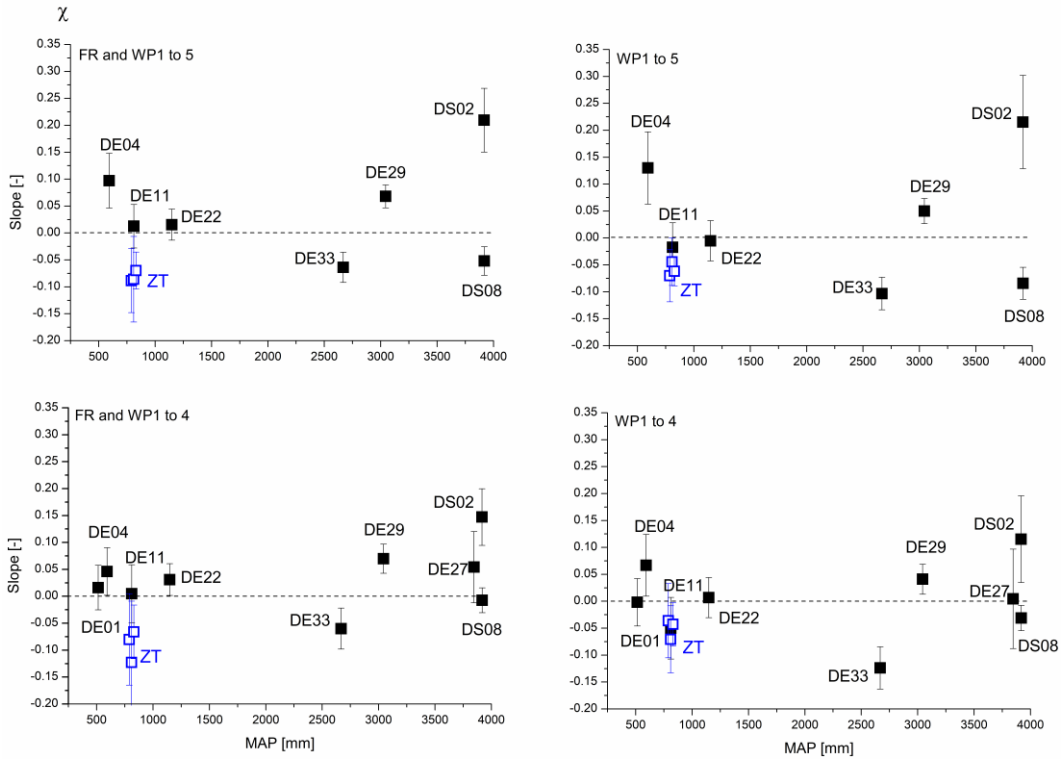

Figure B6. Slope values of *SIRM* sample sets with linear regression analysis for the different groups of fresh rock and weathered pebble WP1 to 5.

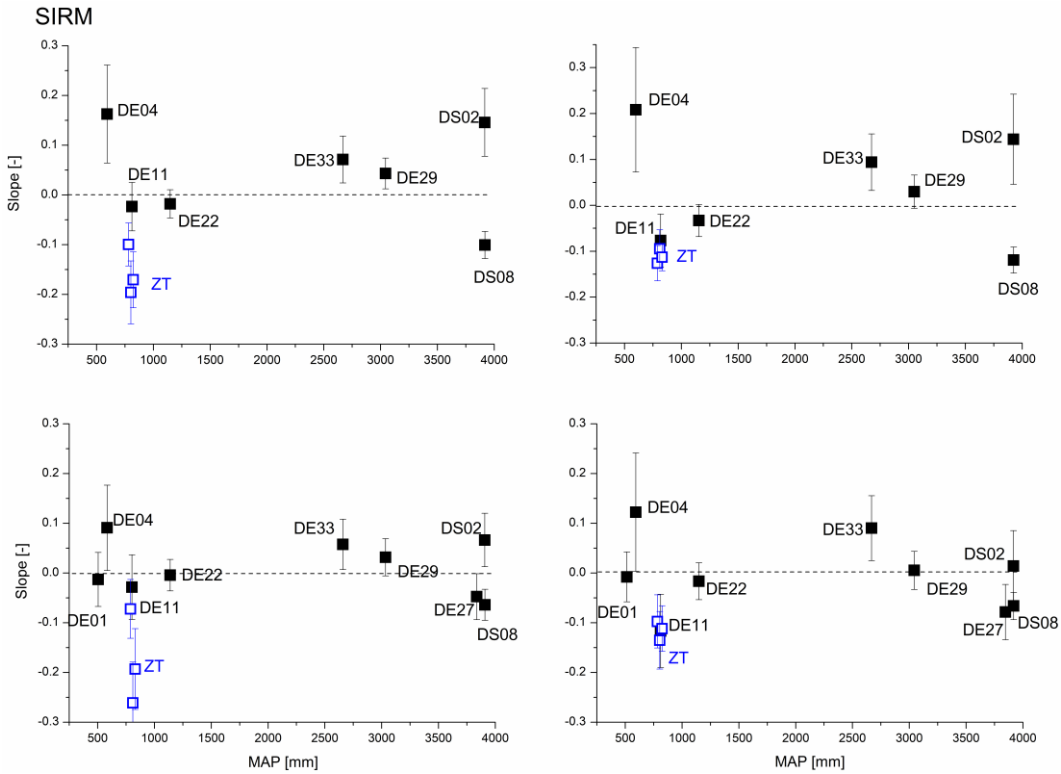

Figure B7. Slope values of *S-ratio* sample sets with linear regression analysis for the different groups of fresh rock (FR) and weathered pebble (WP1 to 5).

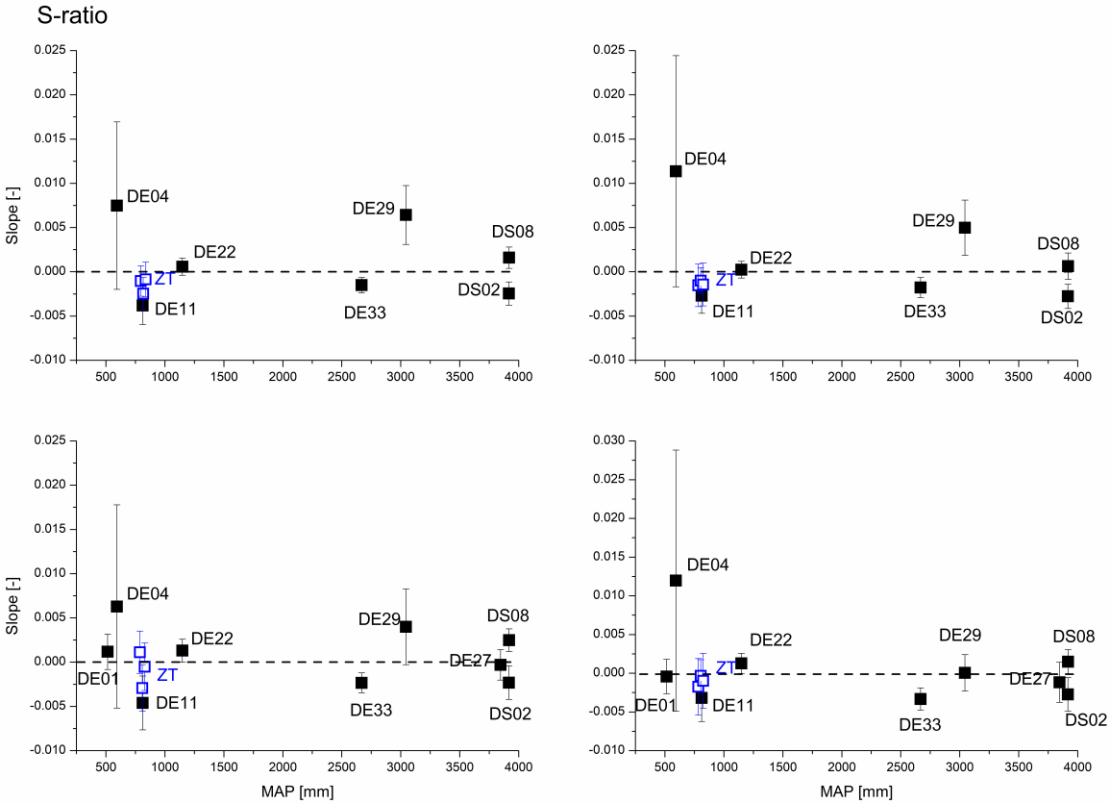

Figure B8. Slope values of χ_{fd}% sample sets with linear regression analysis for the different groups of fresh rock (FR) and weathered pebble (WP1 to 5).

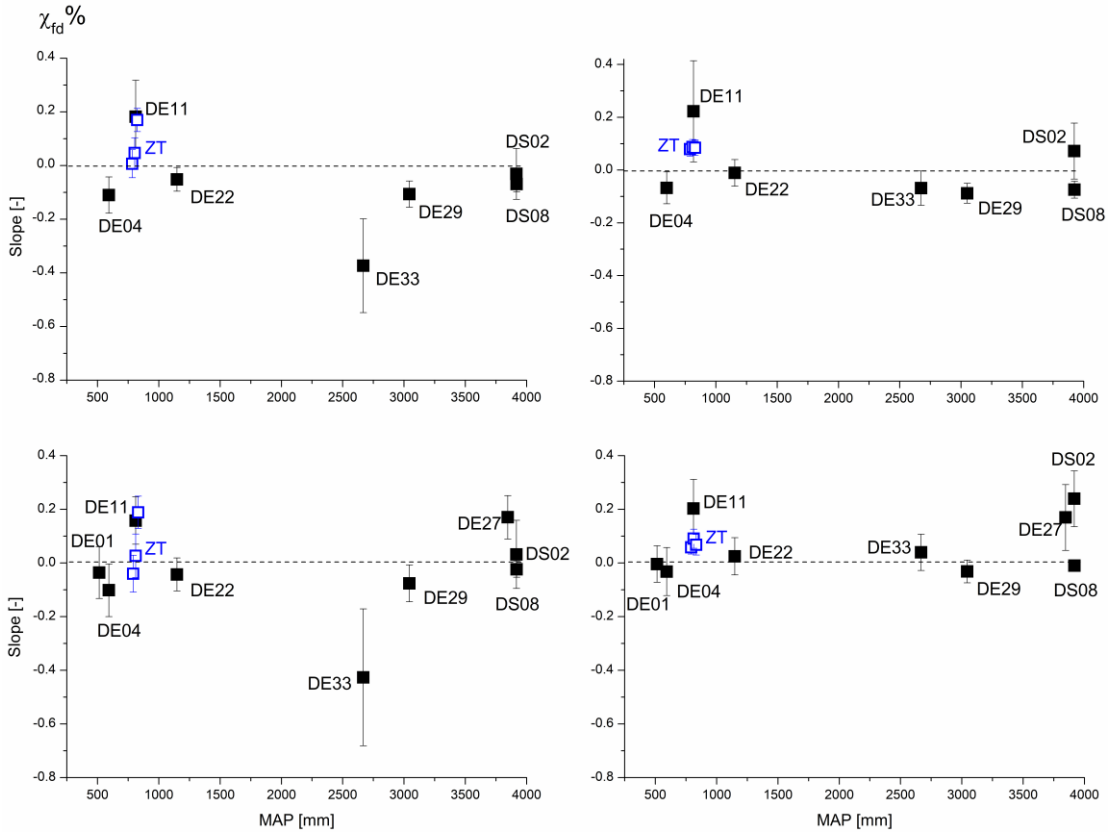

Figure B9. Slope values of *SIRM/χ* sample sets with linear regression analysis for the different groups of fresh rock (FR) and weathered pebble (WP1 to 5).

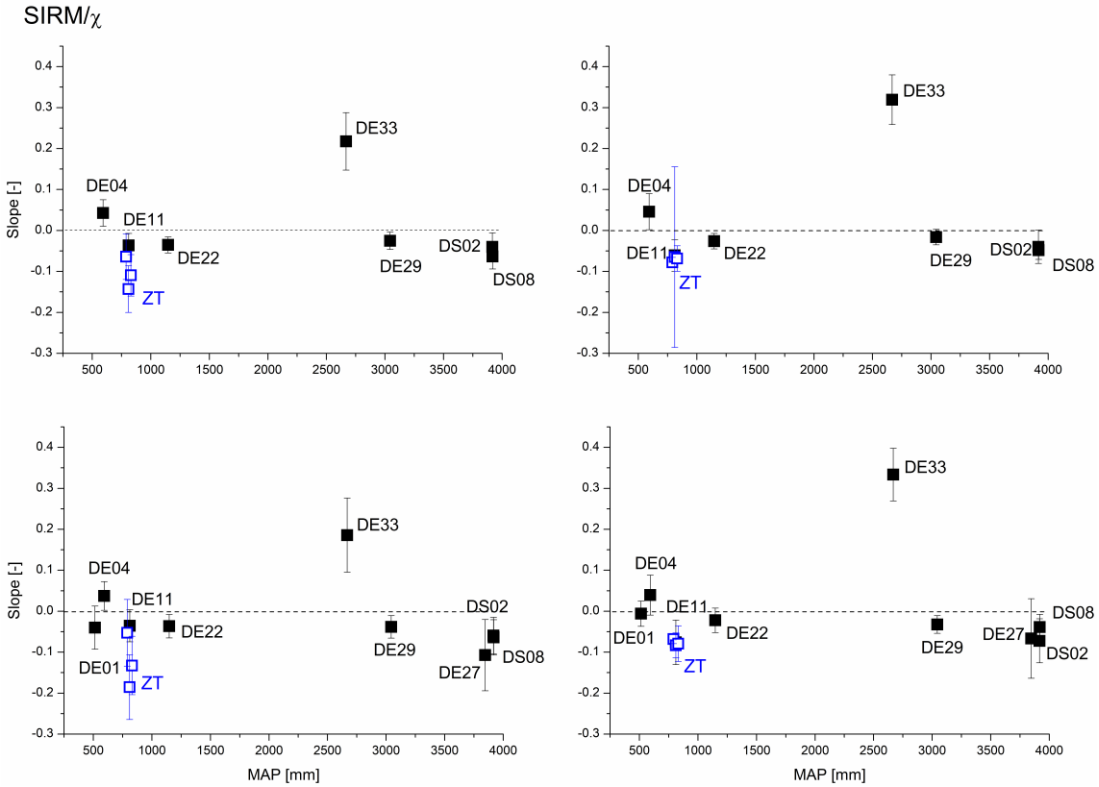

Figure B10. Slope values of *ARM/SIRM* sample sets with linear regression analysis for the different groups of fresh rock (FR) and weathered pebble (WP1 to 5).

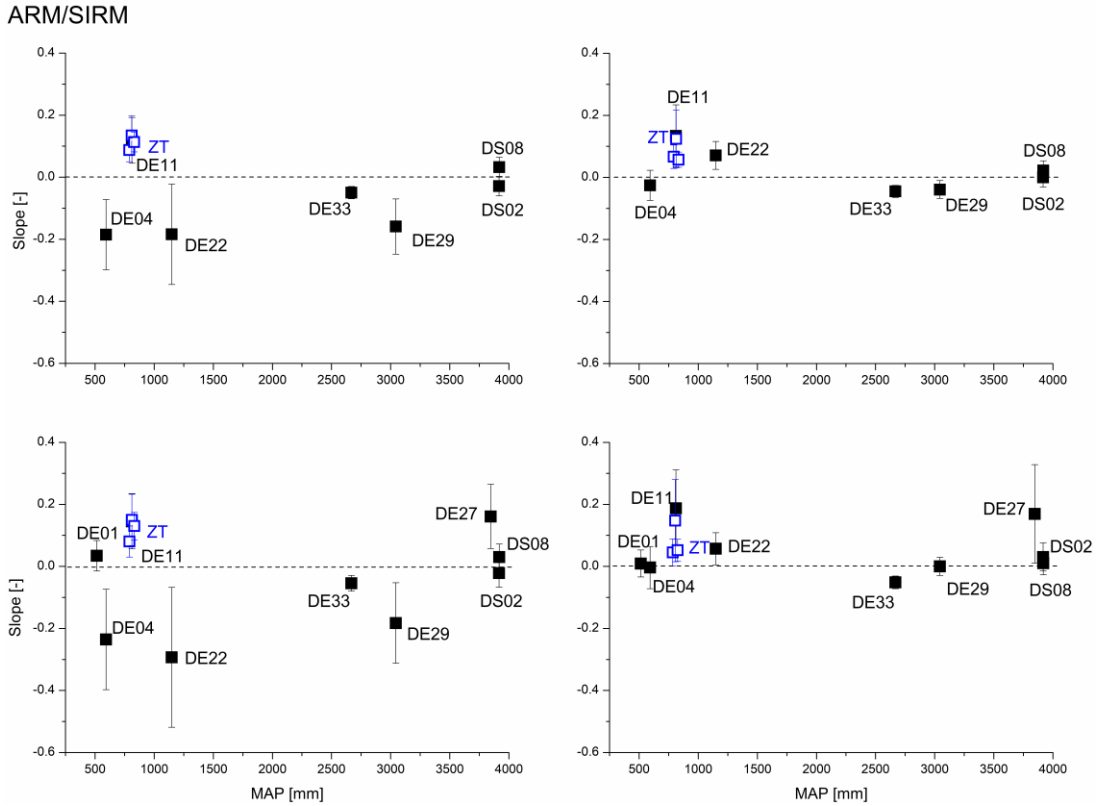

Chapter V: Nano-magnetite aggregates in red soil on low magnetic bedrock, their change during transport and implications for paleoclimate studies

Author	**Author position**	**Scientific ideas %**	**Data generation %**	**Analysis & interpretation %**	**Paper writing %**
Qi Zhang	1	40	60	35	60
Erwin Appel	2	30	-	30	40
Shouyun Hu	3	30	-	5	-
Robert Pennington	4	-	10	5	-
Jannik Meyer	5	-	5	5	-
Udo Neumann	6	-	5	5	-
Michael Burchard	7	-	5	5	-
Frederik Allstädt	8	-	5	5	-
Longsheng Wang	9	-	5	-	-
Andreas Koutsodendris	10	-	5	5	-
Status in publication process:			Accepted		

Nano-magnetite aggregates in red soil on low magnetic bedrock, their change during transport and implications for paleoclimate studies

Qi Zhang[1], Erwin Appel[1], Shouyun Hu[2], Robert S. Pennington[3,4,5], Jannik Meyer[3,4], Udo Neumann[1], Michael Burchard[6], Frederik Allstädt[6], Longsheng Wang[7], Andreas Koutsodendris[6]

[1]*Department of Geosciences, University of Tübingen, Hölderlinstr.12, 72074 Tübingen, Germany*

[2]*Nanjing Institute of Geography and Limnology, Chinese Academy of Sciences, 73 East Beijing Rd, Nanjing 210008, China*

[3]*Institute of Applied Physics, University of Tübingen, Auf der Morgenstelle 10, 72076 Tübingen, Germany*

[4]*NMI Natural and Medical Sciences Institute, University of Tübingen, Markwiesenstr. 55, 72770 Reutlingen, Germany*

[5]*Department of Physics, Humboldt-Universität zu Berlin, Newtonstr. 15, 12489 Berlin, Germany*

[6]*Institute of Earth Sciences, Heidelberg University, Im Neuenheimer Feld 234–236, 69120 Heidelberg, Germany*

[7]*Coast Institute, Ludong University, Yantai 264025, China*

Abstract

Soil and lake sediments are important paleoclimate archives often forming a source-sink setting. To better understand magnetic properties in such settings, we studied red soil on low-magnetic bedrock, and sub-recent sediments of Caohai Lake (CL) in Heqing Basin (HB), China. Red soil is the only important source material for the CL sediments, it is highly magnetic with susceptibilities (χ) of ~10^{-5} m^3/kg. The red soil is dominated by pedogenic nano-magnetite (~10-15 nm) arranged in aggregates of ~100 nm, with particle interaction that causes a wide effective grain size distribution in the superparamagnetic (SP) range tailing into stable single-domain (SSD) behavior. Transmission electron microscopy and broadband-frequency χ(f) suggest partial disintegration of the aggregates and increased alteration of the nanoparticles to hematite during transfer of red soil material to CL. This shifts the domain state behavior to smaller effective magnetic grain sizes, resulting in lower χ_{fd}% and χ values, and a characteristic change of χ(f). The SP-SSD distribution of the aggregates in red soil could be climate-dependent, and the ratio of saturation remanence to χ is a potential bedrock-specific paleoclimate proxy reflecting it. Magnetic properties of the CL sediments are controlled by an assemblage of nanoparticle aggregates and larger sized bedrock-derived magnetite. The results challenge the validity of the previous paleoclimate interpretation from the 168-m long Core-

HQ (900-30 ka) in HB. Disintegration of aggregates could lead to SP behavior with low χ_{fd}% without extinction of individual magnetite nanoparticles, and the χ_{fd}%-based assumption of SP magnetite dissolution may be wrong.

1. Introduction

Soil properties can serve as an important indicator for paleoclimate conditions (Tabor & Myers, 2015). Soil also contributes as source material for basin deposits such as lake sediments (Lavrieux et al., 2019). In settings where the catchment is well-defined and where soil is the major source for lake sediments, the relationship between the source (soil) and the sink (lake sediment) can be systematically studied.

Lake sediments are important paleoclimate archives (Gasse et al., 1991; An et al., 2011; Koutsodendris et al., 2018). Magnetic properties were often used to deduce information on paleoenvironmental conditions and processes (Peck et al., 1994; Geiss et al., 2003; Hu et al., 2015). The origin of ferro(i)magnetic minerals in lake sediments are either detrital or authigenic. Magnetic minerals from the catchment transported to lakes by surface water or wind may reach their sink without notable changes, but often they are subjected to alteration such as change or fractionation of grain size, and mineral transformation (Oldfield et al., 1985; Snowball et al., 1993). Ferro(i)magnetic minerals can form authigenically in lake sediments by inorganic processes (Maher et al., 1988) or through bacterial activity (Kodama et al., 2013). Biomineralization also happens in soil, forming magnetosomes (Fassbinder et al., 1990) and extracellular magnetite (Maher, 1998). The complexity of magnetic mineral sources and the possible change of their properties during transport and residence time in lake sediments are a great challenge when using magnetic properties as paleoenvironmental proxy. Environmental magnetic studies of lake sediments mostly focus on proxies recorded in drill cores, whereas the catchment is less considered. However, knowledge of materials and processes in the source area can provide a better understanding of response mechanisms to paleoclimate conditions, and therefore allow better-founded interpretations of lake sediment records.

Heqing Basin (Fig. 1) in Yunnan province (SW China) is an example of thick lacustrine sediments deposited in a basin-wide paleolake that existed from 2.78 Ma until sub-recent (An et al. 2011, Deng et al., 2019). It represents an important terrestrial archive for studying Indian monsoon evolution in the southeastern margin of the Tibetan Plateau (An et al., 2011; Hu et al., 2015). Hu et al. (2005, 2015) interpreted magnetic properties of a 168-m deep lacustrine drill

core (Core-HQ; Fig. 1) in terms of paleoclimate evolution since ~900 ka until the large lake drained at ~30 ka. They identified magnetite, maghemite and hematite as the main ferro(i)magnetic components and concluded that the variation in the sediment magnetic properties is mainly controlled by low-temperature oxidation of magnetite (maghemitization) and transformation of magnetite to hematite. Hu et al. (2015) also noted that superparamagnetic magnetite that dominates the highly magnetic red soil all around the basin is practically absent in Core-HQ. They speculated that the superparamagnetic magnetite in the red soil was lost during transport due to dissolution in surface water, and concluded that the detrital fraction inherited from the very low-magnetic bedrock in the Heqing Basin catchment dominates the magnetic properties of the lacustrine deposits in Core-HQ.

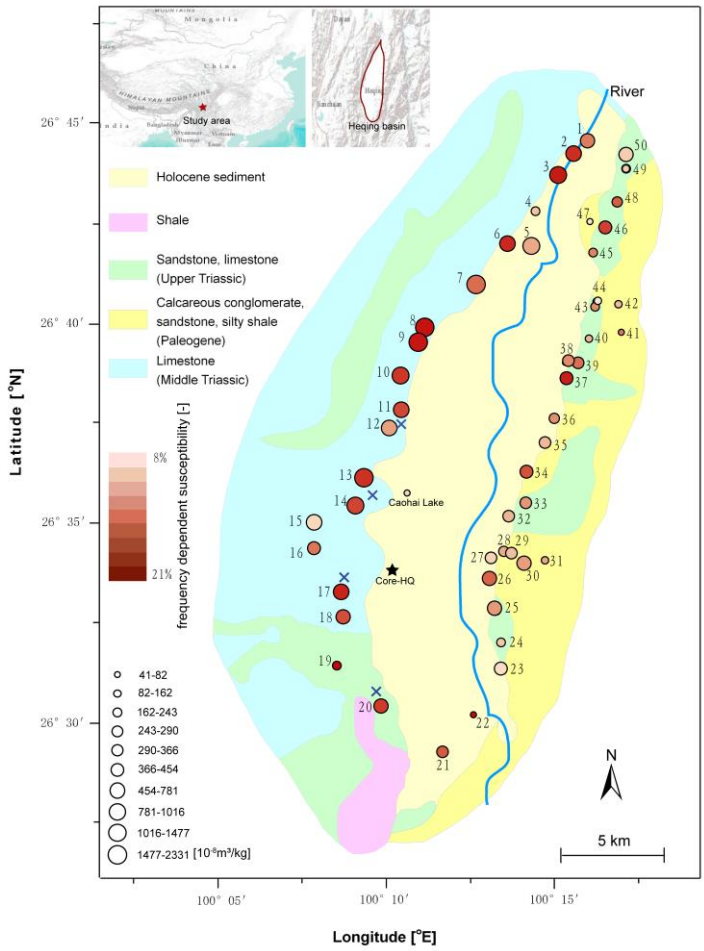

Figure 1. Mass-specific magnetic susceptibility (χ) and percentage frequency-dependence of susceptibility (χ_{fd}%) of red soil samples distributed around the basin (for data see Table 1 and Table S1), visualized by circle size (χ) and fill color (χ_{fd}%). The locations of Core-HQ and Caohai Lake are shown and labeled (referring to site-specific data in Table S1), and sampling sites of limestone bedrock fragments are marked by crosses. Map modified from Hu et al. (2015).

Red soil is a common soil type in subtropical China (He et al., 2004) and in other subtropical and tropical parts of the world (Yaalon et al., 1997; Bronger et al., 1997). In China, it developed since the mid-Pleistocene during warm and humid periods (Wang et al., 2013). Highly magnetic red soil is found above strongly magnetic basalt (Liu et al., 2017), but also on low-magnetic sedimentary bedrock (Lu et al., 2012; Khadkikar & Basavaiah, 2004). Magnetic properties of red soil are climate sensitive (Liu et al., 2012; Wang et al., 2013; Yin et al., 2018), and the soil may also serve as important source material for lake sediment archives as in Heqing Basin. Using magnetic properties as paleoclimate proxies in the context of such scenarios requires an understanding of the formation and characteristics of pedogenic ferro(i)magnetic minerals, as well as subsequent alterations that occur during transport, deposition and diagenesis.

Heqing Basin is not only a suitable target for investigating the magnetic signature of modern red soil, but also for assessing its spatial variability as a function of bedrock lithology and the possible change of magnetic properties during relocation of soil material. As exclusively very low-magnetic bedrock occurs in the Heqing Basin catchment, and the highly magnetic soil cover is widely distributed, it is expected that the magnetic properties of lake sediments in the basin are dominated by material derived from red soil. In consideration of the favorable setting, we performed a study in Heqing Basin, investigating in detail the magnetic characteristics and spatial variability of red soil in the catchment, and comparing its magnetic signature with sub-recent lake sediments of a small modern lake in the basin (Fig. 1).

2 Samples and Methods

2.1 Geological setting and sampling

Heqing Basin is situated at about 2200 m above sea level. Present-day climate conditions are subtropical, mean annual temperature and precipitation are 13.5 °C and ~1000 mm, respectively, with strong seasonality in humidity due to monsoon-related major rainfall in the summer months (Xiao et al., 2010). Rock types around the basin (Fig. 1), forming the main sources of detritus for lakes in the basin, consist of very low-magnetic limestones at the western side of the basin, sandstone and conglomerates (composed of sandstone and limestone) at the eastern side, and some shales at the southwestern basin margin (Yang et al., 2009). All around Heqing Basin, the bedrock is covered by red soil with thicknesses of some ten centimeters to few meters. The red soil is undoubtedly formed in situ as there is a gradual transition of the soil into the bedrock, which is also described for southwestern China in general (Feng et al., 2009).

Caohai Lake (26°35'43''N, 100°11'04''E) (lake area 1.8 km^2) is the largest of few small modern lakes in the basin, with shallow water depth (~1 to 2 m) and about half meter of sediments. The lake sediments formed above the fluvial sediments that were deposited after the termination of the large Heqing paleo-lake. According to the positions of Caohai Lake and the Core-HQ drilling site (Fig. 1), it is expected that sediments for both Core-HQ and Caohai Lake mainly derived from the limestone terrain at the western basin margin.

We studied samples from the red soil and the Caohai Lake sediments, and from the bedrock. In 2016-2019, we collected red soil of the uppermost ~10 cm from a total of 45 sites all around the basin, avoiding possible anthropogenic influence; additionally, we included the results of five samples published by Hu et al. (2015). At three sites at the western basin we collected soil material from short (5 cm) vertical sections, in particularly discriminating between loose material at the surface (carefully sampled with a soft brush) and underlying compact soil. In addition, we sampled limestone fragments from four sites at the western basin margin (Fig. 1). To compare properties of red soil with a sink of red soil material, we recovered three sediment cores from Caohai Lake penetrating through the entire sediment thickness (~0.5 m) using a gravity corer.

In the lab, we cut the cores into sub-samples at intervals of 1 cm, then air-dried and sieved the sample material. All red soil and lake sediment samples were placed in 2x2x2 cm cubic plastic boxes (weighed for determining mass-specific magnetic parameters), which were used for most measurements. For part of the analyses smaller sub-samples were used. Some of the analyses were performed with magnetic extracts. We prepared the extracts by mixing several samples of the same type, sieved the material through a 74-μm wire mesh, stirred it in about one-liter Milli-Q water adding a deflocculant to suppress clumping of clay, and dispersed the suspension for several minutes in an ultrasonic bath while continuing stirring. Taking about 0.5 l of the obtained suspension and putting it in a magnetic stirrer (HI190M) at ~500 rpm, we performed magnetic separation for about two hours, using a separate latex-covered cylindrical magnet (length/diameter 20/12 mm) with relatively weak magnetic moment (20 mAm^2) for extraction. The material was collected several times during this procedure, and before removing the latex cover from the magnet, the extracted material was carefully flushed with Milli-Q water to wash out clay minerals.

2.2 Magnetic measurements

In the field we used an SM30 sensor (ZH Instruments) to quickly obtain magnetic susceptibility values from the red soil and the bedrock for overview. All laboratory magnetic measurements were carried out at University of Tübingen, Germany, Department of Geosciences. We determined susceptibility with an MFK-1 Kappabridge (Agico), normalized the results to mass-specific values (χ), and calculated the percentage frequency-dependence of χ (χ_{fd}%) by [(χ_{lf} - χ_{hf})/χ_{lf}]x100 (Dearing et al.,1996), χ_{lf} and χ_{hf} representing readings at frequencies of 976 Hz and 15616 Hz. Additionally, we measured the broadband-frequency dependence at eight frequencies between 125 Hz and 16 kHz with an SM150L device (ZH Instruments). Using an KLY-3 Kappabridge combined with a CS-3 furnace and a CS-4 cryostat (Agico), we obtained low-temperature and high-temperature thermomagnetic curves of magnetic susceptibility (χ-T curves) for sample masses of ~0.15 g, warming the sample from liquid nitrogen to room temperature and heating it to 700 °C in argon atmosphere, respectively.

We obtained anhysteretic remanent magnetizations (ARM) using a DC-SQUID magnetometer (2G Enterprises) with attached degausser and DC coil, superimposing a 50 µT DC field and a decaying alternating field (max. 100 mT). Subsequently, we imparted an isothermal remanent magnetization (*IRM*) at a 2 T field with an MMPM9 pulse magnetizer (Magnetic Measurements), which we consider as saturation *IRM* (*SIRM*), then applied a 300 mT reverse field ($IRM_{-0.3T}$), and calculated the *HIRM* (high-coercivity *IRM*) by [(*SIRM*+$IRM_{-0.3T}$]/2 and an S-ratio by [1- $IRM_{-0.3T}$/*SIRM*]/2 (Bloemendal et al., 1992). For selected samples, we obtained detailed IRM acquisition curves with 46 steps up to 2.0 T and applied unmixing with log-normal distributions using the MAX UnMix routine of Maxbauer et al. (2016). For some samples the *SIRM* was thermally demagnetized in a TD48 (ASC Scientific) furnace. All *IRM* intensity measurements were performed with a Minispin spinner magnetometer.

Using small sub-samples of ~0.01 g, we obtained hysteresis curves and backfield curves on an PMC MicroMag 2900 AGM (Lake Shore Cryotronics). We analyzed these results in terms of magnetic domain state properties using the Day diagram (Day et al., 1977) and mixing curves of Dunlop (2002). For some samples, we measured first-order reversal curves (FORC) using the MicroMag AGM and processed these results with the software FORCinel (Harrison & Feinberg, 2008).

Moreover, we subjected ten samples to citrate-bicarbonate-dithionite (CBD) treatment, which removes a large part of fine iron oxide particles in the samples (Hunt et al., 1995). Before the treatment, we gently grinded and sieved the samples through a 74-µm mesh. The further

experimental procedure followed the method of Mehra and Jackson (1960) and processing of van Oorschot and Dekkers (1999); a detailed description of the CBD-treatment is given in Supporting Information. Using ~3-4 g, we measured χ-values and χ-T curves of the same sample before and after CBD treatment.

2.3 Non-magnetic analyses

We performed high-resolution imaging of the magnetic extracts by transmission electron microscopy (TEM), using a JEOL ARM-200F TEM operated at 200 kV equipped with a cold field emission gun, a CEOS probe corrector for spherical aberrations, and a Gatan Quantum electron energy loss spectrometer (EELS) with DualEELS capability. Samples were prepared by putting droplets from suspension on carbon-coated copper grids. For TEM observation of original red soil, we put material into alcohol, shaking it carefully to avoid changes of the original texture, before taking droplets. Core-loss EELS spectroscopy was used to identify magnetite (or maghemite) and hematite by examining both the core loss peaks and the related energy-loss near-edge structure (ELNES). Spatial elemental mapping was done using spectrum imaging (SI) combining EELS spectroscopy and scanning transmission electron microscopy (STEM) imaging modes; reciprocal-space information was obtained from both Fourier-transformed high-resolution STEM/TEM images and from diffraction-mode data.

For detecting larger ferro(i)magnetic minerals, we carried out reflected light microscopy (at University of Tübingen, Department of Geosciences) with oil immersion objectives on embedded polished samples prepared from magnetic extracts. For identifying strong magnetic phases, we used ester-based ferrofluid on the sample surface covered with a glass slip.

X-ray diffraction (XRD) analysis of the magnetic extracts was performed using a Bruker D8 ADVANCE Eco diffractometer with a Cu Kα tube (40 kV, 25 mA) and an LYNXEYE 1-D SSD160 detector. The samples were measured with an angular range of 5° to 80° 2Θ, an increment of 0.02° and a measurement time of 1 s per step. Total time of all detector pixels sum up to 160 s measurement time per step 2Θ; samples used for quantitative analyses were measured until the strongest peak reached at least 40,000 counts. The X-ray powder diffraction data were evaluated using DIFFRAC.EVA V4.2 and Diffrac.TOPAS V5 with an ICSD database. Refined parameters of the Rietveld analysis are background parameters, zero-error, sample displacement error, scaling factors, cell parameters, crystallinity and preferred orientation values of all phases except nano-crystalline kaolinite. The parameters of nano-

crystalline kaolinite were refined only in an early stage of the analysis and then fixed to stabilize the optimization process.

Bulk sediment samples were scanned with an Avaatech (GEN-4) X-ray fluorescence (XRF) core scanner, using a Rh anode X-ray tube following the protocol of Kern et al. (2019). Prior to scanning, about 0.5 g of bulk sediment was placed in a Micro X-Cell® and was covered with 4-µm-thick Ultralene® foil. Measurements were carried out at 10 kV without a filter and a current of 1000 mA, and at 30 kV with a Pd-thick filter and a current of 2000 mA. Counting time was 30 seconds, and the slit size was 3x3 mm. Data processing of the X-ray spectra was performed using the bAxilBatch software (Version 1.4, July 2016; www.brightspec.be). Single element counts were normalized to total counts.

To analyze the organic matter content, the loss on ignition (LOI) method after Dean (1974) and Bengtsson (1986) was applied, in which weight loss is measured after heating. About 1 g of homogenized dry material was put in crucibles and heated in a ROHDE TC304 muffle furnace at 550 °C for four hours to combust organic matter to ash and CO_2 (Heiri et al., 2001). From the dry weights before and after the combustion (DW and DW_{550}) the LOI_{550} is obtained by $100x(DW-DW_{550})/DW$ (Heiri et al., 2001).

For two red soil and three lake sediment sample sets (mixed from several samples), we determined the content of dissolved organic carbon (DOC) with a TOC analyzer (Elementar, highTOC II, version “L”), and the inorganic carbonate ($CaCO_3$) by titration with NaOH, after digestion with 0.8 % HCl.

The TEM studies were carried out at the NMI Reutlingen; XRD, XRF and DOI analyses were done at Heidelberg University, Germany (Institute of Earth Sciences); organic and inorganic carbon contents were measured at University of Tübingen, Germany (Department of Geosciences).

3 Results

The experimental results comprise the identification of ferro(i)magnetic minerals (section 3.1), their grain size and magnetic domain state (section 3.2), and the determination of the spatial (red soil) and vertical (lake sediments) variabilities of magnetic parameters (section 3.3). Means and standard deviations are listed in Table 1, and for detailed sample results see Tables S1-7 in Supporting Information.

3.1 Magnetic mineralogy

χ-T curves (Fig. 2a) allow the identification of ferro(i)magnetic phases by their Curie temperature and other typical phase transitions. The measured high-temperature χ-T runs are partly compromised by the formation of new magnetite starting around 400-450 °C during heating. Despite this effect, the shape of the heating curves together with the single Curie temperature observed at ~580 °C prove the existence of magnetite in both the original red soil and lake sediment materials. The low-temperature χ-T dependence does not show the Verwey transition of magnetite. Non-stoichiometry induced by low-temperature oxidation is known to suppress this transition at an already low degree of oxidation (Aragón et al., 1985).

A striking feature of the red soil results is the increase of χ-values between -196 °C and ~250 °C with a hump and subsequent decrease. This effect is also seen in the χ-T curves of the lake sediments, however, less pronounced. At a first glance, partial heating-cooling curves (Fig. S1) to subsequently increasing maximum temperatures of about 210 °C, 250 °C and 280 °C look irreversible and seem to indicate destruction of maghemite during heating as it is often argued in literature (Bilardello & IRM, 2020). In fact, this might be the case. Remarkably the χ-values in the cooling curves of the first two runs return to about the starting value before heating, which is incompatible with maghemite destruction. The increase and hump could be alternatively explained by fine magnetite particles, which show a typical maximum-type χ-T dependence when transforming from stable single domain (SSD) to the superparamagnetic (SP) state (see review in Bowles et al., 2009). For magnetite the SP-SSD transition is at ~25 nm (Worm, 1998). A broad hump will result from superposition of fine magnetite particles with different grain sizes and therefore different SSD-SP transition temperatures. We interpret the apparent irreversible behavior in the χ-T curves as thermal hysteresis residing in fine particle behavior, which so far seems unrecognized in rock magnetism, however, such kind of magnetocaloric effects are reported in literature related to technical applications (Souza et al., 2019). After the CBD treatment, which destroyed a large fraction of fine magnetite particles (but not all), the hump is less distinct for red soil and no more detectable for lake sediments.

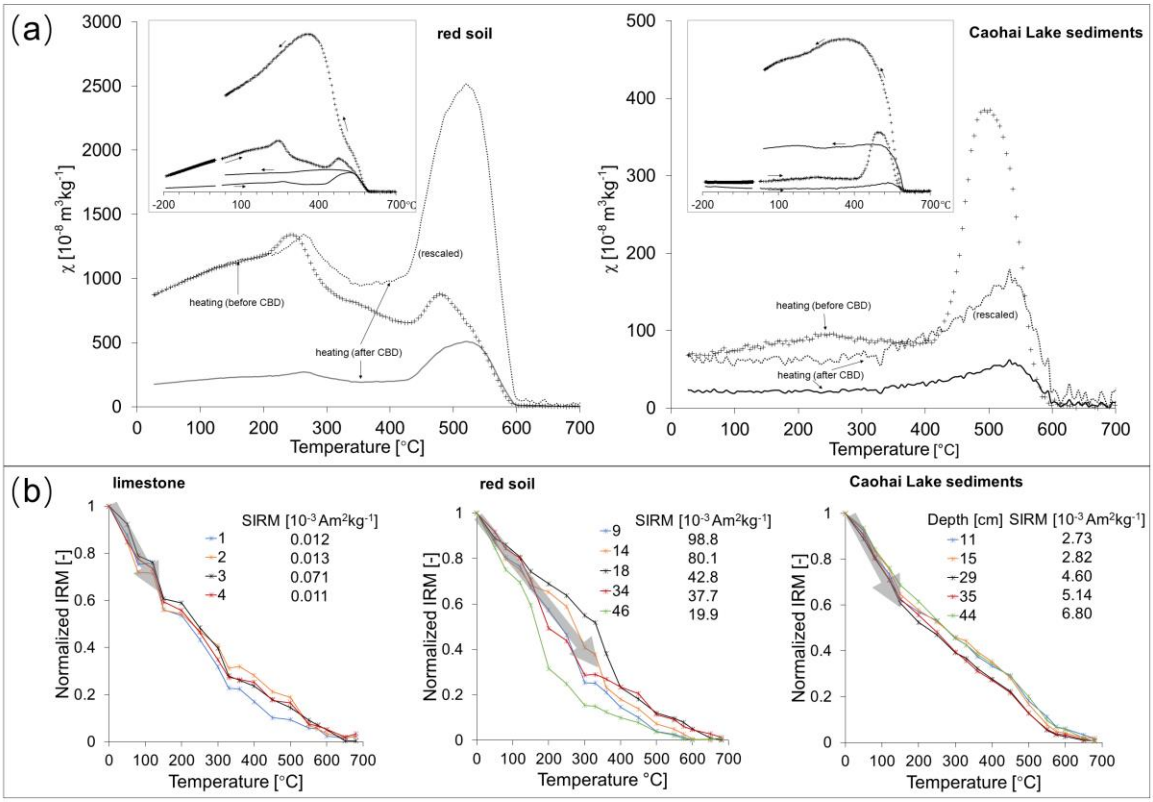

Figure 2. (a) χ-T curves for red soil and Caohai Lake sediments(out of 5 measured samples for each) of magnetic susceptibility (χ) before and after citrate-bicarbonate-dithionite (CBD) treatment, and (b) SIRM thermal demagnetization (all measured samples) for limestone, red soil, and Caohai Lake sediments (starting values of SIRM are listed and labeled; for red soil numbers relate to sites in Fig. 1, for the lake sediments numbers are depth levels). Large plots in (a) show heating curves with absolute χ-values (bold curves); rescaled curves are post-CBD results normalized to the starting value of the pre-CBD curves (allowing better comparison of their shapes); the smaller plots in (a) show heating and cooling runs, together with low-temperature χ-T results; partial heating-cooling curves for red soil are shown in Supporting Information (Fig. S1). Gray arrows in (b) indicate pronounced IRM intensity loss.

A distinctly stronger drop of the remanence intensity close to 580 °C in thermal demagnetization curves of *SIRM* (Fig. 2b) suggests the presence of magnetite in all samples, including the limestone bedrock despite its weak *SIRM*. Moreover, the presence of hematite is evidenced for all measured lake sediment samples and part of the red soil samples, shown by a residual remanence beyond 580 °C that is demagnetized until 700 °C.

XRD results for magnetic extracts from both red soil and lake sediment material confirm the presence of magnetite and hematite (Fig. 3). The diffraction peaks are shifted to larger 2Θ-angles than expected for stoichiometric magnetite, corresponding to a lattice constant of 0.833 nm (Rietveld analysis of the red soil extract), which indicates a strong degree of

maghemitization (Readman and O'Reilly, 1972). The strong degree of maghemitization, as documented by the XRD results of the red soil sediment material, implies a transition process from magnetite to (potentially tetragonal) maghemite, which we will further discuss in section 4.1. The XRD result of the original red soil allows to estimate the content of hematite (~5 vol.%), while magnetite is below the detection limit. The hematite peaks are close to pure α-Fe_2O_3, which means that Al-substituted hematite that is often found in soil (Jiang et al., 2012) is of minor importance in our samples. The cell volume (0.3013 nm^3) determined from the Rietveld fit corresponds to an Al_2O_3-content of 1-3 vol.% according to the cell parameters of Feenstra et al. (2005) for Fe_2O_3-Al_2O_3 solid solutions. The mineral assemblages revealed by the XRD results show obvious similarities between red soil and lake sediment materials, indicating that there is a notable relationship between them. A difference is a strong XRD signal of calcite for the lake sediment extract, which is not appearing in the red soil result. Chemical analysis of inorganic carbonate yielded a much higher content in the lake sediment (~25 wt.%) compared to red soil (4-5 wt.%), which hints at a large amount of calcite that was directly transferred from weathered limestones to the lake, either by detrital input or authigenic precipitation of dissolved carbonate.

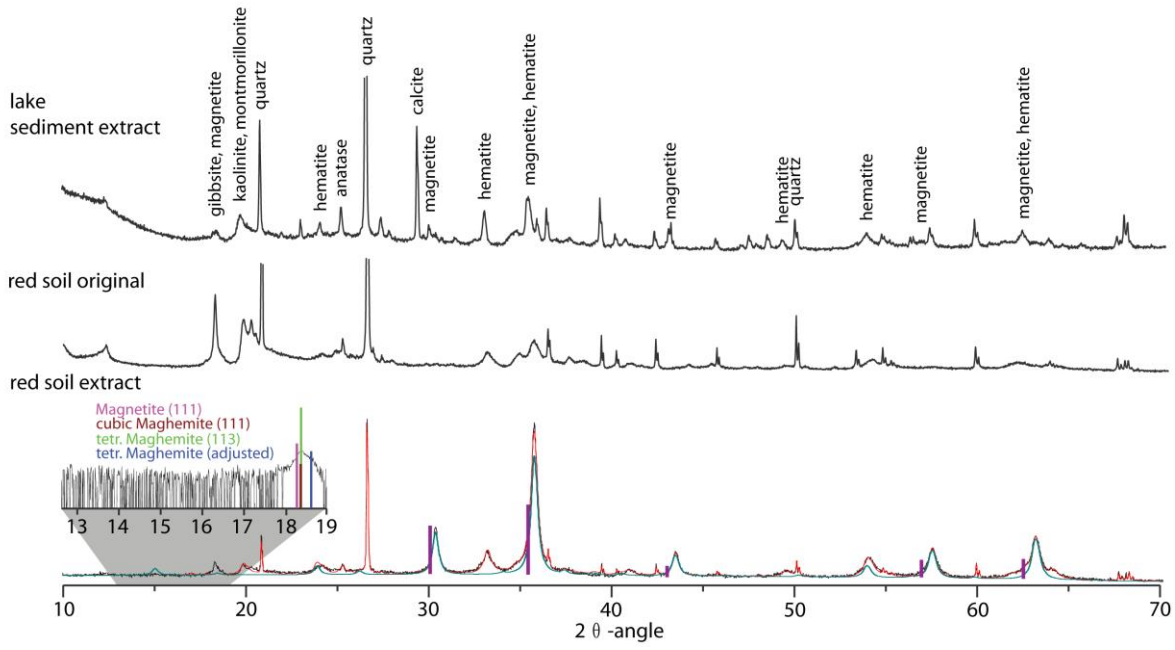

Figure 3. X-ray diffractograms of original red soil and for magnetic extracts of red soil and Caohai Lake sediments. Main peaks are labeled. For the red soil extract, a Rietveld model for 49.2 vol.% nano-maghemite (16 nm size; *a*=0.833 nm according to Pecharromán et al., 1995) is shown (green diffractogram). The entire model diffractogram (red) fitting the measured diffractogram involves the nano-maghemite, 12.6 % quartz, 15.8 % hematite, 8.1 % Illite, 10.9 % kaolinite, 2.1 % muscovite and

1.4 % anatase (all values vol.%). Purple bars show the expected positions of magnetite peaks (a=0.8397 nm according to O'Neill & Dollase, 1994). The inset plot above the red soil extract diffractogram shows a high-resolution measurement of this material for the 2Θ-range of 12.5-19°; vertical bars mark the position of theoretical magnetite and maghemite peaks. From the XRD result of the original red soil the hematite (a=0.5026 nm, c=1.377 nm, cell volume 0.3013 nm^3) content is estimated at ~5 vol.%.

3.2 Grain size of the magnetite fraction

The width of the magnetite (maghemite) diffraction peaks were modeled by a Rietveld fit (Fig. 3) using a crystal size of 16-nm (cube-shaped). Direct measure of the physical grain size results from TEM observations and optical microscopy. In the first set of TEM analyses we used magnetic extracts with an enrichment of magnetite to roughly 10-15 wt.% (estimated from χ-values).

TEM images (Figs. 4 and 5) reveal the presence of numerous up to >100 nm large aggregates of ultrafine particles with individual sizes of ~5-20 nm (mostly ~10-15 nm). High-resolution transmission electron microscopy (HRTEM) images (Figs. 4d and 5c) show coherent lattice structures across ~10-15 nm dimension. ELNES point-analysis along line scans (Figs. 4b,c and 5b) with a beam width of ~5 nm allows the discrimination between magnetite (or maghemite) and hematite by the existence (in case of magnetite or maghemite) or absence (in case of hematite) of a small peak or shoulder (marked by dashed boxes in Figs. 4e and 5d) in the O K-edge (Colliex et al., 1991; Golla-Schindler et al., 2006). We found that ELNES results are more useful for discrimination between magnetite/maghemite and hematite than power spectra of Fourier transforms because the determinative lattice spacings are not necessarily present in any particular high-resolution image due to orientation, and many reciprocal-space lattice spacings are similar between the materials. The ELNES characteristics of the red soil (Fig. 4e) clearly reveal magnetite (or maghemite) in the nanoparticles of the aggregates, and variable expression of the sensitive peak/shoulder indicates that some spots represent a significant contribution of hematite. Likewise, the nanoparticles in the aggregates of the lake sediments show ELNES patterns (Fig. 5d) typical for magnetite (or maghemite) and hematite. The discrimination between magnetite (or maghemite) and hematite is less clear than for the red soil sample, indicating a larger contribution of hematite than in red soil.

Results of reflected light microscopy (Figs. 4f and 5e) prove the additional presence of large detrital magnetite particles with grain sizes up to several tens of micrometer. Surfaces with

ferrofluid provide unambiguous evidence strong magnetic particles, and these particles could be identified as magnetite or maghemite by the appearance of magnetite-ilmenite exsolution structures and an isotropic behavior in crossed polarizers. Besides the magnetite (maghemite), oxidation to hematite (martitization) is observed in surface areas not covered by ferrofluid (optically anisotropic).

In order to check whether the aggregates of magnetite nanoparticles were formed by clumping during the magnetic extraction process, we performed a further TEM analysis using the original red soil material. No noteworthy differences between original red soil and magnetic extracts from red soil were found in the appearance of the aggregates (Fig. 6a). Within the aggregates, it's hard to distinguish individual particles, except through lattice fringes. HRTEM images (Fig. 6b, c) indicate that lattice fringes aren't aligned, suggesting that the particles didn't grow epitaxially. Around the aggregates we found splattered smaller crystalline particles (Fig. 6d), which are typically thinner in the interior than at the rim (identified by HAADF scanning mode). This observation might indicate that some parts of the aggregates fell apart. Such donut-like shapes unlikely represent minimum-energy structures, which means they didn't form as separate nanoparticles. Moreover, if the aggregates were formed during sample preparation, then particle splatter away from the aggregates too should be seen. Because of these observations, clumping of the magnetite nanoparticles during magnetic extraction or any other sample preparation process is unlikely, but the opposite, i.e., breakup of aggregates, might be the case.

After CBD treatment, the χ-values at room temperature decreased on average by 70.6 % for red soil and 55.1 % for lake sediments (Table S4). The CBD procedure efficiently dissolves fine magnetite particles smaller than about 1 μm, while larger particles are much less affected because of their smaller surface-to-volume ratio (Hunt et al., 1995). After CBD treatment, the hump in the χ-T curves is still clearer for red soil than for the lake sediments, which together with the larger decrease of χ-values indicate a higher proportion of fine magnetite particles in red soil. This is further confirmed by the χ_{fd}% values before and after CBD treatment (Table S4), which are quite stable for red soil (decrease of the mean from 18.5 % to 18.3 %) and decrease substantially for the lake sediments (from 12.9 % to 5.2 %). The CBD treatment dissolves SP particles efficiently, but not completely. According to the χ-decrease, about ~1/3 of the magnetite is still existing in the red soil after CBD treatment, and the rather unchanged χ_{fd}% proves that SP grains are still highly predominant after the CBD treatment. This means that larger multi-domain (MD) magnetite grains inherited from the bedrock contribute only very

little to the total magnetite content in the red soil. In the lake sediments, where the χ-decrease after CBD treatment is less and χ_{fd}% decreases significantly, the relative χ-proportion of SP magnetite compared to bedrock-derived larger grains is clearly lower than in red soil.

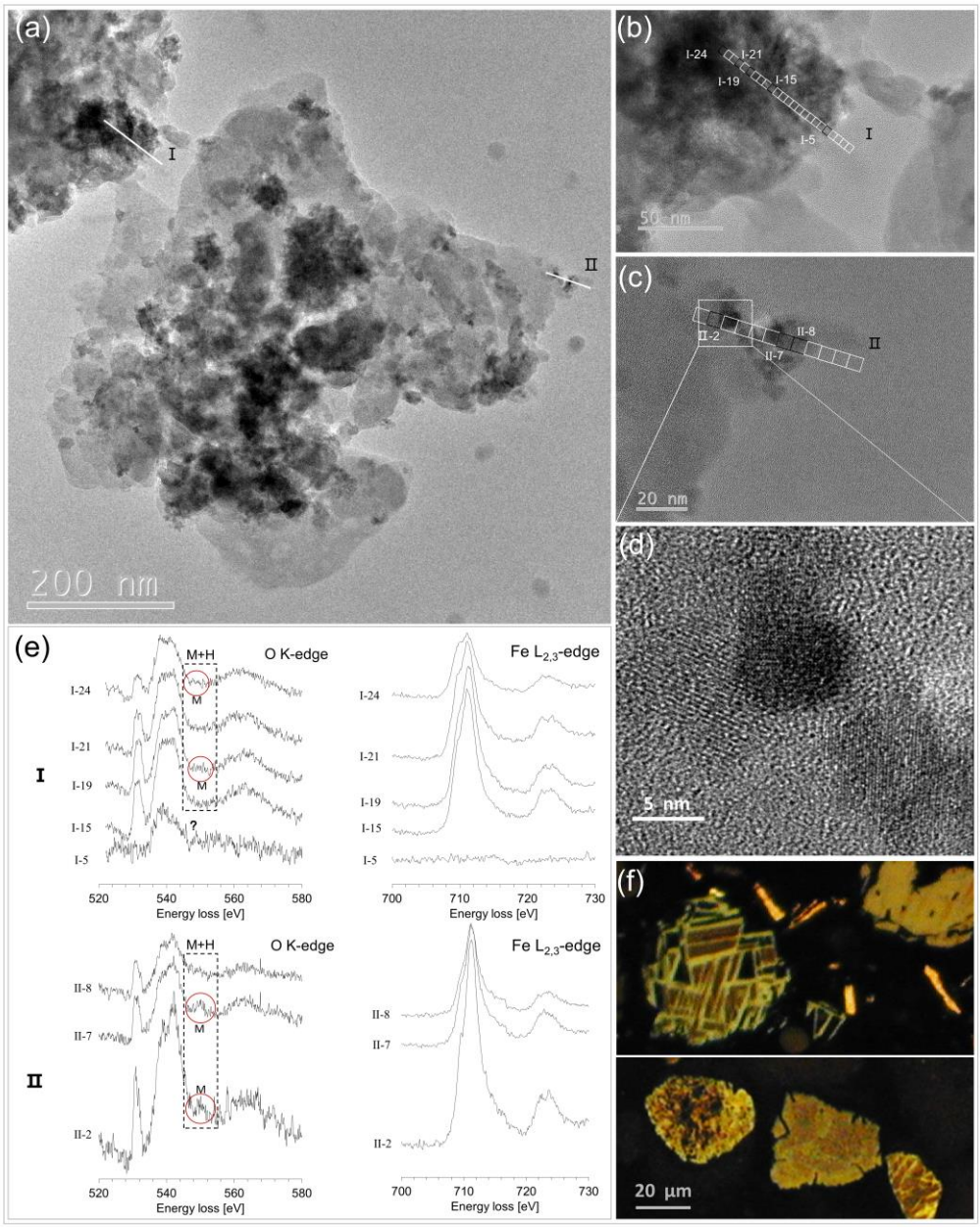

Figure 4. TEM images of the magnetic extract from red soil (a) with enlargements (b, c), showing aggregates of nanoparticles. The HRTEM image (d) shows coherency of lattice structures across ~10 nm. In (e) ELNES results of the O K-edge and Fe $L_{2,3}$-edge structures are shown for selected spots (marked in b, c) along two traverses (marked in a,b,c), identifying magnetite or maghemite (M) by a peak or shoulder in the O K-edge (clear magnetite-maghemite signals are marked by red circles within the dashed box); the additional contribution of hematite (H) is indicated by the variable expression of the peak. Unclear interpretation or absence of Fe-oxides is marked by "?". All other measured ELNES spectra from red soil are shown in Supporting Information (Figs. S2 and S3).

Reflected light microscopy images in (f) show several 10-µm large detrital magnetite particles (the dark brown ferrofluid cover evidences strong magnetic phases).

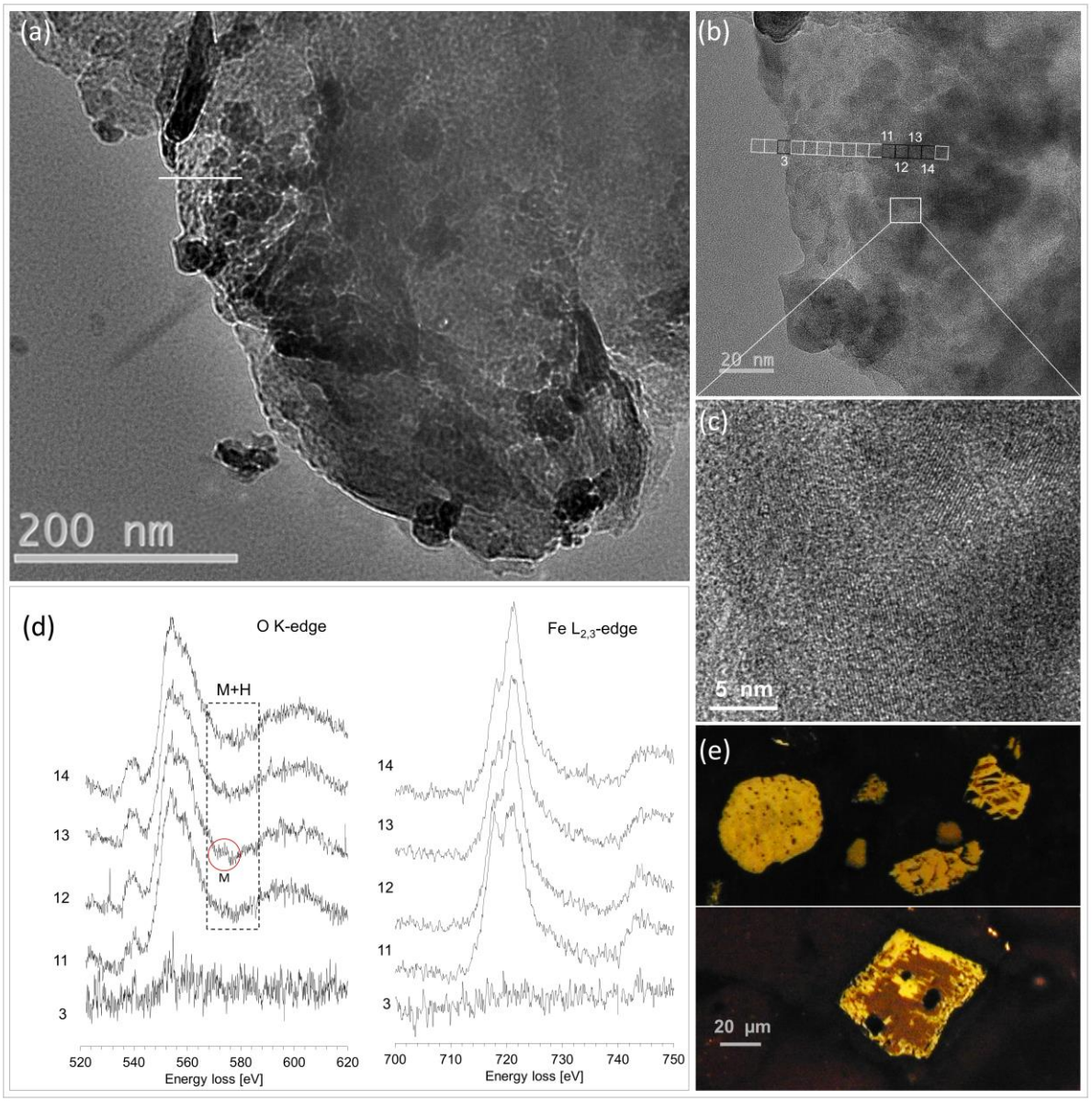

Figure 5. TEM images of the magnetic extract from lake sediments (a) with and enlargement (b), showing aggregates of nanoparticles. The HRTEM image (c) shows coherency of lattice structures across ~10 nm. In (d) ELNES results of the O K-edge and Fe $L_{2,3}$-edge structures are shown for selected spots (marked in b) along a traverse (marked in a, b), identifying magnetite or maghemite (M) and by a peak or shoulder in the O K-edge (clear magnetite-maghemite signals are marked by red circles within the dashed box); the additional contribution of hematite (H) is indicated by the variable expression of the peak. Unclear interpretation or absence of Fe-oxides is marked by "?". The EELS spectrometer was operated to capture two simultaneous core-losses in dual-EELS mode, thus the exact energy offset was not recorded and energy offsets between 6d and Fig. 4e are not interpretable. All other measured ELNES spectra from lake sediments are shown in Supporting Information (Fig. S4). Reflected

light microscopy images in (e) show several 10-µm large detrital magnetite particles (the dark brown ferrofluid cover evidences strong magnetic phases).

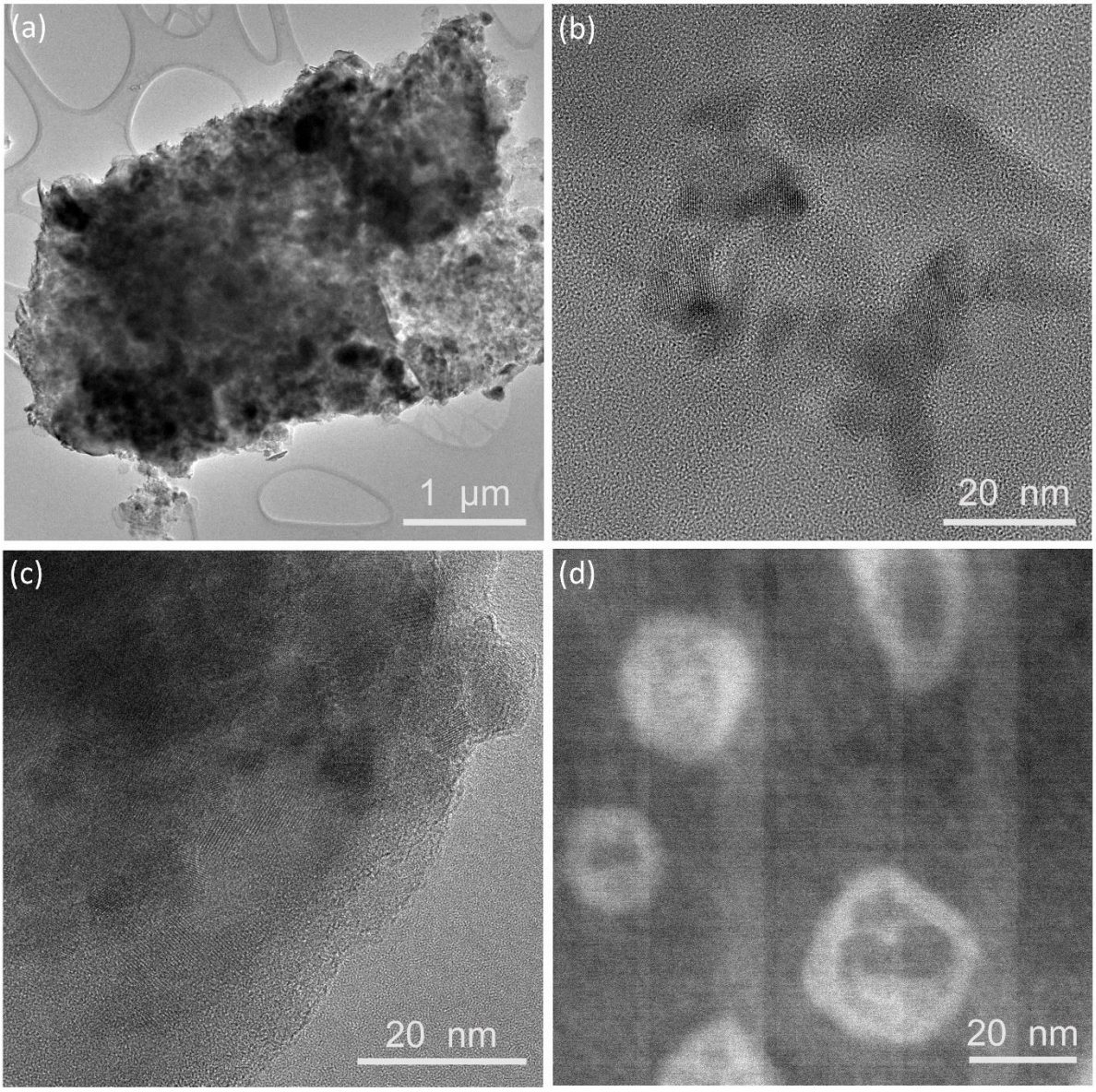

Figure 6. (a) TEM image of original red soil showing an overview of a sample patch with different particles, including numerous aggregates of nanoparticles. (b,c) HRTEM images of nanoparticle aggregates. The image in (d) obtained in high-angle annular dark-field (HAADF) scanning mode shows donut-like nanoparticles with thicker rims (lighter) and thinner interior, which were found splattering around aggregates.

The broadband-frequency results of χ between 125-16,000 Hz show a decrease of χ with frequency (f) (Fig. 7 and Table S5) as expected for superparamagnetic behavior. The shape of the χ(f)-dependence is related to the specific grain-size distribution of particles in the SP range, with larger SP particles showing a stronger χ(f) decrease at lower frequencies and vice versa (Kodama, 2013). It is obvious that the χ-log(f) dependence of the lake sediment samples with

lower susceptibility (lake sediments L) flattens in the lower frequency range. Calculating regression lines separately for the lower-frequency (0.125-1 kHz) and higher-frequency (1-16 kHz) parts allows a quantitative assessment of the χ-log(f) slopes in the two frequency ranges. For the red soil H samples, the slope at 0.125-1 kHz is slightly steeper than at 1-16 kHz. For the lake sediments L, it is the opposite and the slopes at 0.125-1 kHz and 1-16 kHz are different at a 95 %-confidence level (for statistical results see Table S6). This indicates a loss of SP behavior in the larger SP grain size range for the lake sediments, which we will elaborate further in the discussion.

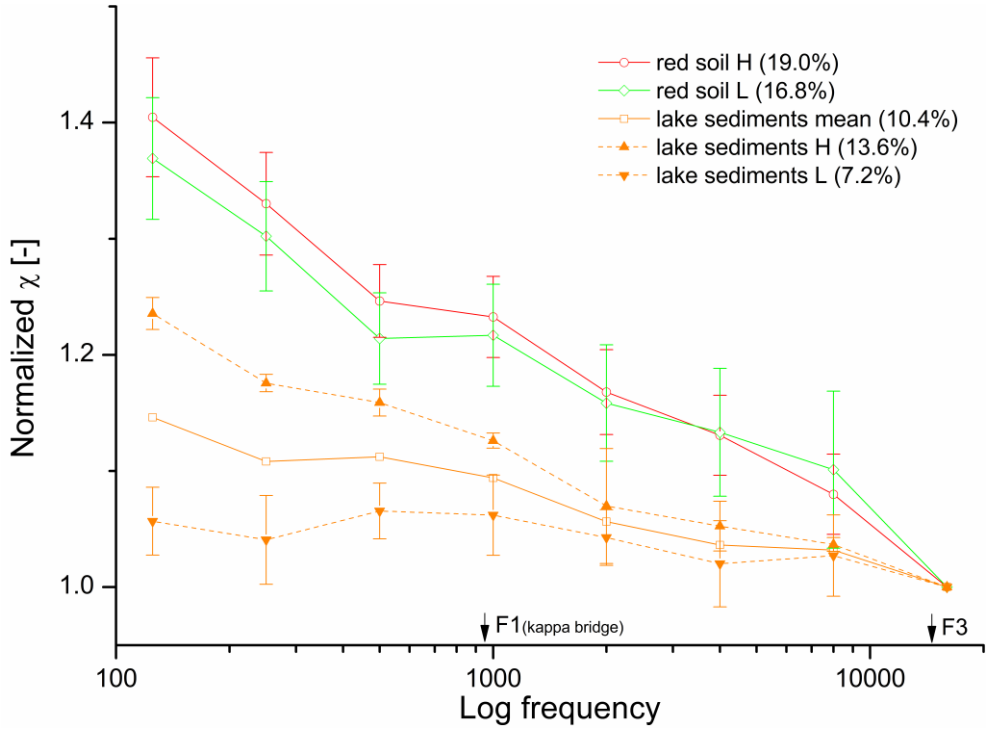

Figure 7. Broadband-frequency dependence of magnetic susceptibility for red soil (red: samples with $\chi>10^{-5}$ m^3/kg, green: samples with $\chi<10^{-5}$ m^3/kg; ten samples each) and Caohai Lake sediments (orange; broken curves represent samples with higher-H and lower-L χ-values taken from 31-35 cm and 9-13 cm depths, respectively; the full curve shows the means of both). For the full curves the mean values represent an average of ten samples, for the broken curves the mean is obtained from five samples. The χ-values were first normalized by their 16-kHz value, then means and standard deviations of the normalized values were calculated (thus the 16-kHz value has no standard deviation). The two frequencies used for the MFK-1 for determining (χ_{fd}%) of bulk samples are marked (F1, F3), and mean values of χ_{fd}% for the used samples are listed in the legend (in brackets). For detailed data see Table S5.

The IRM results provide information about the ferro(i)magnetic fraction in the SSD to MD state. During thermal demagnetization most of the remanence intensity is lost far below the Curie temperature of magnetite (Fig. 2b). This lower-temperature loss is much stronger in red

soil than in lake sediments (indicated by gray arrows in Fig. 2b). The decay of SIRM at low to medium temperatures likely reflects remanence unblocking of fine magnetite particles when they undergo the SSD-SP transition. This is in line with the interpretation of the hump in the χ-T curves (Fig. 2a) in terms of fine-particle behavior, and with the IRM unmixing results (Fig. S5). Values of B_h for the lower coercivity component range from few mT to several 10 mT. The lowermost B_h-values can be related to magnetite particles at the transition from SSD to SP, and the relatively higher B_h-values indicate magnetite with SSD behavior and/or larger magnetite particles in the MD range (which cannot be discriminated by *IRM* unmixing). For the limestone samples, only the relatively higher coercivity fraction is observed.

In the Day diagram, the data of the red soil and lake sediment samples plot in a region of mixed SP, SSD and MD particles (Fig. S6). Despite the criticism on the significance of the Day plot (Roberts et al., 2018), we think that the results can be considered as a rough estimate of similar portions of SSD and MD, plus a substantial SP contribution. The red soil samples from the western basin deviate most from the SSD-MD mixing line towards an increasingly larger SP contribution. The lake sediments plot closest to the SSD-MD mixing line indicating a relatively lower SP proportion. FORC diagrams (Fig. S6) support a wide grain size range of the fine magnetite fraction, but a conclusive comparison of red soil and lake sediments is not possible because the latter are too weakly magnetic to obtain meaningful FORC results without magnetic extraction.

3.3 Spatial and vertical magnetic parameter distribution of red soil and lake sediments

An overview of the spatial distribution of χ and χ_{fd}% for red soil is shown in Figure 1. Means and standard deviations are listed in Table 1 (site-specific data in Table S1), together with other parameters. All red soil samples show high χ-values, higher above the limestone bedrock at the western basin (ranging from 216×10^{-8} m^3/kg to 2331×10^{-8} m^3/kg, mean of 1085×10^{-8} m^3/kg) than above conglomerates and sandstones at the eastern basin (ranging from 60×10^{-8} m^3/kg to 751×10^{-8} m^3/kg, mean of 302×10^{-8} m^3/kg). Values of χ_{fd}% are much less different between the western (mean of 17.8 %) and eastern (mean of 15.1 %) sides of the basin.

The samples from the short surface-near vertical profiles taken at three sites were studied to check for possible differences between loose material at the surface (carefully sampled with a soft brush) and the underlying 5-6 cm of red soil. The χ-values of the surface samples and deeper levels do not differ systematically and the differences are within the range of surface χ-

variations measured in situ within an area of few m^2 (Fig. S7a, b). Likewise, χ_{fd}% values do not show a clear difference (Fig. S7a).

Table 1. Mean values with standard deviations for magnetic parameters from red soil and lake sediments.

	units	**Red soil W**	**Red soil E**	**Caohai sediments**
		(N=20)	**(N=30)**	**(N=44)**
χ	[10^{-8} m^3/kg]	1085.3 ± 579.5	302.0 ± 160.4	41.0 ± 15.1
χ_{fd}	[%]	17.8 ± 3.0	15.1 ± 3.1	10.6 ± 2.5
		(N=17)	**(N=28)**	**(N=44)**
SIRM	[10^{-3} Am^2/kg]	38.8 ± 17.6	18.3 ± 10.7	3.7 ± 1.1
HIRM	[10^{-5} Am^2/kg]	84.2 ± 62.3	110.4 ± 85.8	35.8 ± 11.7
S-ratio	[-]	0.98 ± 0.02	0.93 ± 0.07	0.9 ± 0.02
SIRM/χ	[kA/m]	4.2 ± 1.6	6.5 ± 3.1	9.4 ± 1.1
HIRM/χ	[kA/m]	0.12 ± 0.13	0.58 ± 0.92	0.94 ± 0.26
		(N=17)	**(N=28)**	**(N=13)**
$\mathbf{M_r/M_s}$	[-]	0.18 ± 0.01	0.20 ± 0.05	0.20 ± 0.04
$\mathbf{H_{cr}/H_c}$	[-]	2.82 ± 0.30	2.61 ± 0.45	2.47 ± 0.24

Note. Definition of parameters see Methods (section 2.2). N: number of samples included. Red soil separated into western and eastern basin sides. For detailed sample results see Tables S1-3 in Supporting Information.

Magnetic data and geochemical data of the Caohai Lake sediments versus depth are shown in Figure 8 and listed in Table 1 (for data see Table S2). Part of the magnetic parameter means from red soil are also plotted in Figure 8 for comparison. Compared to the red soil, the χ-values of the lake sediments are much lower (ranging from 20x10^{-8} m^3/kg to 61x10^{-8} m^3/kg, mean of 41x10^{-8} m^3/kg). They show an increase from ~15 cm downward and reach about twice as high values compared to the top part at ~30 cm. Values of χ_{fd}% are between 6.2 % and 14.2 %, (mean of 10.6 %) with downward increasing trend. The SIRM is relatively stable in the upper ~15 cm, increases gradually by a factor of about two at ~15-40 cm, and then shows a strong increase in the lowermost ~5 cm. The HIRM is only slightly increasing downward to ~40 cm, and then doubles within the lowermost ~5 cm.

The XRF data show two distinctive features in the downcore sediment geochemistry, i.e., a gradual increase in the Fe/Mn ratio towards the top of the sequence and pronounced increases in the Fe/Ti and Si/Ti ratios, and the S and Br counts in the uppermost 10 cm, with a drop of these values for the topmost samples, in particular for Fe/Mn, S and Br. The LOI that is a proxy of the organic carbon content follows the vertical trend of the various XRF results also shows a distinctive drop at the top. Organic carbon (OC) analyses of mixed samples from three

different depth intervals confirm the trend of the LOI values (Fig. 8). The OC contents range between 2.2 and 5.0 wt.%, which is relatively low for lake sediments, and not much higher than in the red soil (2.1 and 3.4 wt.% for two samples analyzed). From comparison of data in Figure 8, we notice that the increase of the geochemical parameters occurs at a clearly shallower depth as for the magnetic parameters χ and χ_{fd}%. In the discussion, we will assess the relationship of magnetic and geochemical in terms of possible solution of Fe-oxides based on the significance of the geochemical parameters for reductive conditions.

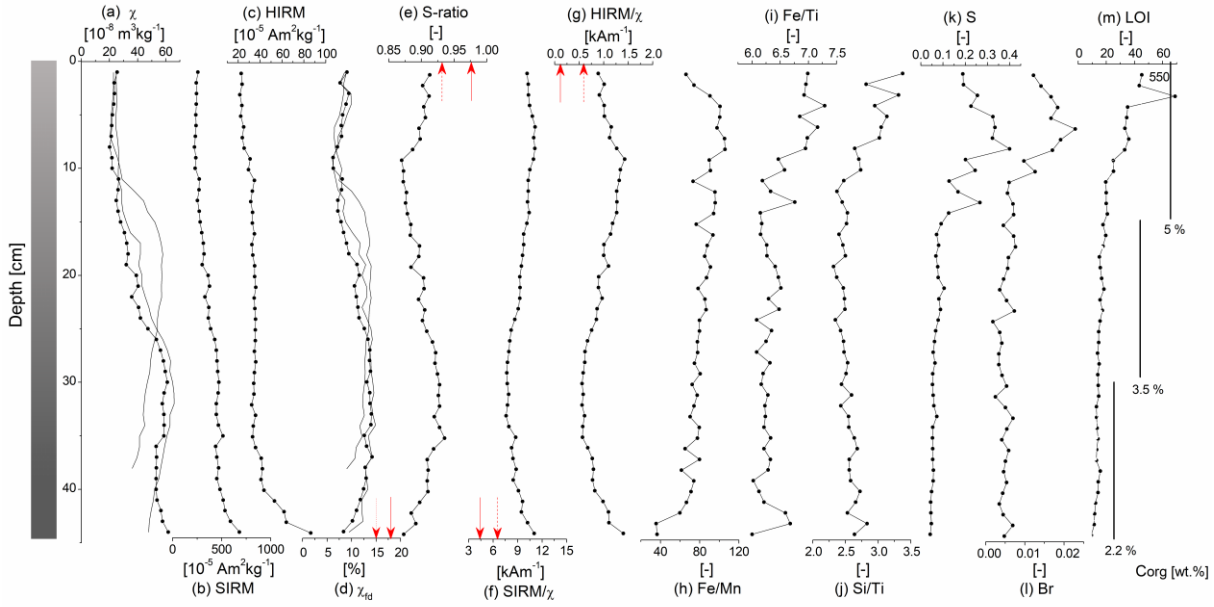

Figure 8. Magnetic and geochemical parameter variations versus depth for the Caohai Lake sediments: (a) magnetic susceptibility (χ); (b) saturation isothermal remanence (*SIRM*): (c) hard isothermal remanence (*HIRM*); (d) percentage frequency-dependence of χ (χ_{fd}%); (e) *S-ratio*; (f) *SIRM*/χ ratio; (g) *HIRM*/χ ratio; (h) iron/manganese (Fe/Mn) ratio; (i) iron/titanium (Fe/Ti) ratio; (j) silicon/titanium (Si/Ti) ratio; (k, l) relative contents of sulphur (S) and bromine (Br), (m) loss of ignition at 550 °C (LOI) and wt.% of organic carbon content for three mixed samples. Curves in (a) and (d) without symbols show data from two additional cores for consistency check. In (d-g) magnetic parameter means of red soil at the western and eastern basin are shown by red full and dashed arrows, respectively, for comparison. Concentration-dependent parameters (a-c) see Table 1 and Table S2. The column at the left side indicates that the sediment color is getting darker downcore.

4 Discussion

In the discussion, we focus on the following aspects: (i) The nature of ferro(i)magnetic minerals in the red soil and the Caohai Lake sediments; (ii) the spatial variability of magnetic parameters of modern red soil in Heqing Basin in order to identify possible environmental proxies; (iii) characteristic differences of magnetic properties of the red soil and the Caohai Lake sediments

with regard to changes during transfer from in situ to the sink (lake sediments); (iv) relevance of the results for using magnetic properties as paleoclimate proxies in settings as studied.

According to the presented results, the studied samples contain magnetite with different degree of maghemitization. The resulting assemblages of particles may range from near-stoichiometric magnetite to fully altered maghemite, which we interpret to reflect a causal relationship of alteration. For the sake of simplicity, we will speak of 'magnetite' in the further course of the discussion when interpreting the results in principle, unless the difference between magnetite and maghemitized magnetite plays an important role.

4.1 Magnetic characteristics of red soil versus lake sediments

In previous works, magnetic signals in modern soils and paleosols were mainly ascribed to pedogenic formation of magnetite or maghemite in the SP and SSD range, with χ-values ranging up to ~500x10^{-8} m^3/kg, mostly centered around 100x10^{-8} m^3/kg (Dearing et al., 1996; Maher, 1998; Deng et al., 2004; Song et al., 2014). An exceptionally large amount of fine magnetite in the SP range was observed throughout a ~7 m thick section of red soil above low-magnetic calcareous rock in southwest China, with the highest χ-values (up to ~6000x10^{-8} m^3/kg) ever reported in soil (Lu et al., 2012). Khadikar and Basavaiah (2004) also observed high values up to ~1000x10^{-8} m^3/kg for modern red soil on karst terrain in India, however, with surprisingly low χ_{fd}% of around 2 % that cannot be explained by the specific frequencies of the used instrument (Bartington MS2B). The χ-enhancement in the red soil of Heqing Basin is approximately similar to these previous studies of red soil.

In Heqing Basin, the highly magnetic red soil above low magnetic bedrock occurs on large spatial scale. It contains magnetite and hematite, as verified by XRD results (Fig. 3), ELNES spectra (Figs. 4d and 5c), and χ-T curves. Their molar contents are roughly ~0.5 vol.% and ~5 vol.% for magnetite (estimated from χ and M_s) and hematite (estimated from XRD results and HIRM), respectively. The extremely asymmetric 2Θ-peak at 18.4° degree in the XRD results (Fig. 3) suggests a mixture of maghemitized magnetite with a cubic structure and a tetragonal superstructure (Bowles et al., 2011), which would explain the small lattice constant observed by Rietveld refinements using magnetite structures. The intensity maximum of this peak fits to magnetite, cubic maghemite and synthetic maghemite. If the tetragonal maghemite cell is adjusted to the shoulder of the 18.4° 2Θ-peak, the position 102 and the 112 peak move to areas where no peaks are measured. This observation may fit to cubic maghemites which

suffer a higher loss of iron that may change the structure from cubic to tetragonal. The observed material seems to be in a transitional state between both structures or it contains oxides of both structures. The mixture would also explain the extremely small cell constants observed by Rietveld refinements using magnetite structures. The value of the maximum intensity at the 18.4° 2Θ-peak is located in the known range of common magnetite or maghemites.

The generally high χ_{fd}% of the red soil (~15-18 %; Table 1), together with the almost stable χ_{fd}% after CBD treatment (Table S4), prove a strong dominance of fine magnetite in the SP range, even in samples with relatively lower magnetic concentrations as shown by χ_{fd}% values >15 % for χ-values above several hundred 10^{-8} m^3/kg (Fig. 9a). The SP fraction hides the presence of larger-sized bedrock-derived MD magnetite that is revealed by reflected light microscopy. The results of χ-T behavior, broadband-frequency dependence χ(f), thermal demagnetization of *SIRM*, *IRM*-unmixing, and data distribution in the Day plot, all together suggest that the fine magnetite fraction occurs in a wide grain size distribution of SP particles that also tails into the SSD range. The presence of magnetite nanoparticles with sizes from <10 nm to about 20 nm, mostly occurring in aggregates of up to ~100 nm is clearly evidenced by the TEM results (Figs. 4 to 6).

From the values of χ and M_s we can roughly estimate the magnetite content. Because of its very high intrinsic susceptibility, the measured χ-value is a function of the inverse of the demagnetization factor (N) and the magnetite content. Assuming spherical single domain particles (N=1/3 SI), the mean χ-value of the red soil at the western basin (1085×10^{-8} m^3/kg) corresponds to ~0.5 vol.% of magnetite. As SP particles have a higher susceptibility than SSD or MD particles (Worm, 1998) the content is probably overestimated. The mean of M_s (0.32 Am^2kg^{-1}) obtained from the hysteresis data yields a consistent magnetite content of ~0.35 vol.%. For hematite, which contributes only very little to the χ-values, we can estimate a content of ~5 vol.% from the XRD result of original red soil from the western basin. The HIRM allows another crude estimation of the hematite content. The result is consistent with the ~5 vol.% from XRD, if the M_{rs}/M_s ratio is ~0.05 (M_s for hematite: 0.4 Am^2/kg). This low M_{rs}/M_s ratio indicates very soft hematite, either existing as fine viscous grains or large MD grains. An alternative explanation would be an imperfect hematite with much lower M_s.

According to the position of the Caohai Lake, the predominant source area of the lake sediments is the nearby limestone terrain at the western basin (Fig. 1). Magnetic concentration values in the Caohai Lake sediments vary by a factor of three, and they are more than one order lower

than the mean of the red soil. The quite high χ_{fd}% values (mean 10.6 %) indicates that a substantial part of the SP magnetite in the red soil material that was delivered to the lake is still existing after deposition.

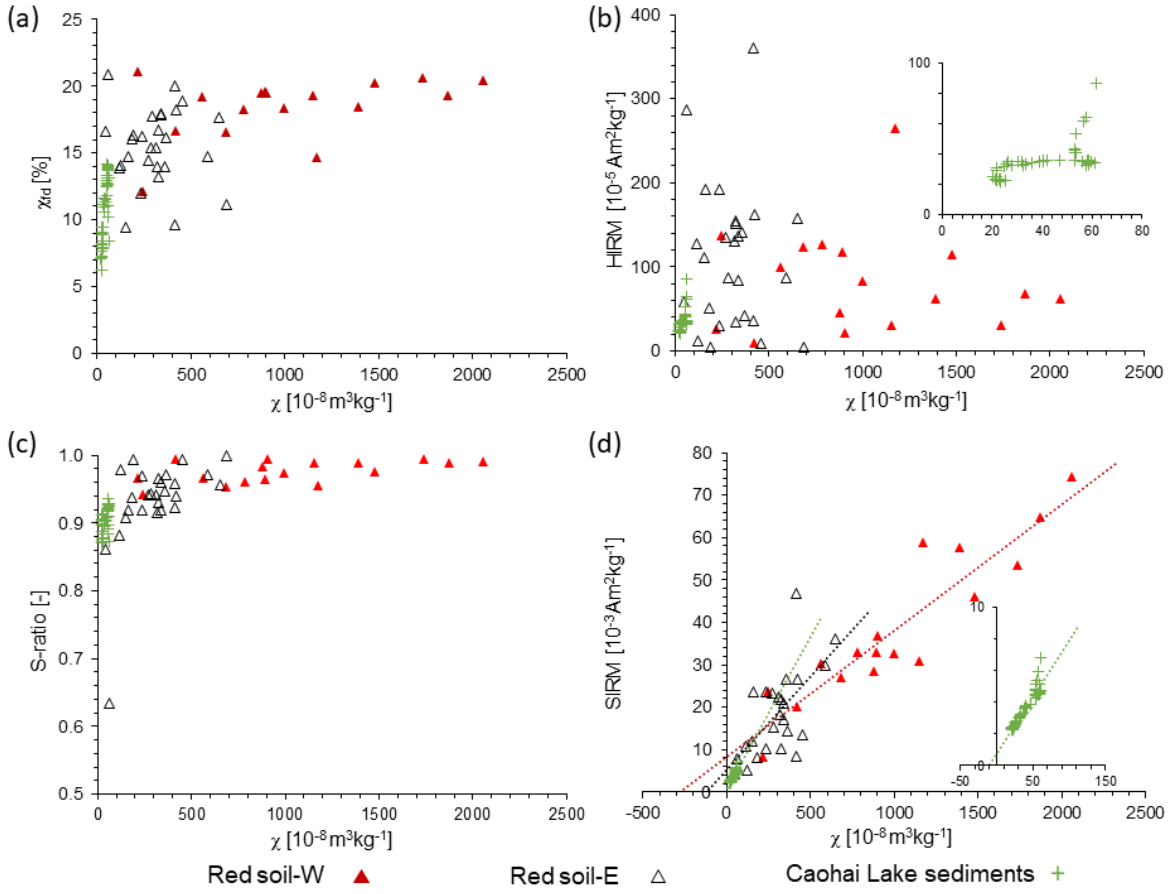

Figure 9. Magnetic parameters plotted versus magnetic susceptibility (χ); (a) χ_{fd}%, (b) *HIRM*, (c) *S-ratio*, (d) *SIRM*. Data are separated for red soil at the western and eastern basin, and Caohai Lake sediments. Dotted lines in (d) show linear regressions of the three sub-datasets. The small plots in (b, d) amplify the results of the lake sediments.

The lake sediments show a similar appearance of magnetite nanoparticles in aggregates as revealed by the TEM observations (Fig. 5a). However, other contributions strongly dilute the red soil material in the sediment. These contributions stem from the bedrock directly (measured carbonate content ~25 %), from enrichment of clay minerals, and fragments of shell or snail shells. The amount of these non-ferro(i)magnetic contributions is large, and therefore the lower χ-values in the lake sediments do not allow any statement on possible loss of magnetite during material transfer to the lake. However, the lower χ_{fd}% of the Caohai Lake sediments compared to the red soil (mean of 10.6 % versus 17.8 % at the western basin), the strong decrease of χ_{fd}%

values after CBD treatment (from 12.9 % to 5.2 %) compared to stable values for red soil of the western basin, a smaller decrease of χ-values after CBD treatment (55 % compared to 70 %), and a much higher *SIRM*/χ ratio (Fig. 8f) are compatible with a higher relative contribution of larger-sized bedrock-derived MD magnetite to the magnetic properties in the lake sediments compared to red soil. From these data one may conclude that a large part of the SP magnetite did not reach the lake. However, in the following section, we will present a model that could explain the observed difference of magnetic properties in the red soil and lake sediments without a loss of SP particles.

4.2 Magnetic changes in red soil material during source-sink transfer

The appearance of the magnetite nanoparticles in the red soil and the Caohai Lake sediments is similar as observed by Lu et al. (2012) in the afore-mentioned thick red soil sequence in southwest China and by several authors in paleosols of the Chinese Loess Plateau (Chen et al., 2005; Ahmed & Maher, 2018; Liu et al., 2007). It was suggested that the nanoparticles are formed as extracellular precipitates due to bacterial activity, consisting of magnetite that is aging by maghemitization and final oxidation to hematite (Chen et al., 2005; Nie et al., 2010; Ahmed & Maher, 2018). Clear evidence for such bacterial-driven processes is provided by laboratory experiments, showing extracellular production of 20-50 nm large magnetite nanoparticles within days or weeks by Fe-reducing bacteria, arranged in framboidal aggregates with sizes <100 nm or even up to ~500 nm (O'Loughlin et al., 2015). The question how the magnetite nanoparticles in the red soil of Heqing Basin were formed is not a key part of this paper, but in consideration of previous literature, we assume that they are a product of bacterial processes at the weathered limestone top, where iron is released from paramagnetic minerals through weathering of the limestone.

Comparison of the red soil and the Caohai Lake sediments allows the analysis of changes in the magnetic signatures during source-sink transfer. In this respect, the Caohai Lake acts as a sink of red soil material after translocation through wind and surface water. Any model explaining the magnetic changes of red soil material during this transfer must account for the decreased contribution of the SP fraction to the χ-signal and the decreased χ_{fd}% in the lake sediments. As mentioned above, the lower χ-values of the lake sediments cannot be interpreted directly in terms of SP-loss because of unknown dilution effects by other input materials.

Reflected light microscopy revealed that the larger magnetite particles in the Caohai Lake sediments are clearly detrital (i.e., not authigenic). Sediment input from far-distant sources such as eolian dust can be excluded (Yang et al., 2009), and besides the red soil only very low-magnetic sedimentary rocks exist in the catchment of Heqing Basin. Input of MD magnetite directly from bedrock weathering certainly contributes to the magnetic signal, but the question is whether this can significantly modulate the magnetic properties. In the red soil, the contribution of bedrock-inherited magnetite to the total magnetite fraction is minor as shown by the high χ_{fd}% that is stable after CBD treatment. In contrast, the lower χ_{fd}% of the lake sediments indicates roughly equal proportions of SP magnetite (pedogenic) and larger MD magnetite (bedrock-related). To explain this by dilution due to direct input of MD magnetite released from limestones, the weathered bedrock has to deliver about the same amount of magnetite to the lake as the deposited red soil. In situ χ-measurements of the limestone-bedrock mostly yielded negative χ-values. Taking a χ-value of zero (which is higher than mostly measured in situ) and $\chi = -1.2 \times 10^{-5}$ SI for calcite (Schmidt et al., 2006), and assuming that the limestone is composed of nearly 100 % calcite plus a minor magnetite fraction (i.e., ignoring a paramagnetic contribution), we yield a magnetite content of $<0.5 \times 10^{-3}$ vol.%, i.e., three orders of magnitude less than the total magnetite content in red soil. Therefore, an at least a 10^3 times larger volume of weathered and eroded limestones than red soil has to be delivered to the lake to achieve the necessary dilution. Such a dilution scenario can be ruled out, as red soil is widely covering the catchment area of Heqing Basin and is easily movable.

Differences of the magnetic characteristics between the red soil and the Caohai Lake sediments are therefore undoubtedly associated with changes of the nano-sized magnetite fraction. A possible process is dissolution of a large part of the fine magnetite particles in surface water or during the initial contact with lake water, as it was speculated by Hu et al. (2005). In order to test this, we filled several kg of red soil material from Heqing Basin into plastic containers and placed them permanently in the Caohai Lake at the sediment surface. The containers were perforated, allowing drainage by lake water. Measurements of samples taken every six months did not show significant changes after four years of permanent exposure. Although the experimental conditions do not reflect the conditions of fine particles suspended in the lake water or at the top of the sediment column, the absence of any change in magnetic concentration can at least be taken as a hint that dissolution is not a major mechanism during initial contact with lake water.

The XRF and LOI results and comparison with variations of magnetic parameters versus depth (Fig. 8) allow further assessment of possible dissolution effects. Because in a reducing environment the solubility of Fe and Mn increases but Mn is more readily affected, the Fe/Mn is used as an indicator for bottom-water oxygenation in lakes (e.g., Croudace and Rothwell, 2015; Morellón et al., 2016; Koutsodendris et al., 2017). On this basis, the Fe/Mn ratio suggests a gradual decrease of bottom-water oxygen content through time that can be either attributed to enhanced stratification in the water column or to de-oxygenation from organic decay following enhanced biological productivity. Because the water depth of Caohai lake is only 1-2 m, the first scenario can be firmly excluded; hence an increase in biological productivity appears to be the driving mechanism behind the increase in reducing conditions in the lake. The biological activity appears particularly enhanced in the uppermost 10 cm if considering the increasing Si/Ti ratio, which has been widely used to differentiate between biogenic silica (predominantly related to diatom blooms in lakes) and detrital input reflected in Ti (e.g., Croudace and Rothwell, 2015; Morellón et al., 2016; Koutsodendris et al., 2017). Increased productivity in the uppermost 10 cm could be responsible for an intensification of oxygen reduction in the water column leading to an increase in organic material deposition and preservation. This view is supported by the elevated counts of S and Br, which can be attributed to increased pyrite formation in organic sediments and formation of strong covalent bonds with organic molecules, respectively (e.g., Croudace and Rothwell, 2015). The downward variation of the LOI that represents the organic carbon is well matching with the S and Br results.

Under such a reducing environment with increased influx of organic matter, dissolution of magnetite could be expected; this view is supported by the increase in the Fe/Ti ratio in the uppermost 10 cm, on the basis that Fe is redox-sensitive in contrast to Ti (e.g., Aufgebauer et al., 2012; Croudace and Rothwell, 2015). Altogether, the XRF-based geochemical data suggest a strengthening of the oxygen depletion only in the uppermost 10 cm of the Caohai Lake sediment profile that could be responsible for magnetite dissolution. Comparing the geochemical and magnetic results, we notice that the geochemically indicated possible dissolution zone is at a much shallower level than the change in the χ-values that represents a magnetite-concentration measure and is starting to increase substantially at ~20-25 cm. Moreover, the χ-values are stable in the upper part until the top, whereas the LOI, Fe/Mn, S, Br, and in a less degree also Fe/Ti decrease at the top few cm.

The comparison of downcore variations strongly supports the view that the content of magnetite nanoparticles is not driven by dissolution effects, at least not to a degree that matters for the

major changes of magnetic parameters. The broadband-frequency χ(f) results (Fig. 7) confirm this conclusion. The lake sediments show a decrease of the χ(f)-variation in the lower-frequency range, which indicates a depletion of the larger-sized SP contribution (Kodama, 2013), contrary of what is expected for dissolution that erases smaller grains faster.

The observed differences may be associated with oxidation of fine magnetite to hematite. The redox potential in red soil (Wheeler et al., 1999) favors low-temperature oxidation and transformation to hematite in situ. In fact, presence of hematite in the nanoparticles is indicated by the ELNES results (Figs. 4d and 5c). According to modeling results of Ahmed & Maher (2018), complete oxidation of small (10 nm) magnetite particles into maghemite takes about one million years at pH=8, but it may also work much faster by bacterial activity (Byrne et al., 2015). As shown by the results from the vertical sections (Fig. S7), there is no indication that cease of nano-magnetite production in red soil happens in situ. However, it can be speculated that bacterially induced production of nano-magnetite in red soil ceases when the red soil material is eroded and transferred to the sink (lake) by wind and surface water, while magnetite alteration still continues.

The higher *SIRM*/χ and *HIRM*/χ ratios (Fig. 8f, g) in the Caohai Lake sediments compared to the red soil are compatible with such a scenario. However, it is questionable whether the time for oxidation during transfer from the origin to the sink is long enough to accomplish the conversion of a large part of magnetite into hematite. Moreover, it is unclear whether the hematite content in the red soil is generally related to oxidation of magnetite. If hematite originates from magnetite oxidation, be it via maghemite or by direct transformation, more nano-magnetite will lead to more hematite for the same degree of oxidation, and thus the HIRM in the red soil should correlate positively with χ, the S-ratio should be constant for different χ-values, and in the lake sediments the HIRM should inversely vary with χ, as higher χ-values in the sediments implies that less nano-magnetite is oxidized to hematite. However, none of these relationships is observed (Fig. 9b-d). In summary, partial loss of magnetite by oxidation to hematite in red soil material during transfer to the lake is possible and is supported by the higher hematite content in the nanoparticles of aggregates as we observed by the ELNES results (Figs. 4e and 5d), but it unlikely is the major process that causes the observed differences of magnetic properties in red soil and the Caohai Lake sediments.

The TEM results (Figs. 4 to 6) and the broadband-frequency dependence χ(f) (Fig. 7) provide the crucial clue to understand the key mechanism of magnetic differences. Close contact of

nanoparticles within aggregates causes magnetostatic interaction between them, leading to larger effective grain sizes in terms of the domain state behavior than the physical size of the individual particles, as it is shown by theoretical models and experimental data studying such kind of ultrafine particle assemblages (Chen et al., 2008; Mørup et al., 2010; Souza et al., 2019). According to these results, variable arrangement of nanoparticles within different aggregates in the red soil and the Caohai Lake sediments will lead to a wide distribution of the effective grain sizes throughout the SP range, which can tail into the range of SSD behavior as shown by the cited works above. The resulting distribution of effective grain sizes will depend on the overall size of the aggregates, a denser or looser packing of the nanoparticles, and partial alteration (maghemitization or hematite formation) of the nano-magnetite. In our observations, the size of individual nanoparticles is similar in the red soil and the lake sediments, but their arrangement in the aggregates appears to be tighter in the red soil. Moreover, the size of the aggregates in the red soil are apparently larger. If these differences between the aggregates as seen in the TEM samples are representative of the materials as a whole, then it is plausible that mechanical stresses (e.g. during wind stress) led to differences in the aggregates. The donut-like small nanoparticle that are splattered around aggregates in the original red soil (Fig. 6d) are not compatible with minimum-energy shapes that formed separately. They likely broke away from the aggregates, indicating that the aggregates are mechanically fragile.

The measured χ-values are a function of the effective grain size and the applied frequency. The theoretical background has been presented by Worm (1998) and Shcherbakov and Fabian (2005). In Figure 10, we present a conceptual sketch that explains the expected dependence of χ-values as a function of grain size and frequency. The dependence of χ versus grain size shows a peak-shaped behavior with highest values and strong frequency dependence in the range of thermal activation, a constant and frequency-independent lower χ when approaching the SSD range, and decreasing χ-values towards smaller SP particle sizes (underlying χ-relationships are given in Fig. 10). For aggregates in state (A), with a denser packing of nanoparticles and less hematite, we assume a similar difference of χ-values between the shown frequencies, whereas for aggregates in state (B), with looser packing and more hematite, the frequency dependence is stronger in the higher frequency range. This will lead to a typical difference in the broadband-frequency dependence χ(f), together with a decrease of χ-values due to the shift to smaller effective grain size, as shown by the principle χ(f) sketch (Fig. 10).

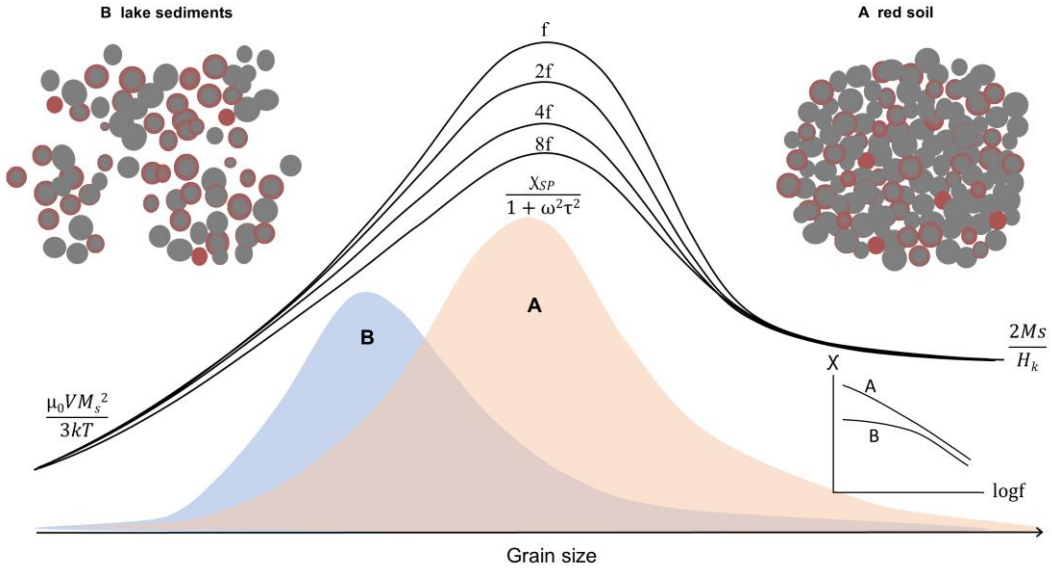

Figure 10. Conceptual sketch of the principle relationship of χ versus grain diameter (d) for four frequencies in logarithmically equal increments (increasing from f to 8f), modified from Kodama (2013), and following the theory presented by Worm (1998) and Shcherbakov and Fabian (2005). The principle relationships for smaller SP grains (below thermal activation), SP grains in the range of thermal activation (frequency-dependent; in-phase part), and larger grains in the SSD range are shown (M_s: saturation magnetization, H_k: microcoercivity, χ_{SP}: superparamagnetic susceptibility for zero frequency, V: grain volume, τ: relaxation time, T: temperature, f: frequency, ω: angular frequency, μ_0: magnetic permeability of free space, k: Boltzmann constant). The orange and gray fields display schematic distributions of effective grain sizes of the nano-magnetite aggregates in red soil (A) and lake sediments (B), respectively. Aggregates in red soil are assumed to be tighter packed and possibly also larger than in lake sediments, and according to the ELNES results more hematite is existing in the nanoparticles of the lake sediments.

Such difference can be seen in the measured broadband-frequency behavior of red soil and Caohai Lake sediment samples (Fig. 7). The curves for red soil show an approximately linear decay of χ with log(f) throughout the frequency range of 125 Hz to 16 kHz, whereas for the low-χ samples from the lake sediments the frequency dependence mainly occurs at f >1 kHz. For the difference between red soil H and lake sediment L samples, the slope change is statistically significant at 95 % confidence (Table S6). Kodama (2013) presented a method to determine the particle size from broadband-frequency data. Even without a quantitative inversion it becomes obvious from χ(f) that the effective SP grain size is smaller in the Caohai Lake sediments than in the red soil, which can be explained by the less compact aggregates of nanoparticles in the lake sediments as observed in the TEM studies.

With this model the macroscopic magnetic differences (χ, χ_{fd}%) between red soil and the Caohai Lake sediments can explained without a loss of individual magnetite nanoparticles. The nano-

magnetite fraction does not vanish, it simply becomes magnetically hidden as fining of the effective grain sizes due to increased separation of magnetite nanoparticles will lower the χ-values (Fig. 10) and will lead to a decline of χ_{fd}%. Partial transformation of magnetite to hematite as indicated by the ELNES results will cause an additional decrease of the χ-value and χ_{fd}%. Hematite in the nanoparticles, either existing as full nanoparticles or as shells of magnetite cores (Fig. 10), will also contribute to a shift towards smaller effective grain sizes through an increased distance between neighboring magnetite. Both the hematite fraction in the aggregates and the tighter or looser packing of nanoparticles affect the interaction between the magnetites, and therefore will have an impact on the resulting χ_{fd}% and χ values. How much both effects contribute to the observed differences between the red soil and Caohai Lake sediment properties is an open issue.

4.3 Relevance for paleoclimate studies

Heqing Basin accommodates two types of paleoclimate archives, the red soil and lake sediments, the latter concerning the modern lake sediments of Caohai Lake and the thick lacustrine sediment sequence accumulated in the large paleolake which existed in the basin throughout the Pleistocene until ~30 ka. The latter depends on the former by source-sink relationships. Lake sediments with red soil in the catchment is a frequently occurring setting in tropical and subtropical regions. Possible changes of pedogenic fine magnetite in red soil material, during transfer from the source (in situ) to the sink, and further changes in the lake have to be understood when employing magnetic proxies for paleoclimate studies. In Heqing Basin, red soil is the only relevant source of ferro(i)magnetic materials, and thus our investigation area provides a unique opportunity to study possible magnetic changes in the red soil material, which happened during material transfer to lake. In the context of our study, the Caohai Lake acts as a sink of red soil material. It is not our aim to reconstruct the paleoenvironmental evolution as a function of the geological age, thus dating of the Caohai Lake sediments is not required for this purpose.

One of the questions regarding red soil archives is the possible environmental control of the amount of pedogenic ferro(i)magnetic minerals. In the Chinese Loess Plateau, paleorainfall was quantified from χ-enhancement in the paleosols (Maher & Thompson, 1995). In red soil, the relationship between environmental conditions and fine magnetite production seems to be more complex. Liu et a. (2012) and Wang et al. (2013) suggested that magnetic signatures related to transformation of magnetite (maghemite) to hematite can be used to detect the degree of

pedogenesis in vermiculated red soil. According to Wang et al. (2013) stronger pedogenesis leads to more hematite formed under warm climate with dry-moist seasonality. Yin et al. (2018) used the ratio of hematite and goethite contents in red soil as an indicator for climate conditions, determined by reflectance spectrophotometry, but they also concluded that its climate sensitivity is limited. As addressed above, the origin of magnetite or maghemite in soil has often been related to bacterial activity (Maher & Thompson, 1995; Chen et al., 2005; Hu et al., 2015), either by formation of extracellular SP magnetite as a metabolism product (Lovley et al., 1987; Sundaram et al., 2012; Ahmed & Maher, 2018), or intracellular magnetosomes in the SSD range (Fassbinder et al., 1990). In the studied red soil of Heqing Basin, the observed aggregates of nanoparticles likely represent extracellular magnetite; magnetosomes were not detected. The appearance of the aggregates resembles Fe-oxyhydroxide nanoparticle aggregates of up to >100 nm large attached to the outer membrane of living bacteria (Luef et al. 2013), which could be a hint on the origin of the aggregates in the red soil. This issue is an exciting research question for future study, but it is beyond the scope of this paper.

The about threefold higher mean χ-values of red soil above the limestone bedrock at the western basin (χ=1085x10^{-8} m^3/kg) compared to red soil on sandstone and conglomerate at the eastern basin (χ=302x10^{-8} m^3/kg) indicates that there is no matching climate-related χ-enhancement. As calcite dissolves relatively fast during weathering, more efficient release of Fe is expected for limestone bedrock. However, the spatial distribution of the χ-values (Fig. 1, Tables 1 and S1) clearly shows that the amount of pedogenic magnetite does not only strongly differ for the different bedrock types, but also varies within the same type (standard deviation of χ for red soil on both limestones and sandstones/conglomerates is 53 % of the mean χ-value). Therefore, neither χ-values nor χ_{fd}% of red soil are suitable to discriminate different environmental conditions. If hematite derives from alteration of fine magnetite, as suggested by earlier studies of red soil (Liu et al., 2012; Wang et al., 2013), and also proposed by Torrent et al. (2006) for aerobic soil, the relative proportions of fine magnetite and hematite could provide useful information on environmental conditions, and the *HIRM*/χ ratio may be a suitable proxy. However, the bivariate plot of *HIRM* versus χ (Fig. 9b) shows strong scattering of the data.

In contrast, there is a good linear relationship of *SIRM* and χ (Fig. 9d) for the red soil above limestones (r = 0.92) and still reasonable for red soil above sandstones/conglomerates (r = 0.64). The latter correlation is probably lower because of the more variable bedrock lithology. The *SIRM*/χ ratio is strongly different for the limestones (4.20 kA/m) and

sandstones/conglomerates (6.52 kA/m), but if it is possible to establish separate transfer functions for different bedrock types, this ratio may be a suitable proxy parameter for the degree of pedogenesis as previously suggested (Liu et al., 2012; Wang et al., 2013). The scattered HIRM versus χ distribution, point out that there is no simple systematic mechanism of magnetite-to-hematite transformation. The about 1:10 molar ratio of magnetite (estimated from χ and M_s) and hematite (estimated from XRD) contents in the red soil suggests that only a smaller part of the hematite sits in the nanoparticle aggregates.

But why does the *SIRM* correlate with χ? If there is a climate-specific development of the nanoparticle aggregates, expressed by denser/looser packing of nanoparticles, different size of aggregates, or different proportion of hematite, a characteristic SP-SSD behavior distribution (according to the schematic relationship shown in Fig. 10) could be imprinted in the relative proportions of SSD magnetite (controlling SIRM) and SP magnetite (dominating χ) behaviors. In such case, the *SIRM*/χ-ratio is mainly dependent on the nano-magnetite in the aggregates, with only very little contribution of hematite. Further studies are needed to understand the underlying processes and to develop meaningful transfer functions.

Studies of lake sediments in settings with red soil as the dominating source material, as in Heqing Basin, suffer from several uncertainties. According to our model presented in section 4.2, the pedogenic fine magnetite fraction of the red soil material is to a large extent still existing after deposition. However, due to the decreased effective magnetic grain size of the nano-magnetite aggregates it is less contributing to the χ-values and χ_{fd}% (Fig. 10). Comparison of geochemical and magnetic parameter variations throughout the Caohai Lake sediment sequence (Fig. 8a-c) indicate that there is no substantial loss of the nano-magnetite by dissolution. Magnetic concentration values in the lower part of the Caohai Lake sediments are about double as high as in the upper part (Fig. 8a-c). This variation with depth may indicate a response to climate change or a change in the hydrological conditions during the deposition period, residing in both the nanoparticle aggregates and the bedrock-inherited MD magnetite. As it is a mixed signal, the underlying control of magnetic properties require further detailed study, which is beyond the scope of this paper.

What is the meaning of the new results for the interpretation of magnetic proxies in the long Core-HQ from the large paleolake in Heqing Basin (Fig. 1)? Hu et al. (2015) concluded from the very low χ_{fd}% throughout the 168-m long sequence (mean χ_{fd}% ~2.5 %) that SP magnetite derived from red soil is absent, and they reconstructed paleo-humidity conditions assuming an

alteration mechanism of the remaining bedrock-inherited larger sized magnetite. Results from other lakes in southwestern China, with similar setting as Heqing Basin, suggest that SP fractions are indeed effectively dissolved below a certain depth in the sediment column. In Erhai Lake this depth occurs at ~50-60 cm (Dearing et al., 2008), and in Xingyun Lake below ~1 m sediment depth (Chen et al., 2014), both lakes having a similar size as the Heqing paleo-lake. In the modern Caohai Lake efficient dissolution is not observed, which could be due to the only ~0.5-m sediment thickness. Moreover, redox conditions in the small Caohai Lake with low water depth cannot directly be compared to the much larger and deeper Heqing paleolake.

According to our model presented in section 4.2, there is a possible completely different explanation. Advanced disintegration of the aggregates of magnetite nanoparticles could drive the effective magnetic grain size to an SP range with low χ_{fd}% (i.e., a smaller effective size). For this reason, the validity of the paleo-humidity reconstruction of Hu et al. (2015) for the ~900-30 ka period in Core-HQ, based on the assumption that SP magnetite from red soil has been erased, is challenged by our new results. A substantial SP magnetite fraction originating from disintegrated aggregates may still exist in the sediments, forming separated nanoparticles or small aggregates. Although not contributing to magnetic remanence parameters, this SP fraction would carry part of the χ-signal on which Hu et al. (2015) partly built their interpretation.

5. Conclusions

Heqing Basin is a useful example for studying changes of magnetic properties in a setting of lake sediments with red soil as the only important source of ferro(i)magnetic input. The results detect the nature and macroscopic expression of magnetic changes in red soil material during transfer from the origin to the sink (Caohai Lake sediments), with implications for paleoclimate studies:

(1) Highly magnetic red soil on low-magnetic sedimentary bedrock with up to ~0.5 % magnetite (according to χ and M_s) occurs throughout the Heqing Basin catchment. Extremely high χ_{fd}% (~15-20 %) shows that SP magnetite is strongly dominating, which is likely an extracellular product of bacterial activity during pedogenesis.

(2) The TEM results reveal ~100 nm large aggregates of mainly ~10-15 nm sized nanoparticles in the red soil and in the Caohai Lake sediments. The nanoparticles in the aggregates are tighter packed in red soil than in the lake sediments, and the aggregates in the red soil appear to be

larger. ELNES results identify the nanoparticles as magnetite and/or maghemite (which cannot be discriminated), with higher contribution of hematite in aggregates of the Caohai Lake sediments. Interaction of the nano-magnetite particles leads to a wide range of effective grain sizes in terms of their domain state behavior. The effective grain size is naturally larger than the physical size of individual nanoparticles, and tails into the SSD range. Interaction is less for looser packing and for larger hematite content that creates larger distances between magnetites. This model explains the observed differences of macroscopic magnetic characteristics between red soil and lake sediments by a shift of the effective grain size distribution towards smaller size. The results of broadband-frequency dependence of χ support the model.

(3) Spatial distributions of magnetic parameters in the red soil around Heqing Basin clearly show that the amount of pedogenically produced nano-magnetite is bedrock-dependent, and even varies within the same bedrock type. The *SIRM*/χ ratio is relatively constant for red soil above the same bedrock type, it is assumed to be controlled by a shift of the specific SP-SSD distribution in the aggregates possibly related to environmental conditions and is therefore a potential paleoclimate proxy. Further research is required to elucidate whether bedrock-specific transfer functions can be determined.

(4) The magnetic signature of the Caohai Lake sediments is controlled by both magnetite nanoparticle aggregates and MD magnetite inherited from bedrock weathering. A composed paleoclimate signature of the magnetic parameter variations might exist, but a complex control mechanism is expected, which requires further research. The validity of the paleoclimate reconstruction of Hu et al. (2015) from the 168-m long Core-HQ in Heqing Basin, spanning the period of ~900-30 ka, is challenged. The underlying assumption of SP magnetite extinction by dissolution, derived from low χ_{fd}% values, could be wrong. According to the new results, disintegrated magnetite aggregates may represent an SP state with low χ_{fd}%, without loss of nanoparticles.

Acknowledgments

This research was supported by the National Natural Science Foundation of China (NO. 41572152), the German Research Foundation (DFG; AP 34/44-1), and the Chinese Academy of Sciences Visiting Professorship for Senior International Scientists (NO. 2012T1Z0004, 131432WGZJTPYJY20150002). We thank James Byrne and Julian Sorwat for their help in CBD treatment, Timm Bayer for preparation of samples for TEM analysis, and

Daniel Buchner for enabling the carbonate and OC analysis. The data used in this paper are displayed in Figures 1-10 and Table 1, and primary data are listed in Tables S1-7 of Supporting Information, also shown in Figures S1-7. The data are available in the Mendeley database for public download at http://dx.doi.org/10.17632/m4gvh8p4cf.1

References

Ahmed, I.A.M., & Maher, B.A. (2018). Identification and paleoclimatic significance of magnetite nanoparticles in soils. Proceedings of the National Academy of Sciences, 115(8), 1736-1741. https://doi.org/10.1073/pnas.1719186115

An, Z.S., Clemens, S.C., Shen, J., Qiang, X., Jin, Z.D., Sun, Y.B., et al. (2011). Glacial-interglacial Indian summer monsoon dynamics. Science, 333, 719-723. https://doi.org/10.1126/science.1203752

Aragón, R., Buttrey, D.J., Shephard, J.P., & Honig, J.M. (1985). Influence of non-stoichiometry on the Verwey transition. Physical Review, B 31(1), 430-436. https://doi.org/10.1103/PhysRevB.31.430

Aufgebauer, A., Panagiotopoulos, K., Wagner, B., Schaebitz, F., Viehberg, F.A., & Vogel, H. (2012). Climate and environmental change in the Balkans over the last 17 ka recorded in sediments from Lake Prespa (Albania/F.Y.R. of Macedonia/Greece). Quaternary International, 274, 122-135. https://doi.org/10.1016/j.quaint.2012.02.015

Bengtsson, L. (1986). Chemical analysis: Handbook of Holocene palaeoecology and palaeohydrology, 423-451. John Wiley and Sons, Chichester (UK).

Bilardello, D. & IRM. (2020). Practical Magnetism II: Humps and a Bump, the Maghemite Song. The IRM Quarterly, 30(1), 15-17. ISSN: 2152-1972

Bloemendal, J., King, J.W., Hall, F.R., & Doh, S.J. (1992). Rock magnetism of Late Neogene and Pleistocene deep-sea sediments: Relationship to sediment source, diagenetic processes, and sediment lithology. Journal of Geophysical Research: Solid Earth, 97(B4), 4361-4375. https://doi.org/10.1029/91JB03068

Bowles, J.F.W., Howie, R.A., Vaughan, D.J. & Zussman, J. (2011). Rock-Forming Minerals: Non-Silicates: Oxides, Hydroxides and Sulphides, Geological Society.

Bowles, J., Jackson, M., Chen, A., & Solheid, P. (2009). Interpretation of Low-Temperature Data Part 1: Superparamagnetism and Paramagnetism. The IRM Quarterly, 19(3), 1, 7-11. ISSN: 2152-1972

Bronger, A., & Bruhn-Lobin, N. (1997). Paleopedology of Terrae rossae-Rhodoxeralfs from Quaternary calcarenites in NW Morocco. Catena, 28, 279-295. https://doi.org/10.1016/S0341-8162(96)00043-4

Byrne, J., Klueglein, N., Pearce, C., Rosso, K.M., Appel, E., & Kappler, A. (2015). Redox cycling of Fe(II) and Fe(III) in magnetite by Fe-metabolizing bacteria. Science, 347, 1473-1476. https://doi.org/10.1126/science.aaa4834

Chen, D.X., Sanchez, A., Xu, H., Gu, H.C., & Shi, D.L. (2008). Size-independent residual magnetic moments of colloidal Fe3O4-polystyrene nanospheres detected by ac susceptibility measurements. Journal of Applied Physics, 104, 093902. https://doi.org/10.1063/1.3005988

Chen, F.H., Chen, X.M., Chen, J.H., Zhou, A.E., Wu, D., Tang, L.Y., et al. (2014). Holocene vegetation history, precipitation changes and Indian Summer Monsoon evolution documented from sediments of Xingyun Lake, south-west China. Journal of Quaternary Science, 29(7), 661-674. https://doi.org/10.1002/jqs.2735

Chen, T.H., Xu, H.F., Xie, Q.Q., Chen, J., Ji, J.F., & Lu, H.Y. (2005). Characteristics and genesis of maghemite in Chinese loess and paleosols: Mechanism for magnetic susceptibility enhancement in paleosols. Earth and Planetary Science Letters, 240, 790-802. https://doi.org/10.1016/j.epsl.2005.09.026

Colliex, C., Manoubi, T., & Ortiz, C. (1991). Electron-loss-spectroscopy near-edge fine structures in the iron-oxygen system. Physical Review, B 44, 11402-11411. https://doi.org/10.1103/PhysRevB.44.11402

Croudace, I.W., & Rothwell, R.G. (Eds.). (2015). Micro-XRF studies of sediment cores. Developments in paleoenvironmental research, Vol. 17. pp. 507-534. Springer, Dordrecht.

Day, R., Fuller, M., & Schmidt, V. A. (1977). Hysteresis properties of titanomagnetites: Grain size and composition dependence. Physics of the Earth and Planetary Interiors, 13, 260-267. https://doi.org/10.1016/0031-9201(77)90108-X

Dean, W.E. (1974). Determination of Carbonate and organic-matter in calcareous sediments and sedimentary-rocks by Loss on Ignition - Comparison with other methods. Journal of Sedimentary Petrology, 44(1), 242-248. https://doi.org/10.1306/74D729D2-2B21-11D7-8648000102C1865D

Dearing, J.A., Dann, R.J.L., Hay, K., Lees, J., Loveland, P.J., Maher, B.A., & O'Grady, K. (1996). Frequency-dependent susceptibility measurements of environmental materials. Geophysical Journal International, 124, 228-240. https://doi.org/10.1111/j.1365-246X.1996.tb06366.x

Dearing, J.A., Jones, R.T., Shen, J., Yang, X., Boyle, J.F., & Foster, G.C. (2008). Using multiple archives to understand past and present climate-human-environment interactions: the lake Erhai catchment, Yunnan Province, China. Journal of Paleolimnology, 40, 3-31. https://doi.org/10.1007/s10933-007-9182-2

Deng, C.L., Hao, Q.Z, Guo, Z.T & Zhu, R.X. (2019). Quaternary integrative stratigraphy and timescale of China. Science China Earth Sciences, 62, 324-348. http://doi.org/10.1007/s11430-017-9195-4

Deng, C.L., Zhu, R.X., Verosub, K.L., Singer, M.J., & Vidic, N.J. (2004). Mineral magnetic properties of loess//paleosol couplets of the central loess plateau of China over the last 1.2 Myr. Journal of Geophysical Research, 109, B01103. https://doi.org/10.1029/2003JB002532

Dunlop, D.J. (2002). Theory and application of the Day plot (Mrs/Ms versus Hcr/Hc) 1. Theoretical curves and tests using titanomagnetite data. Journal of Geophysical Research: Solid Earth, 107, B3. https://doi.org/10.1029/2001JB000486

Fassbinder, J.W.E., Stanjek, H., & Vali, H. (1990). Occurrence of magnetic bacteria in soil. Nature, 343, 161-163. http://dx.doi.org/10.1038/343161a0

Feenstra, A., Sämann, S., & Wunder, B. (2005). An experimental study of Fe–Al solubility in the system corundum–hematite up to 40 kbar and 1300°C. Journal of Petroleum Science and Engineering, 46(9), 1881-1892. https://doi.org/10.1093/petrology/egi038

Feng, J.L., Cui, Z.J., & Zhu, L.P. (2009). Origin of terra rossa over dolomite on the Yunnan–Guizhou Plateau, China. Geochemical Journal, 43, 151-166. https://doi.org/10.2343/geochemj.1.0014

Gasse, F., Arnold, M., Fontes, J.C., Fort, M., Gibert, E., Huc, A., et al. (1991). A 13,000-year climate record from western Tibet. Nature, 353, 742-745. https://doi.org/ 10.1038/353742a0

Geiss, C.E., Umbanhowar, C.E., Camill, P., & Banerjee, S.K. (2003). Sediment magnetic properties reveal Holocene climate change along the Minnesota prairie-forest ecotone. Journal of Paleolimnology, 30, 151-166. https://doi.org/10.1023/A:1025574100319

Golla-Schindler, U., Hinrichs, R., Bomati-Miguel, O., & Putnis, A. (2006). Determination of the oxidation state for iron oxide minerals by energy-filtering TEM. Micron, 37, 473-477. https://doi.org/10.1016/j.micron.2005.11.002

Harrison, R.J., & Feinberg, J. M. (2008). FORCinel: An improved algorithm for calculating first-order reversal curve distributions using locallyweighted regression smoothing. Geochemostry, Geophysics, Geosystems, 9, Q05016. https://doi.org/10.1029/2008GC001987

He, Z.L., Zhang, M.K., & Wilson, M.J. (2004). Distribution and classification of red soils in China. In: Wilson M.J., He Z., Yang X. (eds) The Red Soils of China, pp 29-33. Springer, Dordrecht. https://doi.org/10.1007/978-1-4020-2138-1_3

Heiri, O., Lotter, A.F., & Lemcke, G. (2001). Loss on ignition as a method for estimating organic and carbonate content in sediments: reproducibility and comparability of results. Journal of Paleolimnology, 25, 101-110. https://doi.org/10.1023/A:1008119611481

Hu, S.Y., Goddu, S.R., Appel, E., Verosub, K., Yang, X.D., & Wang, S. (2005). Palaeoclimatic changes over past one million years derived from lacustrine Sediments of Heqing Basin (Yunnan, China). Quaternary International, 136, 123-129. https://doi.org/10.1016/j.quaint.2004.11.013

Hu, S.Y., Goddu, S.R., Herb, C., Appel, E., Gleixner, G., Wang, S.M., et al. (2015). Climate variability and its magnetic response recorded in a lacustrine sequence in Heqing basin at the SE Tibetan Plateau since 900 ka. Geophysical Journal International, 201, 444-458. https://doi.org/10.1093/gji/ggv033

Hunt, C.P., Singer, M.J., Kletetschka, G., Tenpas, J., & Verosub, K.L. (1995). Effect of citrate-bicarbonate-dithionite treatment on fine-grained magnetite and maghemite. Earth and Planetary Science Letters, 130, 87-94. https://doi.org/10.1016/0012-821X(94)00256-X

Jiang, Z.X., Liu, Q.S., Barrón, V., Torrent, J., & Yu, Y.J. (2012). Magnetic discrimination between Al-substituted hematites synthesized by hydrothermal and thermal dehydration methods and its geological significance. Journal of Geophysical Research: Solid Earth, 117, B02102. https://doi.org/10.1029/2011JB008605

Kern, O.A., Koutsodendris, A., Mächtle, B., Christanis, K., Schukraft, G., Scholz, C., et al. (2019). X-ray fluorescence core scanning yields reliable semiquantitative data on the elemental composition of peat and organic-rich lake sediments. Science of the Total Environment 697, 134110. https://doi.org/10.1016/j.scitotenv.2019.134110

Khadkikar, A.S., & Basavaiah, N. (2004). Morphology, mineralogy and magnetic susceptibility of epikarst-Terra Rossa developed in late Quaternary aeolianite deposits of southeastern Saurashtra, India. Geomorphology, 58, 339-355. https://doi.org/10.1016/j.geomorph.2003.07.001

Kodama, K. (2013). Application of broadband alternating current magnetic susceptibility to the characterization of magnetic nanoparticles in natural materials. Journal of Geophysical Research Solid Earth, 118, 1-12. https//doi.org/10.1029/2012JB009502

Koutsodendris, A., Brauer, A., Reed, J.M., Plessen, B., Friedrich, O., Hennrich, B., et al, (2017) Climate variability in SE Europe since 1450 AD based on a varved sediment record from Etoliko Lagoon (western Greece). Quaternary Science Reviews, 159, 63-76. https://doi.org/10.1016/j.quascirev.2017.01.010

Koutsodendris, A., Sachse, D., Appel, E., Herb, C., Fischer, T., Fang, X.M. & Pross, J. (2018). Prolonged monsoonal moisture availability preconditioned glaciation of the Tibetan Plateau during the Mid-Pleistocene Transition. Geophysical Research Letters, 45(23), 13020-13030. https:/doi.org/10.1029/2018GL07930300

Lavrieux, M., Birkholz, A., Meusburger, K., Wiesenberg, G.L.B., Gilli, A., Stamm, C., & Alewel, C. (2019). Plants or bacteria? 130 years of mixed imprints in Lake Baldegg sediments (Switzerland), as revealed by compound-specific isotope analysis (CSIA) and biomarker analysis. Biogeosciences, 16, 2131–2146. https://doi.org/ 10.5194/bg-16-2131-2019

Liu, C.C., Deng, C.L., & Liu, Q.S. (2012). Mineral magnetic studies of the vermiculated red soils in southeast China and their paleoclimatic significance. Palaeogeography, Palaeoclimatology, Palaeoecology, 329-330, 173-183. https://doi.org/10.1016/j.palaeo.2012.02.035

Liu, Q.S., Deng, C.L., Torrent, J. & Zhu, R.X. (2007). Review of recent developments in mineral magnetism of the Chinese loess. Quaternary Science Reviews, 26, 368-385. https://doi.org/10.1016/j.quascirev.2006.08.004

Liu, Z.F., Ma, J.L., Wie, G.J., Liu, Q.S., Jiang, Z.X., Ding, X., et al. (2017). Magnetism of a red soil core derived from basalt, northern Hainan Island, China: Volcanic ash versus pedogenesis. Journal of Geophysical Research Solid Earth, 122, 1677-1696. https:/doi.org/10.1002/2016JB013834

Lovley, D.R., Stolz, J.F., Nord, G.L.Jr, & Phillips, E.J.P. (1987). Anaerobic production of magnetite by a dissimilatory iron-reducing microorganism. Nature, 330, 252-254. https://doi.org/10.1038/330252a0

Lu, S.G., Chen, D.J., Wang, S.Y., & Liu, Y.D. (2012). Rock magnetism investigation of highly magnetic soil developed on calcareous rock in Yun-Gui Plateau, China: Evidence for pedogenic magnetic minerals. Journal of Applied Geophysics, 77, 39-50. https://doi.org/10.1016/j.jappgeo.2011.11.008

Luef, B., Fakra, S.C., Csencsits, R., Wrighton, K.C., Williams, K.H., Wilkins, M.J., et al, (2013). Iron-reducing bacteria accumulate ferric oxyhydroxide nanoparticle aggregates that may support planktonic growth. The ISME Journal, 7(2), 338-350. https://doi.org/10.1038/ismej.2012.103

Maher, B.A. (1998). Magnetic properties of modern soils and Quaternary loessic paleosols: paleoclimatic implications. Palaeogeography, Palaeoclimatology, Palaeoecology, 137, 25-54. https://doi.org/10.1016/S0031-0182(97)00103-X

Maher, B.A., & Thompson, R. (1995). Paleorainfall reconstructions from pedogenic magnetic susceptibility variations in the Chinese loess and paleosols. Quaternary Research, 44, 383-391. https://doi.org/10.1006/qres.1995.1083

Maher, B.A., & Taylor, R.M. (1988). Formation of ultrafine-grained magnetite in soils. Nature, 336, 368-370. https://doi.org/10.1038/336368a0

Maxbauer, D.P., Feinberg, J.M., & Fox, D.L. (2016). MAX UnMix: A web application for unmixing magnetic coercivity distributions. Computers & Geosciences, 95, 140-145. https://doi.org/10.1016/j.cageo.2016.07.009

Mehra, O. P., & Jackson, M. L. (1960). Iron oxide removal from soils and clays by a dithionite-citrate system buffered with sodium bicarbonate. Clays and Clay Minerals, 7, 317-327. https://doi.org/10.1016/B978-0-08-009235-5.50026-7

Morellón, M., Anselmetti, F.S., Ariztegui, D., Brushulli, B., Sinopoli, G., Wagner, B., et al, (2016). Human-climate interactions in the central Mediterranean region during the last millennia: The laminated record of Lake Butrint (Albania). Quaternary Science Reviews, 136, 134-152. https://doi.org/10.1016/j.quascirev.2015.10.043

Mørup, S., Hansen, M.F., & Frandsen, C. (2010). Magnetic interactions between nanoparticles. Beilstein Journal of Nanotechnology, 1, 182-190. https://doi.org/10.3762/bjnano.1.22

Nie, J.S., Song, Y.G., King, J.W., & Egli, R. (2010). Consistent grain size distribution of pedogenic maghemite of surface soils and Miocene loessic soils on the Chinese Loess Plateau. Journal of Quaternary Science, 25(3), 261-266. https://doi.org/10.1002/jqs.1304

Oldfield, F., & Robinson, S.G. (1985). Geomagnetism and paleoclimate. Tooley M.J., Sheail G.M. (Eds.), The Climatic Scene, pp. 186-205. Allen & Unwin, Boston.

O'Loughlin, E.J., Gorski, C.A., & Scherer, M.M. (2015). Effects of phosphate on secondary mineral formation during the bioreduction of akaganeite (β-FeOOH): Green rust versus framboidal magnetite. Current Inorganic Chemistry, 5, 214-224. https://doi.org/ 10.2174/1877944105666150421001126

O'Neill, H.S.C., & Dollase, W.A. (1994). Crystal structures and cation distributions in simple spinels from powder XRD structural refinements: MgCr2O4, ZnCr2O4, Fe3O4 and the temperature dependence of the cation distribution in ZnAl2O4. Physics and Chemistry of Minerals, 20, 541-555. https://doi.org/10.1007/BF00211850

Pecharromán, C., González-Carreño, T., & Iglesias, J.E. (1995). The infrared dielectric properties of maghemite, γ-Fe2O3, from reflectance measurement on pressed powders. Physics and Chemistry of Minerals, 22, 21-29. https://doi.org/10.1007/BF00202677

Peck, J.A., King, J.W., Colman, S.M., & Kravchinsky, V.A. (1994). A rock magnetic record from Lake Baikal, Siberia: evidence for Late Quaternary climatic change. Earth and Planetary Science Letters, 122, 221-238. https://doi.org/10.1016/0012-821X(94)90062-0

Readman, P.W., & O'Reilly, W. (1972). Magnetic properties of oxidized (cation-deficient) titanomagnetites, (Fe,Ti,□)O4. Journal of Geomagnetism and Geoelectricity, 24, 69-90. https://doi.org/10.5636/jgg.24.69

Roberts, A. P., Tauxe, L., Heslop, D., Zhao, X., & Jiang, Z.X. (2018). A critical appraisal of the "Day" diagram. Journal of Geophysical Research: Solid Earth, 123, 2618-2644. https://doi.org/10.1029/2018JB017049

Schmidt, V., Günther, D., & Hirt, A.M. (2006). Magnetic anisotropy of calcite at room-temperature. Tectonophysics, 418, 63-73. https://doi.org/10.1016/j.tecto.2005.12.019

Shcherbakov, V.P., & Fabian, K. (2005). On the determination of magnetic grain-size distributions of superparamagnetic particle ensembles using the frequency dependence of susceptibility at different temperatures. Geophysical Journal International, 162, 736-746. https://doi.org/ 10.1111/j.1365-246X.2005.02603.x

Snowball, I.F. (1993). Mineral magnetic properties of Holocene lake and soils from the Karsa Valley, Lappland, Sweden, and their relevance to paleoenvironmental reconstruction. Terra Nova, 5, 258-270. https://doi.org/10.1111/j.1365-3121.1993.tb00257.x

Song, Y., Hao, Q.Z., Ge, J.Y., Zhao, D., Zhang, Y., Li, Q., et al. (2014). Quantitative relationships between magnetic enhancement of modern soils and climatic variables over the Chinese Loess Plateau. Quaternary International, 334-335, 119-131. https://doi.org/10.1016/j.quaint.2013.12.010

Souza, C.M., Pedrosa, S.S., Carriço, A.S., Rebouças, G.O.G., & Dantas, A.L. (2019). Thermal hysteresis of superparamagnetic Gd nanoparticle clusters. Physical Review B, 99, 174441. https://doi.org/10.1103/PhysRevB.99.174441

Sundaram, P.A., Augustine, R., & Kannan, M. (2012). Extracellular biosynthesis of iron oxide nanoparticles by Bacillus subtilis strains isolated from rhizosphere soil. Biotechnology and Bioprocess Engineering, 17(4), 835-840. http://dx.doi.org/10.1007/s12257-011-0582-9

Tabor, N.J., & Myers, T.S. (2015). Paleosols as Indicators of Paleoenvironment and Paleoclimate. Annual Review of Earth and Planetary Sciences, 3, 333-361. https://doi.org/ 10.1146/annurev-earth-060614-105355

Torrent, J., Barron, V., & Liu, Q.S. (2006). Magnetic enhancement is linked to and precedes hematite formation in aerobic soil. Geophysical Research Letters, 33, L02402. https://doi.org/10.1029/2005GL024818

van Oorschot, I.H.M Dekkers, M.L. (1999). Dissolution behaviour of fine-grained magnetite and maghemite in the citrate–bicarbonate–dithionite extraction method. Earth and Planetary Science Letters, 167, 283-295. https://doi.org/10.1016/S0012-821X(99)00033-3

Wang, S.Y., Lin, S., & Lu, S.G. (2013). Rock magnetism, iron oxide mineralogy and geochemistry of Quaternary red earth in central China and their paleopedogenic implication. Palaeogeography, Palaeoclimatology, Palaeoecology, 379-380, 95-103. https://doi.org/10.1016/j.palaeo.2013.04.010

Wheeler, D.B., Thompson, J.A., & Bell, J.C. (1999). Laboratory comparison of soil redox conditions between red soils and brown soils in Minnesota, USA. Wetlands, 19(3), 607-616. https://doi.org/10.1007/BF03161698

Worm, H.U. (1998). On the superparamagnetic-stable single domain transition for magnetite, and frequency dependence of susceptibility. Geophysical Journal International, 133, 201-206. https://doi.org/10.1046/j.1365-246X.1998.1331468.x

Xiao, X.Y., Shen, J., Wang, S.M., Xiao, H.F., & Tong, G.B. (2010). The variation of the southwest monsoon from high resolution pollen record in Heqing Basin, Yunnan Province, China for the last 2.78 Ma. Palaeogeography, Palaeoclimatology, Palaeoecology, 287, 45-57. https://doi.org/10.1016/j.palaeo.2010.01.013

Yaalon, D.H. (1997). Soils in the Mediterranean region: what makes them different? Catena, 28, 157-169. https://doi.org/10.1016/S0341-8162(96)00035-5

Yang, T., Liu, Q.S., Zeng, Q.L., & Chan, L.S. (2009). Environmental magnetic responses of urbanization processes: evidence from lake sediments in East Lake, Wuhan, China. Geophysical Journal International, 179, 873-886. https://doi.org/10.1111/j.1365-246X.2009.04315.x

Yin, K., Hong, H.L., Algeo, T.J., Churchman, G.J., Li, Z.H., Zhu, Z.M., et al. (2018). Fe-oxide mineralogy of the Jiujiang red earth sediments and implications for Quaternary climate change, southern China. Scientific Reports, 8, 3610. http://doi.org/10.1038/s41598-018-20119-4

Appendix

Text S1. CBD (Citrate-bicarbonate-dithionite) treatment procedure:

1. Milling soil and sediment samples and sieving through a 0.074-mm mesh
2. Measuring magnetic susceptibility at two frequencies (976 Hz and 15616 Hz) and running thermomagnetic curves (under argon)
3. Adding ~4 g sample in a 100 mL centrifuge tube
4. Adding 40 mL 0.3 M citrate solution and 5 mL 1 M sodium bicarbonate solution
5. Heating to 70 ℃
6. Adding 1 g sodium dithionite
7. Heating in a water bath for 15 min (70 ℃) and stirring gently while heating
8. Centrifugation at 4000 rpm for 10 min, then decant the supernatant
9. Drying in an anoxic glove box (100 % N_2) for 5 days
10. Measuring magnetic susceptibility at two frequencies (976 Hz and 15616 Hz) and running thermomagnetic curves (below)

Figure S1. Temperature dependence of magnetic susceptibility of a red soil sample for three partial heating-cooling cycles (red/black denote heating/cooling).

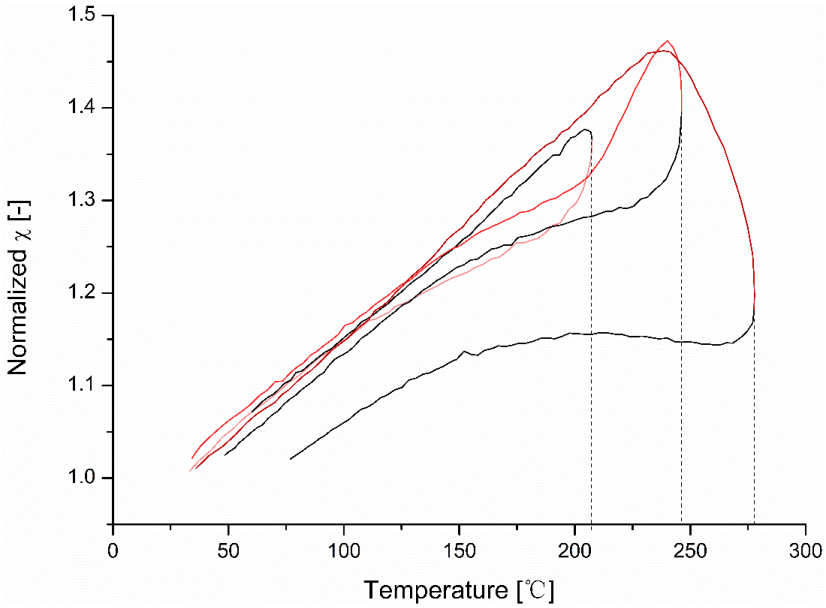

Figure S2. ELNES results from red soil profile I (Fig. 4b shows the measured traverse, Fig. 4e shows part of the ELNES results). Spaces between each curve were adjusted in order to plot the curves clearly.

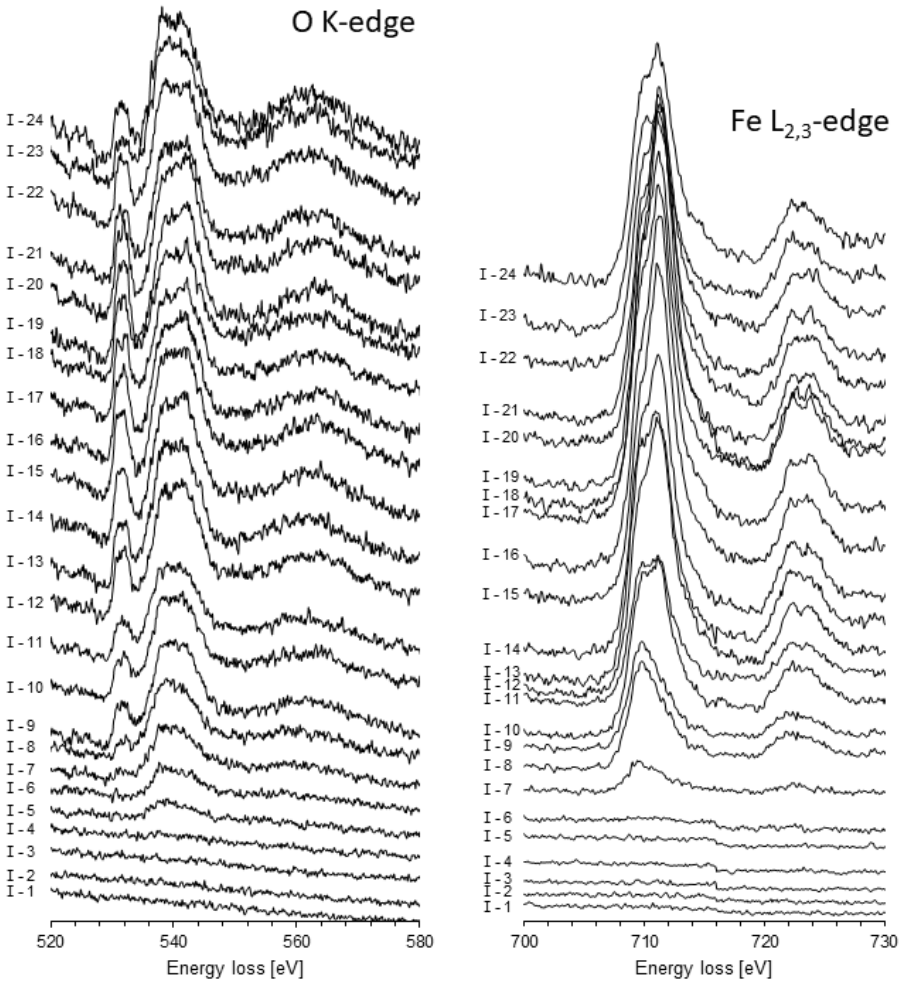

Figure S3. ELNES results from red soil profile II (Fig. 4c shows the measured traverse, Fig. 4e shows part of the ELNES results). Spaces between each curve were adjusted in order to plot the curves clearly.

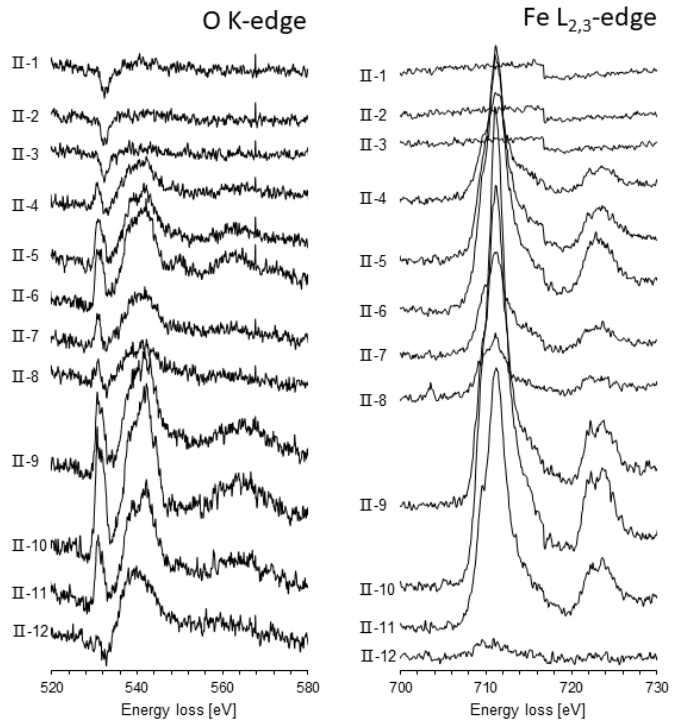

Figure S4. ELNES results from Caohai Lake sediments (Fig. 5b shows the measured traverse, Fig. 5d shows part of the ELNES results). Spaces between each curve were adjusted in order to plot the curves clearly.

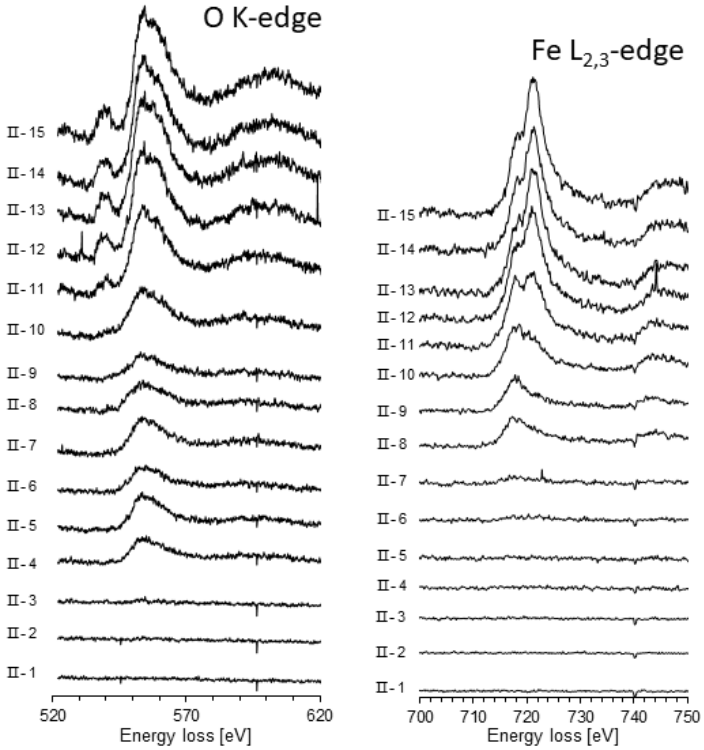

Figure S5. Unmixing of *IRM* acquisition curves after Maxbauer et al. (2016) for limestone bedrock, red soil, and Caohai Lake sediments. Blue, green and pink show model distributions (two components for red soil and lake sediments, three components for limestone), yellow ones display their sum, and gray ones are measured results. For numerical results of Bh, *DP* and *IRM* contribution of measured samples (3 from limestone; 4 from red soil; 3 from Caohai Lake sediments) see Table S7.

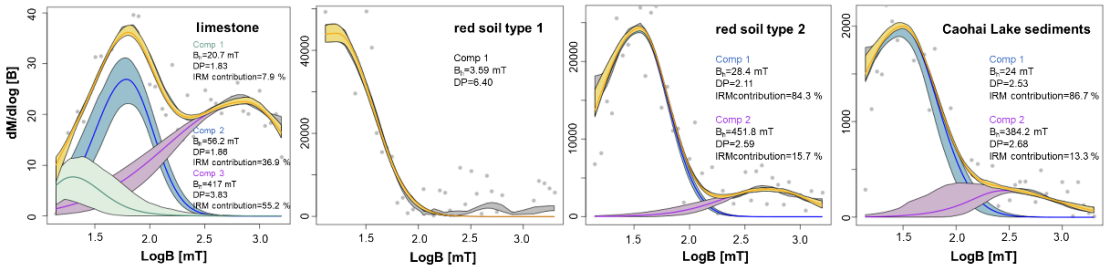

Figure S6. Hysteresis and back-field data (separated for red soil at the western and eastern basin, and Caohai Lake sediments), plotted in the Day diagram with mixing lines (Dunlop, 2002) (Note: 'SD' means stable single domain, termed 'SSD' in this paper). M_s: saturation magnetization, M_{rs}: saturation remanence, H_c: coercivity, H_{cr}: coercivity of remanence. The small figures show typical FORC diagrams (smoothing factor 4) for the red soil (original sample) and lake sediments (magnetic extract). For numerical results of M_{rs}/M_s *and* H_{cr}/H_c (17 from red soil-W; 27 from red soil-E; 13 from Caohai Lake sediments) see Table S3.

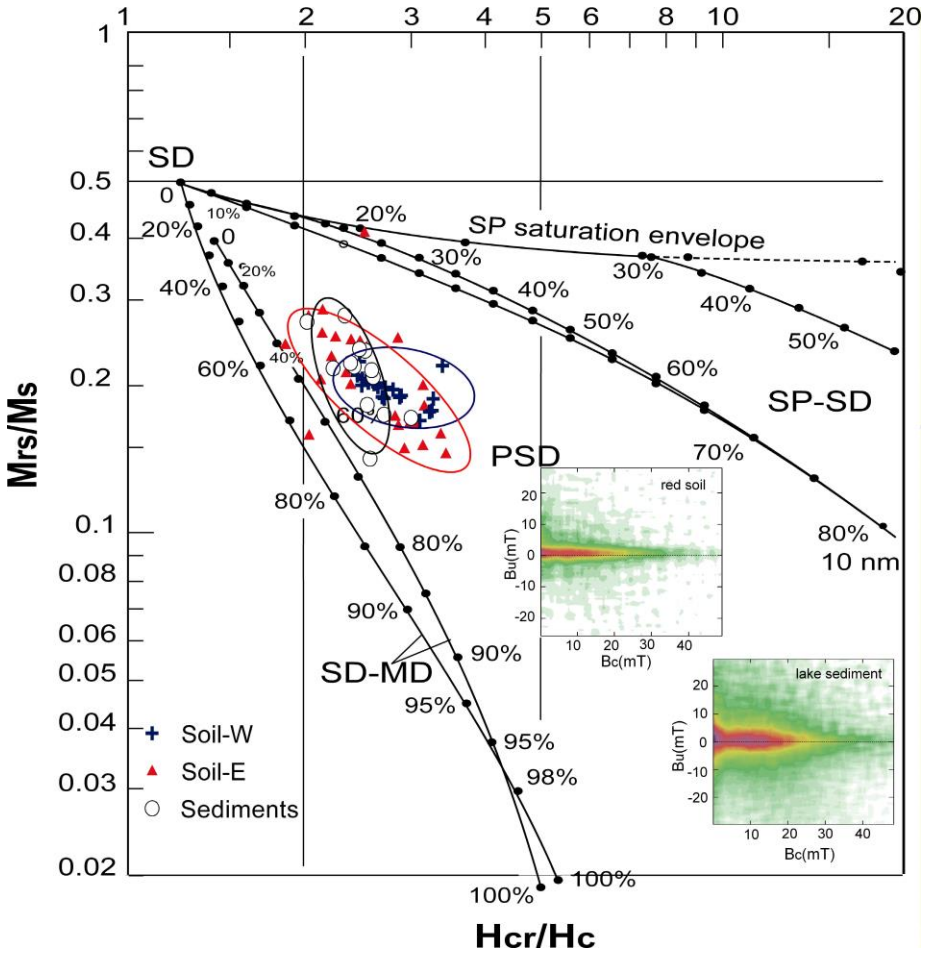

Figure S7. (a) Mass-specific susceptibility (χ) and percentage frequency-dependence χ_{fd}% in three vertical sections of red soil (1 & 2 close to site 13; 3 closes to site 7 in Fig. 1); crosses denote loose surface material collected with a soft brush. (b) Spatial variability of surface volume-specific magnetic susceptibility (κ) at the sampling sites shown in Fig. 1 (mean value of each sites obtained from 7 readings, including standard deviations (except 5 additionally samples from Hu et al., 2015).

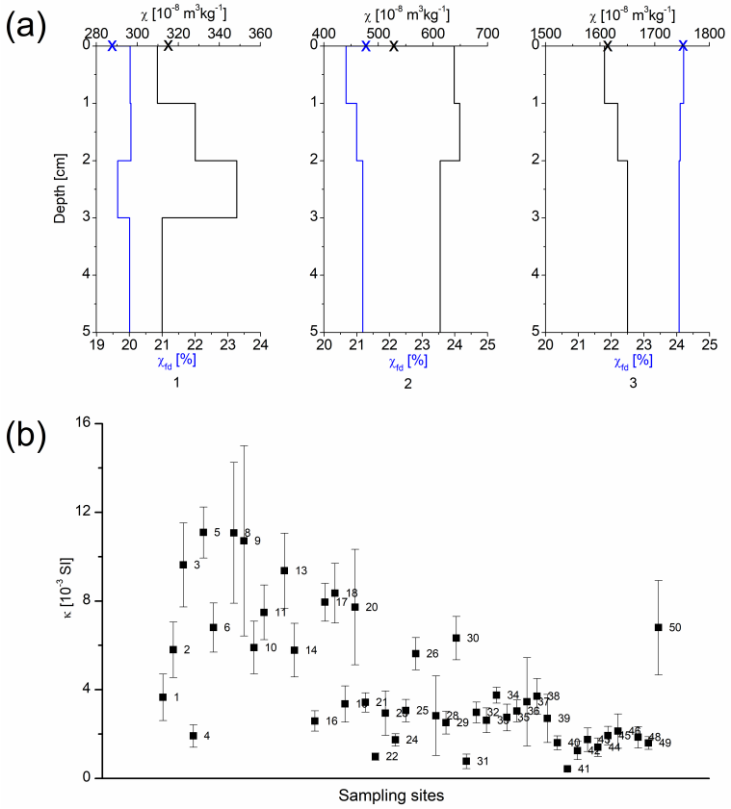

Table S1. Magnetic parameters for red soil (numbers according to Fig. 1), with mean values and standard deviations (std): magnetic susceptibility (χ), saturation isothermal remanent magnetization (*SIRM*), anhysteretic remanent magnetization (*ARM*), hard isothermal remanent magnetization (*HIRM*), S-ratio, percentage frequency-dependence of χ (χ_{fd}%), *SIRM*/χ ratio, *HIRM*/χ ratio. Samples marked by star (*) are from Hu et al. (2015).

		χ [10^{-8} m^3/kg]	SIRM [10^{-3} Am^2/kg]	ARM [10^{-3} Am^2/kg]	HIRM [10^{-5} Am^2/kg]	S-ratio [-]	χ_{fd} [%]	SIRM/χ [kA/m]	HIRM/χ [kA/m]
West	1	683.1	26.98	0.99	124.34	0.95	16.6	3.95	0.18
	2	875.3	28.62	1.56	46.26	0.98	19.5	3.27	0.05
	3	1477.7	46.01	2.60	115.04	0.97	20.2	3.11	0.08
	4	243.3	23.81	0.36	137.02	0.94	12.2	9.79	0.56
	5	1171.6	59.02	1.54	265.02	0.96	14.6	5.04	0.23
	6	903.0	36.82	2.01	22.20	0.99	19.5	4.08	0.02
	7*	2331.0					16.7		
	8	1735.8	53.50	3.26	30.65	0.99	20.6	3.08	0.02
	9	2055.2	74.27	4.22	62.56	0.99	20.4	3.61	0.03
	10	1152.2	30.97	2.45	31.49	0.99	19.3	2.69	0.03
	11	995.3	32.78	1.67	83.53	0.97	18.4	3.29	0.08
	12*	1016.0					14.7		
	13	1870.1	64.75	3.62	67.86	0.99	19.3	3.46	0.04
	14	1390.4	57.78	2.84	62.61	0.99	18.4	4.16	0.05
	15*	940.0					9.8		
	16	417.7	20.24	0.60	10.24	0.99	16.7	4.85	0.02
	17	890.7	32.87	1.78	117.73	0.96	19.6	3.69	0.13
	18	781.5	32.89	1.48	127.23	0.96	18.3	4.21	0.16
	19	216.3	8.17	0.36	26.88	0.97	21.1	3.78	0.12
	20	560.0	30.28	0.96	100.54	0.97	19.2	5.41	0.18
	mean	1085.3	38.81	1.90	84.19	0.98	17.8	4.20	0.12
	std	579.5	17.61	1.13	62.34	0.02	3.0	1.61	0.13
East	21	337.5	20.94	0.75	83.61	0.96	17.9	6.20	0.25
	22	59.9	7.87	0.13	287.44	0.63	20.8	13.14	4.80
	23	413.4	46.81	0.55	360.14	0.92	9.7	11.33	0.87
	24	234.7	23.68	0.40	192.60	0.92	12.0	10.09	0.82
	25	337.9	16.93	0.53	136.80	0.92	18.0	5.01	0.40
	26	650.8	36.09	1.46	157.44	0.96	17.6	5.55	0.24
	27*	323.0					10.9		
	28	271.2	23.34	0.68	134.68	0.94	14.5	8.61	0.50
	29	324.8	21.86	0.56	151.36	0.93	13.2	6.73	0.47
	30	589.4	29.80	0.89	86.49	0.97	14.7	5.06	0.15
	31	162.6	23.51	0.50	191.99	0.92	14.7	14.45	1.18
	32	358.4	26.70	0.58	141.07	0.95	14.0	7.45	0.39
	33	313.0	22.46	0.71	131.42	0.94	15.4	7.18	0.42
	34	420.4	26.68	0.93	162.51	0.94	18.3	6.35	0.39
	35	318.9	18.26	0.44	154.32	0.92	14.0	5.73	0.48
	36	283.5	15.27	0.49	86.50	0.94	15.4	5.39	0.31
	37	414.0	8.49	0.55	35.53	0.96	20.0	2.05	0.09
	38	366.2	14.46	0.53	42.87	0.97	16.2	3.95	0.12
	39	324.0	10.20	0.41	35.34	0.97	16.7	3.15	0.11
	40	122.4	5.28	0.13	11.62	0.98	14.1	4.31	0.09
	41	44.8	4.23	0.05	58.74	0.86	16.6	9.45	1.31
	42	114.6	10.78	0.19	127.75	0.88	13.9	9.41	1.11
	43	183.6	8.23	0.21	51.01	0.94	16.1	4.48	0.28
	44	151.5	11.98	0.15	110.94	0.91	9.5	7.91	0.73
	45	236.9	10.07	0.35	30.07	0.97	16.3	4.25	0.13
	46	454.1	13.61	0.64	9.64	0.99	18.9	3.00	0.02
	47*	82.0					9.2		
	48	290.5	8.89	0.46	0.00	1.00	17.7	3.06	
	49	188.8	6.85	0.24	4.47	0.99	16.4	3.63	0.02
	50	687.6	38.61	0.84	4.47	1.00	11.2	5.62	0.01
	mean	302.0	18.28	0.51	106.46	0.93	15.1	6.52	0.58
	std	160.4	10.72	0.30	86.72	0.07	3.0	3.10	0.92

Table S2. Magnetic and geochemical parameters for Caohai Lake sediments (depths according to Fig. 8), with mean values and standard deviations (std): magnetic susceptibility (χ), saturation isothermal remanent magnetization (*SIRM*), anhysteretic remanent magnetization (*ARM*), hard isothermal remanent magnetization (*HIRM*), *S-ratio*, percentage frequency dependence of χ (χ_{fd}%), *SIRM*/χ ratio, *HIRM*/χ ratio, Fe/Mn, Fe/Ti, Si/Ti, S, Br, loss of ignition (LOI).

Depth	χ			SIRM	ARM	HIRM	S-ratio		χ_{fd}		SIRM/χ	HIRM/χ	Fe/Mn	Fe/Ti	Si/Ti	S	Br	LOI (550)
[cm]	[10^{-8} m^3/kg]			[10^{-5} Am^2/kg]	[10^{-6} Am^2/kg]	[10^{-5} Am^2/kg]	[-]		[%]		[kA/m]	[kA/m]	[-]	[-]	[-]	[-]	[-]	[-]
0-1	25.5	22.9	24.2	259.1	93.0	22.64	0.91	9.1	9.4	8.9	10.17	0.89	65.97	6.99	3.38	0.19	0.0122	45.27
1-2	23.4	22.9	24.3	241.2	95.1	23.63	0.90	7.7	8.9	8.0	10.30	1.01	74.07	6.96	2.82	0.19	0.0142	43.37
2-3	23.6	22.7	24.3	243.7	95.9	21.50	0.91	9.5	8.9	10.2	10.34	0.91	90.42	6.92	3.31	0.25	0.0167	68.92
3-4	23.0	22.0	24.6	241.4	92.1	23.25	0.90	8.9	8.5	10.3	10.48	1.01	100.65	7.29	2.95	0.23	0.0184	35.16
4-5	22.0	21.3	24.0	238.0	98.3	22.33	0.91	8.2	8.1	9.4	10.81	1.01	100.43	6.85	3.13	0.32	0.0167	34.53
5-6	21.6	21.2	23.7	240.6	91.3	24.91	0.90	7.9	7.1	8.7	11.15	1.15	97.59	7.16	3.05	0.33	0.0229	33.18
6-7	21.2	20.6	24.9	232.6	86.1	23.72	0.90	8.0	7.0	7.6	10.98	1.12	105.27	6.98	3.02	0.32	0.0192	36.00
7-8	20.1	23.3	25.8	223.7	74.2	25.39	0.89	7.1	7.3	7.6	11.13	1.26	105.90	6.95	2.64	0.40	0.0170	33.10
8-9	21.7	25.9	26.1	237.6	65.3	30.92	0.87	6.2	7.9	6.4	10.96	1.43	89.85	6.47	2.70	0.20	0.0098	24.93
9-10	21.9	27.7	25.7	230.0	63.1	29.31	0.87	6.3	8.6	6.6	10.50	1.34	91.01	6.58	2.73	0.24	0.0126	25.15
10-11	26.5	29.1	25.6	273.0	76.6	34.82	0.87	8.1	8.0	7.1	10.32	1.32	73.33	6.18	2.47	0.13	0.0060	19.61
11-12	26.1	37.1	28.0	268.9	76.2	32.98	0.88	8.0	10.6	7.5	10.32	1.27	95.68	6.33	2.37	0.17	0.0056	19.90
12-13	24.8	44.5	28.0	253.4	72.5	31.50	0.88	7.2	12.1	9.0	10.22	1.27	95.81	6.76	2.45	0.27	0.0070	19.90
13-14	26.1	47.2	29.0	272.1	71.3	33.04	0.88	7.2	13.3	8.5	10.42	1.27	94.12	6.15	2.53	0.13	0.0072	20.81
14-15	27.8	52.6	31.5	282.4	77.5	32.85	0.88	7.9	13.6	9.1	10.14	1.18	76.46	6.17	2.52	0.09	0.0045	17.70
15-16	30.6	55.2	34.3	298.1	85.9	34.83	0.88	8.4	14.1	10.5	9.76	1.14	93.60	6.15	2.40	0.07	0.0072	19.59
16-17	32.3	56.9	41.5	314.9	98.7	32.45	0.90	9.0	14.3	12.1	9.76	1.01	87.75	6.26	2.46	0.08	0.0076	17.66
17-18	33.3	58.1	41.6	320.0	103.1	33.27	0.90	9.5	13.6	11.8	9.61	1.00	85.13	6.27	2.50	0.07	0.0058	15.13
18-19	31.9	57.1	40.1	302.7	102.9	35.09	0.88	11.1	14.6	13.2	9.47	1.10	90.98	6.41	2.32	0.08	0.0057	15.78
19-20	39.0	57.5	42.7	362.5	124.6	35.02	0.90	11.6	14.4	12.4	9.28	0.90	87.07	6.47	2.37	0.08	0.0046	16.62
20-21	40.4	57.1	42.7	376.5	131.0	36.09	0.90	10.6	14.3	13.3	9.32	0.89	78.26	6.51	2.47	0.10	0.0036	18.34
21-22	35.7	57.3	44.9	331.1	115.8	34.52	0.90	11.0	14.5	13.4	9.27	0.97	85.42	6.29	2.48	0.08	0.0054	15.63
22-23	40.7	55.4	47.6	370.3	123.0	35.15	0.91	11.3	14.2	12.5	9.09	0.86	86.41	6.48	2.49	0.09	0.0073	17.10
23-24	42.0	54.4	49.4	364.4	123.7	35.84	0.90	11.5	14.1	13.4	8.68	0.85	79.87	6.08	2.35	0.08	0.0019	15.63
24-25	47.3	54.4	52.9	389.0	139.0	35.64	0.91	12.6	14.1	14.3	8.23	0.75	79.80	6.35	2.42	0.07	0.0036	14.60
25-26	53.2	52.5	57.4	429.4	158.6	35.72	0.92	13.3	13.5	14.5	8.06	0.67	77.62	6.25	2.47	0.06	0.0041	14.54
26-27	56.3	50.5	60.7	447.3	178.8	34.89	0.92	13.7	13.4	14.0	7.94	0.62	77.99	6.08	2.48	0.06	0.0034	13.85
27-28	58.4	49.4	62.9	454.2	183.9	35.94	0.92	13.7	13.3	14.3	7.78	0.62	74.67	6.32	2.53	0.06	0.0034	14.87
28-29	59.7	48.9	62.5	459.6	192.2	34.69	0.92	13.9	13.4	14.3	7.70	0.58	80.40	6.20	2.51	0.05	0.0042	13.93
29-30	61.1	47.1	64.5	472.6	193.3	34.13	0.93	13.1	13.2	14.6	7.74	0.56	72.28	6.16	2.44	0.05	0.0053	14.26

30-31	58.8	45.6	65.4	464.4	188.0	34.30	0.93	13.7	12.9	14.8	7.90	0.58	77.34	6.28	2.59	0.06	0.0025	14.53
31-32	57.6	44.8	65.6	446.9	170.8	32.27	0.93	13.8	12.9	14.4	7.76	0.56	74.12	6.23	2.43	0.06	0.0050	12.99
32-33	58.6	44.1	62.7	446.1	181.3	35.76	0.92	14.0	13.2	14.6	7.61	0.61	70.22	6.24	2.55	0.07	0.0070	13.07
33-34	58.9	45.2	62.6	466.8	186.5	33.75	0.93	14.0	12.3	15.2	7.93	0.57	79.42	6.21	2.55	0.05	0.0054	13.38
34-35	58.6	41.5	60.5	514.5	178.6	33.17	0.94	12.6	12.7	13.8	8.78	0.57	77.70	6.33	2.63	0.05	0.0041	14.15
35-36	53.2	41.5	58.7	439.9	167.6	35.73	0.92	13.1	11.5	14.1	8.28	0.67	65.18	6.21	2.68	0.05	0.0059	13.12
36-37	53.5	39.8	57.5	451.8	170.4	41.11	0.91	14.2	11.3	14.5	8.44	0.77	79.88	6.33	2.56	0.05	0.0050	12.90
37-38	53.3	36.3	56.1	470.5	166.2	42.17	0.91	12.8	9.6	13.1	8.83	0.79	61.39	6.28	2.56	0.06	0.0046	15.68
38-39	53.2		54.6	450.0	162.1	40.92	0.91	13.0		13.4	8.47	0.77	74.05	6.02	2.58	0.06	0.0053	14.22
39-40	53.2		51.7	484.8	158.3	43.59	0.91	12.4		13.6	9.12	0.82	71.14	6.12	2.72	0.05	0.0044	14.04
40-41	53.8		50.8	517.1	152.6	53.09	0.90	11.8		12.4	9.62	0.99	66.43	6.21	2.65	0.04	0.0035	12.24
41-42	56.5		49.1	535.4	132.2	61.88	0.88	11.0		12.4	9.48	1.10	59.77	6.59	2.53	0.05	0.0045	11.63
42-43	57.7		47.9	589.8	136.9	63.99	0.89	10.2		12.6	10.22	1.11	35.57	6.68	2.83	0.05	0.0069	11.37
43-44	61.7		47.4	680.3	107.6	86.31	0.87	8.4		9.8	11.02	1.40	36.55	6.00	2.64	0.04	0.0048	9.48
mean	**41.0**	**41.9**	**43.8**	**372.5**	**125.9**	**35.77**	**0.90**	**10.6**	**11.7**	**11.6**	**9.40**	**0.94**	**80.06**	**6.43**	**2.62**	**0.12**	**0.0075**	**20.41**
std	**15.1**	**13.2**	**14.8**	**114.3**	**41.8**	**11.69**	**0.02**	**2.5**	**2.6**	**2.7**	**1.12**	**0.26**	**14.99**	**0.33**	**0.25**	**0.10**	**0.0051**	**11.49**

Table S3. M_s: saturation magnetization, H_c: coercivity and hysteresis ratios M_{rs}/M_s, H_{cr}/H_c of red soil (separated into samples from the western and eastern basin) and Caohai Lake sediments, with mean values and standard deviations (std).

Red soil west	M_s [nAm^2]	H_c [mT]	M_{rs}/M_s	H_{cr}/H_c	**Red soil east**	M_s [nAm^2]	H_c [mT]	M_{rs}/M_s	H_{cr}/H_c	**Caohai sediments**	M_s [nAm^2]	H_c [mT]	M_{rs}/M_s	H_{cr}/H_c
1	1801.00	5.68	0.17	3.21	**21**	873.70	8.77	0.22	2.52	**HQ01-1**	36.27	12.14	0.17	2.69
2	2902.00	5.19	0.19	2.79	**22**	169.40	24.16	0.38	2.50	**HQ01-5**	35.31	14.80	0.22	2.50
3	4670.00	5.01	0.19	2.71	**23**	2173.00	11.86	0.19	2.37	**HQ01-7**	41.47	14.21	0.21	2.40
4	14150.00	6.31	0.19	2.59	**24**	1099.00	10.84	0.20	2.33	**HQ01-9**	18.61	13.65	0.14	2.55
5	5802.00	6.74	0.18	3.25	**25**	1231.00	7.07	0.16	2.96	**HQ01-11**	38.78	16.88	0.25	2.00
6	1541.00	5.85	0.21	2.45	**26**	1231.00	6.42	0.19	2.55	**HQ01-15**	62.98	12.45	0.20	2.58
8	5732.00	4.77	0.18	2.68	**28**	3159.00	9.30	0.24	2.12	**HQ01-23**	53.65	11.46	0.17	2.52
9	3333.00	4.89	0.19	2.54	**29**	1568.00	10.27	0.27	2.13	**HQ01-27**	56.46	11.44	0.22	2.45
10	4927.00	5.49	0.19	2.47	**31**	951.50	12.17	0.26	2.02	**HQ01-28**	70.45	11.49	0.26	2.32
11	3312.00	5.20	0.16	3.09	**32**	1178.00	7.32	0.15	3.35	**HQ01-29**	73.45	9.81	0.20	2.57
13	3299.00	4.82	0.18	2.70	**33**	1889.00	8.00	0.24	2.24	**HQ01-35**	56.51	11.41	0.20	2.21
14	1969.00	5.70	0.19	2.62	**34**	972.20	7.92	0.23	2.37	**HQ01-39**	70.65	11.87	0.21	2.37
16	738.20	5.64	0.18	2.86	**35**	1539.00	7.20	0.21	2.20	**HQ01-44**	150.50	10.86	0.16	2.99
17	1590.00	5.64	0.18	2.88	**36**	1273.00	7.32	0.20	2.56	**mean**	**58.85**	**12.50**	**0.20**	**2.47**
18	1279.00	6.24	0.20	2.56	**37**	1562.00	4.09	0.14	3.41	**STD**	**32.05**	**1.91**	**0.04**	**0.24**
19	409.90	5.57	0.17	3.24	**38**	1673.00	4.76	0.16	2.97					
20	1503.00	8.18	0.21	3.37	**39**	1070.00	4.78	0.16	2.81					
mean	**3468.12**	**5.70**	**0.18**	**2.82**	**40**	480.80	4.59	0.15	2.03					
STD	**3224.58**	**0.84**	**0.01**	**0.30**	**41**	635.10	14.64	0.23	2.84					
					42	1532.00	9.99	0.23	1.84					
					43	460.20	7.05	0.19	3.13					
					44	1524.00	8.92	0.16	2.85					
					45	775.20	5.88	0.17	3.14					
					46	1059.00	4.66	0.14	3.13					
					48	514.30	5.07	0.16	3.04					
					49	313.70	4.58	0.14	2.91					
					50	8016.00	7.93	0.19	2.11					
					mean	**1441.56**	**8.35**	**0.20**	**2.61**					
					STD	**1456.00**	**4.13**	**0.05**	**0.45**					

Table S4. Magnetic susceptibility (χ) and percentage frequency-dependence of χ (χ_{fd}%) before and after CBD treatment, with mean values and standard deviations (std)

	Before CBD		**After CBD**		**% change after CBD**	
	χ [10^{-8} m^3/kg]	χ_{fd} [%]	χ [10^{-8} m^3/kg]	χ_{fd} [%]	χ [%]	χ_{fd} [%]
Red soil	268.6	18.2	92.1	17.5	-65.7	-3.6
	455.9	18.0	47.4	19.4	-89.6	+7.5
	706.1	19.7	399.3	20.4	-43.5	+3.5
	172.2	18.7	35.5	18.3	-79.4	-2.1
	167.5	17.7	41.8	16.1	-75.0	-9.0
mean	**354.1**	**18.4**	**123.2**	**18.3**	**-70.6**	**-0.8**
std	**228.8**	**0.8**	**155.9**	**1.7**	**17.5**	**6.4**
Caohai lake sediments	7.8	11.8	4.2	4.7	-46.3	-60.3
	8.2	11.9	4.5	5.4	-45.1	-54.5
	18.3	15.8	5.1	5.2	-72.1	-67.4
	17.9	14.7	5.9	5.7	-67.2	-61.4
	19.1	10.2	10.6	5.1	-44.5	-50.2
mean	**14.3**	**12.9**	**6.1**	**5.2**	**-55.1**	**-58.8**
std	**5.7**	**2.3**	**2.6**	**0.4**	**13.5**	**6.6**

Table S5. Broadband-frequency dependence of magnetic susceptibility for red soil separated in samples with $\chi>10^{-5}$ m^3/kg (red soil H) and $\chi<10^{-5}$ m^3/kg (red soil L) and Caohai Lake sediments with lower χ (L) from 9-13 cm and higher χ (H) from 31-35 cm.

Frequency [Hz]	125	250	500	1000	2000	4000	8000	16000
Red soil H normalized χ	1.440	1.356	1.262	1.255	1.192	1.147	1.102	1.000
	1.308	1.254	1.171	1.190	1.143	1.119	1.090	1.000
	1.457	1.404	1.254	1.292	1.231	1.193	1.095	1.000
	1.441	1.353	1.262	1.245	1.174	1.133	1.085	1.000
	1.451	1.359	1.248	1.255	1.193	1.153	1.110	1.000
	1.446	1.354	1.238	1.259	1.200	1.165	1.124	1.000
	1.401	1.328	1.276	1.223	1.134	1.085	1.003	1.000
	1.364	1.292	1.243	1.190	1.131	1.090	1.049	1.000
	1.411	1.337	1.289	1.239	1.176	1.137	1.095	1.000
	1.326	1.265	1.220	1.177	1.105	1.085	1.046	1.000
mean	**1.405**	**1.330**	**1.246**	**1.233**	**1.168**	**1.131**	**1.080**	**1.000**
std	**0.054**	**0.047**	**0.033**	**0.037**	**0.038**	**0.036**	**0.036**	**0.000**
Red soil L normalized χ	1.380	1.301	1.179	1.239	1.192	1.179	1.163	1.000
	1.345	1.277	1.137	1.238	1.202	1.190	1.181	1.000
	1.461	1.380	1.216	1.291	1.240	1.216	1.189	1.000
	1.422	1.374	1.195	1.282	1.234	1.207	1.191	1.000
	1.331	1.273	1.233	1.186	1.113	1.068	1.006	1.000
	1.342	1.279	1.232	1.186	1.119	1.096	1.057	1.000
	1.350	1.287	1.236	1.173	1.126	1.096	1.056	1.000
	1.321	1.254	1.215	1.171	1.115	1.078	1.047	1.000
	1.297	1.242	1.202	1.169	1.106	1.084	1.053	1.000
	1.442	1.354	1.296	1.235	1.138	1.119	1.067	1.000
mean	**1.369**	**1.302**	**1.214**	**1.217**	**1.158**	**1.133**	**1.101**	**1.000**
std	**0.055**	**0.050**	**0.041**	**0.046**	**0.053**	**0.058**	**0.071**	**0.000**
Lake sediments L normalized χ	1.065	1.006	1.036	1.067	1.028	0.978	1.027	1.000
	1.034	1.044	1.080	1.057	1.051	1.035	1.002	1.000
	1.047	1.077	1.072	1.091	1.075	1.062	1.080	1.000
	1.033	0.997	1.047	1.006	1.012	0.984	0.989	1.000
	1.104	1.080	1.094	1.089	1.048	1.041	1.037	1.000
mean	**1.057**	**1.041**	**1.066**	**1.062**	**1.043**	**1.020**	**1.027**	**1.000**
std	**0.029**	**0.038**	**0.024**	**0.034**	**0.024**	**0.037**	**0.035**	**0.000**
Lake sediments H normalized χ	1.234	1.177	1.168	1.126	1.097	1.016	1.033	1.000
	1.245	1.186	1.166	1.126	1.093	1.061	1.039	1.000
	1.247	1.175	1.168	1.136	1.095	1.073	1.044	1.000
	1.240	1.175	1.149	1.127	0.982	1.057	1.029	1.000
	1.213	1.165	1.144	1.117	1.082	1.055	1.039	1.000
mean	**1.236**	**1.176**	**1.159**	**1.126**	**1.070**	**1.052**	**1.037**	**1.000**
std	**0.014**	**0.008**	**0.012**	**0.006**	**0.050**	**0.021**	**0.006**	**0.000**

Table S6. Statistical results for the broadband-frequency dependence of magnetic susceptibility for red soil H and lake sediments L samples (see Fig. 7): slopes of χ-log(f) in the frequency ranges 0.125-1 kHz (lf) and 1-16 kHz (hf), slope difference between these two ranges (Δslope), and 95 % confidence range of the slope difference (product of slope standard error and t-score). For slope calculation, χ-values normalized to their 16 kHz result are used, and log(f) is obtained by inserting f in Hz. Values (a) result by calculating slopes using all data points, values (b) result from averaging sample slopes (values in brackets list the number N of data points in the analysis, defining the degree of freedom N-2 for determining the t-score).

	red soil H		**lake sediment L**	
	(a)	**(b)**	**(a)**	**(b)**
slope lf	-0.19920(40)	-0.19920(10)	+0.011343(20)	+0.011342(5)
slope hf	-0.18378(50)	-0.18268(10)	-0.04634(25)	-0.04634(5)
Δslope	+0.01542	+0.01652	-0.05977	-0.05976
95 % range of Δslope	±0.05014	±0.08294	±0.04281	±0.04417

Table S7. B_h, *DP* and *IRM* contribution obtained from *IRM* unmixing.

				comp 1	comp 2	comp 3
limestone	1	Bh	[mT]	79.9	1269	19.32
		DP	[-]	2.03	10.8	1.38
		IRM contribution	[%]	58.1%	30.5%	11.5%
	3	Bh	[mT]	56.2	417	20.69
		DP	[-]	1.86	3.84	1.83
		IRM contribution	[%]	32.8%	58.1%	9.1%
	4	Bh	[mT]	74.4	1612	17.24
		DP	[-]	1.91	6.39	1.64
		IRM contribution	[%]	70.7%	12.5%	16.8%
red soil	9	Bh	[mT]	3.59		
		DP	[-]	6.40		
	14	Bh	[mT]	18.8		
		DP	[-]	2.06		
	18	Bh	[mT]	18.3	314	
		DP	[-]	2.20	2.15	
		IRM contribution	[%]	89.1%	10.9%	
	23	Bh	[mT]	28.4	452	
		DP	[-]	2.11	2.59	
		IRM contribution	[%]	83.0%	17.0%	
Caohai sediments	8	Bh	[mT]	38.4	384	
		DP	[-]	2.36	1.96	
		IRM contribution	[%]	83.4%	16.6%	
	29	Bh	[mT]	24.0	384	
		DP	[-]	2.53	2.68	
		IRM contribution	[%]	83.6%	16.4%	
	44	Bh	[mT]	27.6	421	
		DP	[-]	2.62	1.97	
		IRM contribution	[%]	80.5%	19.5%	

Chapter VI: Conclusions and outlook

The fundamental question of the study was the possible humidity control of magnetite alteration in rock weathering. The entity of the results supports the hypothesis that humidity favors magnetite oxidation, most clearly shown by the laboratory experiment. However, the laboratory results also indicate that the alteration of magnetite does not systematically vary with humidity. From the results of the actualistic study we learn that the original rock composition and the type of weathering (i.e., physical or chemical) will very likely override climate-related effects of magnetite weathering. At least for basalts, which are the by far strongest magnetic rocks delivering weathered materials to sinks, the rock magnetic inhomogeneities are too much different within spatial scales of several meters and even less, and thus varying mixtures of weathered materials from eroded areas will produce considerable differences in the magnetic properties. Even if climate conditions matter for the type and degree of magnetite alteration, material mixtures due to spatial variation of erosion and transport by surface water and wind will very likely also change in different climates, and the mixed materials arriving in sinks such as lake sediments will be strongly affected by the variation in material mixing. It is thus expected that magnetic variation in paleoclimate archives will likely not record magnetite alteration in the catchment due to climate, although the alteration may be climate-specific. On the one hand this is a disappointing message for interpreting magnetic proxies in paleoclimate archives, on the other hand the results suggest that within the multiple processes that could influence magnetic properties in sediments, the climate-specific magnetite alteration during rock weathering can be excluded as a major control.

The actualistic study shows that magnetite alteration in the basalts is relatively mild, even when the properties of strongly weathered pebbles and fresh rock properties are compared. The degree of magnetite alteration at partially weathered rock surfaces was not investigated in detail in this study, but it is certainly even less than in the pebbles that are already released from the solid rock. A good message from these results is that weathering of basalts will not or at least not generally affect the properties of magnetite in an extensive way and therefore will not easily destroy natural remanent magnetizations that are used in paleomagnetic studies.

In detail, we can summarize that according to the results of laboratory experiment, alteration of magnetite is observed in all 70 °C setups with a shift of the Verwey transition temperature. The Verwey transition and lattice constant turns out to be the most sensitive indicators of maghemitization. Even though, the experiment proved that humidity is important for LTO, and

higher and long-lasting humidity causes the strongest degree of alteration (HH setup), but there is no linear humidity dependence as we can recognize from the larger alteration of the very dry setup compared to the intermediate humidity setup. Additionally, the χ-T curves, in particular low-temperature curves, suggest that alteration is not producing a shell-core structure but instead the entire volume of particles is similarly affected.

The actualistic study is not as straightforward as the laboratory experiment. As mentioned, the alteration of magnetite is relatively small, and it seems that magnetic properties variations of magnetite in basalts and their weathering materials mainly depend on the rock types, and there is no evidence that climate conditions control the alteration of magnetite in the basalts beyond the effects caused by rock mineralogy. Differences in original rock composition and in type of weathering (physical/chemical) will very likely override climate-related effects of magnetite weathering.

The source-sink study in Heqing Basin suggest a surprising explanation for the absence of a superparamagnetic signature in the long Heqing core (Core-HQ) that was used for paleoclimatic interpretation for the past ~1 Ma (Hu et al., 2015). The TEM results reveal ~100 nm large aggregates of mainly ~10-15 nm sized nanoparticles in the red soil and in the Caohai Lake sediments. The nanoparticles in the aggregates are tighter packed in red soil than in the lake sediments, and the aggregates in the red soil appear to be larger. ELNES results identify the nanoparticles as magnetite (and/or maghemite), with higher contribution of hematite in aggregates of the Caohai Lake sediments. Interaction of the nano-magnetite particles leads to a wide range of effective magnetic grain sizes in terms of their domain state behavior. The effective grain size is naturally larger than the physical size of the individual nanoparticles, and tails into the SSD range. Interaction is less for looser packing and in the presence of hematite that creates larger distances. This model explains the observed differences of macroscopic magnetic characteristics between red soil and lake sediments by a shift of the effective grain size distribution towards smaller size. The results of broadband-frequency dependence of χ support the model. In view of these results, it can be speculated that in Core-HQ, the magnetite nanoparticles are not or only partially erased, and the absence of a superparamagnetic signature could be explained by strong disintegration of the nanoparticle aggregates. In this case, the properties of the nano-magnetite fraction would still contribute to the overall magnetic properties of the lacustrine sediments, at least to magnetic susceptibility and saturation magnetization, in contrast to the interpretation of Hu et al. (2015), who related the magnetic

proxy signal to climate-specific alteration of the bedrock-inherited larger sized magnetite fraction assuming complete dissolution of the superparametic magnetite particles.

Another aspect from the source-sink study concerns the possible climate-specific properties of the nano-magnetite. Spatial distributions of magnetic parameters in the red soil around Heqing Basin clearly show that the amount of pedogenically produced nano-magnetite is bedrock-dependent, and even varies within the same bedrock type. The contribution of magnetite nano-particles to the magnetic properties of lake sediments diminishes by disintegration of aggregates and increased magnetite-to-hematite transformation and may even become neglectable compared to the larger sized detrital magnetic fraction. The ratio of saturation magnetization and magnetic susceptibility is suggested as a useful proxy in red soil, caused by climate-related initial LTO degree in the nano-particles of the aggregates.

The obtained results encourage several meaningful future studies, in both ways, laboratory setups and natural environments. One can make use of the advantage of laboratory experiments, i.e. the control of potentially influencing factors as well as the experimental period, and other natural settings could be used for actualistic studies.

In this present work, only one type of natural magnetite sample was used for the laboratory experiment. In future experimental designs, magnetite samples with different grain size, and also natural soil and weathered material from rocks could be taken into consideration. Moreover, setups with a larger temperature range between ~50 °C to 100 °C and more variable humidity options could improve our knowledge on extrapolating to room temperature processes that happen on a longer (i.e., beyond laboratory) timescale. Finally, the experimental time and pH conditions could be varied, and sampling in more time intervals could provide more detailed information about the temporal course of ongoing processes.

In this present work, basalts and their well-related pebbles do not show consistent climate-dependent variations, which partially might be due to the influence of the variability in rock mineralogy that is hiding climate effects. In future studies, other type of rocks with less variability of rock mineralogy, such as granites, could be tested. It is suggested that sampling of weathered pebbles should be done with extreme caution to ensure an intimate relationship with the underlying fresh rock. Studies could be also extended to soil material above the fresh rock, which is further influenced by pedogenic processes.

The source-sink study has indicated several interesting aspects which are worth to be considered for further investigations. Red soil above low-magnetic bedrock is a very common natural setting and therefore deserves more research on potential use of their magnetic properties related to climate conditions. The origin of the high-magnetic red soil is speculated to be a produced by bacterial activities. Aggregates resembles Fe-oxyhydroxide nanoparticle aggregates of up to >100 nm observed by TEM which brings up a possible approach for future studies on the origin of the pedogenic nano-magnetites. Researching the magnetic properties caused by the different structure and magnetic mineral contents of the aggregates are another challenging aspect. Moreover, it is a challenging question, how one could discriminate the magnetic signature of the Caohai Lake sediments into the contributions of the magnetite nanoparticle aggregates and the larger sized multidomain magnetite inherited from bedrock weathering. Finally, the $SIRM/\chi$ ratio is found to be relatively constant for red soil above the same bedrock type, which is assumed to be controlled by a shift of the specific SP-SSD distribution in the aggregates. This could be related to environmental conditions and is therefore a potential paleoclimate proxy. Further research is required to elucidate whether bedrock-specific transfer functions can be determined.

References

Hu, S.Y., Goddu, S.R., Herb, C., Appel, E., Gleixner, G., Wang, S.M., et al. (2015). Climate variability and its magnetic response recorded in a lacustrine sequence in Heqing basin at the SE Tibetan Plateau since 900 ka. Geophysical Journal International, 201, 444-458. https://doi.org/10.1093/gji/ggv033

Zhang, Q., Appel, E. Basavaiah, N., Hu, S.Y., Zhu, X.H., Neumann, U., Is alteration of magnetite in rock weathering related to climate? (in progress)

Zhang, Q., Appel, E., Hu, S., Pennington, R.S., Meyer, J., Neumann, U., Burchard, M., Allstädt, F., Wang, L.S. (2020). Nano-magnetite aggregates in red soil on low magnetic bedrock, their change during transport and implications for paleoclimate studies. Journal of Geophysical Research: Solid Earth. https://doi.org/10.1029/2020JB020588

Zhang, Q., Appel, E., Stanjek, H., Byrne, J.M., Berthold, C., Sorwat, J., Rösler, W. & Seemann, T. (2020). Humidity related magnetite alteration in an experimental setup. Geophysical Journal International. https://doi.org/10.1093/gji/ggaa394

Appendix

Notations and abbreviations

κ	magnetic susceptibility in SI unit
χ	mass-specific magnetic susceptibility
χ_{lf}	low frequency mass-specific magnetic susceptibility
χ_{hf}	high frequency mass-specific magnetic susceptibility
χ_{fd}%	frequency-dependent susceptibility
χ(f)	broadband frequency dependent susceptibility
ARM	anhysteretic remanent magnetizations
IRM	isothermal remanent magnetization
SIRM	saturation isothermal remanent magnetization
HIRM	hard isothermal remanent magnetization
M_s	saturation magnetization
M_{rs}	saturation remanent
H_c	coercive force
H_{cr}	remanent coercive force
T_v	Verwey transition temperature
T_c	Curie temperature
B_h	applied field at which the mineral phase acquires half of its SIRM
DP	dispersion parameter
XRD	X-ray diffraction
XRF	X-ray fluorescence
TEM	transmission electron microscopy
SEM	scanning electron microscope
HRTEM	high-resolution transmission electron microscopy
EELS	electron energy loss spectrometer
ELNES	energy-loss near-edge structure
SI	spectrum imaging
LOI	loss on ignition
DOC	dissolved organic carbon
FORC	first-order reversal curve
CBD	citrate-bicarbonate-dithionite treatment
SD	single-domain
SSD	stable single-domain
MD	multi-domain
LTO	low-temperature oxidation